PASSIVELY ADAPTIVE TIDAL TURBINE BLADES: DESIGN METHODOLOGY AND EXPERIMENTAL TESTING

by

Robynne Murray

Submitted in partial fulfillment of the requirements
for the degree of Doctor of Philosophy

at

Dalhousie University
Halifax, Nova Scotia
July 2016

Dedication

This thesis is dedicated to my loving fiancé, Braden Murphy, for always encouraging me to pursue my dreams and giving me endless support to achieve them.

TABLE OF CONTENTS

LIST OF TABLES

LIST OF FIGURES

ABSTRACT

Composite tidal turbine blades with bend-twist (BT) coupled layups allow the blade to self-adapt to local site conditions by passively twisting to reduce the angle of incoming flow (feathering). Passive feathering has the potential to reduce the fluid forces on both the blades and support structure, as well as shed power at extreme site conditions. Decreased hydrodynamic thrust and power at extreme conditions means that the turbine support structure, generator, and other components can be sized appropriately for rated conditions, increasing their utilization factor and increasing the device cost effectiveness.

This thesis reports the outcomes of research into passively adaptive BT blades. A design tool was developed that couples a finite element model (FEM) and a blade element momentum theory (BEMT) model, to investigate the interactive fluid and structural performance of BT blades. The design tool also incorporated a composite material failure analysis, allowing fast and efficient verification of the structural integrity of different blade designs. Through experimental testing of blades designed using the tool, BT composite blades were shown to have up to 10% lower thrust loads compared to rigid blades, with similar load reductions predicted by the design tool. This proved the concept and demonstrated a design methodology for BT coupling for tidal turbine blades at small-scale.

A case study of a full-scale turbine with 4.0 m BT blades with a pre-deformed blade shape (slightly decreased pre-twist distribution along the blade span) was investigated using the design tool. By reducing the pre-twist of the blade by 2.3º at the blade tip, the blade twisted under load to its optimum shape at design conditions, and continued to twist to feather toward extreme flow speeds. These blades were found to have 10% more power capture between the cut-in and design speeds, and a 10% reduction in power and 5% reduction in thrust loads at extreme flow speeds. This makes pre-deformed BT blades a potential solution to structural load reduction, as well as power capture optimization, which would increase the overall cost-effectiveness of the tidal turbine.

LIST OF ABBREVIATIONS AND SYMBOLS USED

VARIABLES

A blade element area

a axial induction factor

a' tangential flow induction factor

α_s stall angle of attack

α angle of attack

b intercept of linear best fit equation

B number of blades

β_o pre-twist geometry of blade

β_n new pre-twist blade geometry

β_{set} pitch setting at the blade root

c chord length

$[C]$ constitutive matrix

C_L lift coefficient

C_D drag coefficient

C_{F_A} Buhl high induction correction

$C_{L,s}$ lift coefficient at the stall angle

$C_{D,s}$ drag coefficient at the stall angle

$C_{D\,max}$ maximum drag coefficient in the fully stalled regime

C_P power coefficient

C_T thrust coefficient

C_{My} coefficient of blade root bending moment in the axial direction

C_{Mx} coefficient of blade root bending moment in the radial direction

dr radial length of the blade element

dL lift force on blade element

dD drag force on blade element

$dF_{A,1}$ axial force from blade element

$dF_{A,2}$ axial momentum theory force

$dF_{T,1}$ tangential force from blade element

$dF_{T,2}$ tangential momentum theory force

dQ torque on blade element

ε strain

E Young's modulus

F_B buoyancy force

F combined tip and hub loss correction factor

F_{Tip} tip loss correction factor

F_{Hub} hub loss correction factor

F_{load} vector of loads applied

g gravitational constant

G shear modulus

i sample number

I turbulence intensity

j aspect ratio of the blade

k_{xy} Twisting curvature of BT laminate (1/m)

k iteration number

K_L Viterna-Corrigan post stall correction for lift

K_D Viterna-Corrigan post stall correction for drag

K stiffness matrix

λ tip-speed ratio

m mass of turbine blade

$[M]$ mass matrix

n number of sample points

P power captured by the rotor

ρ_{body} body material density

ρ_{fluid} fluid density

ϕ_i induced twist

r radial location of blade element

R_{hub} radius of hub

$R_{e,chord}$ Reynolds number

R radius of turbine

s slope of linear best fit equation

σ stress

σ_1 normal stress, local-1 direction, along fibers

σ_2 normal stress, local-2 direction, perpendicular to fibers

τ_{12} shear stress in 1-2 plane

T thrust load on rotor

θ relative inflow angle

u displacement vector

U_∞ incoming flow velocity

U_d rotor disk velocity

μ_B bias uncertainty

μ_P precision uncertainty

μ_x total uncertainty

ν Poisson's ratio

V_{rel} relative inflow velocity

V_{body} volume of body

ω rotor rotational velocity

Ω wake rotational speed

W weight force

x known value

x_{SEE} standard error of estimate

x_{SS_R} summed square of residuals

y measured value

ACRONYMS

AC   Aerodynamic center

BET   Blade element theory

BEMT Blade element momentum theory

BL   Boundary layer

BT   Bend-twist

CFD   Computational fluid dynamics

CFRP   Carbon fiber reinforced polymer

CLT   Classical lamination theory

CP   Center of pressure

DOE   Design of experiment

FEA   Finite element analysis

FEM   Finite element model

FP   Fixed pitch

FSI   Fluid-structural interaction

HATT   Horizontal axis tidal turbines

I   Turbulence intensity factor

LCOE   Levelized cost of energy

MCT   Marine Current Turbines Inc.

SF   Safety factor

TE   Trailing edge

TEC   Tidal energy converter

TRL   Technology readiness level

TSR   Tip-speed ratio

UD   Uni-directional

VATT   Vertical axis tidal turbines

VP   Variable pitch

VS   Variable speed

SUBSCRIPTS

C   compression

max   maximum

mean   average

T   tension

ult   ultimate

ACKNOWLEDGMENTS

CHAPTER 1
INTRODUCTION

Power utilities are feeling the pressure to diversify their energy sources due to a decrease in the future availability of fossil fuels and increased public pressure to lessen their environmental impact and reduce greenhouse gas emissions. Many governments are setting goals to have large percentages of their energy mix made up by renewable resources. For example, Nova Scotia's Renewable Electricity Regulations, made under Section 5 of the Electricity Act, states that by 2020 40% of the total electricity supplied by Nova Scotia utilities must be from renewable energy resources [1]. Of the renewable energy resources, tidal energy is a predictable and consistent energy source both spatially (in terms of location) and temporally (in terms of time of energy capture). Tidal energy development, particularly in Nova Scotia with the Bay of Fundy's high tides, has the potential to reduce the province's reliance on fossil fuels by introducing a renewable energy source into the provincial mix. Over the next 25 years, the tidal energy industry could create up to 22,000 full time positions and generate as much as $815 million in labor income, according to a study commissioned by the Offshore Energy Research Association (OERA) [2] of Nova Scotia.

There are two approaches to tidal energy extraction: (i) devices that capture potential energy and (ii) devices that capture kinetic energy. Barrage type tidal energy systems are designed with dam-like structures to capture potential energy from the tide as it flows in and out of estuaries, and in-stream tidal energy devices, or tidal energy converters (TECs), are designed to capture the kinetic energy from tidal flow. Tidal barrage technology has been around for decades, with the first system located on the Rance river in France (Rance Tidal Power Station), which has been operating at 240 MW since 1966 [3], and a 20 MW system located in Annapolis Royal, NS, Canada, coming online in 1984 [4]. Although there is great potential in terms of energy extraction, tidal barrages can be damaging to the local environment due to the dramatic change in tidal flow required to run such a generator. By

contrast, TECs have comparatively low environmental impacts and efficient energy capture, making them a viable solution to extracting this predictable energy source [5]. For these reasons, this work is aimed at the development of TECs.

1.1 The Problem

TECs currently suffer large capital [6], installation and deployment [7], and maintenance costs [8, 9]. These costs, often referred to as capital and operating expenditures (cap-ex and op-ex), have a significant impact on the overall economic viability of TECs. For example, TECs with very high cap-ex requirements face significant barriers to market entry because investors are required to absorb considerable financial risk. The difficulty in raising investment capital often limits the advancement of tidal energy technologies [6], and high op-ex requires elevated feed-in tariffs by electrical utility corporations for developers to be attracted to particular sites [10].

To become economically competitive, the cap-ex and op-ex must be decreased by decreasing the costs of turbine components through appropriate design, and increasing device reliability and robustness [11]. Although studies have shown that TECs are within the range of early market adoption (the levelized cost of energy [LCOE] ranging between $0.3 per kilowatt-hour (kWh) and $0.5/kWh), technology advancements that will lead to significant LCOE reductions are still needed to be widely competitive [12]. This is a challenge in an emerging industry, as developers are required to over-design devices (using more material and higher safety factors) to account for uncertainty in the tidal environment which leads to uncertainty in the design loads [13]. For example, design increases of up to 30% have been reported to ensure the required durability [14], making devices larger and more expensive than necessary. As well, unreliable devices with high maintenance requirements result in turbine down-time and expensive un-planned device access. For example, one study showed that, assuming devices operate without access for repairs for a full year, the percentage of survivors after one year in the water was predicted to be less than 2% [8].

Device reliability can be increased by identifying high risk components and improving their design while maintaining structural and operational requirements. Turbine blades

have been predicted to have the highest failure rates among turbine components [8], with the potential to lead to extensive turbine down-time. A large percentage of turbine failures that have occurred since the commencement of the industry has been a result of blade failures and problems with variable pitch (VP) control systems. For example, Open Hydro's 16 m turbine, installed in the Bay of Fundy, lost blades in 2010 [15], and the two Verdant Power tidal turbines installed in the East River of New York City saw blade failures in 2006 [16, 17]. As well, the Atlantis AR1000 turbine experienced blade fracture soon after its installation in the European Marine Energy Centre (EMEC) in 2010 [18], and Marine Current Turbines (MCT) lost blades when the VP mechanisms malfunctioned in Strangford Narrows, Ireland [19]. These blade failures highlight the challenges associated with blade design and the importance of robust components for overall system reliability.

As well as potentially being high risk for failure, the design of tidal turbine blades directly influences the loads on the support structure and the other turbine components; thrust loads are primarily driven by the design of the blades. Although the blade cost represents a fraction of the total cost of a TEC, loads from the blades are transferred into other components of the turbine, and therefore the size and cost of many sub-components are dependent on the performance of the rotor blades [20]. Furthermore, the turbine rotor blades are the components that capture power from the fluid flow, therefore, design optimization of the blades can result in a more efficient power capture. Research has shown that there needs to be a balance between the size and cost of the turbine and support structure required to withstand high thrust loads, and the annual energy output [21].

1.2 Background

Horizontal axis tidal turbines (HATTs) can have either fixed or variable blade-hub connections. Fixed pitch (FP) blades are rigidly attached to the hub, and hence have no moving parts, are less expensive and require less maintenance, making them economically attractive for the harsh underwater environment. However, they lack the ability to adapt their pitch angle to site conditions and therefore the efficiency of the blades can only be optimized for one particular flow speed, called the design flow speed. This means they are exposed to increasingly high thrust loads as flow speeds increase, necessitating a more robust and costly structure.

Variable pitch (VP) blades have mechanisms connecting the blades to the hub which use feedback control to alter the pitch of the blade mechanically [22], enabling the angle of attack (α) of the blade to be adapted to changing flow conditions. This allows the blades to actively feather to limit the thrust loads and peak power produced by the rotor to prevent overpowering the generator and damaging equipment. In the wind industry, VP blades have become standard practice for large scale devices [23]. However, in the subsea environment there are issues with mechanical systems being exposed to corrosive salt water and sealing issues, making it more challenging, in addition to the significantly higher loads that the rotor and structure are subjected to. Therefore, while VP blades allow for optimization of power capture over a range of flow speeds, the inclusion of the VP mechanism at the blade root makes them more expensive and at a higher risk of failure, which can be costly because of the high cost to access devices once deployed [24].

Methods of achieving conceptually similar performance optimization and load reductions using passive techniques for FP blades introduces a potentially lower maintenance and lower cost alternative to VP blades. Blade designs which are tailored such that they passively optimize α as a function of both the inflow conditions and the span-wise location could decrease the complexity and expense of the system while maintaining a high level of energy extraction and decreased structural loads [25]. These blades are called passively adaptive blades.

Passively adaptive blades allow the blade to change shape based on loading, without the use of mechanical actuators. They are less expensive than VP blades and have the potential for lower maintenance requirements due to their simplicity. An example of this is a bend-twist (BT) coupled composite tidal turbine blade which passively adjusts the blade twist as a function of the radius, changing α of the blade.

From ongoing research in the propulsion industry [26] and wind energy industry [27], aero-elastic tailoring of composite materials with BT coupling is a promising way to achieve this passively adaptive behavior for tidal turbine blades. This tailoring of composite materials couples bending and twisting responses so that loading along one material axis causes deformation in another material axis. BT coupled composite turbine blades couple flap-wise blade bending due to thrust loads with span-wise twisting, and can therefore

4

passively change their α as a function of flow conditions. This results in reduced structural loads by twisting toward feather (decreasing α to decrease lift and drag by reducing the angle the incoming flow makes with the blade chord line) or increased power capture by twisting toward stall (increasing α, increasing the angle the incoming flow makes with the blade chord line).

BT blades that twist toward feather with increasing flow speeds can also potentially decrease the rotor power production past the design conditions to provide a more predictable peak level of power output to the generator. Reducing structural loads by feathering the blades also enables a smaller support structure to be used, which could considerably decrease the cost of the overall system since the support structure typically makes up a large percent of the overall capital cost. For example, a report by the Carbon Trust suggested that the support structure made up 39% of the total capital cost of a tidal stream farm [28], and for offshore wind the cost of substructure is estimated to be around 20–30% of the capital cost of a device [29]. Lower loads also means that longer blades can be used with an existing support structure, increasing the power capture of the device by increasing the rotor swept area [30].

1.3   Objectives

This thesis details the investigation of passively adaptive turbine blades for increased cost effectiveness of in-stream TECs. The goal of this project was to demonstrate reduced structural loads by designing and trialing tidal turbine blades which passively adapt their shape based on flow conditions. To achieve this goal, a numerical design tool was developed, verified, and utilized to investigate the effectiveness of BT coupled composite blades. The research was broken into several objectives:

- Design and experimentally test BT adaptive blades to measure structural and hydrodynamic performance differences between adaptive and rigid blades. Experimental test results were intended to provide a correlation between composite layup design and blade performance. As well, test results were intended to be used to demonstrate a design methodology for BT coupled tidal turbine blades.

5

- Develop and verify a finite element model (FEM) of a composite blade to investigate the behavior of composite structures with BT layups. This model was intended to form a foundation for the structural component of a fluid-structural interaction (FSI) design tool. A verified FEM was also envisaged to be used to investigate the sensitivity of BT blade performance to manufacturing accuracy.

- Verify the blade element momentum theory (BEMT) code developed by Nevalainen [31] to predict the global turbine performance (rotor thrust loads and power capture). This model was intended to form the basis of the hydrodynamic component of a fluid-structure interaction (FSI) design tool.

- Develop and verify an FSI design tool by coupling a FEM and BEMT code. Due to the increased flexibility of BT turbine blades, an FSI design methodology is needed such that the effects of blade deformations are captured in the prediction of the global turbine performance. The intended outcome of this objective was a computationally efficient design tool, decreasing the time between design iterations at the early stages of blade engineering compared to commonly used CFD-FEM codes [32]. This tool was intended to be used to further investigate effects of BT coupled tidal turbine blades that are challenging or expensive to examine experimentally, particularly at the early stages of the design process.

1.4 Thesis Structure

This thesis outlines the development of a design tool that iterates between the structural behavior (blade deformation and material stresses) and global hydrodynamic performance (power and thrust loads) of a turbine with passively adaptive BT blades. This chapter introduces the concept of passively adaptive blades and highlights why passive load reduction has the potential to improve the cost effectiveness of TECs.

Chapter 2 reviews literature relevant to tidal turbine performance, including how tidal turbines operate, the structural and hydrodynamic loads they are susceptible to, and methods for power regulation and load control. The application of passively adaptive blades in the wind, marine propeller, and tidal industries are discussed in detail here, highlighting the state of the art of composite BT structures.

Chapter 3 reviews research methodologies utilized in this work, including structural and hydrodynamic experimental testing and the associated uncertainty analysis, as well as the background theory of BEMT and FEM. This chapter also provides background into composite material modeling and failure theories. Finally, this chapter concludes with a brief discussion on FSI models currently used for tidal turbine modeling.

Chapter 4 outlines the structural testing performed on three composite laminate plates with BT layups and three small-scale composite BT turbine blades. An uncertainty analysis is presented to quantify the experimental accuracy of these structural tests.

Chapter 5 presents the setup and results of two sets of hydrodynamic testing undertaken at the Kelvin Hydrodynamics facility at the University of Strathclyde. The first set was done to establish baseline performance data for a turbine with rigid aluminum blades. The second set of towing tank tests were performed to highlight the passive load reduction potential of BT blades by testing two sets of geometrically identical blades: effectively rigid aluminum blades, and graphite-epoxy composite BT blades. The uncertainty and limitations of scale model testing are discussed in this chapter.

Chapter 6 outlines the development of the structural FEM of both the laminate plate and composite BT blades. The deformations (bending displacement and twisting curvature) of the test samples presented in Chapter 4 were used to verify the FEM component of the design tool. A design of experiment investigation was undertaken to quantify the sensitivity of composite structures to manufacturing accuracy (such as voids or ply misalignment). As well, an analytical model of a composite laminate plate is developed and compared to the results of the FEM sensitivity study.

Chapter 7 presents an overview of the correction factors used in the BEMT, as well as several verifications of the BEMT code using different data sets, including the first set of hydrodynamic test results for the turbine with rigid aluminum blades. BEMT results are compared for the rigid aluminum blades using two different airfoil section data sets, and the significant effect of airfoil data on BEMT results is discussed.

Chapter 8 introduces the iterative FEM-BEMT design tool. The process flow chart for the design tool procedure is presented and discussed, and the stress analysis implemented into

the design tool is given. Finally, verification of the design tool using the hydrodynamic test results from the composite BT blades, given in Chapter 5, is presented. Following the verification, further simulations of the turbine tested with composite blades are undertaken to investigate the effectiveness and efficiency of both the design tool itself, and the turbine with BT blades.

A case study for a full-scale turbine with BT blades is given in Chapter 9. This includes a discussion of the composite skin design, as well as an investigation into the effect of skin thickness and composite fiber angle on local blade stresses.

Finally, Chapter 10 gives a general overview of the potential cost reductions associated with using BT blades, and Chapter 11 summarizes the major findings of this research in the conclusion.

1.4.1 Work Flow

Table 1-1 outlines the work undertaken, how it was used in the context of this thesis, and why it was relevant to the overall scope and objectives.

Table 1-1 Work flow for thesis.

Item	Section	Application to objective
Structural testing Laminate plate	4.1	Data used to verify a laminate plate FEM and analytical model (in Section 6.1). The work presented in this section was published in [243].
Structural testing Composite blades	4.2	Data used to verify a BT blade FEM (in Section 6.2) which was used as the structural component of the FSI design tool. The work presented in this section was published in [279].
Hydrodynamic testing Rigid blades	5.1	Data used to verify the baseline BEMT model (in Section 7.2), which relies on the assumption that the blades are rigid. This BEMT formed the base of the hydrodynamic component of the FSI design tool. The work presented in this section was published in [270].

Item	Section	Application to objective
Hydrodynamic testing Composite and rigid blades	5.2	Proof-of-concept for BT blades by comparing the performance of rigid and BT blades of identical geometry. This data was also used to verify the overall coupled FEM-BEMT design tool (in Section 8).
Structural model Laminate plate	6.1	Model used to investigate the fundamental behaviour of BT composite materials as well as the sensitivity to modeling inputs. The work presented in this section was published in [243].
Structural model Composite blade	6.2	Model used to predict the bending and twisting deformation of BT blades as a function of applied hydrodynamic load. The work presented in this section was published in [279].
Hydrodynamic model	7	Model used to predict the thrust and power on a tidal turbine rotor with rigid blades.
Coupled FEM-BEMT design tool.	8	Design tool developed to predict the global performance (thrust and power) of a turbine with adaptive BT blades. The work presented in this section was published in [279].
Case study	9	Performance of a full-scale turbine with BT blades analyzed using the verified design tool to investigate a range of operating conditions and trial blades with pre-twisted geometries.

CHAPTER 2
LITERATURE REVIEW

This section outlines the background and theory of tidal turbine operation, highlighting currently used methods for power and load regulation in the industry. Emphasis is put on passively adaptive blades that use tailored composite materials, discussed in Section 2.4.

2.1 Horizontal and Vertical Axis Turbines

In-stream tidal energy devices are fixed or moored within a tidal stream to capture the kinetic energy of the moving water. Although there are many devices currently under investigation in this relatively immature industry, the most focus has been on horizontal axis tidal turbines (HATT) and vertical axis tidal turbines (VATT), with turbines deployed all around the world [11], both smaller scale proof-of-concept turbines and full-scale devices [33]. The wind industry has converged on the horizontal axis design; however, although there are similarities between wind and tidal energy, the differences (higher fluid density, lower flow speeds, occurrence of cavitation, different stall characteristics) are considered significant enough to merit investigation into vertical axis turbines and possibly other designs for tidal energy extraction [34].

HATTs rotate about an axis parallel to the current stream, and are classified by the number and type of blades they have. Two or three-bladed bladed devices are the most common; however, some developers have designed turbines with more than three blades. Two bladed turbines are lower in cost and easier to install than devices with three or more blades, but have lower theoretical efficiency and higher tip speed ratios which can result in wake effects and cavitation [35]. Three-bladed devices are advantageous due to their greater starting torque (better self-starting) and reduce balancing problems encountered with two-blade devices. For example, three bladed devices satisfy the minimum number of wings for a stable rotating disk and have a lower starting flow velocity. However, hydrodynamic losses such as tip losses increase with increasing number of blades [37].

VATT devices rotate about a vertical axis perpendicular to the tidal current. These devices commonly have blades mounted vertically between a top and bottom support. VATTs are advantageous for their ability to produce power independent of the tidal current flow direction. As well, the hydrodynamic loading of VATT blades is more even compared to HATT blades, where most of the work is done by the outer part of the blade due to the cantilevered setup [34]. However, they have been shown to have torque fluctuations with every rotor revolution [38] and have problems with self-starting. These issues can be reduced by configuring the blades in a helical geometry, as in the Gorlov rotor [39], however the helical-bladed machines typically have a lower efficiency than the straight-bladed designs.

Variable pitch blades and flexible vanes for VATT have been shown to correct self-starting problems and increase efficiency when operated at low blade tip-speed ratios (TSR, λ) [40, 41], but are more expensive and more prone to failure. Experiments showed that flexible fabric vanes modeled after a sail and shaped like an isosceles triangle with two sides fixed to support poles had higher power coefficients than rigid VATT blades because they are able to adapt to the angle of attack automatically [41]. However, vertical axis turbines have a relative material cost of up to 5-10 times greater than horizontal axis devices due to the larger mass of materials required for the same power output [36].

Even though there are benefits of VATTs, the focus of this research is on three bladed HATT devices, as they have the potential for higher power coefficients and more efficient power capture at a relatively lower cost. Therefore, for this research, three bladed HATT designs are considered the most relevant as a starting point for investigation into new blade designs, and the work provided herein is intended for HATTs.

2.2 Turbine Operation

The cost of a HATT rotor are directly related to the loads, since the equipment and support structure have to be designed to withstand the rotor loads as they are transferred through the device. This section gives an overview of the basic principles behind turbine operation, with particular emphasis on the forces developed on the turbine blades, such as:

- Hydrodynamic forces—Lift, drag and aerodynamic moment.

- Body forces—Weight and buoyancy force.
- Inertial forces—Centripetal force caused by rotation.
- Added mass
- Fatigue loading

2.2.1 Hydrodynamic Forces

The operational performance of a HATT depends on many variables. A TEC operating in a tidal flow of U_∞ and rotating with a rotational speed, ω, will have a tangential velocity distribution along the blade span of ωr (where r is the blade radius). The relative inflow velocity that the blade experiences, V_{rel}, is given by:

$$V_{rel} = \sqrt{U_\infty^2 + \omega^2 r^2} \; .$$

2-1

For any blade cross section along the span, the blade pitch angle, β, is the angle between the chord line and the plane of rotation (and is a combination of the root pitch setting, β_{set}, and the blade pre-twist geometry, β_o) and the angle of attack, α, is the angle between the blade chord line and relative inflow velocity, shown in the schematic in Figure 2-1. The relative inflow angle, θ, is the sum of α and β, and is the angle that the relative inflow velocity vector makes with the rotor plane of rotation. α depends on the inflow velocity, rotational velocity, and β, and is a function of the radial position along the blade. Closer to the blade tip, the blade is moving faster, resulting in a greater relative inflow angle. To optimize power capture, a HATT blade tip and root require different twist angles, resulting in a twist distribution along the blade span; called the pre-twist, β_o.

For each 2-D airfoil section along the blade span (as shown in Figure 2-1), lift and drag forces are generated, which vary with α based on the airfoil shape, Reynolds number, and other factors including free-stream turbulence and blade surface roughness.
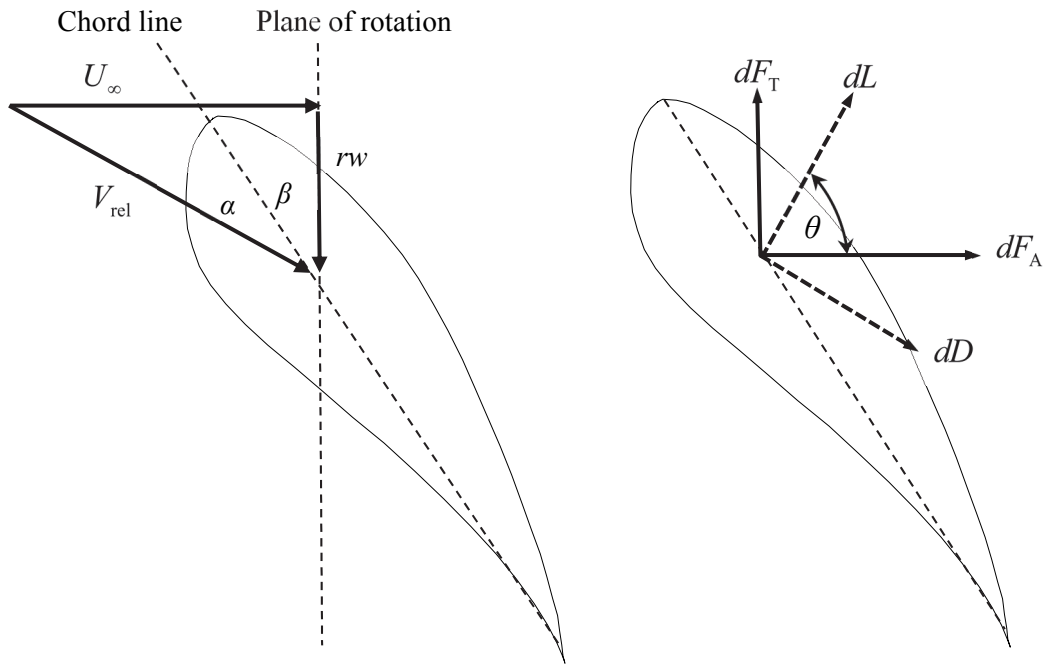
Figure 2-1 Left) Side on velocity vectors, pitch angle and angle of attack, Right) Axial and tangential blade forces, and lift and drag forces, for 2-D airfoil section.

The lift force is a result of the pressure gradient caused by the fluid streamlines around the airfoil [42], and the drag force can be subdivided into two components: frictional drag, and pressure drag. Frictional drag (skin drag or viscous drag) comes from friction between the fluid and the surfaces over which it is flowing, and is associated with the development of a boundary layer (BL), and hence with attached flow, and it is related to the surface area exposed to flow. Pressure drag (form or profile drag) comes from the eddying motions in the fluid as it passes the body, and is associated with the formation of a wake. The pressure distribution that leads to lift also contributes slightly to pressure drag, and it is especially large when BL separation occurs. At low α, where flow remains attached to the airfoil over most of the chord due to a relatively mild pressure gradient, frictional drag in the BL dominates. However, with increasing α, the pressure gradients become such that the BL separates and pressure drag becomes significant. As the airfoil goes into full stall, the pressure drag typically dominates [43]. The physics of flow separation and BL transition are discussed in detail in Section 3.1.3.

The lift and drag forces act at a point called the center of pressure (CP), analogous to the average location of the weight of an object being located at the center of gravity. The lift force is always perpendicular to the relative inflow velocity, and the drag force is parallel to the relative inflow velocity, as shown in Figure 2-1. As α changes during turbine operation, the pressure on the surface of the airfoil changes, and hence the location of the center of pressure varies with α.

A point called the aerodynamic center (AC) is used to describe the airfoil characteristics and is defined as the point on the chord line of the airfoil at which the pitching moment does not vary with α (or at least does not vary significantly over the operating range of angle of attack of the airfoil). Using the AC as the fixed location where the aerodynamic force is applied eliminates the problem of the movement of the CP with angle of attack in aerodynamic analysis. The pitching moment on an airfoil is the moment produced by the aerodynamic forces if that aerodynamic force is considered to act at the AC, and not at the CP, as shown in Figure 2-2. On most low speed airfoils, if the aerodynamic force is applied at a location ¼ of the chord length (¼ c) back from the leading edge (LE), the magnitude of the aerodynamic moment remains nearly constant with angle of attack. The aerodynamic moment is, by convention, considered to be positive when it acts to pitch the airfoil in the stall direction and negative when it pitches the airfoil to feather (as shown in Figure 2-2).

The total axial (thrust) and tangential (force causing torque and power) blade forces can be estimated by segmenting the blade into small span-wise elements (called blade elements, with span-wise length dr) and summing the force contributions from each element. The rotor tangential force, dF_T, and thrust force, dF_A, on each blade element are projections of the airfoil lift, dL, and drag, dD, forces on that blade element in the tangential and axial direction, as shown in Figure 2-1.
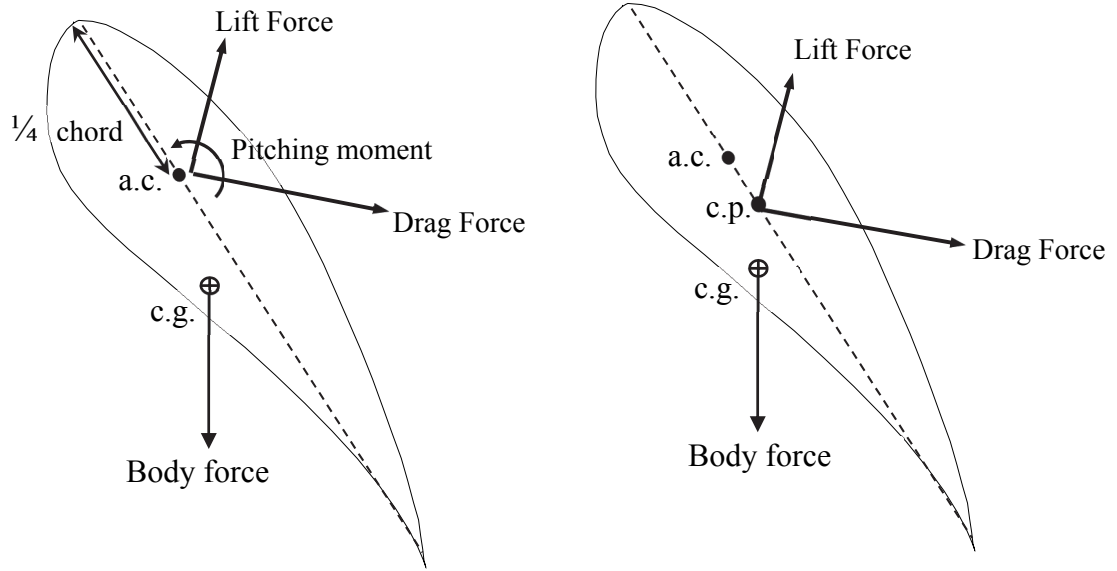
Figure 2-2 Left) Aerodynamic center, and Right) Center of pressure.

The component of force on a blade element in the axial direction, $dF_{A,1}$, as shown in Figure 2-1, is:

$$dF_{A,1} = dL\cos\theta + dD\sin\theta, \qquad\qquad 2\text{-}2$$

and the tangential force, $dF_{T,1}$ (which is multiplied by radius, r, to give torque) on a blade element is:

$$dF_{T,1} = dL\sin\theta - dD\cos\theta, \qquad\qquad 2\text{-}3$$

where dL and dD are the lift and drag components for a 2-D section of the blade, determined from the lift and drag coefficients (C_L and C_D) for a particular airfoil and Reynolds number. The lift and drag forces on a blade element with area $A = Bcdr$ (where B is the number of blades, c is the chord length of the section, and dr is the radial length of the blade element) are:

$$dL = \frac{1}{2}C_L\rho V_{rel}^2 A = \frac{1}{2}C_L\rho V_{rel}^2 Bcdr \quad \text{(normal to } V_{rel}) \qquad 2\text{-}4$$

$$dD = \frac{1}{2}C_D\rho V_{rel}^2 A = \frac{1}{2}C_D\rho V_{rel}^2 Bcdr \quad \text{(parallel to } V_{rel}). \qquad 2\text{-}5$$

15

The lift and drag coefficients (C_L and C_D) are a function of the angle of attack, α, and are unique for a particular airfoil shape and Reynolds number. Based on the lift and drag coefficients for a particular airfoil shape the axial force (thrust), $dF_{A,1}$, and tangential force, $dF_{T,1}$, on a blade element can be summarized by:

$$dF_{A,1} = \frac{1}{2}\rho V_{rel}{}^2 c dr B \left(C_L \cos\theta + C_d \sin\theta \right) \qquad \text{2-6}$$

$$dF_{T,1} = \frac{1}{2}\rho V_{rel}{}^2 c dr B (C_L \sin\theta - C_d \cos\theta). \qquad \text{2-7}$$

The tangential force multiplied by the radial location of the blade element gives the torque, dQ, on the blade element that causes the blade to rotate (driving the generator). The power captured by that blade element is the torque on the element, dQ, multiplied by the rotor rotational speed.

Summing the components of thrust force and power over the blade elements and multiplying by the number of blades gives the total blade thrust load, T, and the power captured by the rotor, P, respectively. Typically, the axial (thrust) force represents the most significant loading on tidal turbine blades [44]. Both the thrust and power are made up of components of the lift and drag on the blade airfoil.

As a blade is operated, it will bend and deform due to loading. This mainly occurs in two directions: stream-wise (edge-wise, or out of plane) bending, and in-plane or flap-wise bending. The force that causes the torque in the blade also results in bending along the span of the blade in the direction of rotation (edge-wise), while the thrust force results in bending of the blade away from the plane of rotation (flap-wise). The magnitude of the out-of-plane bending moment coefficient is considerably larger than the in-plane component, and is indicative of the dominance of the thrust forces over the body and inertial forces.
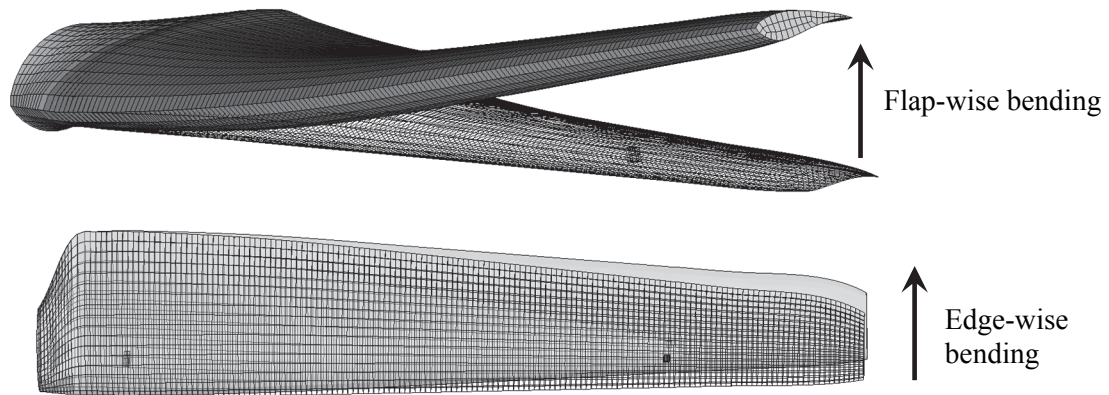
Figure 2-3 Top) Flap-wise (out of plane -about an axis normal to the rotor axis) bending, Bottom) Edge-wise (lead-wise or in-plane) bending.

For example, experiments conducted on a 1:20th scale 3-bladed HATT in a towing tank showed that maximum out-of-plane bending moment were as much as 9.5 times greater than the in-plane bending moment [45]. It is this loading which typically leads to blade failure because the sectional moment of inertia to resist the out-of-plane bending moment is smaller than the other two sectional moments of inertia and their corresponding moments (torque and in-plane bending moment) [13]. The sectional moment of inertia to resist out-of-bending moment failure is proportional to the square of the maximum thickness of the blade section. Therefore, the thicker the section is, the larger the sectional moment of inertia and hence the higher the blade strength. It is this force which is exploited by the BT coupling of a passively adaptive tidal turbine blade.

Due to structural requirements, turbine blades are typically thicker than the hydrodynamic optimum, particularly at the root where the bending loads are the highest. Therefore the root region of the blade will typically consist of thick airfoil profiles with low aerodynamic efficiency. For this reason, the transition between the root diameter and the first hydrofoil section tends to be relatively rapid to avoid losing power from too much of the blade's length. As well, for maximum hydrodynamic efficiency, the blade cross-sectional area has to be relatively small, which means it needs to be constructed of strong material to resist bending moments [46].

2.2.2 Body Forces

Unlike a wind turbine blade, a marine turbine blade experiences substantial buoyancy forces due to the density of the surrounding water. The direction of these forces changes cyclically per each blade revolution, resulting in fatigue loading. To minimize these cyclic forces, the blade can be made to be neutrally buoyant, for example, by filling the blade interior with water or with an epoxy slurry with a comparable density to water [47]. These forces are responsible for in-plane bending moments, and therefore a neutrally buoyant blade will have lower in-plane bending [48]. The weight force of a tidal turbine blade is:

$$W = \rho_{\text{body}} g V_{\text{body}}.$$

2-8

The buoyancy force is in the opposite direction of the weight force, and has a magnitude of:

$$F_B = \rho_{\text{fluid}} g V_{\text{body}}.$$

2-9

If the density of the fluid, ρ_{fluid}, and the body, ρ_{body}, are the same, these forces are the same and the overall effect of buoyancy is negligible.

2.2.3 Inertial Forces

Centripetal forces, or inertial forces, are the apparent outward force that draws a rotating body away from the center of rotation, and for a tidal turbine blade, is given by $mR\omega^2$, where m is the blade mass, R is turbine radius and ω is the rotational velocity. Centripetal loads dominate in the long and slender blades of wind turbines, and these restrict bending. However, in tidal turbines, bending loads tend to dominate [49]; inertial forces increase with the rotational velocity of the blade, and therefore get larger as the blade speeds up. Due to the relatively slow rotation of most tidal turbines, these forces are not typically a significant contributor to the design of full-scale devices. However, for prototype-scale devices operating at higher rotational speeds (upward of 90 RPM), this force has to be considered in the design of the blade-hub connection. For example, a 414 mm radius turbine with a blade mass of 0.4 kg operating at 130 RPM will have a centripetal force of

approximately 30 N. Therefore, the mechanism used to connect the blades to the hub will have to withstand a "pullout" force of at least 30 N.

2.2.4 Unsteady Loads

Grogan *et al.* [44] suggested that a tidal turbine could experience 10^7 cycles of reversed loading over a 20 year lifespan, hence fatigue loading is expected to be a critical design criterion for the blade. As well, the increased flexibility BT composite blades leads to lighter, less stiff blades which tends to lower the natural frequency, making the blade more susceptible to resonance [50]. Fatigue effects are therefore particularly important in the design of composite blades.

The natural frequency of a tidal turbine blade is the frequency at which the system tends to oscillate in the absence of any driving or damping force. If a forced frequency such as the rotor rotational speed is equal to the natural frequency, the amplitude of vibration increases; known as resonance. The way the blade deforms at its natural frequency is called the mode shape, and a blade can have several natural frequencies and associated mode shapes. Resonance can cause severe loading and fatigue difficulties for a tidal turbine blade, and therefore detailed knowledge of the expected frequencies of the excitation forces and the natural frequencies of the structure or substructure are necessary.

The most significant source of excitation in a tidal turbine system is the rotor. The rotational speed of the rotor is the first excitation frequency, referred to as 1P. The second excitation frequency is the rotor blade passing frequency (blade passing the support structure), which is 3P for a turbine with three blades. To avoid resonance, the structure should be designed such that its first natural frequency does not coincide with either 1P or 3P. This can be achieved by having a stiff structure, with a high natural frequency greater than 3P, a natural frequency between 1P and 3P, or a soft structure with a natural frequency less than 1P. For marine propellers, it has been shown that mode shapes are very similar in air and in water, but the natural frequencies are reduced by approximately 65% in water due to the effect of added mass [26].

2.2.5 Added Mass

The "added mass" effect occurs when a mass of fluid surrounding a body is accelerated. It is the effect of "attached" water to the rotor area which increases the effective mass of the blades. Due to the high fluid density, it is proposed that this effect is likely to be more significant for TECs compared to wind turbines [51]. Results of a study done using NREL's (National Renewable Energy Laboratory, USA) aeroelastic simulator code, FAST (Fatigue, Aerodynamics, Structures, and Turbulence) indicated that added mass has a noticeable influence on blade structural loads, increasing thrust loading by up to 4%. A 4% change in blade thrust load is thought to have a noteworthy impact on tidal turbine blade structural design, as this load increment will impact the fatigue load on the blade, which determines the operational lifetime [52]. The consideration of added mass is therefore important in the structural design of a tidal turbine blade.

2.3 Power and Load Regulation

Systems need to be designed to regulate the turbine power and loads with the consideration of the environment for which they are intended to be used; a consideration of the range of flow velocities and associated available power at a specific tidal site is essential to appropriate turbine design. The flow velocities and corresponding power available at an ideal tidal energy site cycle sinusoidally over approximately a 6 hour period. As well, the profile of flow velocities varies over each month, having two limits of velocity: the mean spring peak velocity and mean neap peak velocity. The mean spring peak velocity is the greatest velocity that occurs at the site, while the mean neap is a smaller local maximum velocity which occurs when the spring/neap cycle is at a trough [53].

The peak available power at any tidal site is proportional to the cube of the maximum velocity, and the maximum thrust loads on the rotor are proportional to the square of the maximum velocity at that site. To capture the maximum available power at the site requires generators and turbine components (support structures, blades, *etc.*) to be sized for the peak power capacity and corresponding peak loads. If the power extracted exceeds the capacity of the generator, there is a chance of generator melt-down, which occurs when the voltages and temperatures exceed what the generator can handle and results in expensive equipment repairs. Similarly, the loads on the blades and structure have to be regulated such that the

support system and turbine device (blades, nacelle *etc*.) are able to withstand peak loads. However, this peak power capacity is only available a small fraction of the time at a tidal site, for example spring tides only occur twice a month. Therefore sizing components to meet this peak power results in components that are oversized [11, 54] and hence significantly more expensive, operating at less than 100% capacity for much of the time [54]. This means that power and loads need to be regulated, limiting the power output to less than the site peak available power and shedding mechanical and structural loads at high flow speeds. This decreases the required size of the generator and other turbine components while achieving a higher utilization factor [9]. As well, turbulence and waves cause further variations in flow speeds [54], and although extreme flow conditions are less sudden and severe [25] and more predictable [49] than in the wind industry, there have to be measures in place to handle the excess power and loads that become available when the flow speeds increase beyond the expected maximum. These dynamic loads may occur due to turbulence, passing waves and storms, velocity shear, vortex shedding and static pressure variations [55]. For large diameter turbines, the variation in flow velocity throughout the depth of the water column may require systems that can respond to variations in loads over the rotor area [35].

Tidal turbine operation can typically be categorized into three regions: (1) flow velocities below cut-in speed, where no energy is captured, (2) flow velocities between cut-in and design flow speeds, and (3) flow velocities above design flow speeds (up to extreme conditions). In region (2), the power capture varies with the cube of the flow velocity. In region (3), ideally the power and thrust are limited to protect device components from being over-loaded. This is shown by the thick black line in Figure 2-4. The small double-line in Figure 2-4 shows the turbine power if it is not limited and continues to increase until reaching the peak power at the extreme flow speed.

Power capture and blade loads of a HATT are related to the lift and drag coefficients, which vary with α, as discussed in Section 2.2.1. The number of blades, B, the chord line, c, the fluid density, ρ, and the radial location, r, are fixed during normal turbine operation; however, the relative inflow velocity, V_{rel}, and the lift and drag coefficients can be adjusted to alter the thrust loads and power captured. The inflow velocity and lift and drag

coefficients are not independent, since the lift and drag coefficients are functions of α, which depends on the rotational velocity and inflow velocity at each blade element, as well as the pitch setting, β, of the blade, as shown in Figure 2-1.
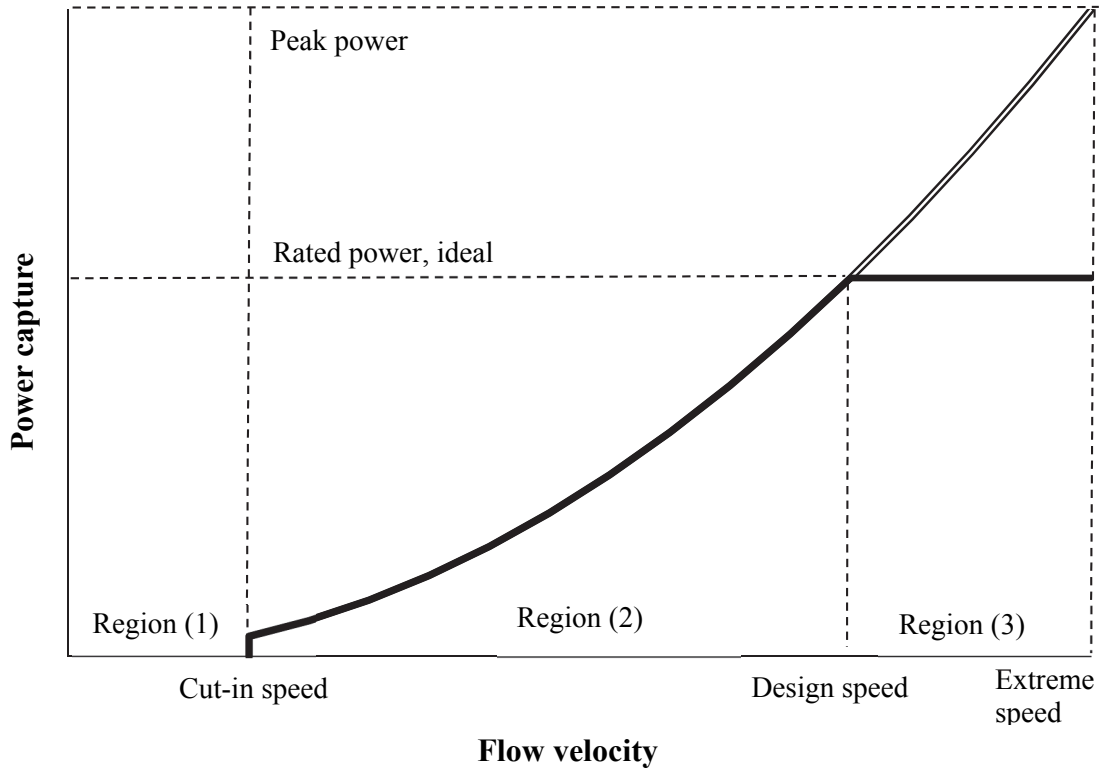
Figure 2-4 Ideal power and flow velocities showing cut-in, design, and maximum (extreme) flow velocities.

Typically optimum turbine operation occurs at an angle of attack just below stall. As α decreases (feathering) the lift and drag coefficients decrease, resulting in a decrease in power capture and thrust loads. However, when α increases (called stalling) the lift coefficient typically decreases but the drag coefficient increases, resulting in an increase in loads. The power and loads on the blades can therefore be controlled by altering β (either β_{set} at the root-hub connection, or the pre-twist geometry, β_{o} along the blade span), or by changing the inflow and rotational velocity vectors, both of which affect α. A VP mechanism controls the power and loads on the rotor by altering β_{set} at the root-hub connection during operation, which alters α to maintain the optimum angle. Changes to β during turbine operation can also be done using blades that passively change their span-

wise twist distribution β_o as a function of loading, which is discussed in more detail in Section 2.4. As well, since the lift and drag coefficients are unique to each airfoil section, changes in the airfoil shape can alter the rotor response.

The following section outlines several blade types and/or load regulation schemes which have been considered for use in the tidal energy environment:

- Stall control turbines
- Yaw control turbines
- Fixed pitch (FP) blades
- Bi-directional blades
- Variable pitch (VP) blades
- Variable-speed controlled rotors
- Passively adaptive blades
- Actively adaptive blades

In the wind industry, VP blades and stall regulated FP turbines have become standard practice [23]. However, in the subsea environment there are issues with mechanical systems being exposed to corrosive salt water, having sealing issues, and being subject to significantly higher loads [56]. As well, because of the high cost to access devices underwater, failures are more costly to repair, increasing the necessity for mechanically robust components. This means that there is not currently one method used across the industry for load control. The following section details some of the above mentioned methods.

2.3.1 Passive Stall Controlled Turbines

Stall occurs when α is such that sudden BL separation occurs, resulting in a decrease in the lift force and a rapid increase in the drag force. Since the drop in lift and rise in drag limits the rotor torque, the power output typically levels off in stalled flow, and hence stall can be used to limit turbine power capture. Stall control requires the design of the turbine blade in such a way that it passively stalls (without the use of additional active pitching) at a particular maximum λ to prevent overpowering the generator. Stall delay is dependent upon

a number of factors such as the blade span-wise pitch distribution, blade λ, centrifugal force on the surface, lift and drag characteristics, and rotor yaw angle [57].

Passive stall is a mechanically simple approach to power regulation, requiring no additional moving components such as VP mechanisms or active yaw control, which may have issues such as sealing and access for maintenance, making them expensive and prone to failure [56]. However, the power output of a stalled turbine is unsteady and difficult to predict. In the wind industry, it was found that a stalled blade also has reduced vibration damping as a result of the separated flow on the blade surface which can lead to fatigue damage [58]. As well, stall-regulated blades are prone to more severe loading due to the increasing drag coefficients with increasing α [58]. These additional loads can lead to a higher capital cost due to the structural requirements to withstand these increased loads.

2.3.2 Yaw Controlled Turbines

The power capture of a turbine is affected by the rotor alignment (yaw angle of the blades) [60]. The yaw angle is the angle between the relative incoming flow and the plane of rotation of the HATT rotor, as shown in Figure 2-5.
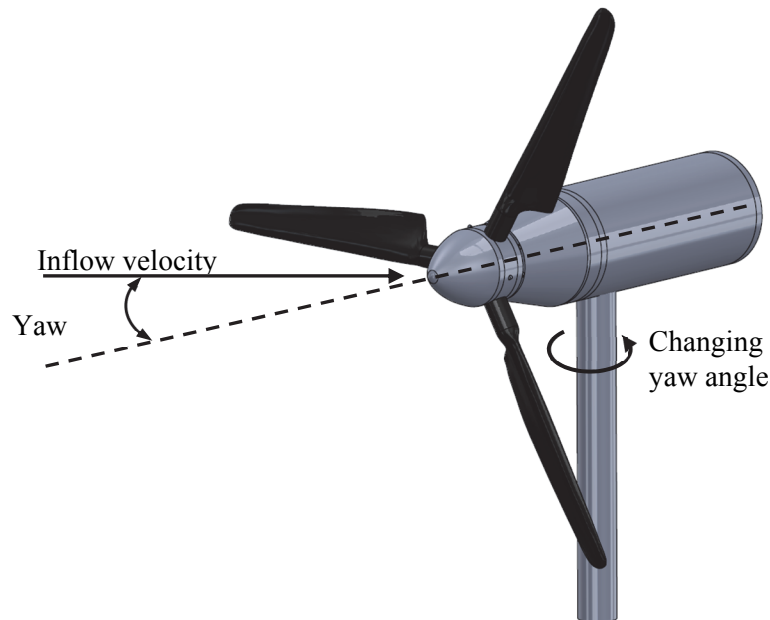
Figure 2-5 Yaw angle for HATT (Cardiff University turbine CAD [62]).

Yaw mechanisms rotate the rotor into, or out of, the direction of flow to control the loads and power capture. Yaw control can be either passive or active, and allows the rotor to extract power from both directions of flow. Passive yaw control means the turbine self-aligns to the flow [61], while an active system has a mechanical device to actively rotate the rotor into the oncoming flow.

Literature suggests that a yawing mechanism could benefit the performance of a device considerably. Experiments have shown that there is a consistent decrease in power (as a function of the cosine of the yaw angle squared) and thrust (as a function of the cosine of the yaw angle) with an increase in yaw angle, where optimal orientation for any turbine is based on the design flow speed [56]. Large amounts of directional swing in the tidal flows are thought to occur particularly around headlands, resulting in a significant reduction in power and increase in dynamic loading if a yaw drive is omitted [48]. Galloway *et al.* [45] developed a BEMT model to account for wave motion and yawed flow effects, and found that steady loading on an individual blade at positive yaw angles was negligible in comparison to wave loading (for the range of experiments conducted on a $1/20^{th}$ scale turbine), but becomes important for the turbine rotor as a whole, reducing power capture and rotor thrust. Frost *et al.* [63] showed that the directionality of flow (upstream vs. downstream relative to the supporting structure) has the most significant influence on the axial bending moment experienced by the turbine, with downstream cases experiencing 10-times greater peak bending moments than upstream cases. This suggests that a yaw mechanism is beneficial to the performance of a turbine with an upright stanchion (support structure), however, alternative solutions such as tethering the turbine would avoid the use of a stanchion altogether. Increasing the clearance distance between the rotor and the support would help as well, but there is an economic and physical limit to this clearance distance. Other work showed that if a yawing turbine, rather than a fixed turbine, were to be used at a site such as Portland Bill, an extra 10% of the energy may potentially be harnessed [64]. However, for sites near the headland at Puget Sound (USA), the mean power generation for a device with no yaw capabilities was shown to be at most 5% lower than for a passive yaw device, and thought to be economically offset by reduced device complexity for fixed yaw turbines [65]. Passive yaw control systems are mechanically

simple, decreasing the likelihood of costly maintenance requirements compared to active yaw mechanisms, which are more expensive and have a higher rate of failure due to more complex mechanical systems and controls [65].

2.3.3   Fixed Pitch and Bi-Directional Blades

FP blades have blade roots which are rigidly connected to the turbine hub, and typically have asymmetric airfoil shapes for optimum efficiency. Both HATT and VATT FP turbines have the advantage of being more reliable, less prone to bending moment fatigue, and less expensive. However, a FP blade that is designed to operate at peak efficiency for a specific λ will underperform at λs above and below the design value. As well, FP blades are normally only designed for optimum power extraction for one tidal flow direction, and therefore, without the addition of a yaw system, their overall power take-off is lower than VP blades that can rotate 180° to capture power from the moving fluid in both directions.

Bi-directional blades are a sub-category of FP blades and have symmetric airfoil shapes designed to extract power from both ebb and flow tides without requiring pitching or yawing. This means they are less expensive, have less maintenance costs, and are more reliable than VP blades or active yaw control. However, because the blade is not designed optimally for either flow direction, the overall turbine efficiency is lower than that of a VP device [25]. Liu and Bose [66] used a numerical code to optimize a series of bi-directional blades in order to increase their power coefficient by optimizing a number of design parameters including pitch-diameter ratio, nominal pitch, shaft rotational speeds and rotor solidity. For a 20 m bi-directional HATT, they showed a substantial improvement in power coefficient was obtained as a result of the optimization process, from 0.28 to a maximum of 0.43. A study done by a contractor in the UK looked at the energy conversion losses of FP bi-directional blades to determine if the lower energy capture was counter-balanced by a reduction in capital and operating and maintenance costs, and found that FP, bi-directional blades are economically competitive with VP blades [67].

2.3.4   Variable Pitch Blades

A VP turbine blade has a mechanism at the blade root (where the base of the blade meets the hub) which rotates the entire blade about the long-axis of the blade in response to

changing operating conditions. Although blades are normally designed with a twist that varies over the span of the blade, they also have a set pitch angle at the root of the blade, β, which is the angle between the blade chord line and the incoming flow at the base of the blade. In the case of VP blades, this pitch angle can be actively altered during turbine operation, as shown in Figure 2-6, allowing greater flexibility in varying operating conditions [68]. VP systems are usually driven by a hydraulic system or electronically controlled motors, which pitch the blades [69]. For large wind turbines, the use of pitch control is essential for protecting the blades in extreme and unpredictable wind conditions and optimizing power capture. However, extreme loads for HATTs are expected to be more predictable [49].
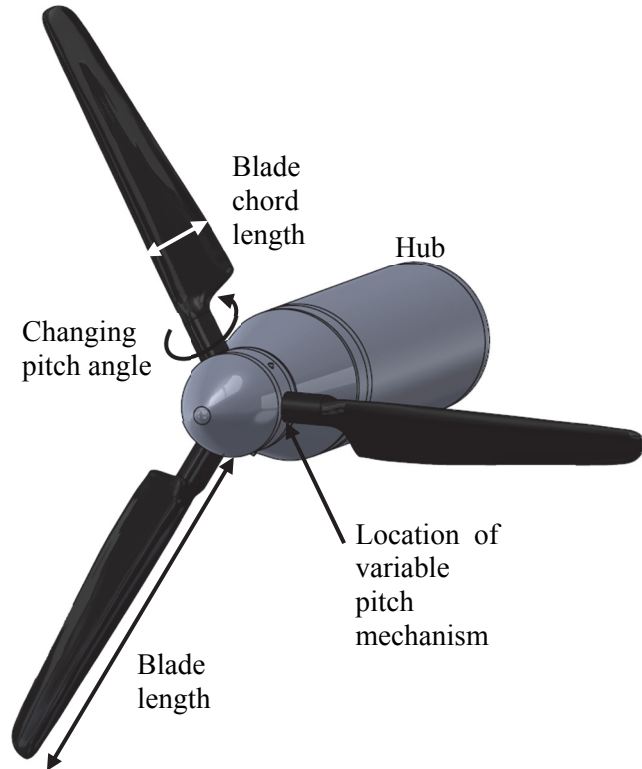
Figure 2-6 Location of pitch mechanism for HATT (Cardiff University turbine CAD [62]).

For optimum performance the pitch of the blade should be continually altering [56], maximizing the absorbed power over a range of flow speeds by optimizing α, with small changes in the pitch angle significantly affecting the power output [70]. However, pitching is typically done relatively slowly, based on the power averaged over a number of seconds,

rather than controlling the instantaneous power [9]. As well, VP blades can have problems with sealing, mechanical complexity, increased cost and reduced reliability [71] due to complex mechanical and electrical control systems [8]. One study demonstrated that the simpler FP system captures less energy, with an overall annual generator capacity factor of 23% for the FP system compared with 25% for the VP system, but, an FP system lowered the unit cost of energy by 10–20% [49].

Using VP control, at current speeds above the rated speed, α can be increased to encourage stall conditions to decrease the lift and increase the drag forces [72], or α can be decreased to feather the blades and decrease both the lift and drag forces. Unlike stall regulation, with feathering, the flow around the blade remains attached, and therefore provides positive damping and avoids the increased loads associated with stall delay [57]. However, larger pitch angle changes are required to control power output using feathering [58].

In the case of HATTs, VP blades that can turn 180° can capture power from both flow directions, and, by adopting large positive pitch angles, large starting torques can be generated. Val [72] showed that for a pitch-controlled HATT, the maximum bending moment at the blade root is reached at the rated current speed and at higher current speeds the bending moment decreases due to increasing pitch angle. However, the pitch control was not able to react quickly enough to high frequency flow fluctuations that may lead to much higher bending moments at the blade root than expected. Bir *et al.* [47] found a similar outcome based on a computational fluid dynamics (CFD) analysis of a variable speed-VP HATT in extreme operating conditions (turbine suddenly experiences a tidal surge that boosts the current velocity to 1.5 times the normal current velocity). They found that the turbine control system was unable to pitch the blades quickly enough to shed the increased loads associated with these higher than expected flow velocities.

VATT turbines have issues with self-starting, low efficiency, and vibration and shake issues [73] and cavitation limitations [34]. VP for VATT turbines offers the possibility of high starting torque [74], high efficiency and reduced shaking [34]. In the case of VATTs such as Darrieus cross flow turbines, VP control leads to a smoothing of the hydrodynamic loading of the blade and therefore reduced variation in output torque [34]. VP VATTs shed loads above their rated maximum velocity which can improve the capacity factor and

reduce stress at a small cost in total annual energy [75] and a VP VATT achieved approximately 70% better performance than a FP VATT turbine [74]. VP control mechanisms for a straight-bladed Darrieus VATT was found to significantly improve turbine efficiency when operated at low tip-speed ratios (TSRs), and to give the turbine the ability to self-start reliably [40, 76]. However, the added mechanical complexity increases both the cost and the likelihood of failure as a result of marine growth, corrosion, and suspended sediment jamming the pitching mechanism [73]. As well, VP blades for VATT must still allow the implementation of an emergency shutdown configuration of the blades [40, 76].

There is a debate in this relatively immature industry between VP and FP blades. VP devices are mechanically and electrically complex [8], therefore FP devices have lower capital costs and lower operational costs [61], while being more robust in design [77]. However, FP blades cannot capture power from both flow directions without additional yaw mechanisms. In an interview by K. Steiner-Dicks [78], Peter Fraenkel, (at the time the Technical Director of Marine Current Turbines [MCT]) stated that the supposed cost and complication of pitch control is more than compensated by savings in the structural strength requirements of stall regulated turbines.

However, in the same article, Sander De Block (Commercial Director at Tocardo International) said that "It all boils down to money. Find the optimum mix between kW (peak performance efficiency) and total kWh (life time production) at the best possible kWh cost price. Having no pitch causes challenges with respect to power electronics and is maybe less "efficient" but is also extremely cheaper to engineer, scale, manufacture and maintain. Furthermore it will potentially even produce more kWh due to its durability and thus longer operating life span. Keep it simple, reliable and cheap is the philosophy at Tocardo."

The FP machine always offers lower initial capital cost and unplanned maintenance cost than the VP machine, but a comparative system cost analysis demonstrated that the energy yield from a FP design is likely to be up to 10% less than that of a VP design [71]. Based on a comparison study using numerical simulations, Turnock [77] showed that VP

machines are about 10% better in terms of energy capture when they are performing without reliability issues, but are about 5.4% more expensive.

In the harsh tidal environment, the sensors and actuators associated with VP mechanisms are ultimately more prone to failure. Therefore, passively actuated (requiring no control system or sensors) pitch systems can potentially decrease the cost and increase simplicity of a VP system while still allowing for pitch control.

The majority of work done in this area in the tidal sector is for VATTs. Passive pitch control mechanisms that control α can greatly improve performance over an equivalent FP VATT turbine, assuming that the physical mechanism can achieve the pitch changes required. Hantoro [79] studied a VATT passive VP concept in which the blade was free to pitch along a span-wise (longitudinal) axis near the leading edge and passively point into the apparent flow, but was constrained by stops. Zhang [80] showed performance advantages using a similar method, with a passive VP turbine characterized by the free swing of its blades within a limited angle and without any additional control mechanism. However, in the case of a VATT turbine, the issue of shaking due to torque fluctuations was found to still be an issue [81]. There has been more work done on passive variable pitch blades in the wind industry [82-84].

In the wind industry there are examples of passively actuated pitch adaptation for horizontal axis turbines, with the majority of these designs being actuated by the centripetal forces pulling the blade along its longitudinal axis as the rotational speeds increase. For example, the WindSpot [85] uses the centrifugal loads to change the angle of weights which pull and pitch the blade, and Yanagihara [86] developed a rubber tube at the root of each blade which has metal fibers arranged at an oblique angle through the rubber. When the rubber tube is subjected to centrifugal forces and stretches, the metal fibers are forced to straighten in the loading direction, yielding the torsional deformation and achieving the change in pitch angle of the blade [86]. As part of the UpWind project, Mroz [87] explored ways to control the dynamic characteristics of the loads transmitted from the blade root to the hub. The concept was to alleviate the torsional stress in the root by equipping the blade-hub connection with controllable elastic and damping elements so that during normal operation active elements would be stiff, whereas under an extreme gust their stiffness

would be decreased for a short period of time allowing free rotation towards feather. Results showed that a device which could free the blade rotation about the blade axis in case of an extreme wind gust can both reduce the aerodynamic forces and turn the profile to feather much faster than a VP control system [87]. Although this seems to be a promising idea for wind turbines, the rotational speeds of tidal turbines are low, resulting in relatively low centripetal forces and may not be sufficient to actuate pitch change.

2.3.5 Variable Speed and Over-Speed Regulated Turbine

The power output of a turbine is a function of the angle of attack. From Figure 2-1, α can be manipulated by changing the inflow velocity vector, the rotational velocity vector, or the pitch of the blade itself. For turbines operating with a fixed rotational speed, there is only one flow velocity corresponding to the optimum λ. This means a fixed rotational speed turbine will operate non-optimally for flow speeds not corresponding to this optimum λ. VS control strategies for HATTs adapt the rotational speed of the rotor as the inflow speed varies to maintain an optimal λ and α [88] between cut-in and design conditions, optimizing the power capture over a wide span of flow conditions [89]. Carlin *et al*. give a description of the fundamentals of this methodology in [89]. However, a similar method can be employed to limit power production pass the turbine rated (design) conditions by allowing the rotor to speed up proportionally faster than the inflow velocity, effectively feathering the blades and reducing power capture. For FP blades, the change in rotational speed required by this control strategy can be achieved by controlling the generator reaction torque [90]. It has been found that, using VS control, a wind turbine will on average collect up to 10% more energy annually than a fixed-speed turbine [89]. However, increasing rotor rotational speeds means the rotor will endure increasing thrust loads, depending on the blade design. For this reason, VS control is particularly compatible with passively adaptive BT blades.

Maximum power point tracking applies this method to achieve the peak power possible for flow velocities in the region (2) in Figure 2-4 [91]. The change in rotational speed required by both control strategies is achieved by controlling the rotor speed through the generator reaction torque [90]. Permanent magnet synchronous generators have been shown to be an attractive option for a turbine with VS control. In comparison to induction generators,

permanent magnet synchronous generators may be designed to rotate at very low speeds, eliminating the need for a gearbox. This configuration was used by Whitby [90], who compared the performance of VP and stall regulated turbines operating with VS control. In the work by Whitby, the turbine was operated in VS mode so that the optimum λ was maintained. They found that above rated flow speed, the dynamics were significantly different, with the VP regulated turbine being stable, whereas the stall regulated turbine showed unstable dynamics.

For wind turbines, the rotor speed changes can be relatively slow compared to the desired rate of changes due to the large inertia involved. This can introduce challenges when operating in a highly variable flow environment [92]. In the wind industry, torque excursions due to wind gusts are usually more severe in fixed-speed turbines, however, wind turbines that have constantly varying rotational speeds to track the changes in inflow velocity due to gusts and turbulence can introduce rapid changes in the rotor torque which propagate through the turbine drivetrain. This results in fatigue damage due to load spikes [89]. As well, the wide range of required operational rotational speeds makes it unlikely that a suitable generator will be available 'off the shelf' [11]. On the other hand, variable speed operation may also help to moderate rotor fatigue loads [89].

2.3.6 Braking

Braking is important as it allows the rotor to be stopped and fixed in place for maintenance. For wind turbines, mechanical drum brakes or disk brakes driven by hydraulic systems are used for emergency stopping during events such as extreme gusts. Brakes are the secondary means to secure the turbine at rest for maintenance and in emergencies; typically blade pitching or electromagnetic braking are applied first to reduce the turbine speed before mechanical brakes are applied [23].

2.3.7 Adaptive Blades

Adaptive blades allow the turbine system to adjust to local conditions, and can either be passive, requiring no control systems and actuators, or active, using control systems and actuators to adapt the shape of the blade. This section outlines these two types of adaptive blades.

2.3.7.A. *Passively Adaptive Blades*

Although FP or bi-directional blades require little maintenance and are potentially less expensive compared to VP devices, they cannot adapt to site conditions. As well, VP devices only linearly adapt to the optimal angle of attack, however, in practice the optimum α varies non-linearly over the span of the blade [93]. This is because the airfoil characteristics vary non-linearly with changing flow conditions, there are non-linear distributions of axial and tangential flow induction factors, and there are irregularities in the inflow over the swept area of the blade due to natural irregularities, all of which affect the optimum α of the blade [25]. Therefore, there are advantages of a blade that can adapt α along the span. Blade designs which are tailored such that they passively optimize α as a function of location along the blade span could decrease the complexity and expense of the system while maintaining a high level of energy extraction and decreased structural loads [25]. These blades are called passively adaptive blades.

Passively adaptive blades have been shown to be advantageous because of their ability to adapt to operating conditions. Rigid blades achieve optimal performance at the design operating condition, however, when the operating condition changes from the design values, the blade geometry becomes sub-optimal relative to the changed inflow. At sub-optimal operation, the blade efficiency decreases and the rotor may be subject to fatigue, vibration and stability issues [25]. Passively adaptive blades decrease the risk of overpowering the generator and overloading the structure by regulating the power and loads. However, care has to be taken to avoid hydro-elastic instability failures, excessive deformations, stability issues, or problems related to the control of tailored blades [94].

Several methods of achieving passive blade adaptation have been proposed in the wind, marine propeller, and tidal industries:

- Bend-twist (BT) coupled composite materials [95]
- Tension-torsion coupled tailored composites [96]
- Eccentricity between shear center and pressure center [97]
- Torsional joints between a modular blade [98]
- Changing airflow using inlets/outlets that increase flow from trailing edge [99]
- Buckling members to change the airfoil shape [100]

From early stage research in the tidal energy industry [101], and from other industries, bend-twist coupling of composite materials has been shown to be a promising way to achieve this passively adaptive behavior [102]. More information on this method can be found in Section 2.4.

2.3.7.B. *Actively Adaptive Blades*

Actively adaptive blades are those that actively transform their shape (pitch angle, camber, *etc.*) according to the loading on the blade to increase efficiency and reduce stress on the blade. An actively adaptive structure involves actuators, sensors, and one or more microprocessors that analyze the response from the sensors. Sensors are used to predict the variation in α based on blade loading, to determine the required shape change to maintain the optimum α, and a control system is used to command the actuators to apply localized strains/displacements to alter the structural response [103]. Control and actuation concepts include pitch control, twist control, camber control, and hinged control surfaces. For active control, these control surfaces should be able to either change the characteristic α curve for specific sections of the blade, or directly change α, in order to affect the thrust and power capture of the rotor [104].

Actively adaptive blades are commonly used in commercial aircraft applications by the Canadian Air Force [105]. They have also been studied for use in the wind energy industry as a way to reduce fatigue loads, especially in the flap-wise blade direction [106]. Some techniques for achieving controlled deformation include hinged flaps, micro-tabs, camber control, "snap-through" morphing surfaces, and BL control. Hinged flaps can be used on the trailing edge of wind turbines, and, by increasing or decreasing the camber of the airfoil, can generate substantial change in the lift coefficient of the airfoil by altering the pressure distribution along the chord [107]. It was shown that with a 10% chord length flap located at the tip of a HAWT blade, all load fluctuations were alleviated with a range in flap deflections of ±12° in normal power production cases [107]. Through a review of techniques used in the helicopter industry, Barlas and van Kuik [107] found that maximum control authority could be achieved using trailing edge flaps in combination with mechanically amplified smart material actuation. However, discrete hinged devices require complicated internal structures which could result in high maintenance costs if there are

failures within the blade structure once underwater. Active twist concepts are a possible solution as well, but have not been further developed due to limited control authority and blade structure changes which may affect the blades weight and stiffness properties [107].

Active camber control involves changing the airfoil shape such that the lift and drag properties are altered. Hulskamp [108] found a significant reduction in the fatigue spectrum by controlling aerodynamic loads using partial camber control. The trailing edge half of the chord, at certain stations in the outboard section of the blade, was made deformable, allowing a change in camber using a piezoelectric actuation. The use of micro-tabs was found to alter the trailing edge flow development, providing changes in lift [107]. Micro-tabs are small devices placed near the trailing edge of an airfoil that have a translational height similar to the BL thickness when actuated, and have no height, or no effect on flow around the airfoil, when they are not in use. BL control, which uses suction/blowing, synthetic jets, vortex generators or plasma actuators to influence the flow close to the surface of the airfoil, was also found to change the overall characteristics of flow, changing the aerodynamic characteristics of the airfoil [107].

Nicholls-Lee proposed using "snap-through" composite material morphing surfaces with an actuation device in the spar to change the camber of a tidal turbine blade. Composites with two stable equilibrium states "snap-through" at room temperature and can be changed from one to the other by a temporary force/moment generated by an actuator. The advantages of "snap-through" materials for tidal turbines is the elimination of the VP mechanism, larger possible operating range of λs, high efficiency energy capture from both ebb and flood tides, and overall efficiency improvements [25]. However the actuation processes required for this type of active adaptation have to overcome the applied hydrodynamic, dynamic, and structural forces and deform the inner structure of the airfoil, which results in very large strains in the skin, limiting material selection [107]. As well, the combination of coupled deformation and actuation mechanisms are heavy and expensive, and the strains and control forces needed to twist the blade could be high [107].

Although there are promising applications of actively adaptive smart structures for the aircraft and possibly the wind industry, actuation devices are more risky in the subsea environment, where maintenance is costly to undertake. As well, the use of blade materials

that significantly change their camber may lead to a reduced load bearing capacity. Other considerations include fatigue, fluid structural dynamics of the blade, and interaction with the turbine support system [25].

2.3.7.C.   *Alternative Adaptive Approaches*

Along with BT coupling, other approaches to passively twisting blades have been explored, primarily in the wind industry. The Dutch FLEXHAT program demonstrated the use of a screw cylinder and preloaded spring to passively control the blade tips of a horizontal axis wind turbine (HAWT). When the centrifugal load on the tip exceeds the preload, the tip of the blade is driven outwards against the spring and pitches [58]. Joose [109] aimed to replace this cylinder-spring device with a heat-resistant synthetic fiber-reinforced epoxy torsional-tension coupled tubular spar called the TenTorTube. This device attaches a pitching tip to the blade and twists in response to centrifugal loads caused by rotor-speed changes, and uses torsional-tension coupling instead of a screw cylinder and spring to reduce costs, weight, and maintenance. The device locks in low wind speeds and is free to twist at higher wind speeds to passively adjust the power. Stork Product Engineering of the Netherlands has shown the feasibility and the mechanical durability of the proposed tip mechanism in a previous project [110]. Wang and Yuan [41] modelled a flexible vane for a VATT after a sail. It was shaped like an isosceles triangle with two sides fixed to support poles. It was proposed that a fabric vane could be able to adapt to α automatically to extract more energy from the fluid.

MacPhee tested a flexible blade with material properties similar to natural rubbers, which was designed to have an airfoil shape the same as its rigid counterpart at the design speed, but to alter its shape passively at non-design conditions. This use of flexible blades has shown a delay in stall, which could possibly help increase the operational range of wind turbines [111]. Hansen [42] used centrifugal forces to activated the outer part of a HAWT blade to rotate 90° and thus act as an aerodynamic brake, limiting the maximum torque. Although passively controlled blade tips have been shown to give a smooth high quality power output in the wind industry, the main problems were the large extra mass, complexity, phase control delays in control for alleviating fluctuating loads, and a high

level of required maintenance resulting in high costs [106]. These issues make this technology less advantageous for the sub-sea tidal energy application.

Moroz [98] proposed to use a modular spar with a joint connecting consecutive HAWT blade sections which can be tailored to allow each blade segment to pitch individually for feather in over rated power. The different blade segments can also be made of different materials to reduce the cost of materials in regions of low interest, such as close to the hub, or decrease the weight of the wind turbine blade at the tip. Along similar lines, Lam proposed a folding tidal turbine blade to reduce the costs of transportation and installation [112]. Kroo [99] used ingress and egress ports (long slits) through an interior channel of a fixed pitch HAWT blade to allow air to enter the blade interior channel from close to the hub and be forced, from the centrifugal forces, to vent out slits at the trailing edge to disrupt the local airflow to cause a net change on the lift of the blade. This is called passive circulation control, and can be used to decrease blade lift as the rotational speed increases, thus regulating power.

DeLeonardo *et al.* [97] proposed using the eccentricity between the shear center and pressure center of an HAWT blade to cause torsion along the long axis of the blade, causing the blade to twist as it bends. They proposed that a 37 to 40 m blade could have a tip twist of 5° using a C-shaped spare, resulting in a reduction of fatigue loads on the order of 10%. Zuteck [113] looked at the possibility of using novel planform and structural combinations to provide response similar to classical BT coupling, but without an off-axis lay-up. A sweep distributed along the span was used to create a moment that induced twist; for a straight blade, thrust loads would be centered at the blade axis, but for a blade with an edgewise curve, the outer blade thrust can be offset from the axis. One concern was that of manufacturing spar caps that curve substantially in their own plane. Hemmelgarn [114] proposed using buckling members to change the airfoil shape of a blade when it is loaded past a critical buckling loading point, and Bianchi [115] proposed an anisotropic tension-torsion coupled composite strip through middle of blade along the longitudinal direction that causes the blade to twist with increasing centrifugal loading.

2.4 Bend-Twist Coupled Blades

From early stage research in the tidal energy industry [101], and from other industries, aeroelastic tailoring of composite materials is a promising way to achieve passive blade adaptation [102]. This section outlines research into BT coupled passively adaptive blades for use in the marine propeller, wind turbine and tidal turbine industries.

2.4.1 Bend-Twist Coupling: Wind Industry

Horizontal axis wind turbines (HAWTs) carry loads primarily in bending (although they can be exposed to high centripetal loads at high rotational speeds) similar to tidal turbines; therefore, there are potentially similar advantages to using adaptive composite blades in the wind industry. However, the wide operating range of wind-flow speeds potentially make it more difficult to design BT blades to meet the requirements of a wind turbine site.

Karaolis *et al.* [116] first introduced BT coupled blade skins using composite layups to change the angle of attack of the blade. By changing the blade skin from an orthotropic fiber layup to a biased fiber layup, they aerodynamically tailored the blade while maintaining the beam stiffness properties and not changing the manufacturing costs [116]. Kooijman [27] related the blade flap-wise bending moment to the optimum pitch angle to determine the required bending-torsion flexibility to achieve optimal performance of a HAWT. He found that the optimal constant speed VP rotor energy production is obtained when the inner span twists to feather, and the outer span twists to stall as the wind speed increases. Twisting to feather is expected to be favorable for dynamic stability and reduced loads, and was found to be best achieved using a combination of carbon/glass reinforcement in the cross ply direction. The carbon fibers induce shear strain for torsion coupling, and the glass fibers add strength in other directions. He concluded, however, that the twist angles required for passive rotor control are too high to be induced by BT coupling alone, and therefore active pitch control is still required [27]. This is potentially a function of the large range of flow speeds that wind turbines are exposed to, necessitating design for extreme wind conditions and making it difficult to design BT blades for a finite range of conditions [117].

Zuteck [113] claimed that a larger and more energy productive rotor may be possible with the use of adaptive blades, which would lead to a lowered cost of energy. He identified two main challenges with aeroelastically tailored HAWT blades: first, the cost of materials and fabrication (for example, manufacturing composites with off-axis fibers) and second, the possible fatigue limits due to ending or curving angled fibers. The goal of their work with Sandia National Laboratory was to look at using novel planform and structural combinations to provide the same BT response but without the difficult to manufacture layup. Reducing the blade thickness while increasing spar cap material (to make up for bending stiffness) was found to increase the tip twist by 0.1° for 0.3048 m of bending (for a 29.87 m blade length), but was restricted by the size and weight limitations of the spar. The spar cap is the part of the spar that provides stiffness and spans the full length of the blade. Substituting carbon fiber for the fiberglass spar cap materials in the outer blade had the largest impact on twist, producing up to 7° of tip twist for 0.914 m of bending displacement, depending on the percent of carbon used (7° of tip twist resulted when 35% of the spar cap material was carbon fiber). A 10° reduction in the angle of attack was identified as the necessary twist required to bring a typical wind turbine to near zero-lift (feathered conditions), therefore this approach shows great potential for future use in passively adaptive HAWT blades [113].

Veers and Lobitz [118] hold a statutory invention registration for a passively adapting wind turbine blade that twists toward feather as it bends to reduce loads using BT coupling composite materials for the skin. In such a blade, as the load on the blade increases, the blade twists to decrease the angle of attack, which in turn decreases the load on the blades. Therefore, the passive design will cause the blade to oscillate between under and over-compensating the load [118]. Aeroelastic tailoring can also be used to produce the twist needed for stall delay in constant speed and variable speed wind turbines using stall control [119]. Lobitz [95] showed substantial performance improvements using BT HAWT blades that twist toward stall proportionally to the wind speed. However, twisting toward stall results in increased blade loads to be withstood by the structure, therefore Veers and Lobitz propose to mitigate loads and optimize performance by passively pitching to feather, but to regulate the maximum power some other way [118].

Liu and Gong [120] used the vein pattern of a plant leaf, which, from the viewpoint of material science, has a kind of composite structure with multiple phases, to design an adaptive spar with fiber orientation design imitating the plant leaf skeleton. Results showed that the integration of a bionic design method into the coupled blade further improves the blade bend-torsion coupling effect. As well, glass/carbon hybrid fibers were found to be the best choice for coupling design, as they increased the coupling coefficient over single glass fibers. However, manufacturing and cost constraints may be a problem for hybrid fibers [120].

Capellaro [121] investigated BT wind turbine blades using an iterative FEM-BEMT design methodology for a variable speed HAWT. Capellaro predicted a 4% reduction in flap loads for a BT blade with a 15º fiber angle for a 126 m diameter HAWT, however, this had an associated ~1.25% decrease in annual energy production compared to a baseline blade with 0º plies [30]. By optimizing the BT blade undeformed geometry by using a pre-twisted blade, he predicted a 1.25% increase in annual energy production.

Different techniques for manufacturing BT coupled HAWT blades have been considered. Goeij's group [122] found that a filament-wound double box beam spar reduced problems with strain incompatibilities at blade skin joints and potentially results in manufacturing advantages. They compared an experimental and FEM double box beam, and found that the twist *vs*. load curve was linear until the load became high enough to cause buckling of the compressed fibers. They also stressed the importance of 0° fibers, which are required because they reduce the fatigue damage, since fibers off-axis get pulled in the load direction and tend to straighten out, creating high stresses in the matrix material [122]. Tsai and Ong [123] created composite D-shaped spars which were designed and fabricated to induce BT coupling. They used D-shaped molds and ply orientations of 20° and 60° to successfully manufacture two symmetric clamshells with a stagger-overlap joint design at the seam. This joint design smoothly spreads out the increased thickness of the joint and also has the highest retention strength among three joint designs they considered (butt joint, overlap joint, and stagger-overlap joint). They concluded that to have a stronger joint strength for a laminate with combination of 0° pies and angled plies, the angle-plies should be placed at the outer layers [123]. Deilmann [93] proposed a BT coupled rotor design which, using

FSI, predicted a 3 to 6% efficiency improvement with twisting to stall. However, results showed that the necessary deformation for optimal blade shape was not feasible [93].

2.4.2 Bend-Twist Coupling: Propulsion Industry

Marine propellers translate rotational motion into thrust. This is done by creating a pressure difference between the forward and rear surfaces of the airfoil-shaped blade and accelerating the fluid behind the blade to move the vessel forward. Similarly to tidal turbines, marine propellers work by creating lift and drag forces on an airfoil, which are primarily a function of the angle of attack of the incoming fluid and the Reynolds number. For a tidal turbine, high thrust loads are undesirable because they have to be resisted by the structure and hence higher thrust loads result in a more expensive support structure. However, for marine vessels, thrust loads propel the vessel forward, and hence it is desirable to maximize thrust and minimize the power required.

Until lately, in the marine industry, propellers have typically been made from metals. As advancements were made in propeller design, the marine industry shifted from cast iron to more corrosion-resistant metals and optimized alloys. Currently, Nickel–Aluminum–Bronze and Manganese–Aluminum–Bronze are the most commonly used metals for marine propellers due to their superior corrosion-resistance, high yield strength, reliability, and affordability [50]. However, metal marine propellers corrode in sea water, set up galvanic action, are easily dented or bent from strong impacts, and are difficult to form into complex shapes [124]. Composite materials, however, never corrode or electrolyze, have longer fatigue lives, and are strong enough to serve in the harsh underwater environment under heavy loading. Tests have shown composite blades used for outboard motors and stern-drive props to be stronger than equivalents in aluminum, but up to 40% lighter and resistant to impact and damage from cavitation [124]. Reduction in production costs of 60 to 70% have also been seen in the marine propeller industry after research into tailored elastic composite propeller blades [125].

Along with the benefits of using composite materials, flexible composite marine propeller blades can be designed to have load-dependent blade deformations. These propellers can be tailored to reduce load variations, delay the onset of cavitation, and improve propeller efficiency by passively adjusting the blade shape [126]. Gowing *et al.* [127] first presented

experimental data for two hydro-elastically tailored composite hydrofoils that were designed to twist under a particular load (BT coupling). The studies showed that under the appropriate loading, tip deflections reduced the effective angle of attack and therefore reduced loading in the tip region. These tailored hydrofoils also were shown to delay the onset of cavitation [127].

There has been significant experimental and numerical research into composite propellers. Young *et al.* [126] tested two 0.6096 m propellers, one rigid and one composite (the composite propeller designed to undergo negative twist under hydrodynamic loading through BT coupling), in the Naval Surface Warfare Center, Carderock Division water tunnel. They found that the rigid propeller only deflected in bending, while the composite propeller underwent bending and twisting. Bending was shown to have negligible effect on the performance, while the combination of bending and twisting of the composite propeller resulted in higher efficiency both above and below the design condition for both uniform inflow and wake inflow. Additionally, in unsteady inflow the composite propeller was even more advantageous since each blade could passively change its pitch to adapt to the local changing conditions [126].

Liu and Young [128] studied self-twisting composite propellers using an analytical model based on classical lamination theory for a cantilevered beam to determine the relationship between material properties, fiber orientations and BT coupled deformation. They found a strong correlation between the twisting deformation, pitch alteration and performance, and showed that a properly designed self-twisting composite propeller can enhance the system performance [128]. Young's group [129] also used an experimentally verified finite element (FEM) and boundary element method (BEM) coupled numerical tool to study the hydroelastic (deformation of the elastic body under water) performance of marine propellers [129]. They used this tool to formulate and implement a two-level (material and geometry) design methodology. The material design stage was used to determine the proper composite material configuration (laminate ply angles and thickness) that exhibits the optimal pitch adaptation behavior. The geometry design stage was used to determine the un-deformed geometry of the BT propeller such that it deforms to match the equivalent ideal rigid propeller shape at the design conditions [130]. The FEM component of the

solver was validated by testing twisted cantilever plates made of 7075-T6 cold drawn aluminum bar stock, and the BEM component was validate through experimental testing of a 72° skew propeller (NSRDC propeller 4383) made of a homogeneous material. To validate the hydroelastic model, numerical results for a rectangular hydrofoil with an elliptic cross-section were compared to an analytical solution obtained using the Timoshenko beam theory [26]. Young *et al.* also developed a reliability based design and optimization methodology which was used to ensure the level of required reliability was achieved with respect to uncertainties in structural parameters and operating conditions. Reliability studies are common for rigid and non-adaptive structures, but are fairly new to structures that are flexible and interact with the environment around them [131].

Lin and Lee [132] came up with a methodology for optimizing the stacking sequence using an FSI model for laminates with fixed ply thicknesses and orientations limited to 0°, ± 45° and 90°, based on the deformation, fluid pressure, and performance of the propeller. The ply stacking sequence was put into a FEM model and iterated until they had an optimized blade that outperformed its metal counterpart. However, it was found that optimizing the propeller just by changing the stacking sequence was not enough, as it reduced the torque coefficient at higher advance coefficients (analogous to tip speed ratio used in the tidal industry), resulting in a move away from the optimal point of operation. A pre-deformed design was chosen in which the initial blade had a larger pitch angle which reduced to the optimum angle under loading [132]. Pre-deformed shapes are commonly used with high-deflection structures such as wings, and were not previously used with propellers because of their high rigidity.

Lin *et al.* [133] experimentally compared a small-scale propeller with a chosen optimum stacking sequence made from carbon fiber-epoxy pre-preg to a composite propeller with a quasi-isotropic stacking sequence in a cavitation tunnel with a transparent window to allow photography to capture deformation. They also tested a pre-deformed composite propeller designed to twist to optimum shape upon loading. An aluminum alloy mold was used to make the propellers, and the pre-preg was laminated on the lower mold and then the upper mold was put on. The propeller had 5 blades with a rotor diameter of 0.305 m and hub-diameter ratio of 0.2. Although the results showed similar trends to those predicted

numerically (whereby the pitch of the optimized propeller decreases as the ship speed decreases, reducing the torque and increasing efficiency), it was found that because the displacements were very small (on the order of 2 mm), the measured results were easily influenced by other factors such as fluid flow, vibration of the blades and vibration of the shaft. This resulted in differences between experimental and numerical results, and they conclude that future studies should use a larger propeller to yield larger changes in pitch and better results [133]. These conclusions agree with Habali's philosophy that the underlying the choice of wind turbine blade size is a compromise between small blades which may be too stiff by nature and unable to exhibit the behavior of full size blades, and large blades which may exceed the capabilities of the technical and financial resources [134].

In collaboration with the Maritime Research Institute Netherlands (MARIN, The Netherlands) Airborne Marine (The Netherlands) designed and built five composite propeller blades (shown in Figure 2-7) to replace NAB blades and interface with an existing controllable-pitch NAB hub on a Royal Dutch Navy mine hunter. The propeller diameter was 2.5 m, with a power of 1.4 MW. The team at Airborne selected a blade structural design comprising a glass fiber/epoxy core and carbon fiber/epoxy skins that were assembled and infused with epoxy resin. A polyurethane coating was applied to the demolded blades to provide impact protection and reduce algae growth. Using composite materials, the propeller weight was reduced by 70% and cathodic protection measures were deemed no longer necessary to retard hull corrosion due to the non-magnetic composite [135].

Figure 2-7 Composite propeller blade, attached to the bronze blade interface to existing metallic propeller hub [135].

44

Despite the advantages of composites, their use in marine vessels is still limited, likely due to the lack of design rules, lack of a large systematic empirical databases, or lack of reliable and proven simulation/design tools. As well, although composites provide superior performance to metals, potential failure mechanisms are more complicated and difficult to predict, resulting in higher safety factors [136]. This is predicted to change as reliable, consistent, and cost-effective manufacturing techniques are proven [129].

2.4.3 Bend-Twist Coupling: Tidal Turbines

For wind turbines, it is difficult to operate the turbine at exactly the target λ because of the transient nature of the wind. However, with tidal turbines, the tides are more easily predicted, and therefore it may be possible to operate a tidal turbine closer to the target λ more regularly than a HAWT [25]. Eisler [137] identified that because of the sudden and drastic changes in inflow with wind turbines, the use of passively adaptive blades may not significantly improve the adaptive pitch method of operating the turbine at peak efficiency. However, because the relative difference between the mean flow speeds and the fluctuating velocities may be less extreme at a typical tidal site, this may not be the case for tidal turbines [25]. As well, although a good solution for the wind industry, passively adaptive blades is an even more attractive option for the tidal energy industry because the added cost to maintain complex underwater devices (such as VP mechanisms) could potentially make a tidal energy project economically unviable.

Nicholls-Lee [25] performed BEMT and FSI studies of tidal turbine blades with BT coupled spars. A primary analysis using an adapted BEMT code for a three-bladed HATT with a diameter of 20 m (8 m blade), a hub/diameter ratio of 0.2 and a maximum free stream tidal velocity of 2.5 m/s showed increases in the annual energy capture of over 2.5% and reductions in thrust coefficient of greater than 14.5% when compared to a base case (fixed pitch rigid blade). The BT spar initially had 20 plies in the mid-layer at 20°, 30 plies in the inner skin at 45° and 5 plies in the outer roving at 90°, each ply with a thickness of 0.281 mm.

Using the FSI tool (fluid and structural solvers operating separately from each other, but coupled by a MATLAB® interface), results indicated a decrease of up to 12% in the thrust

loading and an increase of up to 5% in the power coefficient for an 8 m blade with a tip twist of 8.6° toward feather and tip bending displacement of 1.48 m. The fluid dynamics component of the FSI model used by Nicholls-Lee was solved using Palisupan and the resulting pressure loading across the surface of the blade was calculated for input to FEM using ANSYS 12.1. This simulation was continued in an iterative manner until the deflection of the blade between successive runs was less than 0.05% of the rotor diameter (converged). The maximum stress seen in the blade was monitored and if this stress was larger than a third of the yield stress (effectively giving a safety factor of 3), the number of plies (thickness of composite) was increased until the stress limit was met, and the FEM was re-run. The power coefficient predicted using the FSI was almost double that predicted for the same blade shape using BEMT, which they state was because the CFD model was not accurately predicting stall. As well, there was increasing degrees of induced twist as the turbine size increased, which is counter to the results presented by Cox [138], but may be due to varying levels of BT coupling and varying composite layups between successive blade sizes. Otherwise, the trends were similar between the FSI and the BEMT analysis; however, numerical and analytical results were not verified experimentally. Nicholls-Lee experimentally tested a 1.5 m long double box beam spar with a BT layup under static bending loads, but did not find good correlation between FEM and experimental results. It was thought that this was due to manufacturing issues with the composite spar [25].

Wada [139], from the University of Tokyo and the National Maritime Research Institute, Japan, tested two sets of composite blades, one set that were torsionally rigid, and one set that were torsionally elastic, in order to study the effect of passive pitch control. The diameter of the two-bladed rotor was 1 m (475 mm long blades). For one set of blades, the spar and skin (in this case only a strip of laminate on the skin) were made of carbon fiber reinforced polymer (CFRP) and the core of the blade was made from epoxy resin. They compared this to a blade which was fully laminated with CFRP (skin fully covered with composite to increase stiffness). A spar was made of unidirectional CFRP in the longitudinal direction to carry the bending load. To allow the blade to feather as the flow speed increased, the spar was located along the leading edge. Epoxy resin was used to form the blade core, which gave the blades lower stiffness in torsion, so that loading caused

torsional deformation and feathering of the blades as the flow speed increased. Wada [139] and Minami *et al.* [140] tested these blades in a towing tank. Using stereo cameras to track blade deformation, they found that the power coefficient, C_p, decreased for the elastic blade, but the "coefficient of resistance" (similar to the thrust coefficient, C_T) was also lower, resulting in decreased blade and structure loads. They also performed an FSI study of the elastic blade, and claimed to have a good match of the torsional deformation to the experimental results. However, from the data presented in the paper, although the inner span results match well, there was a 35% difference in the deformed blade pitch angle at the tip (flow speed of 0.8 m/s and 92 RPM) between the experiment and the FSI, with the FSI over predicting the deformed angle (experimental pitch angle change of about 2.6° and FSI of 4°). Based on the FSI results and an economic analysis, they concluded that the elastic blade will have a 10% decrease in energy costs [140].

Their method for experimentally determining deformation in the towing tank using stereo optics is an accurate way to estimate blade deformation under hydrodynamic loading. However, although Wada and Minami [139] towing tank tested elastic blades, there was no mention of composite layups or BT coupling. As well, the FSI under-predicted the twist angle significantly and was not in good correlation with experimental power and thrust results. This leaves a gap in knowledge of how BT coupled blades respond in a towing tank relative to the composite layup and geometry.

SCHOTTEL [141] developed a hydrodynamic blade design which minimizes the thrust forces using passive pitch adaptation to reduce the loads on the support structure. Based on full-scale testing of a 4 m diameter rotor on the front of a tug boat, a 50% reduction in thrust loading at a flow speed of 5 m/s was realizable. Further full-scale testing of the SCHOTTEL tidal turbine was conducted at Queen's University Belfast's tidal site at Strangford Lough, Northern Ireland. The turbine was mounted on a floating barge and tests were conducted for 288 hours (during flood tides in daylight hours). The 50 kW rated device (rated at 2.75 m/s) produced up to 19 kW in flows up to 2.5 m/s, with the thrust on the turbine reaching 17 kN in the maximum flow. However, for these tests, rigid blades were used, as flow speeds were not expected to be high enough to see the benefits of adaptive blades [142].

Recently, Motley and Barber [143] applied an iterative 3-D potential-based boundary element method-finite element method (BEM-FEM) solver (initially developed for marine propellers) to the problem of passive pitch adaptation to describe potential benefits of passively adaptive blades. The reference model used was a two bladed, 20 m diameter, VS-VP turbine with rated (maximum) power of 550 kW and a maximum rotational speed of 11.5 RPM. They showed that a tip twist of about 1.75º to stall resulted in overall increased power capture, but required the use of the VP mechanism at a lower flow speed and resulted in higher blade loads, while twisting to feather resulted in decreased power capture and delayed the onset of mechanical pitching. While pitching to feather resulted in lower blade loads before the onset of active control, the corresponding blade stresses were higher because of the increased flexibility and orientation of the fibers [143]. Further studies showed that passively adaptive blades could increase annual energy capture by delaying the onset of cavitation [127], thus enabling the use of larger blades operating at higher rotational speeds, increasing the annual energy capture [144].

CHAPTER 3
TOOLS AND METHODS

This chapter outlines the current state-of-the-art for modeling and testing methodologies used in the design of tidal turbine blades and components. This includes experimental testing and uncertainty analysis, structural FEM, and hydrodynamic modeling using tools such as BEMT. Composite material modeling methods are also presented in this chapter.

3.1 Hydrodynamic Testing

This thesis uses hydrodynamic testing of a small-scale HATT in a towing tank as a means to verify design tools and prove concepts. This section gives an overview of some of the hydrodynamic testing done in the tidal energy industry.

Many turbine developers use small-scale testing in facilities such as towing tanks or flumes as a way to predict the performance of particular blade designs and prove conceptual designs. Scale testing of model devices is a cost effective and low risk way to conduct early stage device performance testing. Based on the technology readiness level (TRL) system of assessing the maturity of a technology [145], small-scale testing is a TRL level 3 to 4 on a scale from 1 to 9, with 9 being the most mature technology (in this case, a full-scale, commercially ready tidal turbine). The TRL system of identification is used in several industries and enables consistent discussions of the technical advancement across different types of technology.

Experimental testing can be used to validate design tools and to study possible sources of error between numerical tools and real life turbine behavior. As well, although laboratory scale models cannot mimic complex offshore conditions, they allow for the possibility to collect accurate and repeatable data. If used as the primary design method, experimental testing can be costly; however, in the context of this work, laboratory scale experimental studies are used both for proof-of-concept and validation of design tools. Experimental results may be compared to design tool predictions, but with the expectation that the fit

may not be perfect because of simplifying assumptions made in the models. Therefore, it is important to know the limitations and uncertainty involved in testing, as well as in the models used.

Examples of researchers performing small-scale testing include Milne *et al.,* who tested 780 mm diameter 3-bladed (NREL S814) HATT in the towing tank at the University of Strathclyde in order to study the effects of unsteady hydrodynamic loading, and found the out-of-plane bending moment loads were up to 25% greater in unsteady flow than steady flow. This means flow conditions have to be considered when designing larger scale devices, and will be essential in ensuring the blades will not fail [51]. Small-scale hydrodynamic testing proved successful in measuring the performance characteristics of models of MCTs full-scale turbine in a towing tank and a cavitation tunnel [146], and Batten *et al.* used experimental results of an 800 mm diameter rotor tested in a cavitation tunnel to verify a BEMT model, which was used as a design tool to predict the performance of a 20 m rotor HATT [56]. Jo *et al.* [35] used experimental results from testing in a circulating water channel to justify the use of a HATT CFD model, and Clarke *et al.* [147] tested 1/30th and 1/10th scale contra-rotating HATT models in the towing tank at the University of Strathclyde and in the ocean on a frame aside the St Hilda vessel, respectively, for proof of the contra-rotating two-rotor concept. The 2.5 m diameter turbine tested in the ocean showed sufficient proof of the ability to match the torque between the two rotors, proving the cancellation of reactive yawing under normal operating conditions.

Galloway *et al.* [48] studied the effect of yawed flow on the thrust and power of a 1/20th Froude scaled representation of a 16 m diameter HATT and found that a turbine operating in yawed flow has decreased thrust and power. This was also found by Maganga *et al.* [60], who showed that a misalignment of a fixed turbine can cause a significant loss of thrust and power [60]. In 2007, trials were carried out on a 1/30th scale model (0.6 m diameter) model of the turbine developed by TGL (Tidal Generation Limited) to aid the design of a 500 kW fully submerged tidal turbine prototype. More recently, round robin testing was conducted on a 0.7 m diameter turbine at various test facilities as part of the MaRINET program in order to evaluate the impact of different experimental facilities on turbine performance results. The average thrust and power measurements were in good agreement

among facilities, but the effect of blockage was shown to be highly influential on the turbine performance in cases of high thrust coefficients, even at relatively small blockage ratios [148].

Most of the previously discussed tests were performed on rigid blades made of materials such as aluminum. Although small-scale composite blades are not as common as aluminum or plastic blades [149, 150], there are examples of researchers using model scale composite blades for hydrodynamic testing. For example, Davies [151], from the IFREMER Brest Center, France, did flume tests on a 1/30th scale model turbine with a series of different 305 mm long blades with variable stiffness's and a sandwich construction: a polyurethane casting giving the blade its form, with a single external layer of composite reinforcement added to change the stiffness of the blades. Both isotropic (mat fibers) and 90%-unidirectional (UD) glass impregnated with epoxy resin were added to give blades different bending stiffness. Static cantilever bending tests showed that the use of a single layer of 300 g/m^2 glass mat reinforcement more than doubled the bending stiffness, while a layer of 1250 g/m^2 E-glass UD composite increased it by a factor of 6 [151]. As well, Wada, from the University of Tokyo, tested two sets of composite blades, one set that were torsionally rigid, and one that were torsionally elastic, in order to study the effect of the passive pitch control [139]. This is discussed in Section 2.4.3.

3.1.1 Performance Metrics

Typically, non-dimensionalized turbine performance characteristics are used to compare different turbine systems during testing, regardless of size or design [152]. The power coefficient gives a measure of the device efficiency in capturing the available energy in a stream tube of the same diameter, and is given by:

$$C_{\mathrm{P}} = \frac{P}{\left(\rho A u_{\infty}^3\right)/2}$$

3-1

A in this case is the rotor cross sectional area. The thrust coefficient gives a measure of the axial thrust experienced by a rotor disk as a proportion of the thrust a solid disk of the same diameter would experience, and is given by:

$$C_{\mathrm{T}} = \frac{T}{\left(\rho A u_\infty^2\right)/2}$$

3-2

Finally, the tip speed ratio, TSR, λ, is the ratio of the speed of the rotor tip to the incident flow velocity, and is given by:

$$\lambda = \frac{\omega R}{u_\infty}$$

3-3

Presenting the relationship between C_{P} or C_{T} and λ gives the turbine performance over a range of measured flow conditions, enabling a direct comparison to analytical and computational performance estimates, as well as to other turbines. The coefficient of blade root bending moment in both the axial and radial directions, C_{My} and C_{Mx}, respectively, are the ratio of the bending moment measured to the maximum possible bending moment applied by the fluid flow (similar to the thrust coefficient). The axial bending moment results from thrust loads in the axial direction, and the radial bending moment results from loading in the tangential direction (from loads resulting in rotor torque). This is shown in Figure 5-3.

3.1.2 Scaling

In order to extrapolate scale model data to a full-scale prototype, it must be shown that the model and prototype obey the same physical laws and their relevant features are correspondent. Essentially this means that the relationship between the model and prototype behavior have to be well understood in order to obtain useful information from scale-model testing. The relationship between model and prototype is referred to as similarity, and dimensional analysis is typically used to develop the conditions required to ensure similarity [153].

Scaling is done by comparing a set of dimensionless numbers which should be the same for both the model and the prototype of any scale. Models must follow laws of similitude in order for results to be relevant to the prototype. There are three levels of similarity [154]:

1) Geometric—geometric dimensions are scaled.
2) Kinematic—geometric similarity plus all fluid and model velocity ratios are the same.

3) Dynamic—kinematic similarity plus all force ratios must be constant.

It is typically force ratios (dynamic similarity) that are paid the most attention, as geometric and kinematic scaling are usually easily done. Some typical dynamic similarity ratios include Froude number, Reynolds number, Weber number, Cauchy number, and Euler number [154]. Reynolds and Froude numbers are the most widely used for scaling of TECs, but the scale effects of the others also have to be shown to be small. Froude number scaling is not appropriate for determination of power output or structural loads, but is important when considering gravity or buoyancy effects (*i.e.* when gravity provides one of the important forces for equilibrium).

Reynolds number scaling is important for the consideration of inertial forces and viscous forces, and is used to quantify the relative importance between these forces, and is therefore applicable to tidal turbines. Reynolds number scaling is important when the gravity forces are negligible compared to viscous or other forces (for example, at high speeds). In the case of a tidal turbine, the chord-Reynolds number is typically used, which is a function of the blade chord length:

$$R_{e,chord} = \frac{V_{rel}\rho c}{\mu},$$
3-4

where

$$V_{rel} = \sqrt{U_\infty^2 + \omega^2 r^2},$$
3-5

and c and r are the blade chord length and radius, respectively, at 75% of the blade length.

Reynolds number scaling is almost impossible to achieve for small-scale models in a towing tank because of the very fast carriage and rotational speeds required. In most cases during experimental tow tank testing, the carriage speed is limited to under 5 m/s, therefore the rotational speed of the rotor is increased in attempt to match the full-scale Reynolds number. When Reynolds number matching results in very high speeds that are not attainable at the test facility, the Euler or Froude number may be used and kinematic scaling applied, whereby rotational and inflow speeds are determined based on λ matching [154]. Milne used Froude number scaling for the NREL S814 blades tested in Strathclyde's tow

tank in 2000 (Milne, 2013) and Batten chose a rotor size of 0.8 m diameter in order to maximize the Reynolds number to match the prototype as much as possible, while keeping the blockage ratio reasonable [149]. Issues with operating at lower Reynolds numbers than those expected at full-scale are further discussed in Section 3.1.3.

As an example of a scaling analysis for a small-scale tidal turbine, Table 3-1 shows the inputs and Table 3-2 gives several dimensionless numbers for a 0.83 m diameter model turbine compared to a 10.40 m diameter full-scale device.

Table 3-1 Input parameters for scaling analysis.

Parameter	Model	Full-scale
Flow speed (m/s)	1.00	2.25
Rotational speed (RPM)	81.00	14.50
Rotational speed (rad/s)	8.48	1.52
Relative inflow velocity at 75% R (m/s)	2.82	6.33
Diameter (m)	0.83	10.4
Chord at 75% R (m)	0.047	0.59
Gravity (m/s^2)	9.81	9.81
Kinematic viscosity (Pas)	1.10E-06	1.10E-06
Water depth (m)	1.00	15.00
Surface tension (Pa)	7.20E-02	7.20E-02
Water density (kg/m^3)	998	998
Bulk modulus of elasticity (Pa)	2.15E+09	2.15E+09
Pressure change across rotor (Pa)	145.80	1125.00
Atmospheric pressure (Pa)	103000	103000
Pressure at rotor level (Pa)	112790.38	249855.70
Water vapour pressure (Pa)	2.30E+03	2.30E+03

Table 3-2 Results of scaling analysis.

Dimensionless number	Model	Full-scale	Percent difference (%)	Model inflow speed to match scale full-scale dimensionless number (m/s)
Froude	0.32	0.19	26.51	0.58
Reynolds	1.20E+05	3.40E+06	93.16	79.50
Weber	4.55E+04	2.89E+06	96.90	22.00
Cauchy	3.68E-06	1.86E-05	66.98	5.8
Euler	0.018	0.028	20.82	Less than 1.00
TSR	3.51	3.51	0.03	1.00
Cavitation	27.90	12.36	38.59	3.3

Most of the fluid parameters were assumed to be the same for both, and the pressure difference across the rotor was predicted using the BEMT tool discussed in Chapter 7. Table 3-2 also gives the inflow velocity required for the small-scale turbine to match the dimensionless numbers of the full-scale turbine.

The Froude number was close between the small-scale and full-scale turbines, however, the Reynolds number differed drastically between the two and hence it is assumed that it is not possible to match because of carriage speed limitations. For example, in order to match the full-scale turbine Reynolds number, the inflow speed for the small-scale device would have to be 79.50 m/s, which is not feasible for most test facilities. λ was matched for this example by choosing rotational and flow speeds accordingly.

3.1.3 Low Reynolds Numbers Airfoil Performance

As discussed, Reynolds number matching between scale model tests and full commercial scale turbines is often limited by scale model test facilities due to carriage and rotational velocity constraints. For this reason, most model scale turbine testing is done at lower Reynolds numbers than expected for a full-scale turbine. At low Reynolds numbers, the performance of an airfoil may be significantly different than could be expected at higher Reynolds numbers. For this work, due to the small-scale of the HATTs being tested, the operational range of Reynolds numbers is relatively low (between 10^4 and 10^5).

Model scale tidal energy testing, or small river turbine operation, along with some model scale propeller testing, operate in the transition region, with Reynolds numbers around 7×10^4, where the prediction of airfoil performance becomes challenging due to the effects of transition, laminar separation, and laminar bubble behavior. Because of these effects, there is a substantial record of non-repeatability of 2-D airfoil data from tests in different facilities [155]. The global turbine performance predictions from BEMT are dependent on the accuracy of the lift and drag airfoil data, therefore this Reynolds number sensitivity presents a challenge for modeling small-scale tidal turbines. Furthermore, the effect of the Reynolds number is more complicated for a rotating turbine blade than for a 2-D stationary blade section (which are typically used to measure 2-D sectional lift and drag data). These rotational effects are thought to be less significant for full-scale TECs where the rotational

speeds are much lower [156]. The following section outlines the challenges of operating a tidal turbine at low Reynolds numbers.

At low Reynolds numbers, as flow moves over the surface of the airfoil, a laminar BL forms and the velocity decreases based on a no-slip condition between the body surface and the first layer of flow in the BL. Based on Bernoulli's relationship, this decrease in velocity must be driven by an increase in pressure gradient [157]. The BL is traveling against this adverse pressure gradient (increasing static pressure), and energy is dissipated by frictional (viscous) drag inside the BL so that the BL does not have sufficient energy to overcome the adverse pressure gradient. This causes the flow in the BL next to the airfoil surface to stop and reverse direction, which causes the BL to separate from the surface [158].

At very low Reynolds numbers, this flow separation usually occurs close to the leading edge (LE) since laminar BLs can handle only small adverse pressure gradients prior to separation [159]. This adverse pressure gradient increases with increasing α, and hence separation becomes more likely as α increases [158]. The separation point is defined as the point between the forward and backward flow, where the shear stress is zero. The separated layer (which is a BL formed along a free surface as opposed to a solid wall [160]) forms a laminar separation bubble between the solid surface and the BL. This separated BL is unstable, and a transition from laminar to turbulent flow occurs in the BL due to these instabilities [161]. Increased mixing and entrainment of higher speed fluid causes a growth of this now turbulent separated layer [161], and it may entrain enough energy (turbulent flow has more energy and momentum than laminar flow) to overcome the adverse pressure gradient and reattach to the surface of the body, forming a turbulent BL [162].

As Reynolds numbers increases, a short bubble may form which is generally on the order of a few percent of the chord length long and represents the transition-forcing mechanism, but doesn't significantly affect airfoil performance [155]. At high Reynolds numbers, the laminar/turbulent transition occurs upstream of the separation point, and hence the flow remains attached because there is more energy in the turbulent BL and it can withstand higher pressure gradients [161]. Here, separation usually occurs at very high angles from the trailing edge moving forward with increasing α (stalling).

Laminar separation bubbles occur on the upper surface of most airfoils at Reynolds numbers above about 7×10^4, but can occur on both surfaces for thick airfoils or airfoils with significant curvature [163]. Once separation has occurred, the flow behind the separation point typically comprises a vortex filled wake that differs drastically from the predictions of inviscid theory. In particular, it exerts a pressure drag on the body that is typically much larger than any frictional (viscous) drag exerted by the BL itself [157], hence increasing the overall drag on the airfoil, and in some cases, decreasing the airfoil lift as well. Liebeck *et al.* [161] showed that increases in the size or extent of the separation region correlate with increases in drag for a particular airfoil incidence, and O'Meara and Mueller [164] showed that the length of the separation bubble tends to increase with a reduction in Reynolds number, usually resulting in a rapid deterioration in performance, *i.e.*, substantial decrease in L/D.

3.1.3.A. *Turbulence Intensity*

Based on the Reynolds decomposition, the velocity has a steady component and a fluctuating (turbulent) component. The turbulence intensity factor, *I,* is a measure of the level of turbulence in the flow and is defined as the root-mean-square of the turbulent velocity fluctuations divided by the mean free stream velocity. The mean velocity can be based on the volume averaged flow through the circle prescribed by the turbine or by the depth averaged velocity across the vertical diameter of the turbine. Airfoils are particularly sensitive to turbulence intensity factor—it has been found that problems associated with obtaining accurate wind tunnel data for airfoil sections at low Reynolds numbers are compounded by the sensitivity of the BL to the free stream turbulence [165].

Free-stream turbulence improves the lift of an airfoil by influencing its BL. Over a low Reynolds number airfoil, if the free-stream turbulence intensity is low, the flow starts as laminar. Before transition, the laminar BL separates due to the adverse pressure gradient. Depending on parameters such as the local Reynolds number, pressure gradient, surface roughness, and free-stream turbulence intensity, the turbulent BL may entrain enough high momentum fluid to reattach as a turbulent BL behind the laminar separation bubble [166]. If the free-stream turbulence intensity is low, reattachment of the BL is less likely because the separated flow doesn't have as much energy. If the flow does not reattach and remains

separated, the drag on the airfoil increases. However, if the BL has sufficient energy to transition and reattach earlier, the performance of the airfoil can be increased (decreasing drag and potentially increasing lift).

Mueller compared wind tunnel results for tests at I = 0.08% and 0.3%, and obtained a slightly higher maximum lift coefficient and slightly lower minimum drag coefficient for increasing turbulence intensity [165]. Another study showed that with a turbulence intensity of approximately 0.9% at the model location in a wind tunnel, there was a decrease in the length of the separation bubble, earlier transition within the bubble, and an overall reduced drag when compared with measurements obtained at the nominal tunnel conditions with a turbulence level of approximately 0.1% [161]. Data for airfoil α of 0°, 4°, and 8° showed a reduction in separation bubble thickness and an earlier transition and reattachment with an increase in free stream turbulence. In this same study the turbulence intensity did not appear to have an effect on the lift [161]. Even wind-tunnel test facilities with turbulence levels lower than 1/10% showed significant differences in airfoil performance, particularly near the critical Reynolds number of about 7×10^4 [155]. This highlights the extreme sensitivity to even small changes in the free-stream turbulence and makes it critical to accurately define the turbulence intensity and scales in the onset flow when modeling a turbine.

For low Reynolds number airfoil testing, Selig [167] suggested that intensities of 0.1% are acceptable to ensure that laminar flow does not prematurely transition to turbulent flow over the airfoil surface. Tests done by Somers on the NREL S814 airfoil at a Reynolds number of 1.5×10^6 were at a turbulence intensity of 0.02 to 0.04% [168]. However, a real tidal site will have turbulence intensities anywhere from 3% up to 24% [163, 169], depending on the seabed shear effects and other flow disturbances. A maximum turbulence intensity of approximately 58% was recorded by SHOTTEL during barge testing in Strangford Lough, NI (with intensities between 40% and 17% in the turbine operational range) [142]. This makes the effect of turbulence on the prediction of turbine performance very important.

The integral turbulence length scale is a physical quantity which represents the size of the energy-containing eddies in turbulent flows and is a function of the surrounding

disturbances. Two different turbulent flows with the same turbulence intensity may have different turbulence length scales. For example, it is expected that the length scale will be larger for a HATT at full-scale, and smaller in a flume or wind tunnel facility due to the size of the disturbances. The integral length scale has been shown to influence the BL on airfoils, with airfoils tending to have delayed BL separation with a smaller free-stream integral length scale [170]. The smaller size of the energy-containing eddy (smaller length scale) increases the momentum exchange between outer flow and the BL, adding energy for the BL to overcome the adverse pressure gradient and delaying separation, particularly near the rear part of the airfoil for high angles of attack. For larger eddies, the BL lacks the energy to overcome the adverse pressure gradient and remain attached to the airfoil. However, the effect of the integral length scale on the performance of the airfoil is found to be small with higher turbulence intensities [170]. Watkins [171] showed that the integral length scale governs the gradient of the lift curve slope (as the length scale decreased, a reduction in the lift curve slope was observed), and Howard and Kindelspire [172] stated that in order for the free-stream turbulence to affect the boundary-layer behavior, the length scale must be on the order of the boundary-layer thickness.

3.1.3.B.   3-D Effects

There are significant differences between pressure distributions on rotating 3-D blades and the pressure distributions based on stationary 2-D wind tunnel or flume measurements. For a rotor with a finite number of blades the vortex system in the wake is different from that of a rotor with an infinite number of blades (as is assumed by BEMT). For a 3-D blade, fluid on the top surface has lower pressure relative to the bottom surface. Fluid therefore flows from below the blade around the tip to the top of the blade in a circular fashion. This causes a circulatory flow pattern (vortex). Tip vortices create multiple helical structures in the wake, and they play a major role in the induced velocity distribution at the rotor plane, with the most significant effect on induced velocity near the tips of the blades, where the most power is produced by the turbine [173]. Based on vortex theory, these tip vortices decrease lift at the blade tip and cause a loss in aerodynamic efficiency [174]. A similar phenomenon can occur close to the blade root where it connects with the hub, where vortices shed from the hub or blade root connections cause a decrease in aerodynamic efficiency. Corrections in BEMT such as Prandtl's or Shen's Tip Loss Factor can be used

to account for the loss in aerodynamic efficiency at the blade tip and root in BEMT (Shen, Prandtl, Goldstein models). These corrections are discussed in Section 3.4.4.

Blade rotation is thought to cause a radial thinning and chord-wise acceleration of the airfoil BL due to centrifugal forces. When stall occurs, the fluid in the separated region, which is moving very slowly with respect to the blade surface, is rotating with the blade and therefore it experiences a centrifugal force causing it to flow radially outwards. The flow towards the tip on the suction side experiences a Coriolis force in the main flow direction, acting as a favorable pressure gradient. This reduces the displacement thickness of the BL, delaying the onset of stall and resulting in higher lift coefficients, particularly at the blade root.

Himmelskamp studied experimentally the rotational effects on aircraft propellers and observed lift enhancement and stall delay in rotating blades compared to non-rotating blades [175]. Banks and Gadd proposed that rotational effects could stabilize the BL against separation [176], and Schreck and Robinson hypothesized that rotational effects were driven by chord-wise and radial pressure signatures that varied with changes in radial location and inflow conditions [177]. From NREL/NASA Ames tests (S809 airfoil and 7.5×10^5 Reynolds number), deviations from 2-D airfoil data were primarily due to 3-D rotational effects, and effects from the Reynolds number varying were shown to be less important. Large changes in the airfoil characteristics were observed on both the inner part of the blade close to the hub, and at the blade tip. Close to the hub, these effects were significant, with increased lift and increased drag. However, toward the tip of the blade, the lift and drag were both decreased, particularly at high α [178]. Although these results were for a 10 m diameter wind turbine at a Reynolds number of 7.5×10^5, it has been shown that rotational effects are of more importance at lower Reynolds numbers [179], such as those of small-scale tidal turbines, and appear to scale with the Reynolds number, hence rotational effects would be expected to be smaller at a larger Reynolds number. At larger Reynolds numbers the BL thickness is smaller and the viscous effects less, therefore, the Coriolis force will be smaller with increasing Reynolds number [180].

These 3-D rotational effects are accounted for in BEMT for wind turbines by applying a correction factor such as Snel [181] to the 2-D non-rotating airfoil data. Rotational 3-D

corrections (stall delay models) account for the discrepancy of using stationary wind tunnel airfoil data for rotating turbine blades. However, Harrison *et al.* [182] found that corrections used for wind turbines do not work well in BEMT for the tidal energy application. This has the potential to cause turbine performance predictions using BEMT to incorrectly model real turbine performance, which could have implications on the design and overall device reliability.

3.1.3.C.   *Hysteresis*

Hysteresis is observed by differing lift and drag curves during airfoil testing of the same airfoil depending on if α is increasing or decreasing during the testing program. For example, at the same α, tests showed almost attached flow with small unsteadiness, higher lift and lower drag when α was increasing, and large unsteadiness, lower lift, and higher drag when α was decreasing [183]. Another test showed that hysteresis occurred at lower Reynolds number airfoil tests with low turbulence intensities, but when Reynolds number was increased, the hysteresis region was reduced [165]. With a higher turbulence intensity in the test section, the airfoil BL transitions close to the LE, eliminating hysteresis by enabling the flow to reattach at higher angles of attack [165]. Since hysteresis is a measure of actual performance, differences in turbulence intensity could cause problems during operation of an airfoil if it is operating at a lower turbulence intensity than the airfoil data used to predict performance [165]. For example, aircrafts designed using wind tunnel data obtained in a facility with a higher turbulence intensity may not perform as expected in flight where the free stream disturbance level is usually very low and hysteresis may be present [165].

For Reynolds numbers between 3×10^4 and 7×10^4 and turbulence intensities of less than 0.1%, relatively thick airfoils can have significant hysteresis effects caused by laminar separation with transition to turbulent flow [184]. The 21% thick airfoil, NREL S823, showed significant hysteresis at a Reynolds number of 2×10^5, but not at Reynolds numbers of 1×10^5 and 3×10^5. This indicates the sensitivity of hysteresis patterns on Reynolds number, however, hysteresis may also be sensitive to the airfoil thickness. For this work, hysteresis is not expected to have an effect on experimental test results because all tests in

this thesis were run with steady carriage and rotational velocities, and hence the angle of attack was expected to be constant for each test case.

3.1.3.D. *Surface Roughness*

The roughening and fouling of tidal turbine blades due to damage, cavitation, scour by particulates, or marine growth can alter the performance of the device due to the effect of surface roughness on BL behavior, particularly on the leading edge [187]. In the wind industry, surface irregularities on HAWT blades caused by the accumulation of insect debris, ice, and the aging process were shown to significantly reduce the power output [185]. For a rough surface, the transition point moves upstream, which implies an early transition and a prolonged period of transition, leading to degraded turbine performance due to decreased maximum lift coefficient and increased drag coefficient associated with early BL separation [185, 186].

The presence of roughness on turbine blades was shown both experimentally and numerically using BEMT to have an adverse effect on tidal turbine performance and cause a decrease in the power curve compared to a smooth blade [187]. Walker *et al.* [187] found through experimental towing tank tests that a blade with contact cement (giving a mean roughness height of 0.058 mm and maximum roughness height of 0.625 mm, giving a roughness of approximately 1.42% of the chord at 75% R), applied to the surface to increase the roughness had significantly lower performance characteristics than the smooth bladed case. The maximum power coefficient in this case was reduced by 19% from the baseline case, and the thrust coefficient at maximum power coefficient was reduced by 20%. For the NREL S814 airfoil, it was shown through wind tunnel airfoil tests that roughness heights on the order of 0.09% of the chord length resulted in up to 23% reduction in lift, having implications on the performance of the airfoil [168].

The effects of roughness on BL performance depend on both the level and height of roughness elements as well as the Reynolds number [188]. Studies have shown that there is a critical Reynolds number under which the flow field and performance are not affected by the presence of roughness elements [185]. PIV results of experiments performed in a closed-circuit low-speed wind tunnel showed significantly delayed stall and considerable BL stabilization obtained by adding reasonably small roughness elements to the leading

edge region. However, opposite effects, such as advanced stall, were generated if using larger size roughness elements instead. For example, compared to a case with a clean airfoil, 0.25 mm roughness (approximately 0.25% of chord length for a testing airfoil model with a chord length of 0.101 m, and a thickness of 17% chord length) was shown to delay the stall angle to greater than 18º, whereas 0.50 mm (approximately 0.495% of chord length) roughness induced a significantly advanced stall to 12º or 13º [189]. This highlights the sensitivity of airfoil performance to surface roughness and indicates the importance of its consideration in the operational expectations of a TEC. For the blades tested in this thesis, efforts were made to ensure the blade skins were as smooth as possible. This is further discussed in the experimental testing sections of this thesis.

3.1.3.E.   Wall Effects

In wind-tunnel airfoil testing, wall effects can influence the boundary-layer behavior of the test airfoil section [155]. This can pose difficulties in the accuracy of measuring the lift and drag performance. These difficulties are both inviscid, where the confined potential flow must be taken into account (more flow may be forced through the test section), and viscous, where BLs emanating from the walls or the support structures can influence the BL of the test airfoil [155]. Milne stated that at relatively high angles of attack the effect of blockage becomes more pronounced, and that the corrections for blockage and wall effects may introduce uncertainties in α. Milne applied corrections for wall effects based on the methodology provided by Rae and Pope [190] for a closed test section. These corrections accounted for approximately 1.5% decrease in drag coefficient and approximately 2.3% decrease in the lift coefficient [163]. However, the impact of such corrections may vary in other facilities.

3.1.3.F.   Blockage Effects

The blockage ratio is the ratio of the device rotor area to the channel cross-sectional area, and is important when quantifying the thrust force and power generated from a model HATTs. With high blockage ratios, the fluid cannot expand around the device as it would in an unconstrained passage, which causes more fluid to pass through the rotor area, which tends to increase the measured thrust and power [191]. For larger blockage ratios correlations can be used to adjust measured data, however, for "safe" values of blockage

ratios, measured data can be assumed to be unaffected by the tow tank cross-sectional area. Gaurier *et al.* [192] reported blockage ratios of 7.95% and Milne reported blockage ratios 4.7% [51], both of which were considered low and no correction to the experimental data was deemed necessary. However, Bahaj reported blockage ratios during tow tank tests of 7.5% and applied a correction which resulted in a reduction in both C_p and C_T of 8% and 5%, respectively. In the same report corrections applied to a cavitation tunnel with a blockage ratio of 17% resulted in a reduction in C_p and C_T of 18% and 11%, respectively [149]. However, Tedds *et al.* [193] tested a 0.5 m diameter turbine in a tow tank with a blockage ratio of approximately 16% and did not apply correction factors. Marinet project outcomes showed blockage ratios above 10% introduce questionable results [194], and hence it is suggested to apply corrections for blockage above this amount.

In order to correct for blockage, Bahaj used modified Glauert's equations for wake expansion based on an actuator disc model of the flow through the turbine. In such a model the flow is assumed to be uniform at all cross sections of the stream tube enclosing the turbine disc and a discontinuity of pressure is assumed across the disc which is related to the turbine thrust load. The equations used to correct for boundary effects to give results based on free stream inflow speed are presented in [146].

3.2   Structural Testing

Structural requirements and material selection of tidal turbine blades are vital design considerations. Static bending tests are used in this work as a method of verifying the structural integrity of blade designs and material selections based on the relationship between load applied and blade deformation/stress. This section outlines structural testing done for tidal turbine blades.

Static cantilever bending tests of a composite tidal turbine blade showed that the use of a single layer of 300 g/m^2 glass mat reinforcement more than doubled the bending stiffness, while a single layer of 1250 g/m^2 E-glass UD composite increased it by a factor of 6. These static tests also provided data to compare with blade design tool calculations [151]. Satterly *et al.* [195] compared hand-made composite flat plate samples to spars made using the tape winding process. Both the spar and plate were loaded in 3-point bending and results showed

that the flat plates were better quality than the spar sections, the plate having similar strengths and stiffness as predicted. The large difference between the properties of the plate and spar coupons can be explained by a general reduction in quality arising from the production method, including high voids, and the effect of the tape joints. This shows the importance of manufacturing on performance of composite structures, and also indicates that simpler geometry for manufacturing may result in a closer match to theoretical predictions. In order to make the transition from scale models to prototypes and industrial structures, careful consideration must be given to manufacturing, as even the same procedures can result in different structure strengths [151]

With the expectation of a long working lifespan of tidal turbine blades, material testing and aging tests are important. The strength and stiffness of composite materials degrade over time, however, the rate and extent of degradation varies depending on loading sequence, effects of salt water and temperature, and material imperfections [143]. Davies *et al.* [151] performed four point flexure tests using dog-bone specimens to characterize different composite materials after wet ageing; the natural seawater ageing facility at IFREMER in Brest was used to condition specimens before testing. Weight gains of around 1% after a year at 60ºC were measured for two materials (an infused quasi-unidirectional E-glass/epoxy and a unidirectional carbon/epoxy from pre-preg). The absorbed water affected both quasi-static and fatigue behavior of these materials, with a change in flexural failure modes noted after a certain ageing duration. It was concluded that extended ageing can result in significant property losses, which is directly related to the matrix resin formulation and fiber sizing (with non-optimized fiber sizing's resulting in lower fatigue lives). Tual *et al.*'s [196] work on composite seawater ageing showed that the diffusion of sea water into composite materials has a severe effect on static mechanical strength characteristics (a decrease of 20 to 40% in failure strengths), but had little effect on the elastic properties. This is an interesting finding, as, for BT structures, consideration of stiffness degradation is critical to determining the blade performance over a long time span under variable amplitude loading [143]. Tual *et al.* also found that ply thickness and orientation have little influence on the kinetics of water diffusion. Characterization of elastic properties was performed using tensile tests on 90º and 0º laminates according to ISO 527 [197], before

and during different steps of sea water ageing, and fracture toughness was characterized in accordance with ISO 15024 [196].

Ahamed *et al.* [198] investigated the effects of various erosion parameters, such as impingement angle and impact velocity, on the degradation modes of composite materials, with and without particles in sea water conditions. The erosion mechanisms of composite materials were evaluated using scanning electron microscopy techniques, and the surface morphologies following testing were analyzed. Results indicated that erosion processes were characterized by multiple cracks coupled with cavity formation, and indentation sites associated with linear scratches. As well, the combination of the wet environment and solid particles was found to amplify the erosion rate, increasing the depth of penetration and resulting in increased crack propagation on the test samples. This highlighted the importance of considering wet ageing as well as sea water salinity and sediment composition on composite wear rates. This is important in the prediction of the strength and life expectancy for composite tidal turbine blades.

3.3   Uncertainty Analysis

EquiMar deliverable 3.4 [199] and the ITTC protocol [200] present guidelines for design of experiment and standard methods for propagating error in experimental results. The ITTC protocol requires results to be presented as $X = x \pm \mu$ with a y% confidence interval, and the recommended protocol is that all experiments are conducted to give results with under 5% error at a 95% confidence interval. This means that 95 times out of 100, the reported value is no more than 5% different from the true value.

The total uncertainty, μ_x, of a variable X is a combination of the precision uncertainty, μ_P, and the bias uncertainty, μ_B. Precision and bias uncertainties are related to two methods of obtaining uncertainty predictions, Type A and Type B. Type A uncertainty estimates are obtained by the statistical analysis of a sample of measurements. Type B uncertainty estimates are obtained by heuristic means such as past experience, manufacturer specifications, or other information.

A precision uncertainty (Type A uncertainty) is associated with the fact that when a measurement is repeated it will generally provide a measured value that is different from

the previous value. It is random in that the next measured value cannot be predicted exactly from previous values. To determine the uncertainty associated with precision errors, knowledge about an input quantity X is inferred from repeated measurements and the standard deviation, σ, of a number of samples, n.

The precision uncertainty for a repeated measurement is given by the standard deviation of the mean. For a linear regression analysis (used for equipment calibration), the standard deviation is given by the standard error of estimate, which is a measure of the accuracy of predictions made with a regression line [201], and is given by

$$x_{SEE} = \sqrt{\frac{x_{SS_R}}{n-2}} \, ,$$

3-6

where the summed square of residuals (x_{SS_R}) is defined as

$$x_{SS_R} = \sum_{i=1}^{n}\left(y_i - s - bx_i\right)^2 \, ,$$

3-7

where x is the known value (applied load), y is the measured value (voltage), there are n sample points (i is the sample number), and s and b are from the linear calibration equation. The precision uncertainty, $\mu_{P,calibration}$, associated with the linear regression method of calibration, is therefore:

$$\mu_{P,calibration} = x_{SEE} \, .$$

3-8

A bias error (systematic or Type B uncertainty) is associated with the fact that a measured value contains an offset, and is defined as the portion of the total measurement error that remains constant in repeat measurements of a quantity. This type of measurement uncertainty is usually based on relevant information available such as previous measurement data, manufacturer's specifications, data provided from other sources, and uncertainties assigned to reference (such as uncertainty in the water mass density, viscosity, and vapor pressure).

Combining the precision and bias uncertainties, the total uncertainty associated with a measurement is given by:

$$\mu_{\text{tot}} = \sqrt{\mu_P^2 + \mu_B^2} \; .$$

3-9

The combined standard uncertainty, μ_{tot}, in a measured value is calculated using the law of propagation of uncertainty, as detailed in [202] and [199]. For a function f of multiple variables $(x_i, x_{ii}...x_n)$, which are assumed to have no covariance, the uncertainty in the calculated value of f can be estimated:

$$\mu_f = \sqrt{\left(\frac{\partial f}{\partial x_i}\right)^2 \Delta x_i^2 + \left(\frac{\partial f}{\partial x_{ii}}\right)^2 \Delta x_{ii}^2 + ... + \left(\frac{\partial f}{\partial x_n}\right)^2 \Delta x_n^2} \; ,$$

3-10

where the finite differences, Δ, are the uncertainty in each variable.

As an example, the torque measurements during calibration are estimated by:

$$Q = mgl \, ,$$

3-11

where m is the mass of the weight applied, with a bias uncertainty of $\mu_{B,m} = 0.015$ kg (from manufacturer), g is the gravitational constant, with a bias uncertainty of $\mu_{B,g} = 0.001$ m/s^2, and l is the moment arm, with a bias uncertainty of $\mu_{B,l} = 0.0005$ m (half the smallest measurement increment). Following the method given in [200], the calculation of the total bias uncertainty in the torque measurement, $\mu_{B,T}$, is expressed as:

$$\mu_{B,Q} = \sqrt{\left(\frac{\partial Q}{\partial m}\right)^2 \mu_{Bm}^2 + \left(\frac{\partial Q}{\partial g}\right)^2 \mu_{Bg}^2 + ... + \left(\frac{\partial Q}{\partial l}\right)^2 \mu_{Bl}^2} \, ,$$

3-12

where the finite differences are the bias uncertainties, μ_B, for each variable. Eq. (3-12) gives:

$$\mu_{B,Q} = \sqrt{(gl)^2 \mu_{Bm}^2 + (ml)^2 \mu_{Bg}^2 + (mg)^2 \mu_{Bl}^2} \; .$$

3-13

Dividing this equation by the original expression for Q gives the percent uncertainty in the measured torque:

$$\frac{\mu_{B,Q}}{Q} = \sqrt{\frac{\mu_{B,m}^2}{m^2} + \frac{\mu_{B,g}^2}{g^2} + \frac{\mu_{B,l}^2}{l^2}} \; .$$

3-14

A similar method can be applied to calculating the power coefficient, given by Eq 3-1, where the total uncertainty in the calculated parameter is:

$$\mu_{C_P}^2 = \sqrt{\left(\frac{\mu_{B,Q}}{Q_{mean}}\right)^2 + \left(\frac{\mu_\omega}{\omega_{mean}}\right)^2 - \left(\frac{\mu_{B,\rho}}{\rho}\right)^2 - \left(\frac{\mu_A}{A}\right)^2 - \left(\frac{3\mu_{B,U_\infty}}{U_{\infty,mean}}\right)^2} C_P^2 .$$

3-15

The uncertainty values for each variable depend on the variable (the torque uncertainty is based on the combined uncertainty, whereas the uncertainty in the rotor area is based on the sensitivity of the measurement equipment (bias uncertainty).

An expanded uncertainty qualifies the combined uncertainty by including a coverage factor (an interval around a measured value that has a specific probability of containing the true value of the measurement) and is included in the final calculated uncertainty.

The expanded uncertainty, U, comes from the combined uncertainty μ multiplied by a coverage factor, k, and is given by:

$$U = k\mu .$$

3-16

Assuming a normal probability density function for the measurement, a value of 2 can be applied for the coverage factor for a 95% confidence interval, for an acceptable number of repeated observations. For a small sample size, the combined uncertainty is multiplied by the Student's t-statistic, $t_{95,\nu}$, which is the critical value for a 95% confidence interval, based on the degrees of freedom, ν, (which, for example, if $n = 24$, $t_{95} = 2.0638$ for a two-tailed confidence interval).

3.4   Blade Element Momentum Theory

Blade element momentum theory (BEMT) is an analytical model which iterates between momentum theory and blade element theory, both of which are outlined in this section. BEMT was originally published by Glauert [203] and used to estimate the steady-state hydrodynamic performance of propellers. This modeling approach has been applied to wind turbines [58], and has seen significant usage in the tidal energy industry due to its simplicity and computational efficiency. For example, Galloway et al. [48] compared a $1/20^{th}$ Froude scaled representation of a 16 m diameter HATT tested in a towing tank to

BEMT data, and found good correlation for λs of 4 to 7, close to the peak power coefficient. Clarke *et al.* [147] tested 1/30th scale (0.82 m diameter) contra-rotating HATT model and found good agreement with predicted BEMT results. The results from this model scale test were used to design a larger model turbine (2.5 m diameter), which was found to function according to expectations [147].

Similar models can also be used to study the influence of the marine flow environment on rotor performance [31], and can play a major role in the early stage technology development [204]. However, BEMT can be inaccurate due to simplifications in the modeling process and hence typically requires additional correlations found experimentally. In this work, BEMT is used to study the relationship between blade shape and the hydrodynamic performance (loads and power capture) of a tidal turbine rotor.

This section gives a brief description of momentum theory, blade element theory, and the combination and implementation of the iterative blade element and momentum theories that make up BEMT.

3.4.1 Momentum Theory

Momentum theory evaluates the momentum balance on a rotating annular stream tube passing through a turbine rotor and can be broken into an axial and a tangential component.

3.4.1.A.   Axial Momentum Conservation

The rotor reduces the axial velocity of the fluid from the inflow velocity, U_∞, to the rotor disk velocity, U_d, by a factor called the axial flow induction factor [58]:

$$a = \frac{U_\infty - U_d}{U_\infty}.$$

3-17

Due to continuity (assuming an incompressible fluid), the mass flow rate far upstream has to equal the mass flow rate at the rotor cross section and in the far wake. The pressure difference from the front to back causes an axial force on each blade element which balances the momentum lost. This force is found (assuming the disc does not cause rotational flow) by comparing the pressure at different areas of the stream tube using Bernoulli's equation. The thrust or axial force, $dF_{A,2}$, on each blade segment is equal to the

pressure difference (calculated using Bernoulli's equation) multiplied by the area of the blade element in question ($dA = 2\pi rdr$). This gives:

$$dF_{A,2} = 4\rho U_\infty^2 a (1-a)\pi rdr,$$

3-18

where ρ is the fluid density, r is the rotor radius, and dr is an incremental slice along the blade span.

3.4.1.B.   Angular Momentum Conservation

The exertion of a torque on the rotor disc by the fluid (caused by the component of the lift and drag forces perpendicular to the axial direction) requires an equal and opposite torque to be imposed upon the fluid. This reaction torque causes the fluid to rotate in a direction opposite to that of the rotor. Therefore, the fluid gains angular momentum and the fluid in the wake will have a velocity component in the tangential direction.

The angular momentum imparted to the wake increases the kinetic energy in the wake, but the energy is balanced by a reduction in the wake static pressure. Similarly to the change in axial velocity, the change in tangential velocity is expressed in terms of a tangential flow induction factor which is:

$$a' = \frac{\Omega}{2\omega},$$

3-19

where ω is the rotor rotational speed and Ω is the wake rotational speed. Through conservation of angular momentum, the tangential force on a blade element, $dF_{T,2}$, is equal to the rate of change of angular momentum, which is the mass flow rate at the rotor plane multiplied by the change of tangential velocity and the radius. This gives:

$$dF_{T,2} = 4\rho\omega a' U_\infty (1-a) r^2 \pi dr.$$

3-20

The torque on the rotor is given by the tangential force, dF_T, multiplied by the radius, $dQ = rdF_{T,2}$.

3.4.2 Blade Element Theory

The rate of change of the axial and angular momentum of the fluid which passes through the swept area is a result of the lift and drag forces on the span-wise blade elements. Blade

element theory (BET) examines the forces generated by the airfoil lift and drag at various sections along the blade. The blade is broken into a series of 2-D sections called blade elements, and the forces on each element are determined. By integrating over the entire blade during one blade revolution, the forces and moments on the entire blade can be determined. The axial and tangential blade element forces are described in Section 2.2.1. Building on the Eq. (2-6) and (2-7) in Section 2.2, the axial and tangential forces can be written in terms of the axial and tangential induction factors.

$$dF_{\mathrm{A}} = \frac{1}{2}\rho c B dr \frac{U_\infty^2 (1-a)^2}{\sin^2 \theta}(C_L \cos\theta + C_d \sin\theta),$$ 3-21

$$dF_{\mathrm{T}} = \frac{1}{2}\rho c B dr \frac{(1-a)U_\infty (a'+1)\omega r}{\sin\theta \cos\theta}(C_L \sin\theta - C_d \cos\theta).$$ 3-22

3.4.3 Blade Element Momentum Theory

The loads based on the momentum balance are derived from conservation laws and the loads from the blade element theory are derived from the airfoil sectional lift and drag. The loads calculated both ways have to be equal to each other. From momentum theory and blade element theory, four equations (two for thrust, and two for torque) can be used to predict rotor performance. By equating the two sets of equations, the flow induction factors can be expressed as:

$$\frac{a}{1-a} = \frac{Bc}{8\pi r \sin\theta^2}[C_L \cos\theta + C_d \sin\theta],$$ 3-23

$$\frac{a'}{1+a'} = \frac{Bc(C_L \sin\theta - C_d \cos\theta)}{8\pi r \sin\theta \cos\theta}.$$ 3-24

Using an iterative process along the blade, the induction factors can be calculated. An iterative approach is necessary because the 2-D airfoil characteristics are non-linear functions of α. The iterative procedure is to initially set the induction factors to zero (or some estimated value), determine α and power/thrust coefficients, and then repeat until the solution converges.

72

3.4.4 Limitations and Corrections to BEMT

BEMT is computationally fast, and has been shown to be able to predict the hydrodynamic performance of tidal turbines in steady flow conditions, but due to the simplifications made in the model, there are several limitations to consider and corrections that can be used to improve the model accuracy.

The baseline blade element theory relies on two assumptions: 1) there are no interactions between consecutive blade elements and, 2) the forces on the blade elements are based only on the lift and drag forces. Due to the strong dependence on sectional airfoil data, obtaining appropriate airfoil data is one of the main limitations in the implementation of BEMT theory [205]. For tidal turbines, there exists issues with obtaining this lift and drag data for α and Reynolds numbers which are not as widely published as those used for wind turbines. Because there is a strong dependency on the quality of blade airfoil data, this can limit the accuracy of the model, particularly for the tidal energy application. Until more airfoil section data in the appropriate Reynolds number range is available, this will continue to limit the application of BEMT in this industry. However, with the appropriate corrections, BEMT is a useful tool for early stage design work.

As discussed in Section 3.1.3, the pressure difference of the suction and pressure surfaces of a blade causes span-wise flow and vortex shedding, resulting in a loss of efficiency and power production. To account for these tip and hub losses, Prandtl's tip and hub loss factors serve to correct the induced velocity resulting from a vortex being shed near the tip and the hub of the rotor [206]. To implement this correction, the momentum theory forces in the axial, $dF_{A,2}$, and tangential, $dF_{T,2}$, directions (from Eq. (3-18) and (3-20)) predicted by BEMT are multiplied by Prandtl's tip and hub loss factors (Eq. (3-25) and (3-26)) or a combination of both, as given by Eq. (3-27) [207].

$$F_{\text{Tip}} = \frac{2}{\pi}\cos^{-1}\left(\exp\left[-\frac{B}{2}\frac{\left(1-\left(r/R\right)\right)}{\left(r/R\right)\sin\theta}\right]\right), \qquad \text{3-25}$$

$$F_{\text{Hub}} = \frac{2}{\pi}\cos^{-1}\left(\exp\left[-\frac{B}{2}\frac{\left(r-R_{\text{hub}}\right)}{r\sin\theta}\right]\right), \qquad \text{3-26}$$

$$F = F_{Tip}F_{Hub} \; .$$

<div align="right">3-27</div>

Other tip loss models such as Shen [207] have been used in the wind industry, however, Prandtl's models have been shown to work well for tidal energy applications [206], where Shen's correction predicts a slightly lower performance than Prandtl's [208].

BEMT is also limited in accurately predicting heavily loaded rotors operating in the turbulent wake state. At high λ, the axial induction factor can approach or exceed the theoretical upper limit of $a = 0.5$, which leads to inconsistencies in the model, since it implies a flow reversal downstream of the turbine. This means that the momentum equations no longer accurately predict the behavior of the turbine, since in reality, the flow downstream slows and fluid is drawn in from outside of the rotating wake, increasing the turbulence [209]. For heavily loaded cases where the axial induction factor is greater than $a = 0.5$, an empirical relationship is used to predict the rotor thrust loads. The Buhl high induction correction fits a curve to experimentally obtained thrust coefficients for values greater than this critical value of the axial induction factor [210]. Essentially, it corrects the thrust coefficient, when the turbine is heavily loaded, by replacing the $4a(1-a)$ in Eq. (3-18) with the following:

$$C_{Buhl} = \frac{8}{9} + (4F - \frac{40}{9})a + (\frac{50}{9} - 4F)a^2 \; .$$

<div align="right">3-28</div>

The new equation for the thrust from momentum theory, including Prandtl's loss factor, F, is given by:

$$dF_{A,2,Buhl} = C_{Buhl}F\rho U_\infty^2 \pi r dr \; .$$

<div align="right">3-29</div>

At the upper limit of the axial induction factor where $a = 1$, the correction gives $C_{F_A} = 2$. Because tip and hub losses lead to high local induction factors, the tip, hub and high induction correction factors are used in combination [209].

Modeling complex stall behavior is another a limitation of baseline BEMT, and hence stall model corrections are used to compensate for the decrease in blade lift force observed in low λ operation. The Viterna-Corrigan post stall correction has been shown to provide good

agreement between measured and predicted power for stalled wind turbines [211], and has been applied to the BEMT in this work. The Viterna-Corrigan post stall correction assumes that the blade behaves like a 3-D flat plate when fully stalled, and the stall lift and drag coefficients are a function of the maximum drag coefficient in the fully stalled regime, $C_{D,\,max}$, the lift and drag coefficients at the stall angle, $C_{L,s}$ and $C_{D,s}$ respectively, and the aspect ratio of the blade, j, [212]. This is given by:

$$K_L = \left(C_{L,s} - C_{D\,max} \sin \alpha_s \cos \alpha_s\right) \frac{\sin \alpha_s}{\cos^2 \alpha_s} \,, \qquad\qquad 3\text{-}30$$

$$K_D = \frac{C_{D,s} - C_{D\,max} \sin^2 \alpha_s}{\cos^2 \alpha_s} \,, \qquad\qquad 3\text{-}31$$

$$C_L = 0.5 C_{D,\,max} \sin 2\alpha + K_L \left(\frac{\cos^2 \alpha}{\sin \alpha}\right), \qquad\qquad 3\text{-}32$$

$$C_D = C_{D,\,max} \sin^2 \alpha + K_D \cos \alpha, \qquad\qquad 3\text{-}33$$

$$C_{D,\,max} = \begin{cases} 1.11 + 0.018 j & \text{if } j \leq 50 \\ 2.01 & \text{if } j > 50 \end{cases}, \qquad\qquad 3\text{-}34$$

where α_s is the stall angle of attack.

The Viterna-Corrigan post stall correction does not account for stall delay due to 3-D rotational effects. Corrections such as Snel *et al.* [181] can be implemented in BEMT to adjust airfoil performance and account for these rotational effects and stall delay. The 3-D correction of Snel *et al.* was derived from an order of magnitude analysis of the BL equations and accounts for the lift augmentation caused by rotation. In this model, an empirical relationship is used to correct the 2-D lift coefficient as a function of the local blade solidity (*c/r*) for stall-delay. The lift coefficient that would be obtained if the linear part of the static 2-D C_L-α curve was extended beyond stall is used to estimate the new section lift. Although this model improved agreement for power predictions when compared with experimental data for full-scale wind turbines [211], it is limited due to the

fact that the drag coefficient remains uncorrected [182]. Du and Selig built on Snel *et al.*'s model and added corrections for drag [180], and Bak *et al.* developed a model based on the pressure distributions on the airfoil which has shown good agreement to experiment. However, Bak *et al.'s* model requires the knowledge of the airfoil pressure distribution at stations along the blade, which can be challenging to obtain [178]. Although there has been work done to correct for rotational effects in the wind industry, these have been shown to be insufficient for the prediction of tidal turbine performance, and using different models has been shown to give different results [182]. Therefore, 3-D corrections such as these are not included in the BEMT model used for this thesis work.

3.5 Composite Material Modeling

In a FEM, the material model used significantly affects the structure response. For this reason, the theory of composite materials is introduced, with a discussion of the material models developed.

Composite materials are made from two or more constituent materials with different physical or chemical properties, giving composite structures anisotropic properties (different depending on the material direction). Composite materials are replacing metals because of their fatigue tolerance, high strength-to-weight ratio, corrosion resistance, and damage tolerance [213], particularly in harsh operating environments such as subsea [25]. Reduced weight is of particular importance for subsea components due to the high cost of installation lifting equipment [214]. Reduced weight has a two-fold effect on the cost of a tidal turbine; as the weight of the blade decreases, the demands on the hub and support structure decrease, resulting in lower capital expenses, but the maintenance requirements are reduced as well, resulting in lower O&M costs.

Composite materials are of increasing interest in industries where the tailoring of mechanical structural responses can increase cost effectiveness. Anisotropic composite materials can be optimized for specific applications by tailoring the manufacturing techniques and preferentially orienting the fibers. The fibers in a composite laminate can be aligned in the direction of the highest loads so that they are being used efficiently, resulting in a more optimized structure [214]. Also, components made of composite

materials can be structurally tailored to exhibit desirable elastic deformation behavior that is not necessarily proportional to the imposed load, as discussed in Section 2.4.

Classical lamination theory (CLT) describes the derivation of the stiffness matrix for a laminated composite material, and relates stress and strain. This theory forms the backbone for many composite material models. However, it assumes a plane-stress state, making it unsuitable for thick composite materials. See Appendix A for a full explanation of classical lamination theory.

3.5.1 Composite Failure

A composite material fails due to excessive mechanical loads; however, based on loading and composite design, it is possible that some layers fail first and the composite continues to take more load until all of the plies fail. Even after a ply fails, it may still contribute to the stiffness and strength of the laminate. For example a failed ply that has cracks parallel to the fibers can be treated as a load bearing ply but with no transverse stiffness, tensile strength or shear strength. Modeling the degradation of the stiffness and strength properties of each failed lamina is up to the designer. However, once one ply fails, it may be safer to fully discount this ply using near zero stiffness and strength values [215].

In a composite structure, several failure modes are possible, including debonding, matrix cracking, fiber breakage, inter-fiber fracture and delamination. Debonding occurs when an adhesive stops sticking to a material, whereas delamination is related to a failure in the laminated material which leads to separation of the ply layers. Delamination is a result of interlaminar (between ply layers through a laminate thickness) stresses, which include both normal and shear stresses. Delamination is often preceded by a crack that propagates through a ply until it reaches the fibers of an adjacent ply, where it may branch off and go along the interface between the plies, causing a delamination crack to form. Delamination is serious, since any area of delamination destroys the compatibility between the lamina.

Matrix cracking is prone to occur as a result of manufacturing techniques where the matrix resin shrinks upon curing, causing residual stresses in the matrix after curing. Of course, the stress levels in the matrix increase as the structure is strained, but these residual stresses, if not accounted for, can lead to earlier than expected matrix cracking. If these cracks

increase in size and number, they can eventually cause inter-fiber fracture or full delamination [216].

Inter-fiber fracture occurs when a microscopic crack runs parallel to the fibers through the thickness of the laminate. These cracks stop at the interface between plies, which cause small delaminated zones at the crack end. The direction transverse to the cracks (and to the fibers) is weakened, which means the structure becomes weak in transverse tension [216], which is already a weak laminate direction. It can, however, still carry compression in the transverse direction.

Strength predictions of composite materials is complex due to the interaction of various modes of damage which lead to the failure of the composite structure [217]. A typical material stress-strain curve can advise the designer on what failure criteria to use in the design of composite structures. Ultimate strength values are typically used to predict failure of composites due to the generally linear stress-strain relationship and insignificant yielding prior to failure due to the brittleness of the materials [218].

For a composite material, failure theories are based on the stresses in the material or local axes (denoted by 1 and 2) because a lamina is orthotropic and its properties are different along different material directions. This means that the normal stress along the fibers (local direction 1, σ_1), and transverse to the fibers (local direction 2, σ_2), as well as the shear stress in the 1-2 plane (τ_{12}) are required in order to perform the analysis [215] (in a 2-D case, which is the most common). These stresses can be either tensile (positive) or compressive (negative) depending on their sign (subscripts C and T). Figure 3-1 shows these material directions for a typical laminate.

Figure 3-1 Directionality of typical laminate.

Although there are over 100 models for failure for composite materials, with no one model that works for all loading scenarios, the following failure theories are the most commonly used for composite design [219], with the main resource for these theories being "Mechanics of Composite Materials" by Kaw [215].

1. Maximum stress failure theory
2. Maximum strain failure theory
3. Tsai-Hill failure theory
4. Tsai-Wu failure theory

The most commonly used theories in industry are the Maximum stress and Maximum strain failure theories, followed by Tsai-Hill [220].

The Maximum Stress failure theory states that a lamina fails if the compressive or tensile stresses in the local fiber (longitudinal), transverse, or shear directions surpass the ultimate strength in these directions [221]. Each component of stress is compared with the corresponding ultimate strength. In this theory, the components of stress do not interact [215], making it a more conservative estimate of failure but typically leads to errors in the strength predictions when multiaxial states of stress occur in a structure [220]. This model takes into consideration in-plane shear failure as well, which is considered a failure theory on its own [222].

By applying a strength ratio, a safety factor (SF) or failure index (inverse of the SF) can be calculated which indicates the likelihood of failure. This strength ratio is estimated by:

$$\frac{\text{Maximum stress}}{\text{Strength}} < 1.$$

3-35

For example, for a SF of 1, the failure index should always be less than 1, and for a safety factor of 2, the failure index should always be less than ½. While this is a simplistic and easy to apply model, it assumes that there is no interaction between the components of stress in different material directions, and hence does not tend to match experimental failure data well [215].

The Maximum Strain failure theory is based on the maximum normal strain theory by St. Venant and the maximum shear stress theory by Tresca, and is very similar to the

Maximum stress theory. Like the Maximum stress theory, the strains are resolved into the local fiber and transverse directions. Failure is predicted if any of the strains in the local axes exceed the corresponding ultimate strains of the unidirectional lamina. Failure criteria are calculated the same was as in the Maximum stress theory, however, the two failure theories give different results because the local strains in a lamina include the Poisson's ratio effect [215]. This method is useful when the strength values for a particular material are given in terms of strain.

The Tsai-Hill failure theory is based on the distortion energy failure theory of von-Mises' distortional energy yield criterion for isotropic materials but is applied to anisotropic materials [215]. Unlike the Maximum Stress failure theory, Tsai-Hill failure theory considers the interaction among the three unidirectional lamina strength parameters. The Tsai-Hill theory proposes, for a plane stress assumption, that a lamina fails if [215]:

$$\left(\frac{\sigma_1}{\sigma_{1ult}^T}\right)^2 - \frac{\sigma_1\,\sigma_2}{\left(\sigma_{1ult}^T\right)^2} + \left(\frac{\sigma_1}{\sigma_{2ult}^T}\right)^2 + \left(\frac{\tau_{12}}{\tau_{12ult}}\right)^2 > 1\,. \qquad \text{3-36}$$

The original Tsai-Hill theory does not consider compression, and since the transverse direction of a laminate is much stronger in compression, it tends to over predict the likelihood of failure. This is corrected for by adding a condition that if the transverse stress is negative (*i.e.* in compression), Tsai-Hill failure criteria is updated to:

$$\left(\frac{\sigma_1}{\sigma_{1ult}^T}\right)^2 - \frac{\sigma_1\,\sigma_2}{\left(\sigma_{1ult}^T\right)^2} + \left(\frac{\sigma_1}{\sigma_{2ult}^C}\right)^2 + \left(\frac{\tau_{12}}{\tau_{12ult}}\right)^2 > 1\,. \qquad \text{3-37}$$

The Tsai-Wu failure theory is based on the total strain energy failure theory, and is an expansion of von Mises failure theory for the consideration of composites, similarly to the Tsai-Hill failure theory. The Tsai-Wu theory proposes that a lamina fails if [215]:

$$\left(\frac{\sigma_1}{\sigma_{1ult}^T} + \frac{\sigma_1}{\sigma_{1ult}^C}\right) + \left(\frac{\sigma_2}{\sigma_{2ult}^T} + \frac{\sigma_2}{\sigma_{2ult}^C}\right) - \left(\frac{\sigma_1^2}{\sigma_{1ult}^T\sigma_{1ult}^C}\right) - \left(\frac{\sigma_2^2}{\sigma_{2ult}^T\sigma_{2ult}^C}\right) + \left(\frac{\tau_{12}}{\tau_{12ult}}\right)^2 \dots$$

$$\text{3-38}$$

$$\dots + 2F_{12}\sigma_1\sigma_2 + 2F_{16}\sigma_1\tau_{12} + 2F_{26}\sigma_2\tau_{12} > 1$$

where the *F*'s are values obtained experimentally. However, there are empirical equations for determining these constants, which have been shown to match well with experiment. This failure theory is better than the Tsai-Hill failure theory because it differentiates between compressive and tensile stresses and strengths. This model requires tests to determine parameters which makes it more time consuming. If the above correction is applied to Tsai-Hill theory, then the two theories work very similarly. However, both of these models do not account for through-thickness stresses due to the plane stress assumption used in these theories.

The Maximum stress theory inherently indicates the laminate direction at highest risk (failure criteria associated with failure mode), for example, transverse tension might have the lowest safety factor and hence highest likelihood of failure. While this is beneficial in early design stages, it tends to be over conservative, as it does not consider the interaction among stresses in different material directions. Compared to experimental data, both the Tsai-Hill and Tsai-Wu theories shows a better match than the Maximum stress and strain theories, whereas the difference between the Maximum Stress failure theory and the experimental results is quite pronounced [215]. However, the Tsai-Hill and Tsai-Wu failure criteria do not take into account the different damage mechanisms that lead to failure.

All of these models rely on a ply-to-ply analysis (meaning no interaction between layers is considered), and assume that fiber failure constitutes final failure [222]. These four main failure theories are therefore only useful for fiber breakage, matrix cracking, and debonding and are not capable of predicting delamination failure, which can be a dominant failure mode, particularly for structures with high levels of inter-laminar shear stress.

3.5.2 Composite Material Models

Most composite material models in FEM use the CLT description of composite behavior to calculate the effective stiffness of a composite shell. This is done within the code using the properties of individual plies, and the homogenized shell properties are then used in the analysis. After the analysis, the stresses and strains in the individual layers, calculated from the overall shell stresses and strains, are used to assess the failure and damage of the plies based on the material model used [223]. The stresses and strains are calculated at the mid-plane of each ply, and therefore for sufficiently thin plies, these values represent uniform

stresses. However, CLT is based on a plane stress assumption, which in the case of a thick laminate or a highly curved laminate, may not be accurate. However, by discretizating the laminate, each element can be assumed to meet the plane stress assumption. FEA is required to transfer loads from the interfaces between elements, as CLT cannot handle discontinuities.

The constitutive material models differ by which failure theory they use, how the composite laminate is expected to fail, and what element types these models can be used with. Based on the material model used, material properties are degraded as failure is reached according to a specific degradation scheme. Discontinuous failure is modeled by material properties (Young's moduli, shear moduli and Poisson's ratio) going to zero when the ply reaches the pre-described failure condition (in other words, the ply is either 100% ok, or 100% damaged). The continuum damage mechanics model is more physically accurate and reduces the material properties according to the degradation scheme after failure is initiated [224].

In RADIOSS®, there are several material models which can be used for modeling composite materials. The MAT 8 material model can be used to define the properties for planar orthotropic elastic materials in two dimensions, but can only be referenced by PSHELL, PCOMP, and PCOMPG property cards. Solid elements can be used to model composites as well, but each ply needs to be modeled with at least one solid element so it requires a large number of solid elements to model a simple plate. To model failure, there are material models available that use Hashin, Puck, Tsai-Wu (MAT 25), and Hill (MAT 32 or MAT 43) composite failure theories [223]. There are also models available to mimic voids in composite materials (MAT 0 and MAT X0).

Several of the base composite material models used in LS Dyna [such as MAT 116 [225]] do not compute composite stresses, and hence stresses and strains have to be related to nodal displacements in post processing. In LS Dyna, MAT 116-117 uses a pre-integration to compute the extensional, bending, and coupling stiffness coefficients for use with a Belytschko-Tsay shell formulation, which makes this model relatively fast. More complex composite material models include the calculation of composite stresses and typically have a failure criteria or damage model. For example the progressive failure model, MAT 22, in

LS Dyna, models orthotropic materials with Chang-Chang failure criterion implemented to model brittle failure. This model is typically used to model thick composite structures with solid elements [225].

Other models such as MAT 54 and MAT 58 use a specific failure criterion but allow for modified failure where elements fail due to either time step criterion, effective strain, or by reaching a given strain value, and there are allowances for elements to be completely removed after the maximum effective strain is reached. In MAT 54-55, when failure has occurred in all the composite layers, the element is deleted. When this occurs, the elements around the failed one have their material properties "softened" by a user defined level. MAT 58 allows for special control of shear behavior of fabrics, so that shear failure is more realistically predicted, and MAT 59 is similar to MAT 58 but uses Tsai-Wu failure criterion and allows for a softening factor of the tensile stresses. If the softening factor is 0, the material is modeled as fully elastic-plastic (elastic deformation followed by plastic deformation- non-reversible change in shape in response to applied load) with the initial strength values, and a softening factor of 1 means that all tensile strengths drop to zero after tensile failure, and the material can only carry compressive loads and shear. MAT 162 is based on the progressive failure principle of Hashin [226] and the damage mechanics model of Matzenmiller *et al.* [227] which allows for controlled strain softening after failure. Other models such as MAT 132 have optional delamination failure for brittle composites, and MAT 158 allows for rate sensitive stress tensor.

To summarize, most composite material models create the stiffness matrix in the same way, but apply different damage and failure criteria based on the FEM-calculated stresses. A thorough description of more composite models is given in [228].

3.5.3 Scaling of Composite Structures

Scaling composite turbine blades from model scale to prototype and commercial scale is not well understood. The scaling problem is complex for composites on account of the intricate nature of their micro-structure. Also the many possible factors involved, such as manufacturing techniques and conditions, and fiber and matrix materials, further complicate the problem [229]. The marine industry generally uses more variable, hand laid-

up laminates than the aerospace industry, leading to greater variation in mechanical properties.

It is well known that there is a tendency for the strength of laminated composites to decrease with increasing specimen size or laminate thickness, the so-called 'size effect" [230]. The size effect has major implications on the design of large composite structures since if designs are based upon coupon tests, the strength of the full-scale structure may be overestimated. Sutherland [153] found through his literature review that as you go from a small composite structure model to a larger prototype, the probability becomes greater that defects in the larger model are significant enough to cause failure. Due to their size, thicker composite laminates (as in full-scale blades) have an increased likelihood of hidden flaws, and a number of production-related flaws may occur in larger structures which are more easily avoided in smaller structures and test coupons [231]. In other words, a lower quality specimen is obtained when a thicker laminate is produced due to manufacturing variations or defects [153, 232]. The implications of this are that the properties of hand laid-up laminates are sensitive to variations at the fabrication stage.

In one study, three-dimensional scaling effects were investigated for a composite specimen under compression, where all dimensions of the baseline specimen were increased by scaling factors of 2 and 4. The average strengths for a unidirectional composite sample decreased with increasing specimen volume by up to 16% in the sub-laminate level and up to 30% in the ply-level scaled specimens. This shows that size effects are generally more evident in laminates scaled at the ply-level (increasing ply thickness) rather than sub-laminate level scaled plates (increasing the number of repeated ply sequence). Lee concluded that this is because it may not be possible to achieve the same compaction, removal of voids, or cure uniformity for thick laminates compared to thinner ones [233].

This indicates the importance of manufacturing composite structures to maintain strength characteristics close to those obtained from coupon testing. However, if this size effect is well characterized, these factors could be taken into consideration in the design stage using a FEM, enabling the FEM to predict the deformations and stresses accurately. If this is taken into consideration when scaling up the design of a composite structure, it can be assumed that a small composite blade can be used to predict the general performance of a

larger blade. However, this means it is important that FEMs are validated for both small and full-scale structures throughout the design process.

3.6 Fluid and Structural Combined Models

Combinations of tools are often used when designs require the consideration of both fluid dynamics and structural integrity, such as that of tidal turbines. These models are denoted fluid-structural interactions (FSI) models. Iterative coupling between fluid and structural models has been used in the design of composite marine structures such as propellers and tidal turbine blades. An iterative approach means that structural deformations and subsequently changing hydrodynamic forces are in balance so the elastic response of the blade is accurately modeled [234]. Accurate modelling of FSI is particularly important for BT blades, since large bending and twisting deformations will influence the hydrodynamic forces considerably, and vice versa.

For early stage design, a FEM-BEMT coupled approach allows for computationally efficient simulations (BEMT being significantly faster than typically used CFD models) while still enabling investigation of the static behavior of a flexible blade under a hydrodynamic load, and optimization of the blade both structurally (stresses and failure criteria, composite layup optimization) and globally (power curve, thrust loads). However, there are limitations of a coupled FEM-BEMT, such as no dynamic simulations, no fatigue damage assessment, and interactions with other turbine parts are not simulated [234]. This section gives an overview of previous work done using coupled FEM-BEMT design tools for turbine design and analysis.

Maheri *et al.* [235] developed a code for wind turbines with adaptive blades (WTAB), and used a coupled aerodynamic-structural simulation to study the effect of induced twist on the initial loading of a BT coupled blade. In the coupled aero-structure analysis the FEM code predicted the induced twist while the aerodynamic code (BEMT) predicted the blade loading and turbine performance. The FEM code used 3-node shear-deformable triangular elements which were said to be efficient and accurate. They used an adaptive mesh generator to update the FEM mesh after each iteration, and applied the loads determined from BEMT to the skin of the blade on the FEM nodes. The applied loads were determined

based on the BEMT load at the aerodynamic center (¼ chord location), and were moved to nodes on the blade skin with an added correcting moment to make up for the difference between the aerodynamic moment at ¼ chord, and the moment caused by the relocation of the aerodynamic forces to the blade skin. This was done because the blade is assumed hollow and there is hence no node to load the blade at the ¼ chord point.

Maheri *et al.* investigated the induced twist and blade loads for a single stage analysis, with loads from BEMT applied to the FEM, and an aero-structure iterative process between the BEMT and FEM. This showed that a single stage analysis drastically over predicted the induced twist of the blade. Upon further development of this model, and to increase computational efficiency, they used a combined FEM/analytical model to estimate the induced twist at various operating conditions, and the original BEMT code to calculate turbine performance. They used the FEM to calculate the effective stiffness distribution at a reference wind turbine run condition (such that the FEM-based simulation takes place only once), and then used an analytical model of the force-displacement relations to calculate induced twist based on source loads at other run conditions. Because the FEM only had to be run once during the design process, this method was much more efficient than the earlier model in which the mesh was updated and the FEM was run at each iteration. However, in the FEM part of the simulation the emphasis is only on the blade deformations, and hence a stress analysis was not performed. They compared this FEM/analytical-BEMT model to the original fully coupled FEM-BEMT tool and found that the FEM/analytical model gave overall good results but required less than 5% of the computation time of the fully coupled FEM-BEMT model.

Maheri *et al.* [236] applied this tool to the design of a BT coupled fixed-speed stall regulated wind turbine. They found the optimal fiber orientation to be 24º, with respect to the longitudinal axis of the blade, and optimal thickness to be 4.2 mm for a 14.4 m radius wind turbine. This resulted in a 15.5% increase in energy capture for a turbine operating in a site with Rayleigh probability distribution function and an average wind speed of 5.6 m/s. However, it is thought that some amount of this increase in the power captured was due to a 4.7% increase in rotor radius, which could equate to a significant increase in power.

Capellaro and Cheng [121] investigated BT wind turbine blades using an iterative FEM-BEMT design methodology for a VS HAWT. In this work, loads were computed in BEMT and applied to the aerodynamic center of each span-wise section of the blade. An iterative method was employed to determine the required pre-twist of the blade at a particular turbine run condition such that the same geometrical shape as the undeformed blade was obtained after the blade twisted under loading at rated conditions. This means the BT blade twisted to achieve the maximum power coefficient under deflection instead of twisting to lower performance values. By optimizing the BT blade undeformed geometry, a 1.25% increase in annual energy production was obtained.

Knill [237] developed and verified a method of transferring aerodynamic and inertial loads from the results of a BEMT to a FEM. He performed a comparison between the results of a blade FEM loaded by a pressure distribution (pressure applied per element of the FEM model) and a discrete sectional BEMT loading whereby the loads were applied in the FEM by rigid links. To replicate the aerodynamic pressure coefficients (a function of local Reynolds number, α, and position along the chord line) on the blade at any point, a database of pressure coefficients was created with XFOIL. The concluding remarks stated that for detailed stress/strain analysis the pressure distribution delivers much better results. However, almost no difference was noted with regard to the general deflections [237].

Verelst [234], working with TU Delft and 3E, studied flexible wind turbine blades using FEM software Abaqus coupled to the BEMT program WT_Perf (developed at NREL), with the induced twist angle as the convergence criteria. Similar to the method outlined by Maheri [32], aerodynamic loads were applied as point loads on the outer skin of the blade, with a correction moment (calculated based on moment coefficients for the blade sections) distributed over all available section nodes in order compensate for the changed aerodynamic moment around the aerodynamic center. The aerodynamic calculations required lift, drag and moment coefficients at different angles of attack which were obtained using XFOIL. As a verification exercise, results from an FSI study using Abaqus coupled with Numeca's CFD solver Fine/Hexa, were used, and it was found that the deformations and loads calculated by the Abaqus-WT_Perf program were significantly overestimated compared to the Abaqus-CFD (twist angles being off by within a 5% error

range and blade flap- and edge-wise deflections being off by 40% and 50%, respectively, from the CFD results). This was thought to be due to the rotor operating in full stall, which both CFD and XFOIL have trouble modeling. In particular, it was thought that loads were over-predicted because of incorrect stall and post stall airfoil characteristics as predicted by XFOIL. This CFD model had not been verified against experimental results, adding uncertainty to this verification. Computational times for this model were between 30 and 70 minutes on a single core 1.7 GHz, 2GB laptop and required up to 6 iterations [234].

Using design data from BEMT and applying outputs to a FEM, Bechly and Clausent [238] found that FEM predictions compared well with static bending and twisting deflections of the blade during static testing, and with the first two natural frequencies of vibration during dynamic testing. Aerodynamic pressures, determined from a panel code, were added by the program as normal pressures to the FEM. As the panels rarely coincided with the plate elements, linear interpolation of these pressures was done to give a pressure distribution for plates in the FEM. However, they used von Mises stress as a measure of the level of stress in the composite blades, which could limit the ability to perform an accurate failure analysis using this model. Jureczko [239] devised a parametric blade FEM, for the optimization of blade shape and other design parameters, in which the aerodynamic loading was produced from BEMT outputs and concentrated at the aerodynamic center of each blade element. To speed up calculations, the 3-D model of the blade was reduced to Timoshenko beam elements and grid points created along the aerodynamic centers were used to apply the aerodynamic forces. Although computationally efficient, the validity of such concentrated loading when examining the local stress field can be limited, as discussed by [237].

Grogan *et al.* [44] developed a preliminary composite lay-up using PreComp, and a detailed FEM was developed using Abaqus 6.9. The blade was modelled using 4-Node reduced integration (S4R) linear shell elements with enhanced hour-glass control. The two main sources of loading on the blade were the thrust and tangential forces, which were applied to the model as surface traction distributions on the spar caps of the blade at the aerodynamic center. Duan [240] used loads from BEMT to do a strength analysis in FEM for a composite blade using Tsai-Hill failure theory. Loads were applied from BEMT

(including aerodynamic forces, centrifugal forces and gravity forces) over the nodes of each airfoil section for a 600 kW wind turbine. They found, based on their failure analysis that the blade design did not fail.

Mahri and Rouabah [241] studied dynamic loads and stresses acting on wind turbine blades in order to predict fatigue failure. They used BEMT for the turbine performance analysis and FEM for a structural analysis of the dynamic stresses in the root region. They used results obtained (such as loads from BEMT, and mode shapes and frequencies from a modal analysis) to compute dynamic forces (which were required to calculate the dynamic stress). It was estimated that a 10 m diameter wind turbine with composite blades could resist fatigue for twenty years of operation, with an operating speed exceeding 15 m/s. Heege [242] coupled a FEM and BEMT code to study the dynamic wind loads on HAWT power trains. They considered the entire turbine system from blades and rotor to the gears in the drive train. Blades were represented by "super elements" and/or non-linear beam elements, and structural components which are subject to elastic deformations and which have impact on the dynamic properties, were included in the complete wind turbine FEM.

The literature discussed in this section will inform the development of the FEM-BEMT coupled model outlined in this thesis.

CHAPTER 4
STRUCTURAL TESTING

Laminate plates and composite blades with BT layups were tested statically to investigate the bending response of BT composite structures. This section outlines the experimental setup, data acquisition, uncertainty analysis, and results of these tests. These test results were used later in this work as verification data for FEMs of laminate plates and BT blades.

4.1 Laminate Plates

Wind turbine blades, marine propellers and tidal turbine blades are typically loaded along their span, with the largest stresses occurring at the blade root where they are constrained. Therefore, a suitable structural analog for a turbine blade is a cantilevered laminate plate loaded in bending. Laminate plates have a small thickness relative to the width and length dimensions, making them better represented by the plane stress assumption of CLT that is used in most composite FEMs compared to composite turbine blades with greater skin thicknesses and curvature. Laminate plates were therefore used to investigate the BT response of a simple composite structure before moving on to more complex structures such as BT blades. The simplistic geometry and small thickness, as well as increased confidence in the accuracy of the ply angles due to the lack of curvature of the structure, reduces uncertainty in the development of a FEM and increases confidence in the FEM verification detailed in Chapter 6.

Three 500 mm × 200 mm laminate plates were manufactured by Airborne Marine (The Netherlands). A schematic of the laminate plate geometry and loading scenario is shown in Figure 4-1. Based on results of an analytical model developed using CLT, as discussed in [243], the FEM and test samples were manufactured with three ply layers with a layup of [30°, 0°, 30°]. The thickness of the three plates was measured using a coordinate measuring machine (CMM), as discussed in Section 4.1.3, to be 2.72 mm with a standard deviation of 0.18 mm.
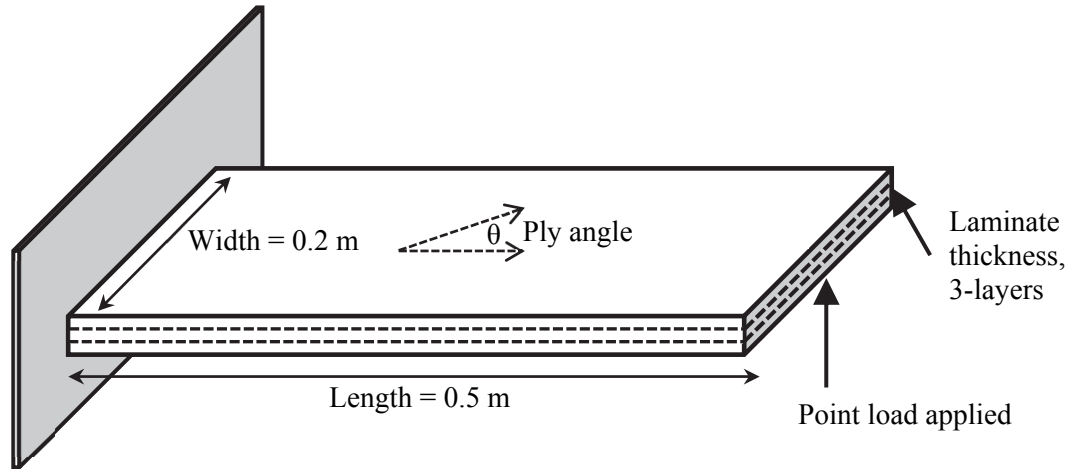
Figure 4-1 Laminate BT plate loaded in bending.

The laminate plate test samples were made out of Zoltek Panex unidirectional carbon fiber [244] and Gurit Prime 27 epoxy [245], for a typical Fiber Volume Fraction (FVF) of 55%, with material properties given in Table 4-1.

Table 4-1 Material properties for laminate plates.

Material property	Value
Standard weight	342 g/m^2
Young's modulus, fibers (E11)	126 GPa
Young's modulus, matrix (E22/ E33)	7.7/7.7 GPa
Shear modulus (G12/G13/G23)	3.9/3.9/2.9 GPa
Poisson's ratio	0.35

4.1.1 Experimental Setup

The objective of the tests was to measure the bending displacement and twist of the tip of the plates as a function of loading in order to obtain the bend-twist coupled response. To do this, a static bending test setup was designed and built to constrain the base of the plate and apply a single point load along the plate length to load it in bending. Figure 4-2 shows the experimental setup used to test the laminate plates.
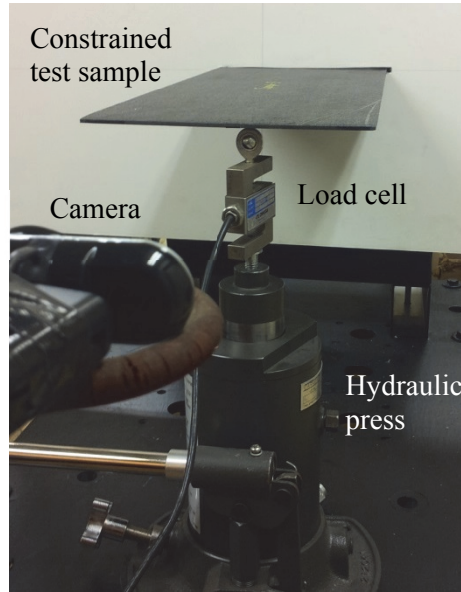
Figure 4-2 Experimental setup for static FEM verification.

A Carver model 3912 hydraulic ram press with a 5.125-in (130 mm) maximum ram stroke was used to load the free-end of the plate, half-way along the plate width. The load was applied to the plate via a 2 mm diameter ball. An LCCB-100 load cell with a 100 lb. (444.82 N) maximum load and a 10 V power source was used to measure the load and data was recorded using a National Instruments data acquisition (DAQ) 9239. The load cell was calibrated following the procedure laid out in ITTC [201]. The method used to calculate the uncertainty in the linear regression analysis is given in Section 3.3. The bias uncertainty of the load cell, u_V, based on the manufacturer specifications, was $u_V = \pm 0.015$ mV. Calibration of the load cell was done by applying weights of a known mass and measuring the voltage output. Based on the standard error of estimate of the measured data, the calibration uncertainty was $u_{\text{Calib}} = \pm 0.094$ N. This gave an overall uncertainty, for a 95% confidence interval, in the load measurement of $u_{\text{load}} = \pm 0.48$ N for a 25 N load.

4.1.2 Optical Measurement System

The tip displacement of the laminate is defined as the greatest out-of-plane bending displacement of the free-end of the plate, and the tip twist is defined as the angle that the free-end of the plate makes with the horizontal. The tip displacement and twist of the plate are a function of the location of the free-end of the plate (Edge 1 and Edge 2 in Figure 4-3).

Locations of the free-end (*x* and *y* coordinates as viewed front on) were obtained using LabVIEW Vision Development Module with an A4 Logitech® PK-920H-1 (1280 x 720p MJPG 30 fps) webcam. Figure 4-3 shows a laminate plate in the unloaded and loaded position, as viewed by the camera.
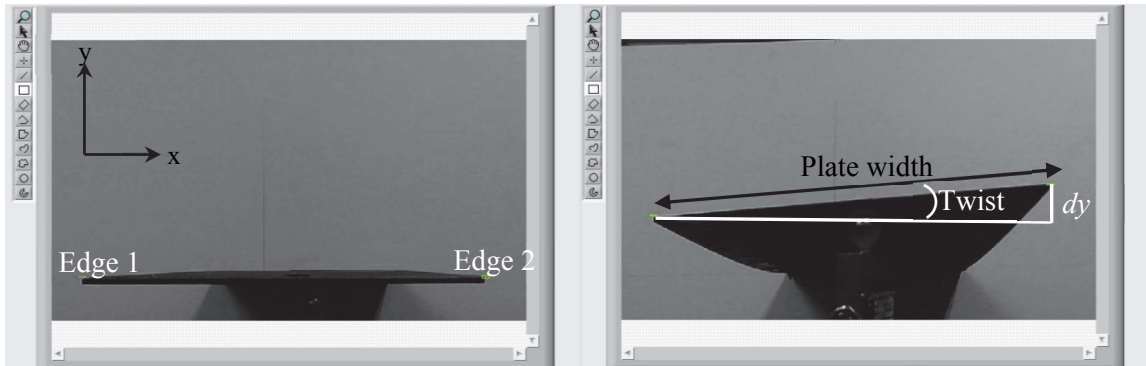

Figure 4-3 Laminate plate as viewed by optical tracking system: Visual output from DAQ for left) initial unloaded position, and right) fully loaded (25N) plate showing twisting.

In LabVIEW, an imaging sensor converts the image being reported by the camera into a discrete number of pixels, each with a gray level that specifies the brightness of the pixel. The geometric matching search function in LabVIEW located the two edges of the plate free-end by matching the same pattern of greyscale pixels in the image captured by the camera to that of a template input by the user [246]. In this case, the template image was that of the top corner of Edge 1 and Edge 2 of the plate. Once the template was matched, the pixel location of the center of a box surrounding this template in the image was recorded by LabVIEW, giving the *x*- and *y*-displacements of Edge 1 and Edge 2 in pixels. The plate twist was calculated by taking the arcsine of the *y*-displacement difference between Edge 1 and Edge 2, *dy* in Figure 4-3, divided by the plate width.

To obtain measurements in real-world units (mm), the optical tracking system was calibrated using a microplane calibration technique, which maps pixel coordinates to real-world coordinates. A calibration grid with equidistant dots, shown in Figure 4-4, was placed at the same distance from the camera as the plate free-edge. The dot diameter and separation distance were measured using calipers to an accuracy of ±0.01 mm and input to LabVIEW. The LabVIEW Vision Development Module identified the dots and calculated

a mapping function, relating their distance in pixels as viewed by the camera to the real world distance [246].
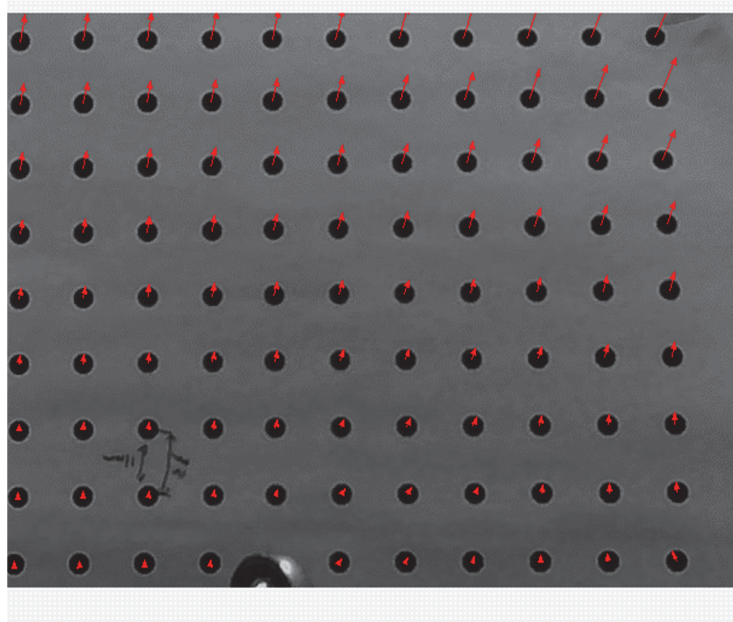
Figure 4-4 Dot-pattern used for calibration of optical tracking system.

Uncertainty in the plate bending displacement and twist was based on the calibration uncertainty in the image sensing system, and on the random error associated with 20 repeat tests. NI Vision calibration software computes an error map that accounts for errors inherent to the imaging setup, and outputs the mean error, maximum error, and standard deviation. This indicates the possible location error for the estimated real-world coordinates with a confidence interval of 95% [246]. In this case the maximum error value was used to give a conservative estimate of the uncertainty in the displacement measurement, which was calculated by LabVIEW to be $\pm$ 0.65 mm.

To obtain the precision uncertainty associated with locating the geometry matching template, repeat tests were done using 20 images of the unloaded plate. The pixel locations of the two edges were recorded using the geometry matching function for all 20 images with a standard deviation of $\pm$0.7 pixels. Based on a calibration conversion of 3.6 pixels/mm, this resulted in a standard deviation of $\pm$0.2 mm. Combined with the uncertainty associated with the calibration, this gave a total uncertainty in the vision tracking system of $\pm$0.68 mm.

4.1.3 Results

Figure 6-4 and Figure 6-5 show results obtained for [30º, 0º, 30º] laminate test samples (labelled Sample 1.1, 1.2, and 1.3), with an average thickness of 2.72 mm. The tip displacement shown is the maximum displacement of the free end of the plate, relative to the initially unloaded plate. The best-fit lines are shown in the plots.

The deformation of the test samples was linear within the range of applied loads, with all coefficients of determination above 0.99 (for the bending displacement $R^2 = 0.9982$ for Sample 1.1, $R^2 = 0.9968$ for Sample 1.2, and $R^2 = 0.9948$ for Sample 1.3, and for the twisting deformation, $R^2 = 0.9987$ for Sample 1.1, $R^2 = 0.9991$ for Sample 1.2, and $R^2 = 0.9985$ for Sample 1.3). In a similar study, Makeev [247] showed non-linear load-twist trends, however, this is thought to be due to the high loads applied (over 1 kN for a 1.168 mm thick laminate). There was slight variance in the bending and twisting response between test samples, which is thought to be due to slight offsets in the ply angles and thicknesses. This is investigated further in Section 6.1.4.

Due to variations in the plate thicknesses observed using caliper measurements, a Mitutoyo CMM was used to better quantify the thickness of one of the plate samples. The CMM has a resolution of 5 μm using a ruby measurement probe with a diameter of 1.5 mm, and the uncertainty in these measurements was at most 1.5 μm based on a 2008 calibration of the CMM [248]. The sample was measured in 10 mm increments, giving a total of 1000 data points. Figure 4-7 shows the thickness distribution for test Sample 1.2.

For Sample 1.2, the average measured thickness was t_{avg} = 2.72 mm with a standard deviation of 0.18 mm. Although only Sample 1.2 was measured using the CMM, based on caliper measurements, the thickness of all of the laminate plates was found to vary similarly.
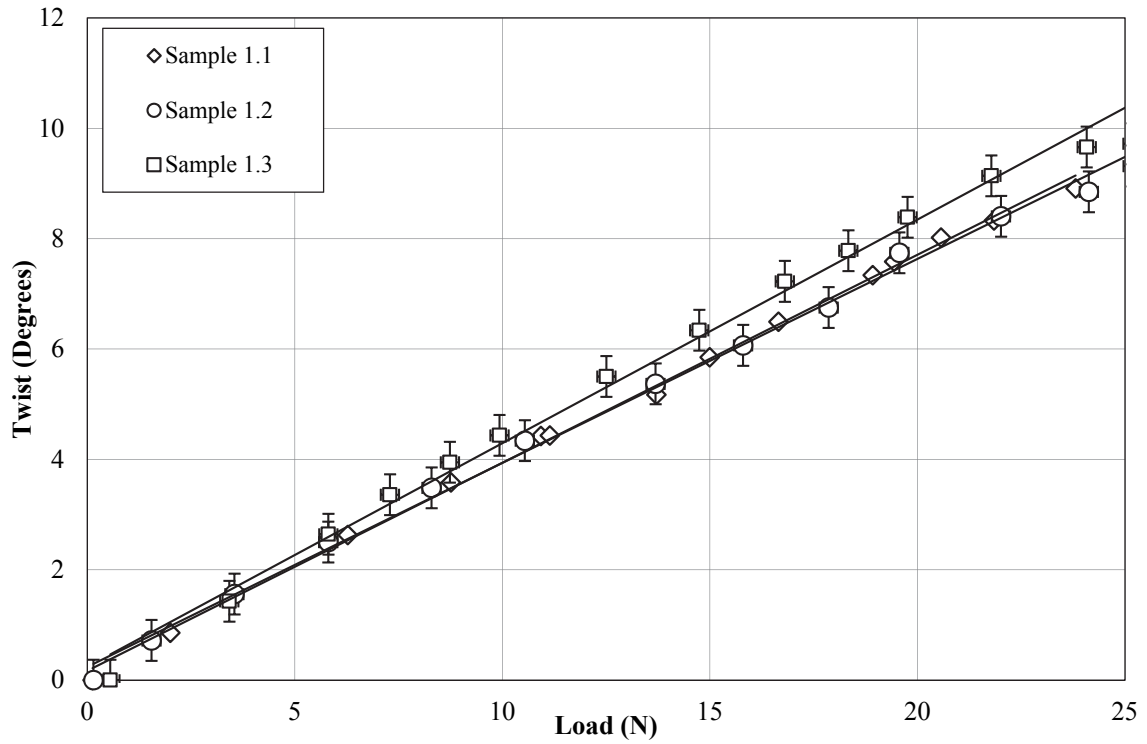
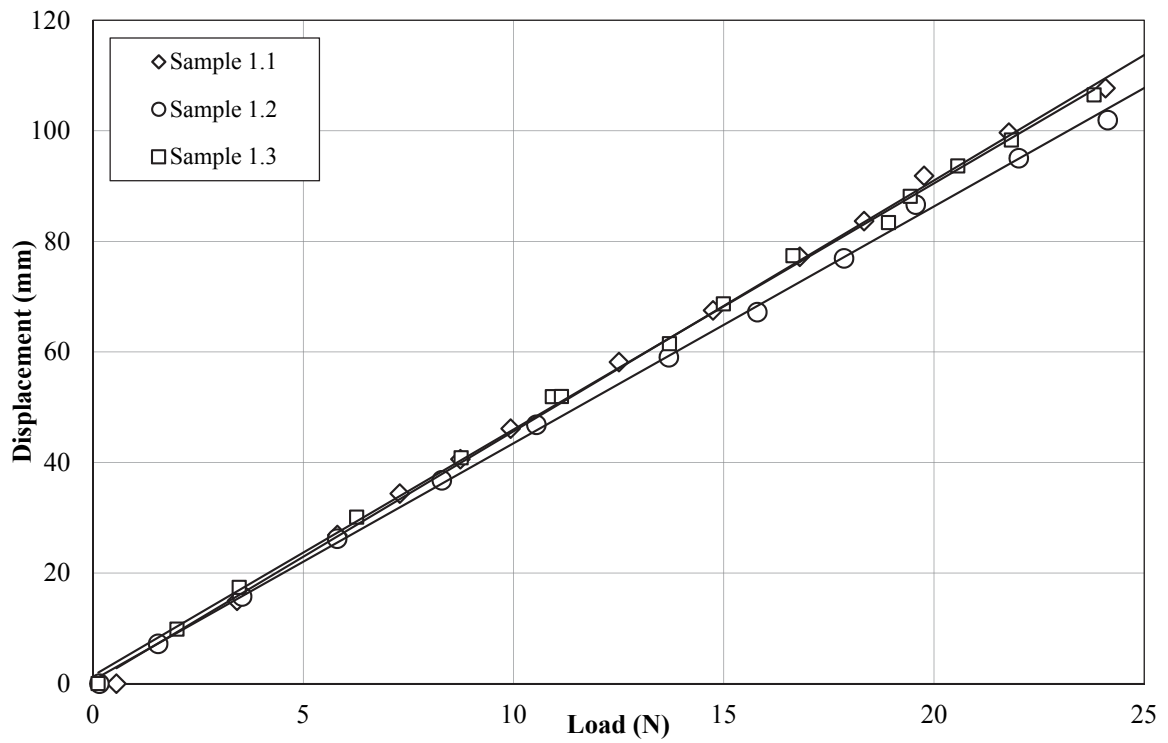*Figure 4-5 Twist vs. load for the laminate plates-experimental results.*

Figure 4-6 Load vs. displacement for the laminate plates-experimental results.
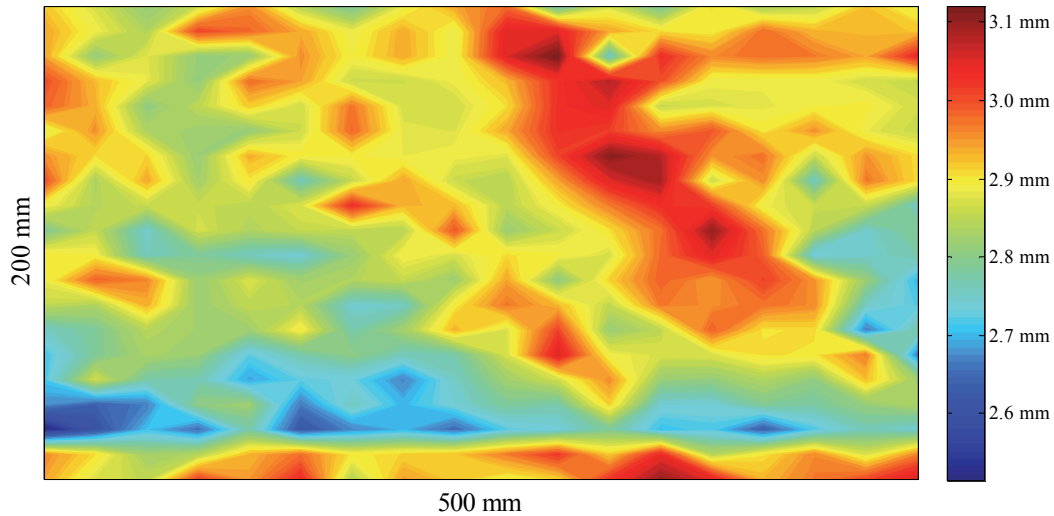
Figure 4-7 Thickness distribution for [30°, 0°, 30°] test Sample 1.2.

4.1.4 Uncertainty

Table 4-2 gives the uncertainty values used in the propagation of error for the measured displacement and twist.

Table 4-2 Uncertainty values, laminate BT plates.

Variable	Uncertainty
Load cell (N)–bias	0.22
Load cell (N)–precision	0.094
Displacement (mm)–precision (calibration)	0.65
Displacement (mm)– precision (repeat tests)	0.20

Both random and bias uncertainties were propagated through the load measurements and calculations of displacement and twist. The method discussed in Section 3.3 was used to determine the combined uncertainty for each parameter based on a 95% confidence interval. Including a 95% coverage factor, the uncertainty in all the components was found to be less than 5% for loads over 7 N, with error bars shown in the results plots (error bars for displacement are not visible behind the individual markers).

4.2 Turbine Blades

Three 360 mm long NREL S814 airfoil shape composite blades were manufactured by Airborne Marine (The Netherlands) and are shown in Figure 4-8. These blades had off-axis plies on the working section of the blade to induce BT coupling, as shown schematically in Figure 4-9. The blades were tested statically to verify deformation

97

predictions made by a FEM, discussed in Chapter 6. Small-scale blades were used for pragmatic testing and manufacturing reasons, as is typically done for early stage device design [152]. Aluminum blades of identical geometry were tested as well to verify their relative rigidity compared to the composite blades.

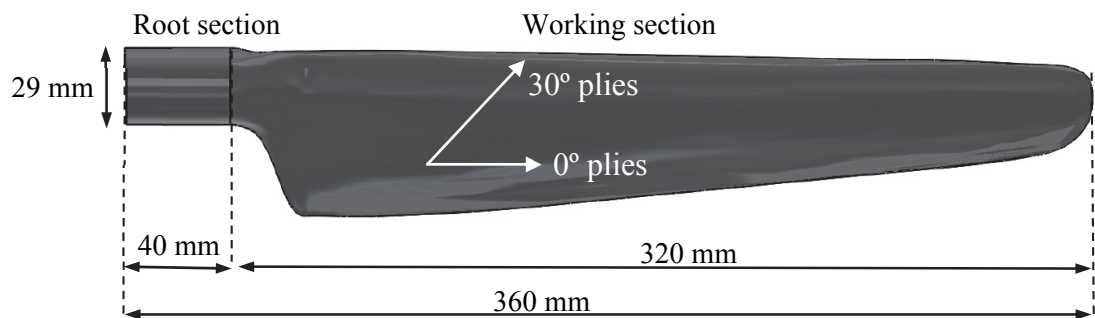*Figure 4-8 Photograph of the three composite blades.*

Figure 4-9 NREL S814 blade with 26.8° composite plies on working section of the blade.

The blades were lofted from a circular root cross section, 40 mm from the base of the blade, to the first NREL airfoil cross section at 68 mm. The working section of the blade (outer

320 mm) had radial chord and pre-twist distributions given in Table 4-3. The root section of the blade (from 0 mm to 68 mm, shaded grey in the table) is given as well.

Table 4-3 Geometry of NREL S814 blade.

Blade length (mm)	Twist (Degrees)	Chord (m)	Airfoil shape
0	N/A	29	Circular root
39	N/A	29	Circular root
40	N/A	29	Circular root
50	N/A	N/A	Lofted (ellipse)
68	0	64.3	NREL S814
93	-4.38	62.9	NREL S814
128	-10.74	59.8	NREL S814
162	-14.8	56	NREL S814
195	-17.33	51.6	NREL S814
230	-18.91	47.3	NREL S814
265	-19.75	42.6	NREL S814
300	-20.39	38.1	NREL S814
334	-20.87	33.7	NREL S814
360	-21.11	24.9	NREL S814

For BT blades, both the composite material and the layup (ply angles) need to be selected to maximize blade strength and induced twist. Glass fiber composites are generally less stiff (lower Young's modulus in the longitudinal direction) than carbon (graphite) fiber composites, therefore using glass fibers instead of graphite fibers may be a way to decrease the blade stiffness and thereby increase the BT response. However, because of the higher transverse stiffness of glass, previous work has shown that the BT coupling effects are actually lower using glass composites, even though the blade bends more [128]. Therefore, a 0.2 mm thick layer of unidirectional graphite-epoxy composite was used for the blade skins, with an average ply angle of 26.8° on the working section of the blade to induce BT coupling. Manufacturing small-scale blades is challenging due to the relatively high curvature of the surfaces, hence the three blades had slightly differing average fiber angles, with blade 1 having a fiber angle of 26°, blade 2 having a fiber angle of 26.5° and blade 3 having a fiber angle of 28°. The upper and lower skin were laid up with a mirror layup, as detailed in [116]. The circular root had a 1-inch diameter steel cylindrical insert for added

strength in compression for a taper-lock bushing connection used to constrain the blade to a bending test platform. This steel insert was overlaid with the continuous 0.2 mm thick plies from outer blade section and additional layers of ±15° plies for added strength, giving a total outer diameter of 29 mm at the blade root.

Having a solid blade core allows for easy manufacturing of the blade and helps prevent flooding. Epoxy was initially considered for use in the blade core, but was too stiff based on initial FEM results. Polyethylene was ruled out based on blade manufacturer recommendations, as it can be difficult to adhere to composites during manufacturing. Foaming epoxy can be manufactured to a desired density, giving the designer control over the material properties and hence the blade core stiffness, as well as the blade buoyancy. Therefore, the blades were constructed of Sicomin PB 250 [249] epoxy closed cell foam core (for hydrodynamic shape and ease of manufacturing).

Table 4-4 gives the material properties used in the blades. Graphite-epoxy ultimate strength values are stated in Table 4-4 for the laminate longitudinal, transverse, and shear directions, in both tension and compression [215]. These values are used later in this work to perform a failure analysis on the blades using a FEM.

Table 4-4 Composite and epoxy material properties [23, 249].

Graphite-epoxy Properties		Sicomin Epoxy Properties	
Young's modulus, longitudinal	137 GPa	Density	250 kg/m^3
Young's Modulus, transverse	7.8 GPa	Young's Modulus	0.0189 GPa
Shear modulus	3.9 GPa	Shear modulus	0.0073 GPa
Poisson's Ratio	0.335	Poisson's Ratio	0.3
Longitudinal tensile strength	1.5 GPa		
Transverse tensile strength	0.04 GPa		
Longitudinal compressive strength	1.5 GPa		
Transverse compressive strength	0.246 GPa		
Shear strength	0.068 GPa		

After the blades were manufactured, a CMM machine was used to scan the blade geometry to identify any features or effects that were not present in the original blade CAD. The CMM had a resolution of 5 μm and a ruby measurement probe with a diameter of 1.5 mm. Measurements of the airfoil sections were taken at 17 span-wise locations in 0.127 mm

increments around the airfoil. Figure 4-10 shows the cross section of the composite blade at 68 mm from the base, compared to the theoretical NREL S8414 airfoil.
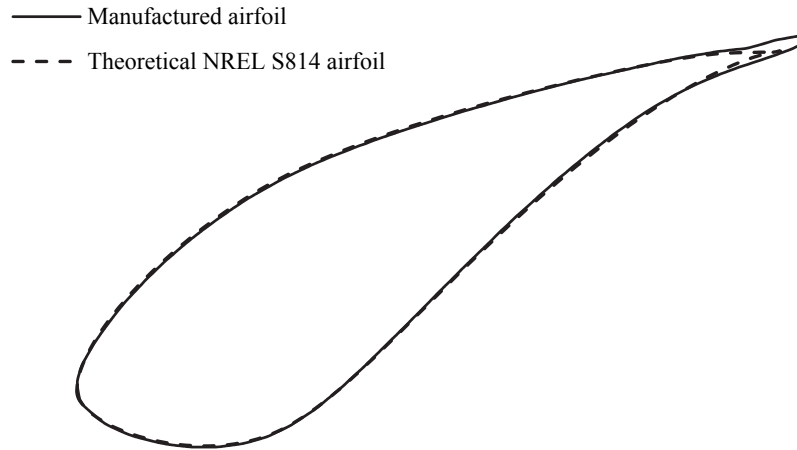
Figure 4-10 Blade CMM scan compared to theoretical NREL S814 airfoil.

Figure 4-10 highlights the differences between the original airfoil and the blade after manufacturing, particularly showing the extended trailing edge (TE) on the manufactured blade. Due to the small size of the blades and the mirror layup required for BT coupling, an additional 5 mm section was required on the TE in order to bond the composite from the top and bottom surfaces of the blade.

To provide a fair comparison between composite BT blades and rigid blades during hydrodynamic testing presented given in Section 5.2, aluminum blades were manufactured from a CAD that was constructed using section profiles obtained with a CMM scan (see Figure 4-10) of the composite blades. The aluminum blades were manufactured using aluminum 6061 material [250] using a 5-axis CNC machine. During machining, the CNC machine experienced vibrations which led to slight surface roughness. After manufacturing, the surface roughness of the blades was measured using a hand held Mahr Federal Pocket Surf III, with a resolution of ± 0.01 μm, and found to be at worst 4 μm (average groove depth) and 25 μm (maximum peak to valley groove depth). To smooth the surface, epoxy was applied to fill any small grooves and 400/P800 grit abrasive paper was used to smooth the surface. The surface was polished such that the final surface finish was

equivalent to the composite blades. This surface finishing procedure resulted in a total uncertainty in the blade airfoil thickness of ±0.05 mm.

4.2.1 Experimental Setup

The experimental setup and DAQ described in Section 4.1.1 for laminate plates was used for the blades as well, with several alterations. In this system, a screw press (maximum stroke of 150 mm) replaced the hydraulic press used in previous static tests for better stability in loading. The clamping mechanism used for the plates was replaced with a quick-disconnect taper-lock bushing, used to connect the circular root of the blade to the bending test platform, as shown in Figure 4-11.
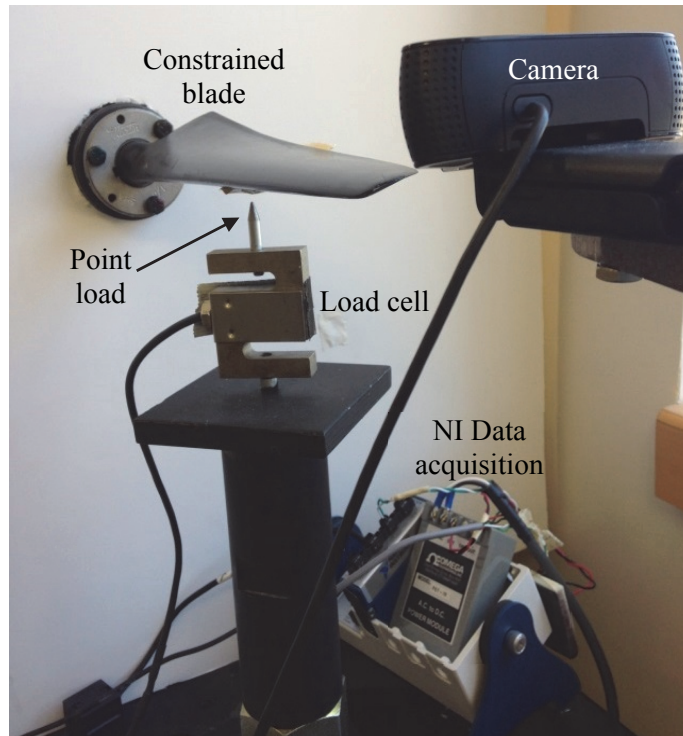
Figure 4-11 Experimental setup for static FEM verification.

A single point load was applied to the blade at 60% along the blade length and 25% along the blade chord line using a 1 mm diameter rounded tip applicator, as shown in Figure 4-11. The blade angle was set at 26.50º from horizontal at the base of the blade using a device that was designed to have a flat edge parallel to the chord line of the blade such that an inclinometer measurement gave the angle of the blade chord relative to the horizontal, as shown in Figure 4-12 for the aluminum blade. For these tests, the blades were set such

that the loading roughly mimicked the direction of the axial (thrust) loads expected during hydrodyntal testing (26.50º from horizontal at the base of the blade).
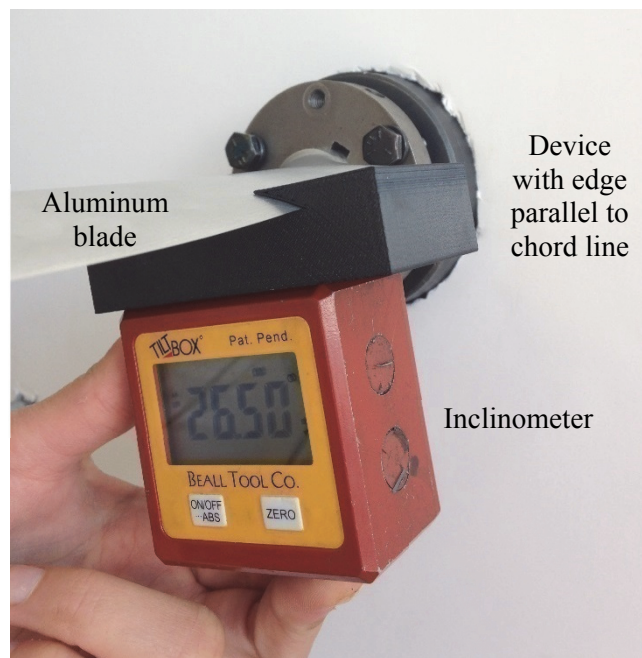
Figure 4-12 Setting blade angle in structural testing setup.

The bias uncertainty of the load cell, u_V, based on the manufacturer specifications, was $u_V = \pm 0.015$ mV, resulting in approximately ± 0.22 N. Based on the standard error of estimate of the measured data the calibration uncertainty was $u_{Calib} = \pm 0.37$ N. This gave an overall uncertainty in the load measurement of $u_{load} = \pm 0.26$ N for a 25 N load. For a 95% confidence interval, the combined uncertainty in the load was less than 5% for loads above 5 N. Each set of tests were performed a minimum of three times to verify experimental repeatability.

4.2.2 Optical Measurement System

The blade bending displacement and twist were measured by obtaining the displacement of the leading and trailing edges (LE and TE) of the blade tip. The blade twist was calculated by taking the arcsine of the difference in the *y*-displacements of the LE and TE divided by the chord line at the blade tip, similarly to the twist measurements of the laminate plate.

In this case, the LabVIEW Vision Development Module used a color matching searching scheme instead of the geometric matching used previously as it was found to better located the LE and TE of the blades. This enabled small red and blue dots to be tracked on the blade tip, as shown in Figure 4-13. Figure 4-13 shows output images from the optical tracking system as a blade is loaded to maximum load. In this figure, two output images are overlaid to illustrate the bending displacement from unloaded to fully loaded, and to show the range of motion expected of the blade tip.
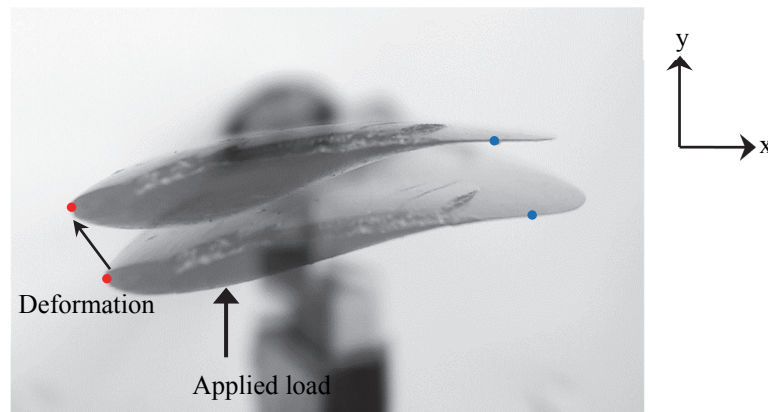

Figure 4-13 Tip displacement as viewed by optical tracking system.

The calibration method discussed in Section 4.1.2 was repeated for this set of tests, and the uncertainty in the bending displacement in real-world coordinates was output from the calibration software. For these tests, the calibration grid used for the LabVIEW image calibration was printed on a high quality plotter, increasing the accuracy of the optical tracking system to ± 0.20 mm. Repeat trials were performed using 20 images of the unloaded blade to obtain the precision uncertainty associated with the color matching algorithm. In this case, the location of the LE and TE for the 20 images had a standard deviation of ± 0.09 mm. This was also improved from the laminate plate testing due to higher resolution image capture. Combined with the calibration uncertainty, this gave a total uncertainty in the measurement of blade tip displacement of $u_y = \pm 0.22$ mm.

4.2.3 Results

Figure 4-14 shows the blade tip as viewed by the optical tracking system as it is loaded. These snapshots show superimposed images with increasing loads from image 1-4.
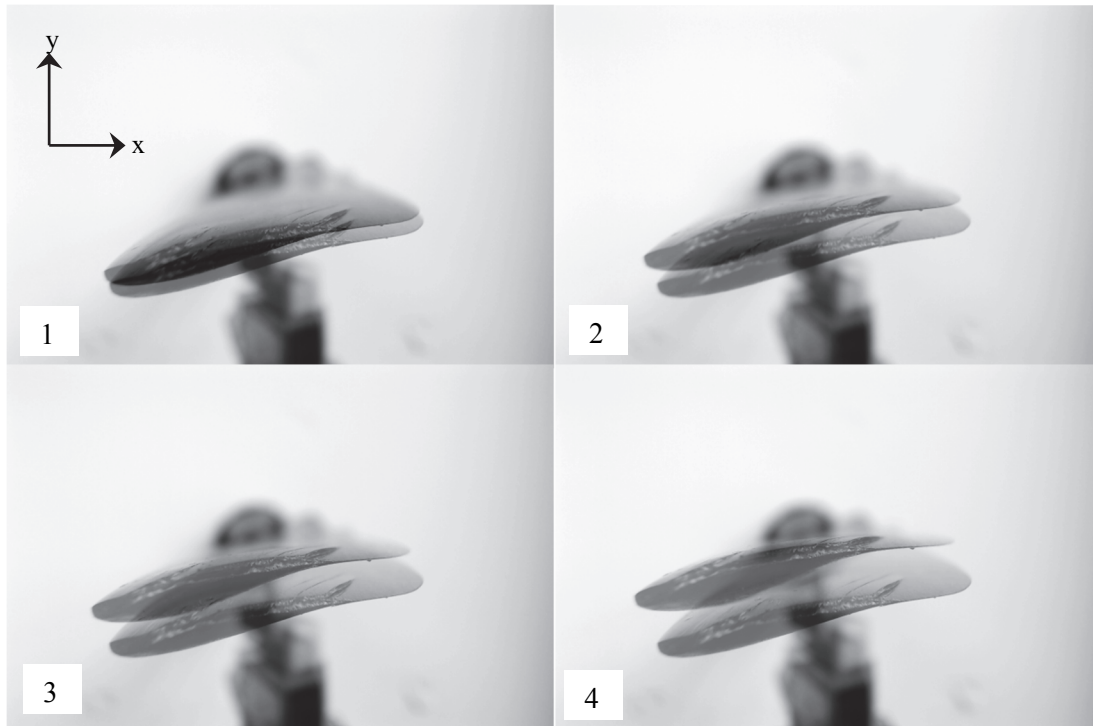
Figure 4-14 Overlaid images of blade tip as loaded (1-4), as viewed by optical tracking system.

As the blade was loaded, it mainly deformed in the *y*-direction, but there was also a slight deformation in the *x*-direction. The crack at the blade tip visible in this figure was from damage during air transportation. This crack was repaired and blade tests repeated. The difference in deformation response between the damaged and repaired blades was less than 1.2% at 25 N load, which is within the uncertainty expected in the measurement and hence considered insignificant.

Figure 4-15 and Figure 4-16 show the blade bending displacement in the *y*-direction (for the TE, which had the largest *y*-displacement) and tip twist, respectively, as a function of applied load. Both the bending displacement and twist were linear (for the bending displacement, $R^2 = 0.9622$ for Sample 1.1, $R^2 = 0.9973$ for Sample 1.2, and $R^2 = 0.9972$ for Sample 1.3, and for the twisting measurement, $R^2 = 0.957$ for Sample 1.1, $R^2 = 0.9847$ for Sample 1.2, and $R^2 = 0.9904$ for Sample 1.3).
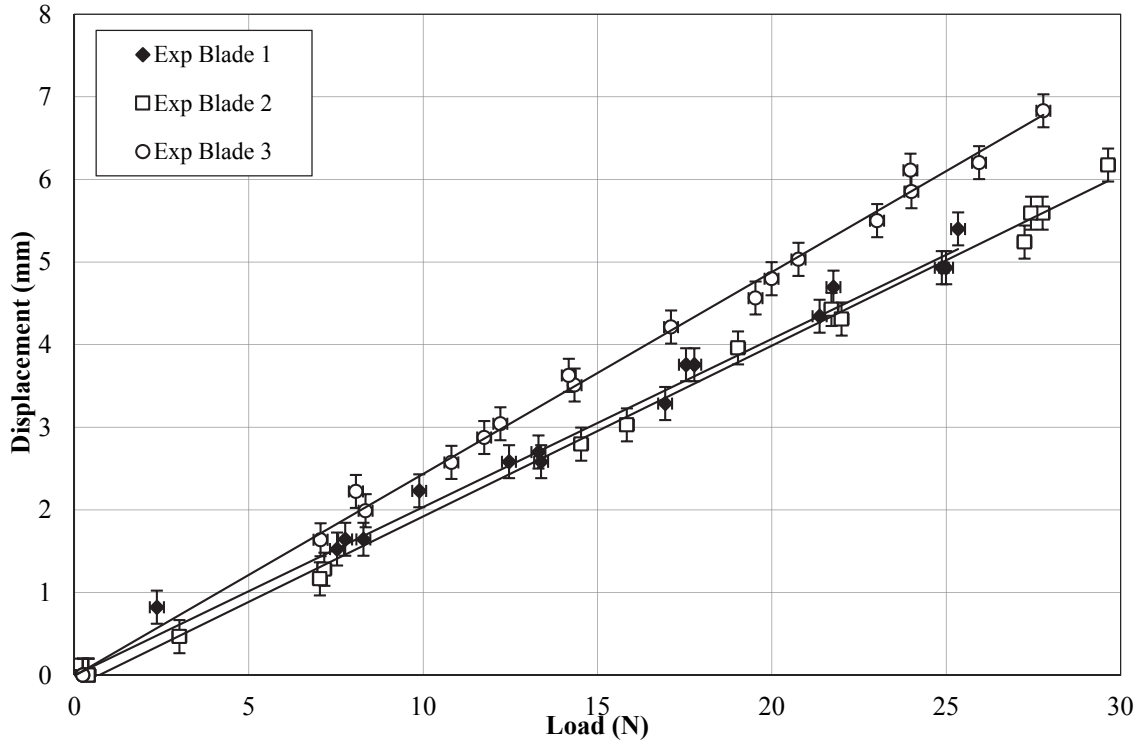
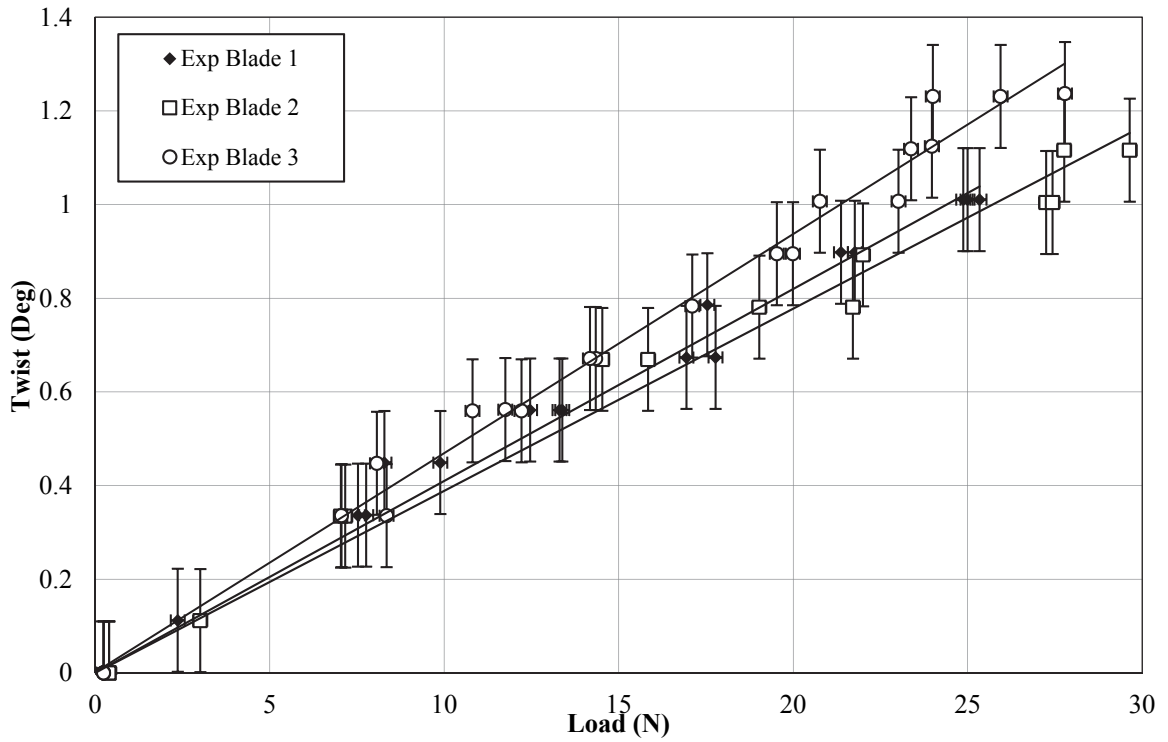*Figure 4-15 Load vs. displacement for composite blades.*

Figure 4-16 Load vs. twisting for composite blades.

Figure 4-15 shows different load-displacement trends for each blade. This is due to slight ply angle misalignments, whereby the three blades had slightly differing fiber angles, with blade 1 having an overall fiber angle of 26°, blade 2 having a fiber angle of 26.5° and blade 3 having a fiber angle of 28°.

As discussed, one of the aluminum blades was also tested in the bending test setup, with bending displacement results shown in Figure 4-17. Tests presented in Section 5.1.4 were designed to compare the hydrodynamic response of BT blades to rigid blades, and hence assumed that the aluminum blades did not deform. It was therefore important to verifying this assumption. Figure 4-17 shows the bending displacement for all three composite BT blades compared to one of the aluminum blades, Sample 1.1.

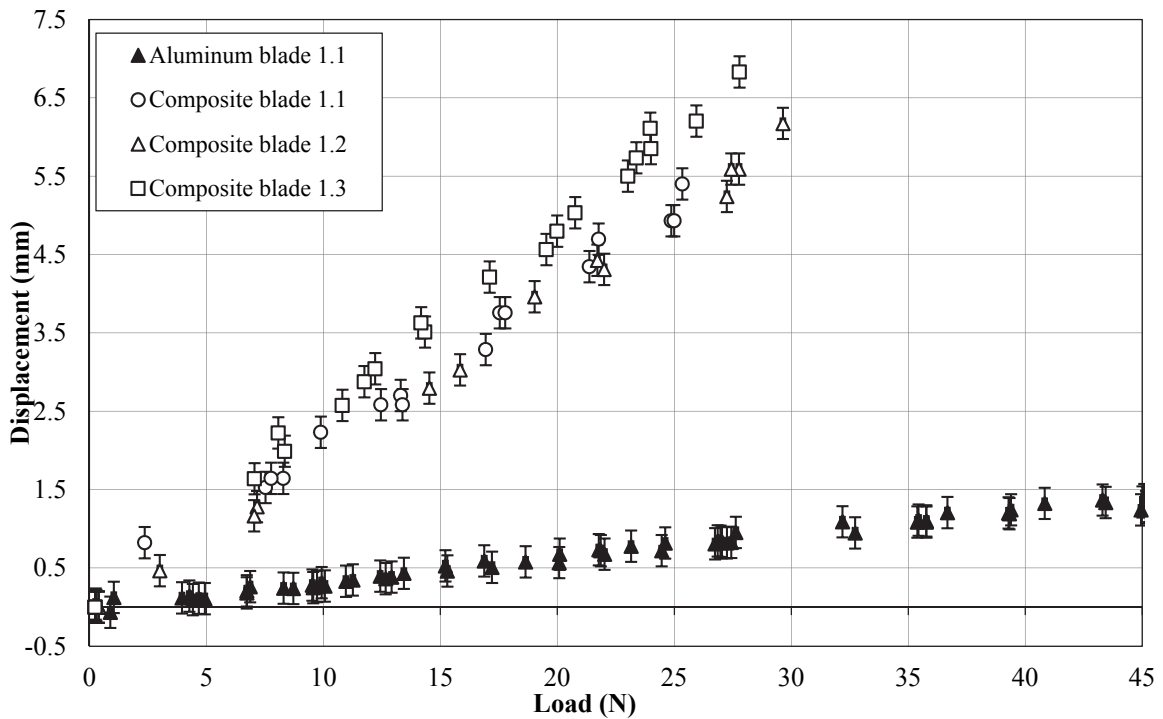*Figure 4-17 Load vs. bending displacement for aluminum and composite blades.*

The bending displacement of the aluminum blade was linear, with $R^2 > 0.98$. For a maximum applied tip load of 45 N, the bending displacement of the aluminum blades was less than 1.5 mm. For a 25 N load, the aluminum blade had less than 12% of the bending displacement compared to the composite blade. As well, the twist of the aluminum blade

was less than 1% of that measured for the composite BT blades. For the purposes of this work, the aluminum blades were considered rigid relative to the composite BT blades.

4.2.4 Uncertainty

Table 4-5 gives the uncertainty values used. The uncertainty in the displacement measurement in this case is improved compared to that shown in Table 4-2 due to more rigorous calibration methods.

Table 4-5 Uncertainty values, composite BT blades.

Variable	Uncertainty
Load cell (N)–bias	0.22
Load cell (N)–precision	0.094
Displacement (mm)–precision (calibration)	0.20
Displacement (mm)– precision (repeat tests)	0.09

The method discussed in Section 3.3 was used to determine the combined uncertainty for each of the parameters. Propagating these uncertainty values through the calculations of displacement twist, and including a 95% coverage factor, resulted in an overall uncertainty of less than 4% for the bending displacement, and less than 11% for the twisting deformation.

CHAPTER 5
HYDRODYNAMIC
TESTING

Turbine developers and researchers use small-scale testing in towing tanks to predict the performance of particular blade designs, verify design tools, and prove conceptual ideas. In this work, the 76 m by 4.6 m by 2.5 m Kelvin Hydrodynamics Laboratory towing tank at the University of Strathclyde was used to perform two sets of hydrodynamic testing. The first set was performed on a three-bladed HATT with rigid aluminum blades to provide data for verification of a steady-state BEMT. The second set of experiments tested three-bladed HATTs to quantify the effects of BT coupled turbine blades by comparing the performance of turbines with composite blades and aluminum blades of the same geometry. This section outlines the experimental setup, data acquisition, uncertainty analysis, and results of these tests.

5.1 Experimental Set 1: Rigid Blades

A small-scale HATT with three rigid aluminum blades was tested for verification of a steady BEMT tool. Figure 5-1 shows the experimental configuration tested in the towing tank at the University of Strathclyde. The turbine was mounted on the speed controlled carriage, which sits on rails along the sides of the towing tank, such that the rotor was fully submerged with the centre of the nose cone of the rotor located 0.70 m below the free surface of the water. The maximum carriage speed for this facility is 5 m/s with speed control accurate to better than 0.3% [148].
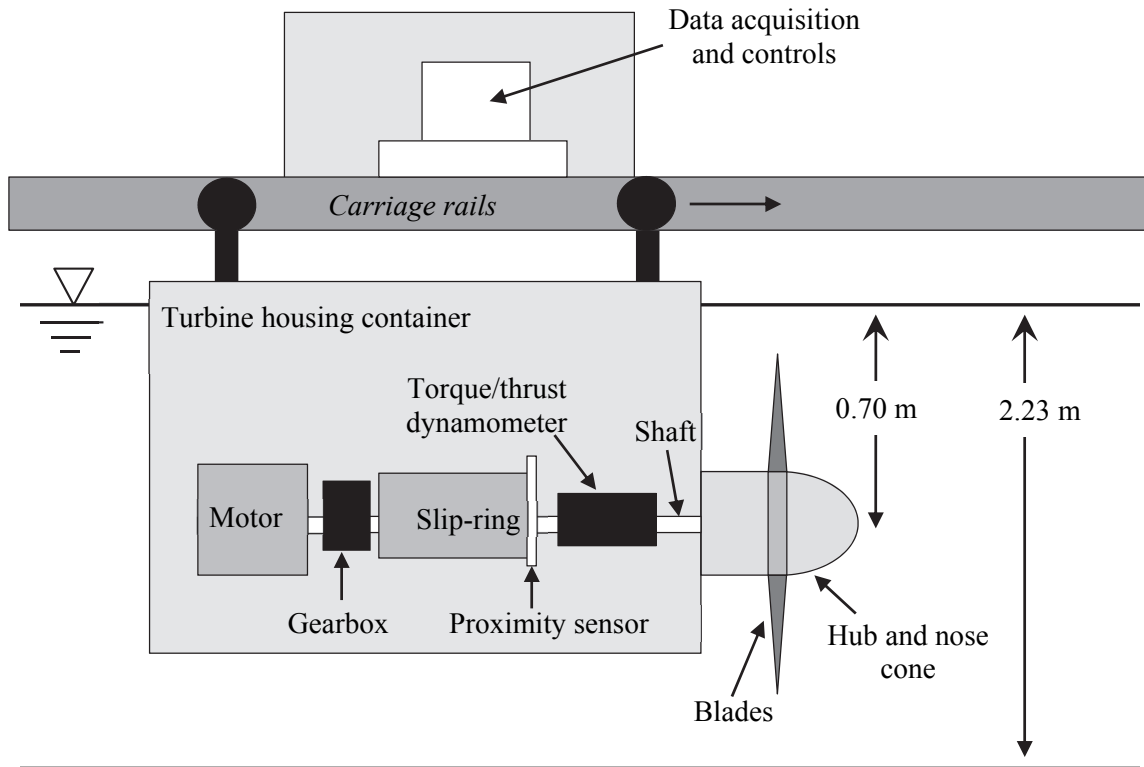
Figure 5-1 Towing tank carriage and turbine test setup.

The turbine rotor (blades and hub) that was tested had a radius of 381 ± 0.05 mm, blade length of 292 ± 0.05 mm, and root pitch setting of $28.00° \pm 0.89°$. Figure 5-2 shows the turbine rotor with NREL S814 airfoil shape blades with the nose cone removed to show the location of blade root strain gauges on all three blades.
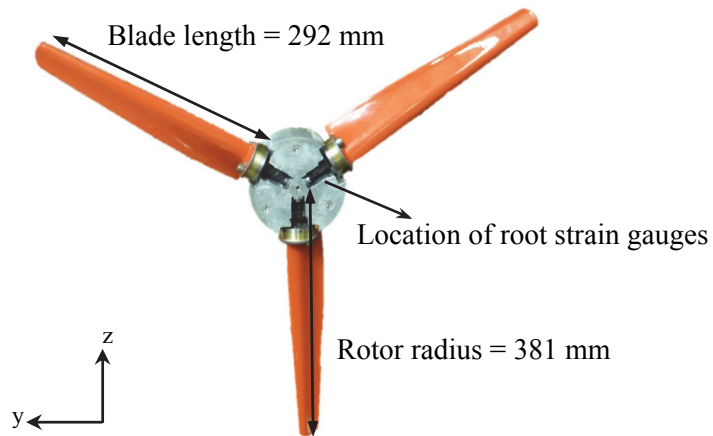

Figure 5-2 Turbine rotor with the nose cone removed.

110

The turbine rotor was driven at a constant rotational speed using a motor and a 10:1 gear box was used to step down the rotational speed of the motor. A proximity sensor was used as a pulse counter to measure the shaft rotational speed and to identify the shaft radial location at any time. The higher frequency motor encoder was also used as a backup to check the rotational speed measured by the proximity sensor. The thrust and the torque loads on the rotor system were measured using a Futek FSH00747 torque and thrust biaxial sensor, and a IS 1163 SW 110/20 CAT slip ring was used to feed the electrical signal from the rotating dynamometer and other electrical components to the DAQ. Data was logged using a Cambridge Electronic Design Power 1401 DAQ and the DAQ program, Spike, and exported as text files for post processing in MATLAB®.

Axial (blade 1 and 2) and radial (blade 3) blade bending moments were measured using strain gauges located on a cylindrical steel root section of the blade internal to the hub, as shown in Figure 5-4. The gauges were isolated from the water with waterproofing material. The direction of the measured bending moments is given in Figure 5-3.

Radial blade root bending

Axial blade root bending
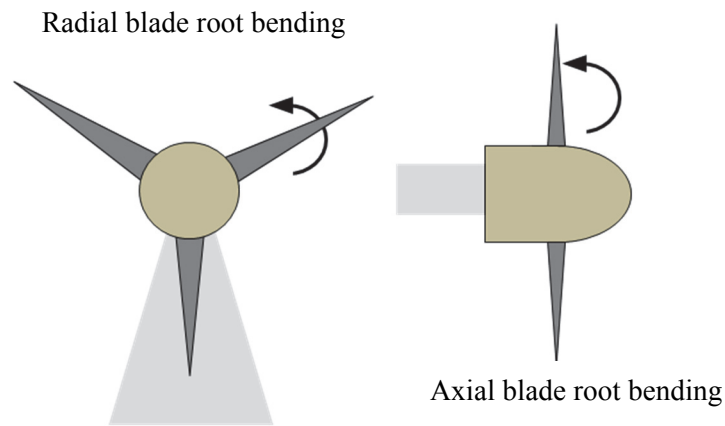
Figure 5-3 Directions of blade bending moments.

Along with bolting the blade flanges to the hub, to ensure an accurate pitch setting between the three blades, a pin was slotted into a hole drilled on the bottom-side of the blades at a set point on the chord line, constraining the blades to one degree of freedom in rotation about the pin, shown in Figure 5-4. A high accuracy depth gauge fixed in the horizontal plane was used to measure the distance between the edge of the rotor hub and the trailing edge of the blade at the root, and ensure this distance was the same for all blades. The blade

pitch angle was then determined from the CAD model of the rotor system. The uncertainty in the blade pitch angle was calculated based on a machining tolerance of 0.005 m for each dimension of the blades, considering the method used to set and quantify the pitch angle.
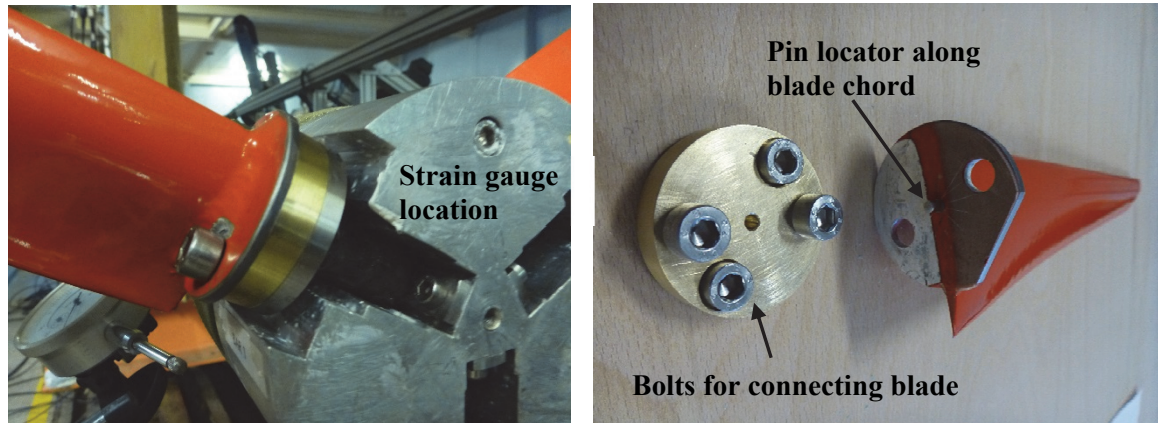
Figure 5-4 Left) blade root connection and strain gauge location, Right) pin locator for pitch setting of blade root.

The blade geometry (radial chord and pre-twist) is given in Table 4-3, however, only the outer 292 mm of the blades were tested in this case, the root section outlined in the table was not manufactured. Instead, the blades had a flange with two bolts to attach it to the hub, as evident in Figure 5-4.

Calibration of the test equipment was undertaken both prior to testing and once the test period had been completed to ensure the measurements taken were reliable and could be processed with confidence. A series of linear calibration equations with a slope s and offset constant a, were applied to convert voltage signals from the DAQ to engineering units for thrust sensor, torque sensor, and bending moment strain gauges. For each sensor, a linear regression analysis of the various applied loads (torques, bending moments and thrust forces) and resulting voltages showed a highly linear calibration curve with coefficients of determination, R^2, above 0.99. A description of the calibration process can be found in Appendix B.

5.1.1 Design of Experiment

A range of inflow speeds (rotor inflow velocities) were used during the towing tank testing, from 0.5 m/s to 1.0 m/s. For each inflow speed, a range of rotational velocities, designed to cover λ from 2 to 7, were utilized to populate rotor performance curves. At higher inflow velocities, a slightly fluctuating torque signal was observed, thought to be due to the motor controller not being able to maintain enough torque to counter the hydrodynamic torque and control the rotor, hence the maximum flow speed was 1.0 m/s.

5.1.2 Test Procedure

To meet the testing requirements outlined in EquiMar Deliverable D3.4 [199], tests were run in a non-sequential order and were scheduled to avoid random errors such as time of day (affecting steadiness of tank), carriage operators (affecting data collection) and tank temperature (which can vary over the day). The carriage tow and rotor velocities of the tests were also chosen at random to ensure that any sources of uncertainty described as "nuisance factors" in the EquiMar Best Practices document [199] could be eliminated. A number of repeat runs were performed as well to determine the repeatability of the tests. In particular one set of conditions, with an inflow velocity of 1 m/s and rotor velocity of 110.7 RPM, was repeated 5 times.

5.1.3 Results

Figure 5-5 and Figure 5-6 show C_P and C_T as a function of λ for the test turbine. In general, the efficiency (C_P) of the rotor increased with increasing λ and with increasing tow velocity, peaking around $\lambda = 4.08$ for the 0.8 m/s tests, 3.90 for the 0.9 m/s tests, and 3.53 for the 1 m/s tests. The power coefficient of the rotor presented here is signifncantly below Betz limit of 0.59 [58], which is thought to be partially due to the non-optimal pitch setting of the blades and the turbine operating at low chord-Reynolds numbers. This pitch setting was used based on the turbine and blade configuration previously developed at the University of Strathclyde, which was not adjustable. Although the NREL S814 airfoil has been shown to be sensitive to roughness [168], the blades tested in the towing tank were powder coated and smoothed, and had a surface roughness height of less than 0.05% of the chord length. Based on the discussion in Section 3.1.3.D, roughness was not thought to be a contributing factor to the poor performance of the blades.

Figure 5-5 C_P–λ curve for varying inflow speeds, rigid blades.

Figure 5-6 C_T–λ curve for varying inflow speeds, rigid blades.

114
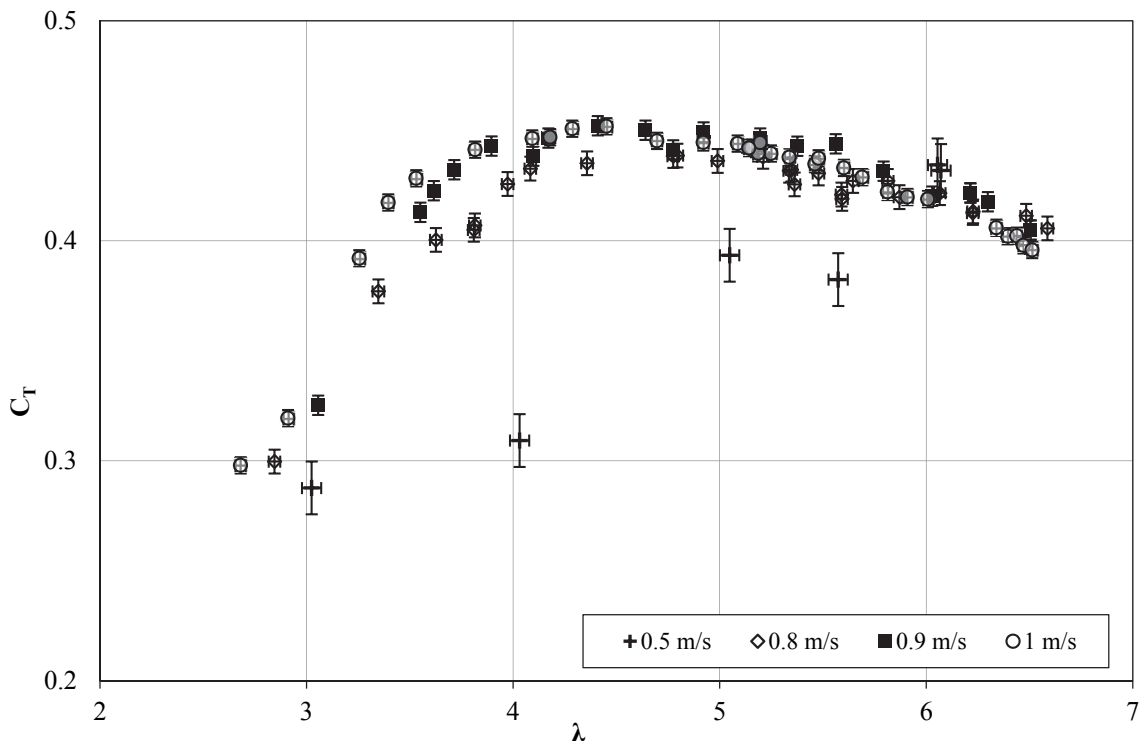
From Figure 5-6, C_T peaked at approximately $\lambda = 4.4$. Note that for the range of λ values investigated, the turbine operated beyond freewheeling (where C_P is negative at λ of between 6 and 6.5), however, this operating condition is not realistic for a real turbine.

Figure 5-7 and Figure 5-8 show the axial and radial root bending moment coefficients. From Figure 5-7, the coefficient of axial bending moment followed a similar trend to the thrust coefficient, as expected, as it is a measure of the bending load in the axial direction at the blade root.

From Figure 5-8, the coefficient of radial bending moment reached a maximum of 0.014 at a λ of 6.5. In this case, some of the C_{Mx} values were negative because the bending moment in the radial direction at the blade root was counter to the direction used in the instrument calibration, giving negative readings.
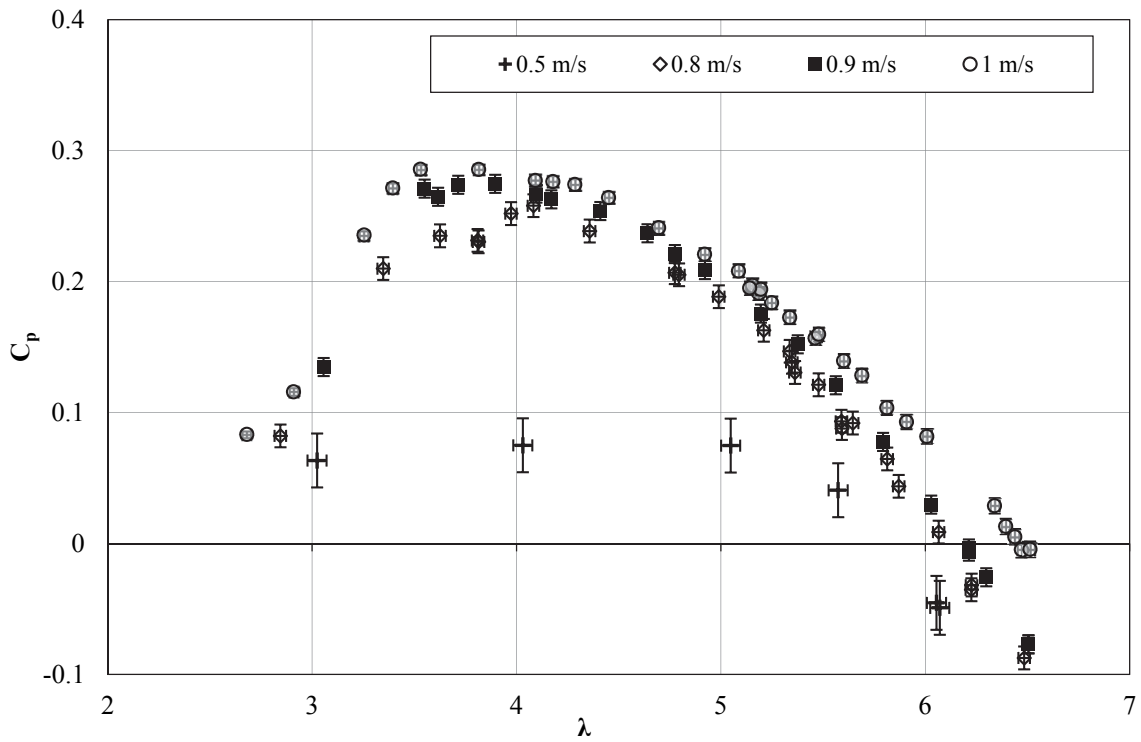

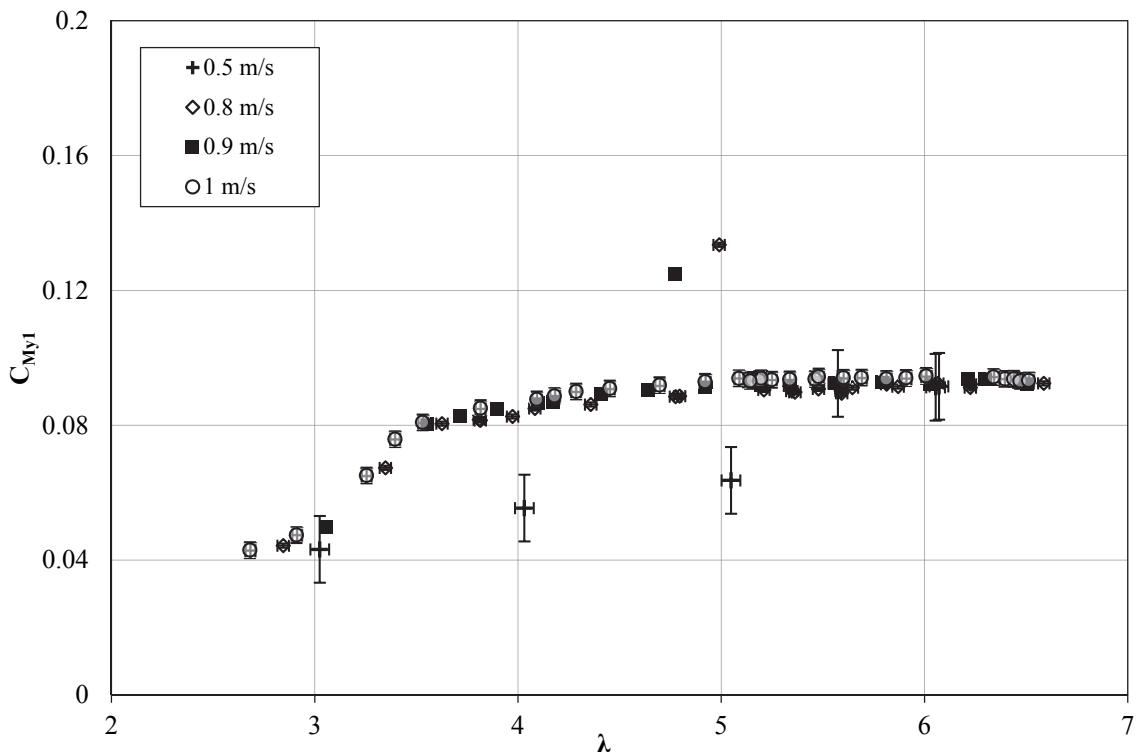*Figure 5-7 C_{My}–λ curve for varying inflow speeds, rigid blades.*
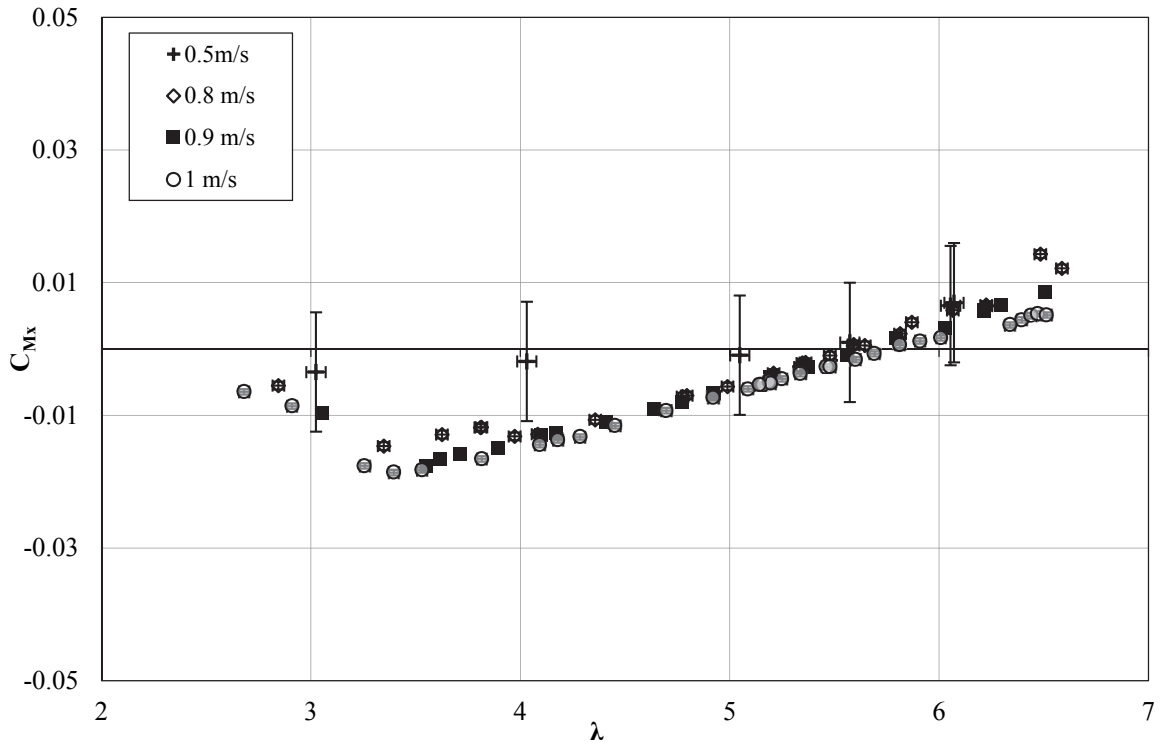
Figure 5-8 C_{Mx}–λ curve for varying inflow speeds, rigid blades.

Figure 5-9 shows the thrust forces on the rotor as a function of both inflow velocity and rotational velocity.
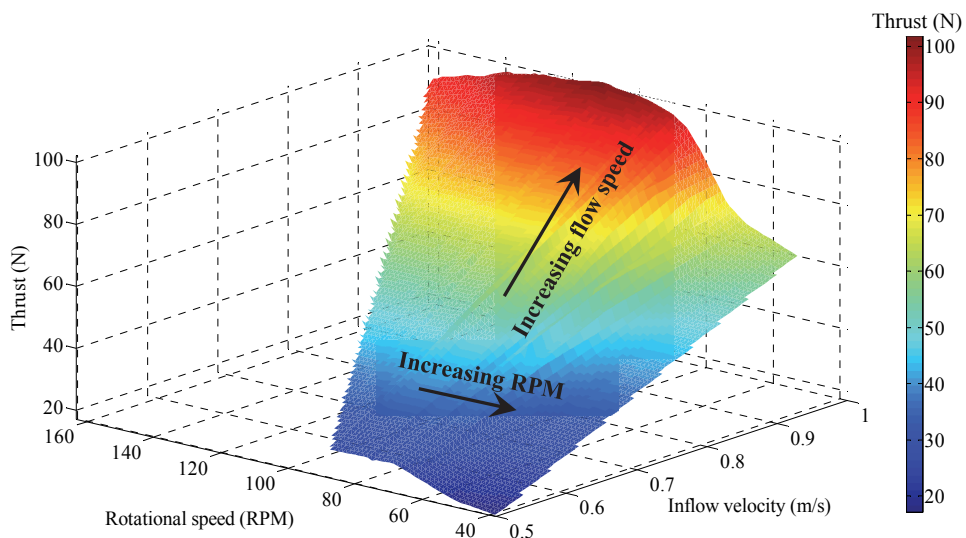
Figure 5-9 Thrust force on rotor as a function of inflow velocity and rotational velocity.

From Figure 5-9, the thrust loads are a strong function of inflow velocity, increasing from 20 N at a velocity of 0.5 m/s to over 80 N at an inflow velocity of 1 m/s, an increase of 80%. However, the loads do not appear to be as strongly influenced by the rotational speeds. For an inflow speed of 0.8 m/s the thrust loads increase from a minimum of 57 N at a rotational speed of 55 RPM to a maximum of 64 N at a rotational speed of 95 RPM, an increase of 11%. These trends are important in the consideration of influential design parameters for the structural design of BT tidal turbine blades.

The outlying data for the 0.5 m/s tests is thought to be due to low Reynolds number operation degrading the lift and making the airfoil more sensitive to flow phenomena. The consideration of Reynolds numbers during the tests is important, particularly when comparing these test results to those of a numerical performance prediction tool. Figure 5-10 shows the Reynolds numbers of the tests, taken at 70% chord.
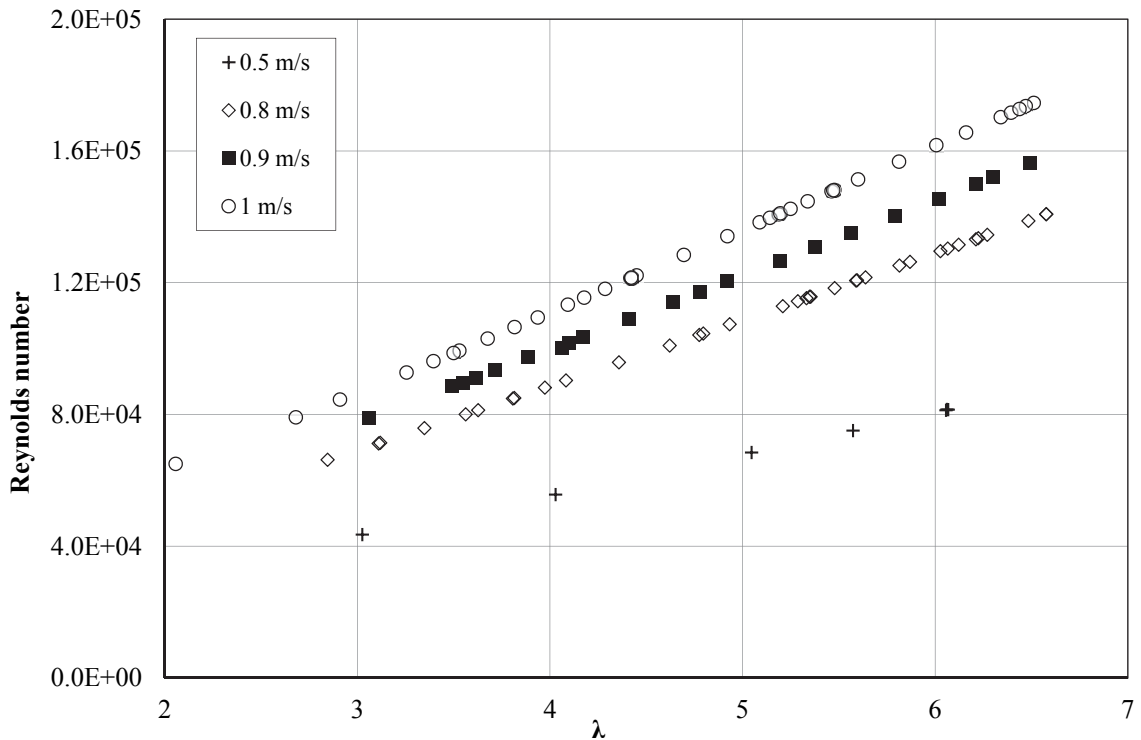
Figure 5-10 Chord-Reynolds numbers, rigid blade hydrodynamic tests.

As shown in Figure 5-10, for the 0.762 m diameter turbine tested at the University of Strathclyde, operating over a range of flow speeds from 0.5 to 1.0 m/s, the chord-Reynolds number ranged from 4×10^4 to 1.7×10^5, based on blade span-wise chord lengths (maximum

chord length of 0.0637 m and minimum of 0.0317 m). The increasing Reynolds number for each flow speed was due to the increasing rotational speed. The average Reynolds number for the 1.0 m/s tests was 1.1×10^5, whereas the average for the 0.8 m/s tests was approximately 1.0×10^5. In this low range of Reynolds numbers, there was clearly an influence on the blade performance. The effects of low Reynolds numbers on these test results are further discussed in Section 7.2.

5.1.4 Uncertainty

The combined uncertainty for each of the performance metrics given in Section 3.1.1, and the uncertainty in the measurements made with the calibrated instruments, was found using the method discussed in Section 3.3. Table 5-1 gives the bias uncertainty values used in the propagation of uncertainty for the performance metrics. This section shows results for the 1.0 m/s test set, however, similar analysis was done for all tests.

Table 5-1 Bias uncertainty values, rigid blade hydrodynamic tests.

Variable	Uncertainty
Density (kgm^{-3})	0.021
Radius (mm)	0.5
Gravitational constant (ms^{-2})	0.001

The temperature was measured with a probe to an accuracy of 0.1°, giving an uncertainty in the water density of 0.021 kg/m^3. The bias, precision and combined expanded uncertainty values for the measured variables are given in Table 5-2. The precision uncertainty is based on the standard deviation for each variable for 5 repeat tests, and the combined uncertainty includes the coverage factor.

Table 5-2 Precision, bias and combined uncertainty values, from calibration, rigid blade hydrodynamic tests.

Variable	Mean value	Uncertainty values			Percent of mean
		Precision	Bias	Combined	(%)
Q (Nm)	6.79	0.067	0.043	0.16	2.34
F_T (N)	83.98	0.68	0.029	1.36	1.62
M_y (Nm)	3.59	0.025	0.016	0.060	1.66
M_x (Nm)	1.99	0.025	0.020	0.032	1.61
Vinf (ms^{-1})	1.01	0.00033	0.0030	0.0031	0.30
ω (rad/s)	11.66	0.0033	0.022	0.022	0.19
λ	4.43	0.0011	N/A	0.0011	0.025

Figure 5-11 shows the combined uncertainty in C_P, C_T, C_{My} and C_{Mx} as a function of tip speed ratio, λ, and Figure 5-12 shows the percentage uncertainty in C_P, C_T, C_{My} and C_{Mx}, for the 1.0 m/s test case. From Figure 5-11, the combined uncertainty in C_T, C_{My} and C_{Mx} were relatively constant. However, the combined uncertainty in C_P increased linearly with λ due to the linearly increasing rotational speed, which is multiplied by the measured torque to calculate the power capture.

The uncertainty in C_T was consistently under 1.7%, and the uncertainty in C_P was less than 5% for tests between $\lambda = 3$ and $\lambda = 5$. However, the percentage uncertainty in C_P was high at the extremes of the λ range, where C_P was small. The percentage uncertainty is estimated by dividing the combined uncertainty in C_P by the calculated C_P, therefore, as C_P approaches zero, the percent uncertainty approaches infinity. Although numerically this calculation of percent uncertainty is accurate, realistically, based on Figure 5-5 and Figure 5-11, the actual uncertainty in the calculated quantity did not increase drastically over the range of λ. A similar trend was found for C_{Mx}, where the percent uncertainty approaches infinity as the value of C_{Mx} approaches zero.
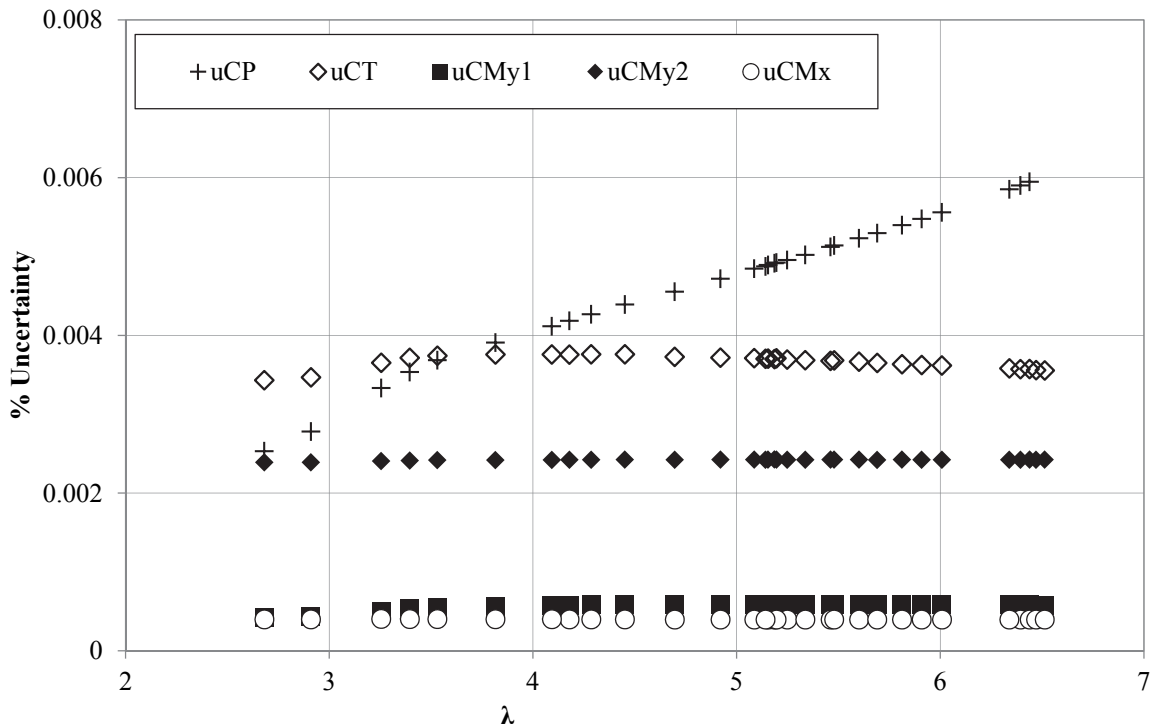
Figure 5-11 Combined expanded uncertainty for calculated parameters, rigid blade hydrodynamic tests.
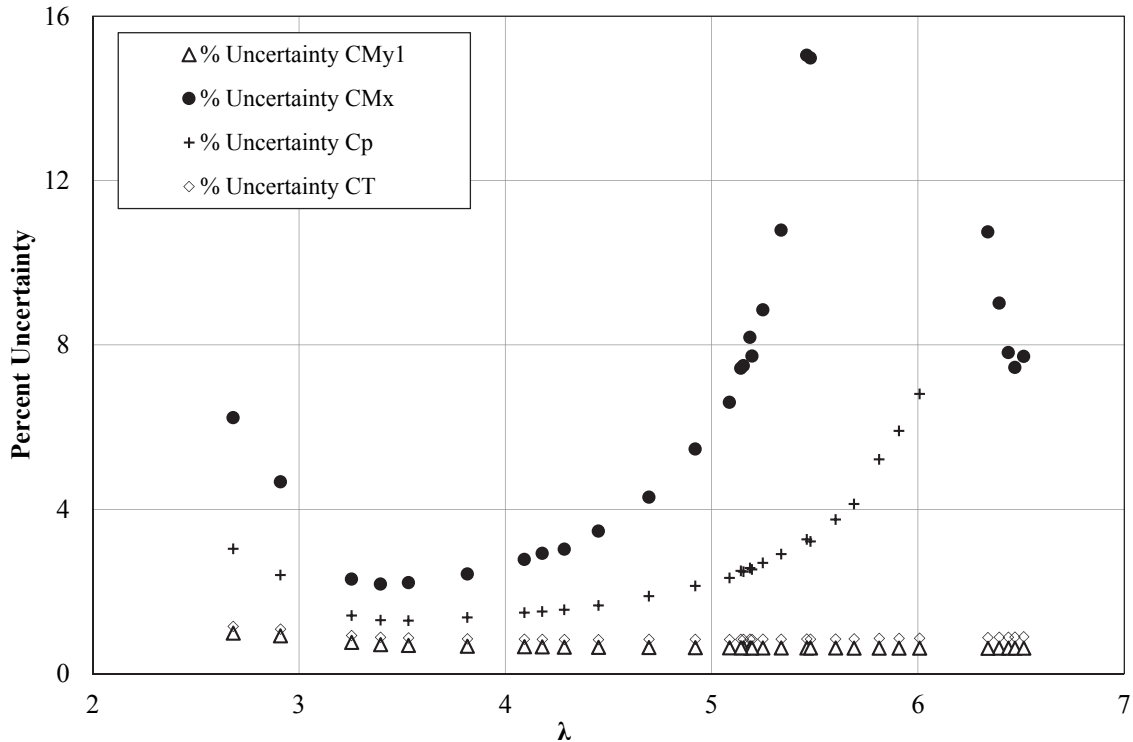
Figure 5-12 Percentage uncertainty for calculated parameters, rigid blade hydrodynamic tests.

The uncertainty in C_{My} was less than 1.4% for over 93% of the tests done, however, C_{Mx} had an uncertainty of over 15% for 37% of the tests done. From Table 5-2, the combined uncertainty in the calibration of the radial blade root bending moment, C_{Mx}, and the axial blade root bending moment, C_{My}, were of the same order of magnitude, however, the measured radial bending moments were small, making the percentage uncertainty high.

From Figure 5-5 to Figure 5-8, the error bars for the 0.5 m/s tests are significantly greater than those at higher flow speeds. This is because, from the propagation of uncertainty (given in Eq. (3.35)), the lower inflow velocity on the denominator of the equation equates to a greater error.

For this system, the blockage ratio was calculated by taking the ratio of rotor area to tank cross sectional area, and was found to be 4.45%. Based on the discussion given in Section 3.1.3.F, and on Marinet project findings [194], this was not considered large enough to require correction.

To further investigate the repeatability of the test program, the standard deviations of C_P, C_T, C_{Mx}, C_{My} and λ for the 5 repeated tests, done with an inflow velocity of 1 m/s and rotor

velocity of 110.7 RPM, are given in Table 5-3, as well as the minimum uncertainty for each of the calculated parameter.

Table 5-3 Results of the repeatability analysis, rigid blade hydrodynamic tests.

Performance characteristic	Standard deviation	Minimum uncertainty
C_P	0.0013	0.0044
C_T	0.0017	0.0039
λ	0.0014	0.0077
C_{Mx}	7.5e-5	0.00038
C_{My}	1.7e-4	0.00063

The standard deviation of the repeated values was consistently lower than the minimum uncertainty. This indicated that the experimental scatter was within the uncertainty bounds of the experiment, providing confidence in the repeatability of these tests.

5.2   Experimental Set 2: Composite & Aluminum Blades

Composite and aluminum blades of the same geometry were tested consecutively on an 828 mm diameter HATT in the Kelvin Hydrodynamics Laboratory towing tank at the University of Strathclyde. Figure 5-13 shows the turbine rig commissioned by Cardiff University [62] and used for this set of tests. Although the turbine configuration differed from that tested in Section 5.15, the experimental concept was the same, with the carriage towing the submerged turbine through the water.

The HATT had a support stanchion welded to the turbine housing which extruded vertically and was mounted to the towing tank carriage by two brackets, as shown in Figure 5-14, with the middle of the hub 1.0 m below the free surface of the water.

The turbine was driven at a constant rotational speed using a Rexroth IndraDyn T Synchronous-Torquemotors motor (IndraDyn T PPM MST 130 E 35) [251] with a rated power of 0.6 kW, rated torque of 22.5 Nm, rated speed of 350 RPM, and data capture frequency of 250 Hz. A drive cabinet housed the power electronics supply unit for the motor, which required a 3-phase, 32 Amp power supply.
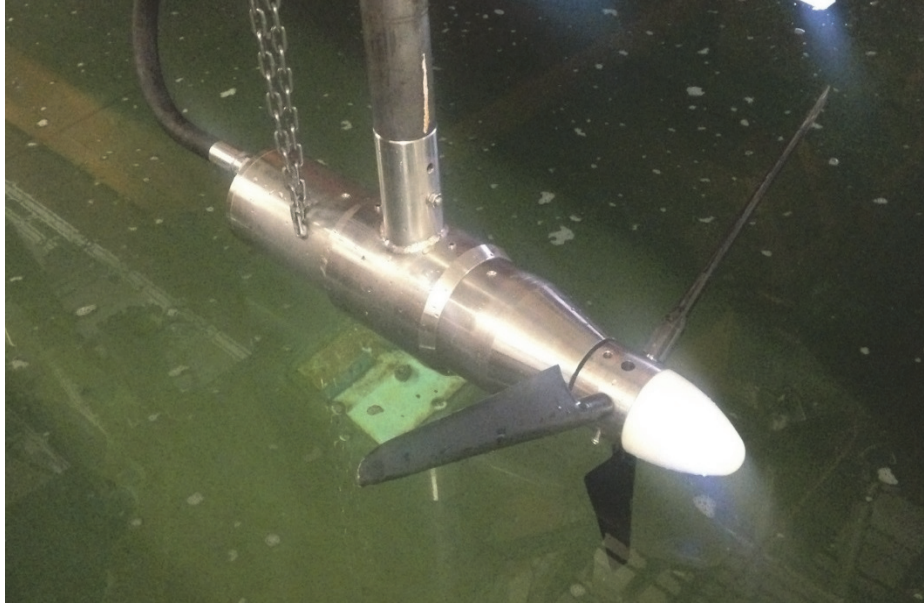
Figure 5-13 Cardiff University turbine with composite BT blades.
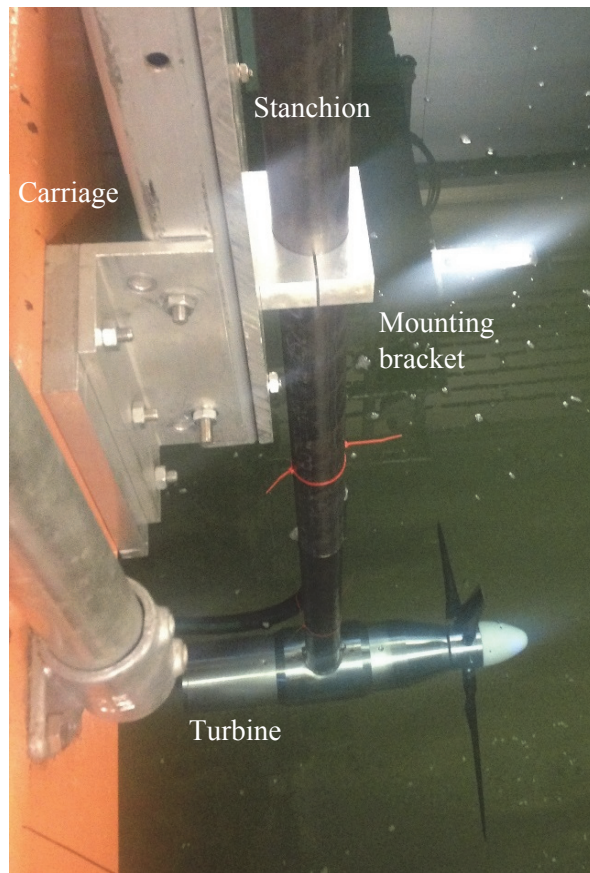
Figure 5-14 Turbine mounted on towing tank carriage at the University of Strathclyde.

Data was logged at 137 Hz using the Cambridge Electronic Design Power 1401 DAQ and the DAQ program, Spike, and exported as text files for post processing in MATLAB®. The rotor rotational speed was obtained from a position output from the motor drive which, using the time stamp recorded in Spike, enabled a calculation of the number of rotations in a given time period. The carriage speed was a direct output from the carriage operating system.

Along with the carriage speed and rotor rotational speed, the main measurements of interest in these tests were the torque and thrust from the rotor blades. The rotor torque was measured using a data stream from the motor which gave a measurement of the torque generating current from the motor (converted to a voltage signal); the rotor torque was the torque generating current minus the required current to spin the turbine at a particular speed without the blades. The required current to spin the turbine was a function of the rotational speed of the motor, and was calibrated by the team at Cardiff University prior to testing.

To measure the rotor thrust, the turbine stanchion was instrumented with a 5 mm long, Y11-FA-5-120 strain gauge, with a 119.9 Ohm resistance and 2.07 ± 1% gauge factor, which was located 1.5 m from the mid hub height (0.5 m above the free surface). The thrust sensor was calibrated by applying known loads to a lever arm and measuring the output voltage, over a range from 0 to 10 V. The calibration showed the strain measurement to be highly linear with a coefficient of determination, R^2, of 0.9999. The calibration curve is given in Appendix C.

Originally, the turbine was fitted with strain gauges on the blade roots which measured the thrust and twist on the blade, passing the voltage signal through an Arduino to a LabVIEW DAQ. However, due to damage of these sensors and communication problems between the Arduino and the DAQ, they were not used during these sets of tests. Additional small circuits, including moisture sensors and a pulse train, were included in the original turbine system, but were also not used for this set of testing.
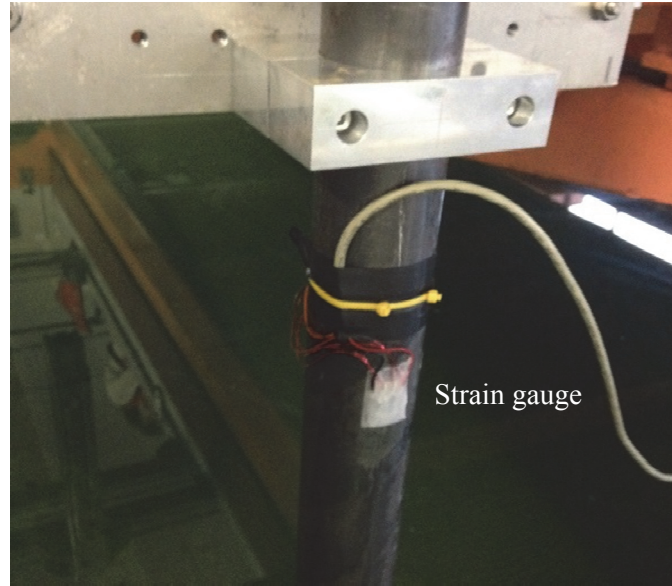
Figure 5-15 Strain gauge located on stanchion to measure thrust.

The materials and composite layup of the BT blades and aluminum blades are outlined in Section 4.2. For these tests, the blades were 364 mm long, making them 4 mm longer than in Section 4.25 due to the addition of a 15 mm diameter cylindrical root section required to mount the blades to the turbine, which protruded 4 mm from the base of the hub. With a hub radius of the Cardiff turbine of 50 mm, this gave a rotor of radius of 414 ± 0.05 mm, a total blade length of 364 mm, and root pitch setting of $28.88° \pm 0.381°$. This is shown in the schematic in Figure 5-16. The additional 5 mm chord length, discussed in Section 4.2, was added to the chord lengths in Table 5-4, for use in the BEMT tool.

A 15 mm diameter stainless steel cylindrical root connection at the base of the blades was inserted into a slot in the hub, as shown in Figure 5-17. The pitch setting of the blade was constrained by a 4.5 mm diameter grub screw that fit into a slot on the blade root. The uncertainty in this setting was estimated based on the machining uncertainty of the slot, which was ± 0.05 mm, equating to $\pm 0.381°$ of uncertainty in the blade root pitch setting.

Uncertainty in the turbine radius came from the machining accuracy of the hub components (± 0.5 mm). The uncertainty in the composite blade length is from the resolution of the CMM scanning machine (± 5 μm) and the uncertainty in the aluminum blade length is from the precision of the CNC machine that was used to manufacture them (± 10 μm).
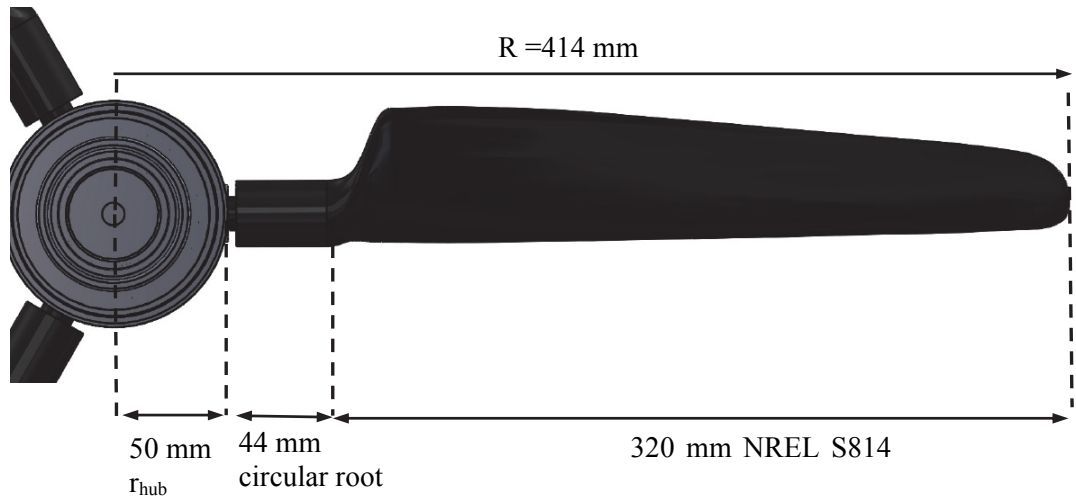
Figure 5-16 Schematic of turbine dimensions.

R =414 mm

50 mm
r_{hub}

44 mm
circular root

320 mm NREL S814

Slot in hub
for blade
root

4.5 mm
grub screw
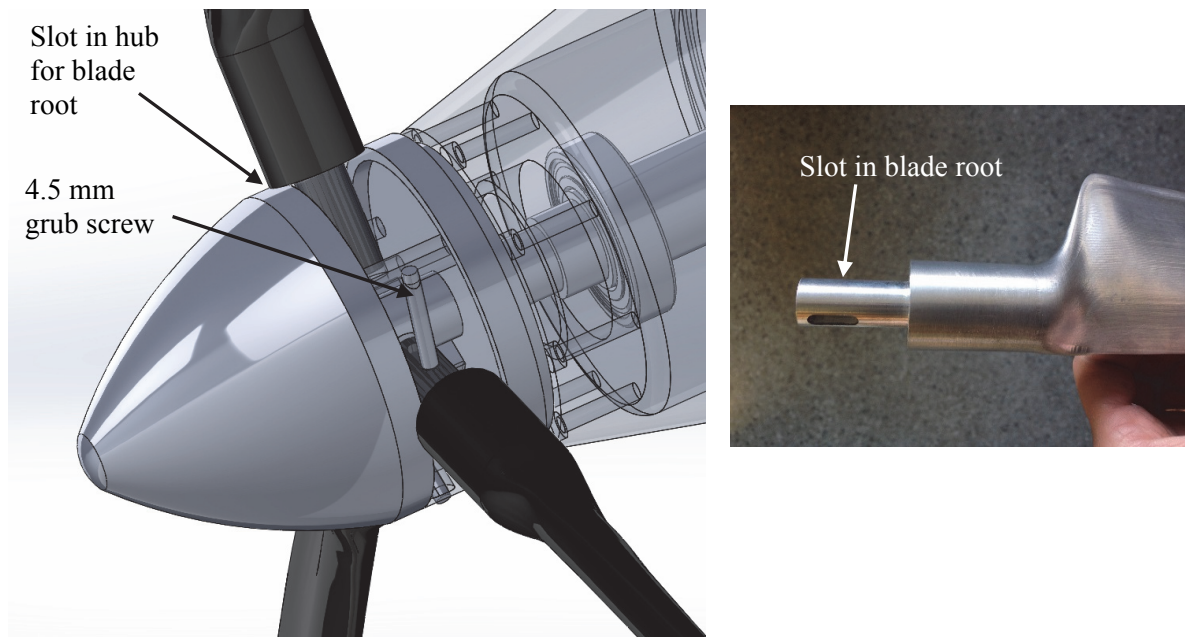
Slot in blade root

*Figure 5-17 Left) blade root connection in hub, Right) Slot in blade root to secure pitch angle
(Cardiff University CAD [62]).*

The blade geometry relative to the Cardiff University turbine is given in Table 5-4. For this
system, the blockage ratio was calculated by taking the ratio of rotor area to tank cross
sectional area, and was found to be 5.25%. Based on the discussion in Section 3.1.3.F, this
was not considered large enough to require correction.

Table 5-4 Turbine and blade geometry for design tool verification.

Turbine radius (mm)	Blade length (mm)	Blade twist (Degrees)	Blade chord (mm)	Airfoil shape
0	0	N/A	N/A	N/A
50	0	N/A	15	Circular root
54	4	N/A	15	Circular root
94	44	N/A	29	Circular root
110	60	N/A	N/A	Lofted (ellipse)
120	66	N/A	N/A	Lofted (ellipse)
122	72	0	64.3	NREL S814
147	97	-4.38	62.9	NREL S814
182	132	-10.74	59.8	NREL S814
216	166	-14.8	56.0	NREL S814
249	199	-17.33	51.6	NREL S814
284	234	-18.91	47.3	NREL S814
319	269	-19.75	42.6	NREL S814
354	304	-20.39	38.1	NREL S814
388	338	-20.87	33.7	NREL S814
414	364	-21.11	24.9	NREL S814

5.2.1 Design of Experiment

Test conditions (ranges of flow and rotational speeds) were determined based on a design of experiment study done using the design tool discussed in Section 8, and were based on a minimum allowable composite material safety factor of 1.5 (similar to the SF of 1.6 used by Grogan [44] and the SF of 1.29 used by Liu and Veitch [13]). Due to limitations in the torque of the motor, the flow speed and rotational speed of the turbine were limited to below 1 m/s and 110 RPM. At rotational and flow speeds above this, the motor was unable to maintain the rotor torque at a steady value during testing. Design speeds of 1 m/s and 0.85 m/s were used, and the rotational speed was varied between 50 and 110 RPM in increments of 5 RPM.

5.2.2 Test Procedure

Tests were aligned with the recommendations outlined in EquiMar Deliverable D3.4 [199]. The torque, thrust, and rotational speed were logged during each test using the LabVIEW

DAQ. A zero for the thrust measurement was taken before and after each test. The motor current signal was filtered and the mean value was taken for each test. The thrust sensor measurement did not require filtering. The carriage speed was recorded for each test from the carriage control system.

To account for losses from the hub and carriage, tests were run with no blades at each of the carriage speeds used in the test program. The thrust measured for these tests was subtracted from the thrust measured with the blades on, hence only the thrust on the blades was reported here.

5.2.3 Results

Figure 5-18 to Figure 5-21 show the thrust and torque of the rotor, respectively, for both the 1.0 m/s and 0.85 m/s tests as a function of λ for both the composite and rigid aluminum blades. Figure 5-18 to Figure 5-21 demonstrated that the rigid blades have higher rotor torque and thrust than the BT composite blades, as expected. The magnitude of the error bars in the thrust plots indicate that the experimental setup was sensitive enough to measure the difference in thrust load between the aluminum rigid blades and the composite blades. Four additional data points for torque were measured during a previous test program, using the same torque generating current and turbine system but with no thrust measurement (thrust sensors were not working). These results were within 3% of the torque measurements made during the tests shown here and were not shown here for clarity.

Although measures were taken to reduce the surface roughness of the tested blades, it is possible that slight surface roughness could be substantial relative to the small size of the blades. The relative surface roughness height was 0.06% of the mean chord length, however, tests at NREL showed that roughness on the order of 0.09% could cause reductions in the blade lift [168]. The effect of surface roughness is to trip the BL into earlier separation (separation close to the LE), resulting in earlier BL separation, and hence lower lift and higher drag. This therefore could have contributed to the poor performance of the blade at low λ.

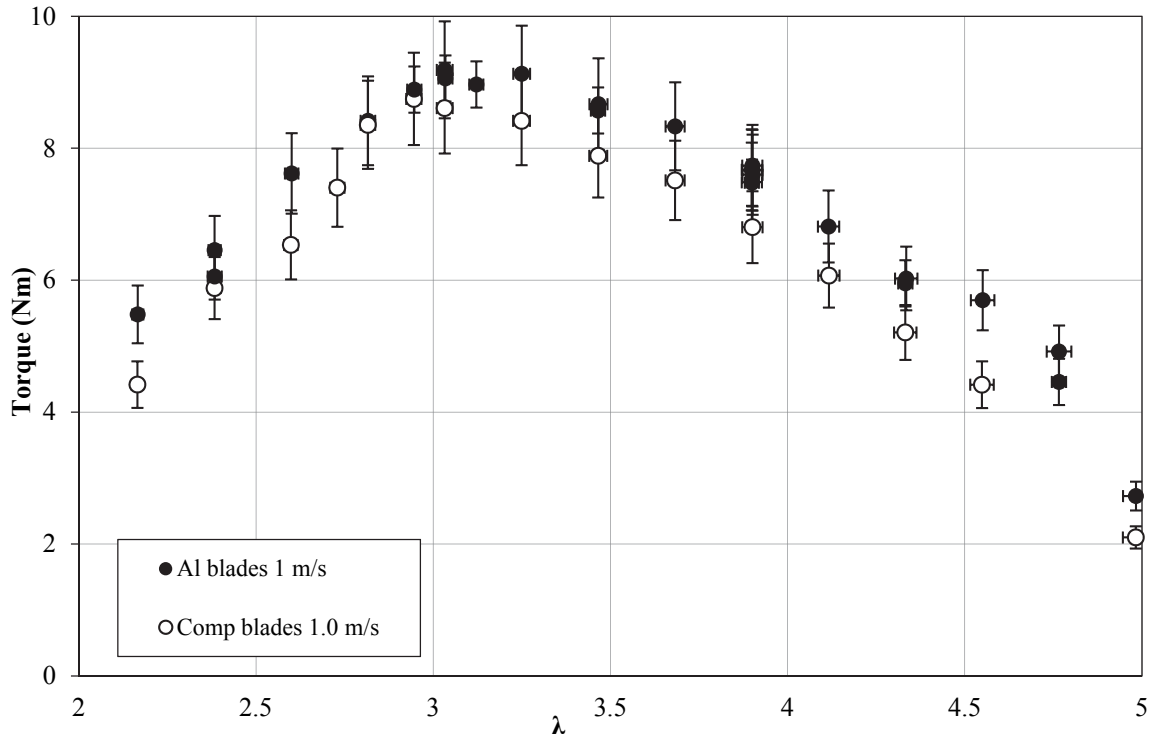*Figure 5-18 Torque–λ for composite and aluminum blades, 1.0 m/s tests.*
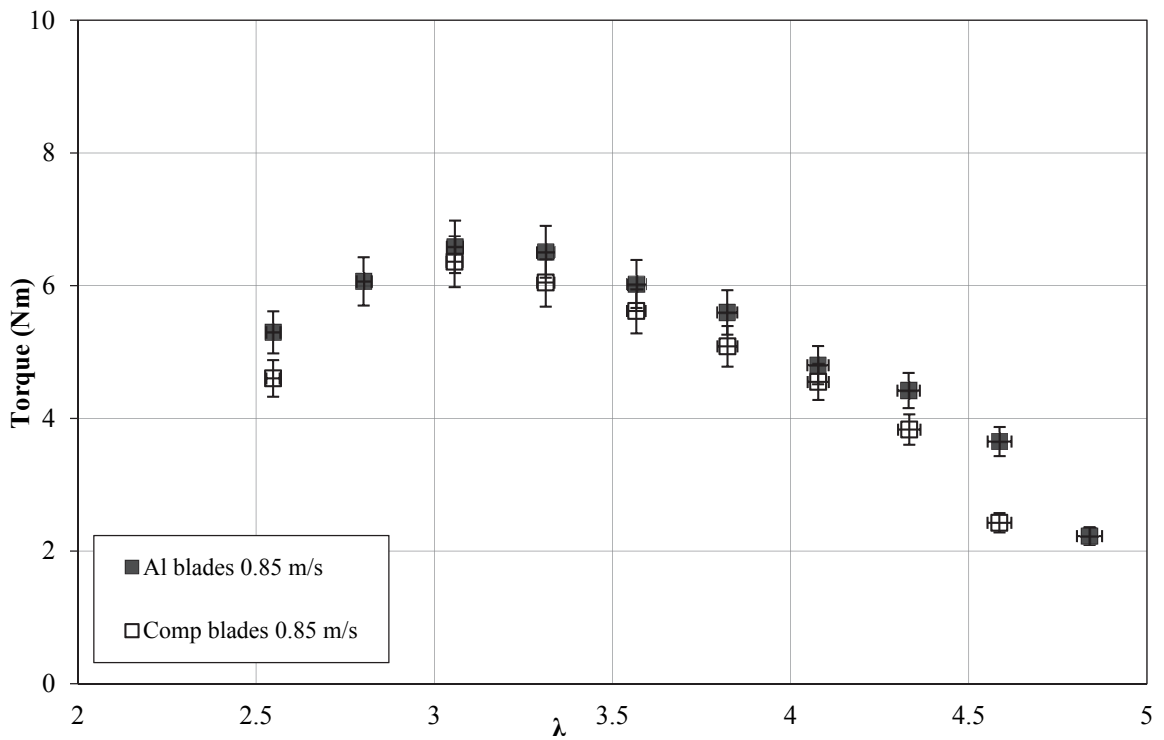
Figure 5-19 Torque–λ for composite and aluminum blades, 0.85 m/s tests.
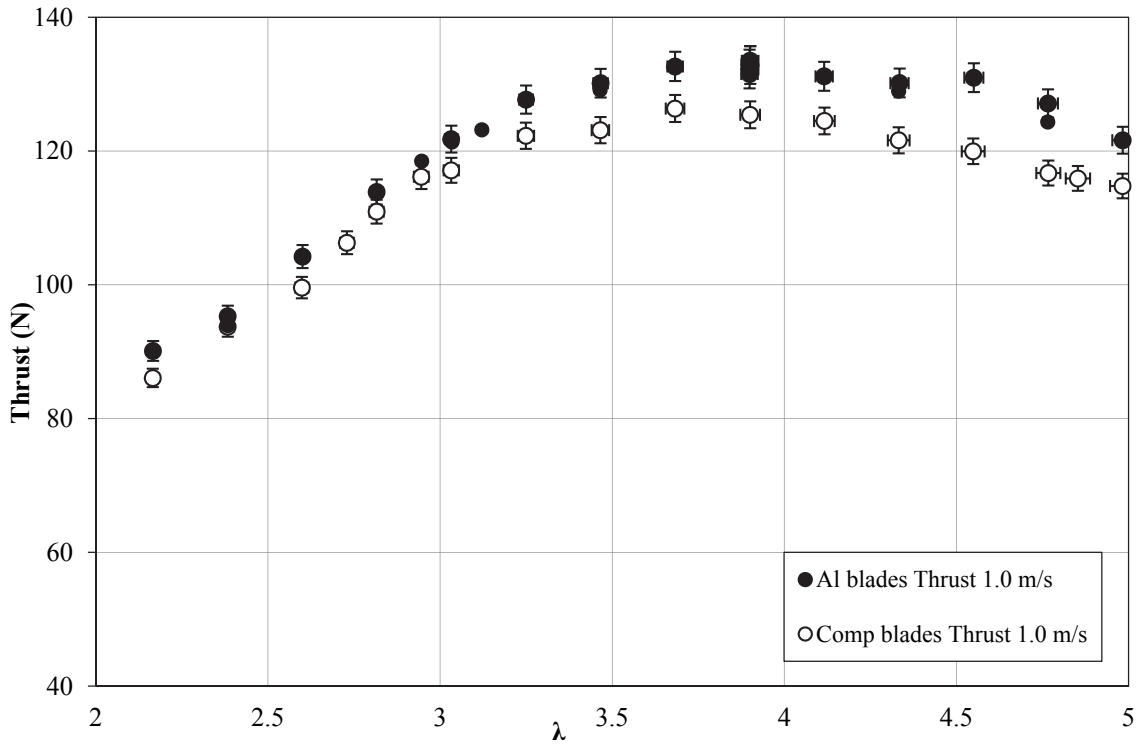
Figure 5-20 Thrust–λ for composite and aluminum blades, 1.0 m/s tests.

Figure 5-21 Thrust–λ for composite and aluminum blades, 0.85 m/s tests.

129

Figure 5-22 shows the reduction in thrust between the composite and aluminum blades (units of [N] on left vertical axis, and % on right vertical axis).
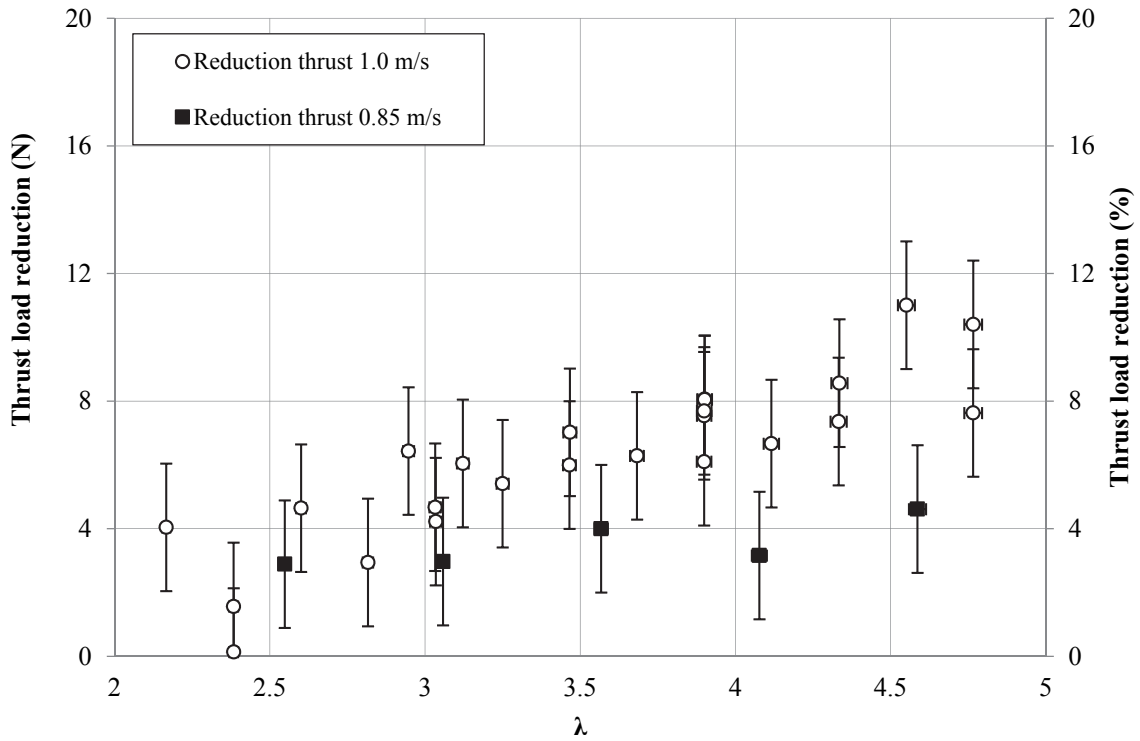
Figure 5-22 Reduction in thrust between the rigid and BT composite blades.

From Figure 5-22, the BT composite blades had reduced thrust loads compared to the rigid blades, particularly at high flow speeds and rotational speeds. For example, the 1.0 m/s tests had more of a reduction in thrust loads than the 0.85 m/s tests, and both had higher thrust reductions at higher λ. This is expected, as the composite blades twisted to feather more with increasingly high loads (as demonstrated by the structural bending tests) which occur at higher relative inflow velocities. The error bars in Figure 5-22 are significant, however, this is due to the relative difference between the composite and aluminum blade thrust measurements (less than 10 N) compared to the combined expanded uncertainty in the thrust measurement, which was ±1.65 N, as discussed in Section 5.2.4.

Figure 5-23 shows the chord-Reynolds numbers for the 1.0 and 0.85 m/s tests. To investigate the influence of Reynolds number on these tests, the power coefficients from the 1.0 m/s and 0.85 m/s tests were compared, as shown in Figure 5-24.
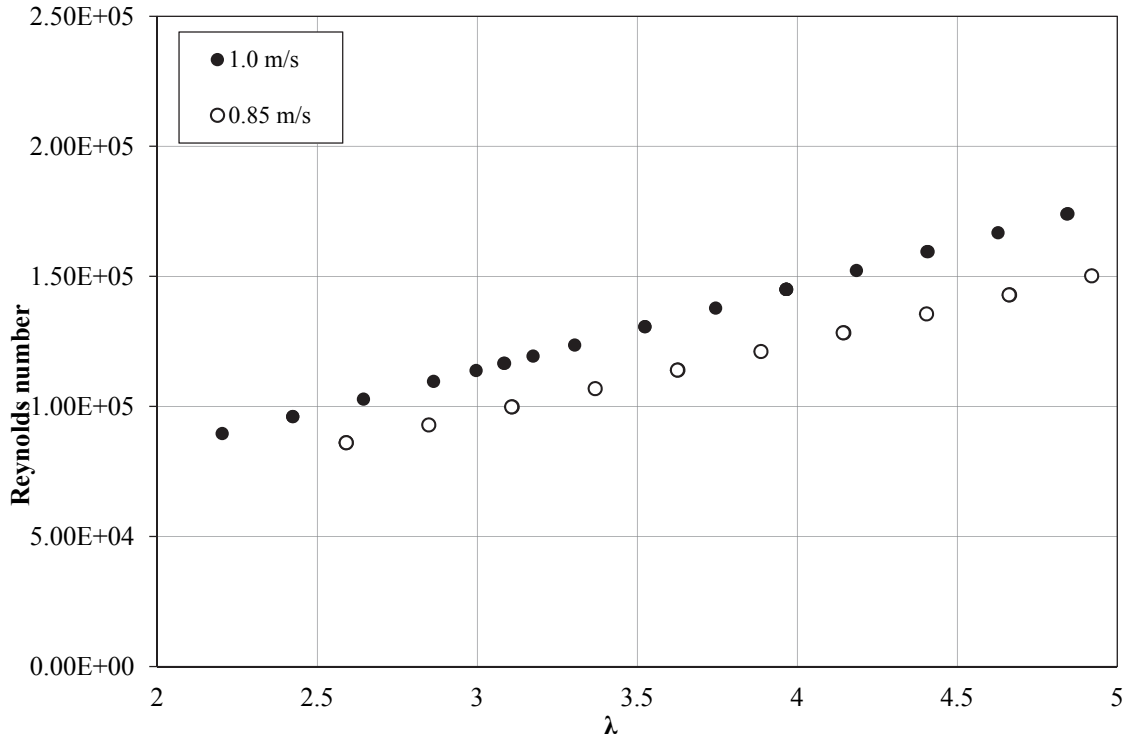
Figure 5-23 Reynolds number for tests as a fucntion of λ, composite and aluminum blades.

In Figure 5-24, the composite blade C_P values are given on the secondary axis for clarity. The C_P values for the rotor for the 1.0 m/s and 0.85 m/s tests were very close, within the uncertainty bounds for the measurements. This indicates that at this range of flow conditions, these tests were not highly sensitive to Reynolds number. This is counter to what was found for the first set of hydrodynamic tests, which is thought to be due to the relatively higher Reynolds number for the second set of tests due to the longer chord length and larger turbine radius. The average Reynolds number for the 1.0 m/s tests was 1.45×10^5. This is based on a chord length of 0.047 m at 75% of the turbine radius. This is higher than for the first set of hydrodynamic tests, which had an average Reynolds number of 1.1×10^5 at 1.0 m/s (25% lower). Interestingly, this is still lower than the critical Reynolds number (based on the turbine diameter) of 5×10^5 which was found by Mason-Jones [252] to be the minimum Reynolds number required to overcome these issues of Reynolds scaling.
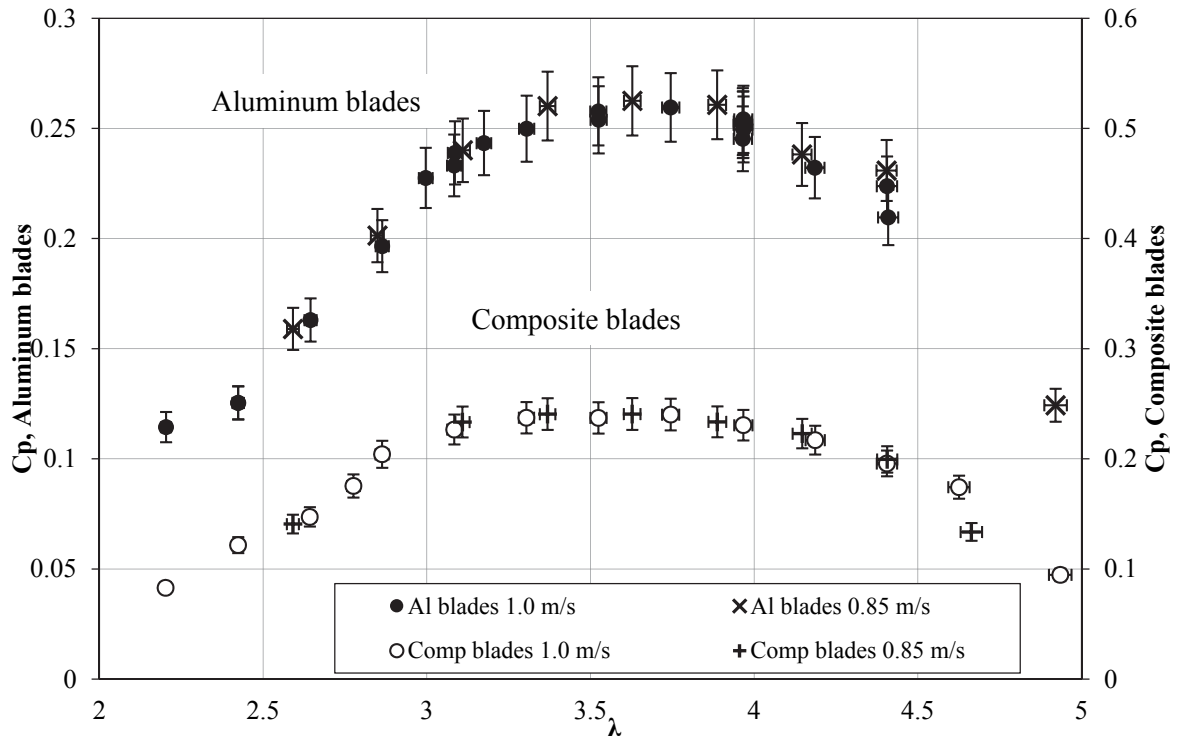
Figure 5-24 $C_P – \lambda$ curve for 1.0 m/s and 0.85 m/s tests, composite and aluminum blades.

Figure 5-25 shows a snapshot taken from a video during a 100 RPM and 1 m/s test on the composite blades.
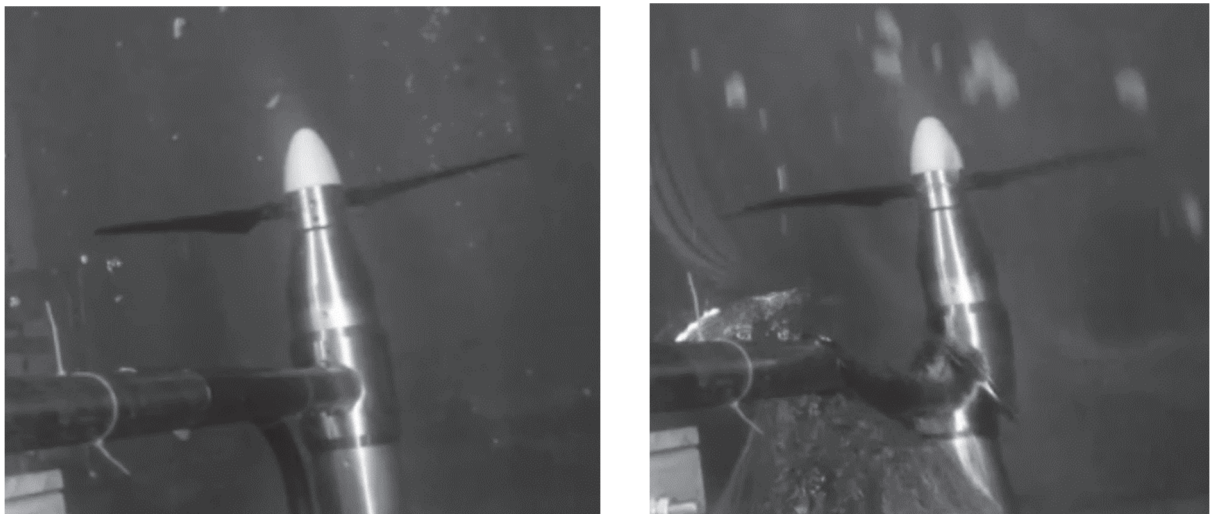
Figure 5-25 Left) Composite blades prior to carriage ramping up (unloaded) Right) Composite blades at 1 m/s and 100 RPM (loaded).

The image on the left shows the blades unloaded, and the image on the right shows the blades once the carriage speed and rotational speed were steady (loaded). From the image on the right, the blades bent under load. The twisting of the blades was more difficult to observe in the images, however, from structural testing of the BT blades, it was shown that when the blades are loaded and bent, they also twist to feather. The observed bending and reduced rotor thrust and torque, suggest that the BT coupled blades performed as desired.

5.2.4 Uncertainty

The uncertainty in the measurements was found using the method discussed in Section 3.3. Table 5-5 gives the bias uncertainty values used in the propagation of uncertainty for the performance metrics.

Table 5-5 Bias uncertainty values, composite and aluminum blade hydrodynamic tests.

Variable	Uncertainty
Density (kgm^{-3})	0.021
Radius (mm)	0.05
Gravitational constant (ms^{-2})	0.001

The precision, bias, and combined expanded uncertainty values for each measured variable are given in Table 5-6. This section shows results for the 1.0 m/s test set, however, similar analysis was done for all tests. The percent of the mean value is included to indicate the relative uncertainty in each of the variables presented. The precision values are the standard deviation multiplied by the coverage factor, 2.2, for 6 tests repeated at 1.0 m/s and 90 RPM.

The bias uncertainty value for the motor torque generating current (which is used to calculate the rotor torque), was not available from the manufacturer. Figure 5-26 shows the percent uncertainty in the thrust and torque as a function of λ, for the 1.0 m/s tests.

Table 5-6 Precision, bias and combined expanded uncertainty values for measurements, composite and aluminum blade hydrodynamic tests.

Uncertainty values	Mean value	Precision	Bias	Combined expanded	Percent of mean value (%)
Torque (Nm)	8.49	0.21	N/A	0.42	4.9
Thrust (N)	125.12	0.83	0.045	1.65	1.32
Rotational speed (RPM)	90.22	0.12	0.20	0.48	0.53
Vinf (ms^{-1})	1.01	0.00053	0.0010	0.0023	0.23
λ	3.97	0.00205	N/A	0.0041	0.11
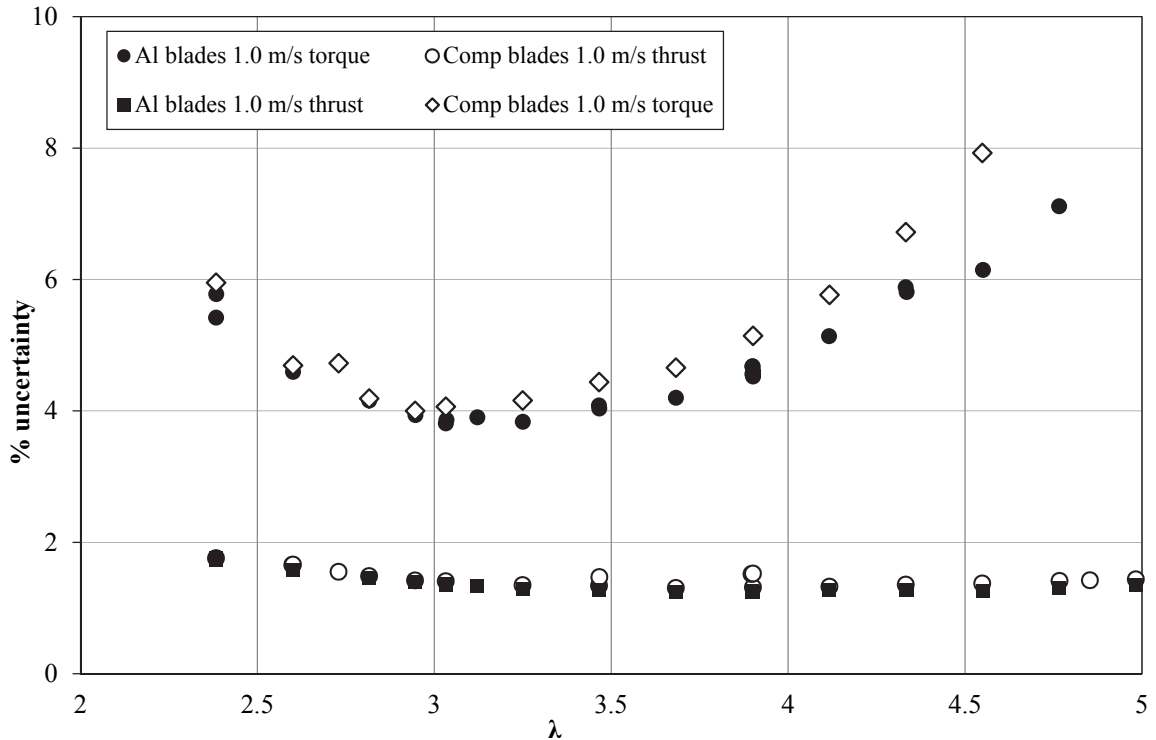
Figure 5-26 Percent uncertainty in parameters for 1.0 m/s tests, composite and aluminum blade hydrodynamic tests.

As evident by the error bars in Figure 5-18 to Figure 5-21, the torque measurements were slightly scattered, giving larger precision uncertainty based on the repeat tests. However, the thrust measurements had an average uncertainty of less than 2%. This is due to both the high repeatability of the thrust measurements, and the high coefficient of determination obtained during the strain gauge calibration. Overall, both the thrust, torque and λ had uncertainties of less than 8%, indicating the overall reliability of this test program and increasing confidence in the measurements.

CHAPTER 6
STRUCTURAL MODEL

Finite element analysis (FEA) is a numerical technique for finding approximate solutions to complex structural problems by discretizing a body into elements. By solving structural mechanics problems using this method, accurate representations of complex geometries can be approximated, capturing the deformation and stresses of a body. FEA solves a set of algebraic equations for initially unknown nodal quantities, typically displacements, using the input geometry, mesh, material properties, load scenario, and nodal constraints [234]. Stresses and strains are computed from the nodal displacements using the constitutive relations for the material [223]. Utilizing a finite element model (FEM), design optimizations can be made and parametric structural design iterations trialed at a low cost.

In this work, Altair Hyperworks RADIOSS® finite element software was used to develop structural models of the laminate plates and composite blades. These FEMs were verified by the static test results outlined in Chapter 4, with results presented in this chapter.

6.1 Laminate Plate

6.1.1 Model Setup
The HyperLaminate module in Hyperworks was used to define ply orientations (fiber angles), ply thicknesses, and fiber and matrix material properties. COMPG first order 4-node CQUAD4 2-D shell elements were assigned to the 2-D geometry, each layer with a given ply thickness and fiber angle, and a MAT 8 material model was used. Material properties used in the laminate plate FEM are given in Table 4-1.

6.1.2 Mesh Convergence Study
Figure 6-1 shows the computational time as a function of element size, and Figure 6-2 shows the bending displacement and tip twist of the plate as a function of element size.
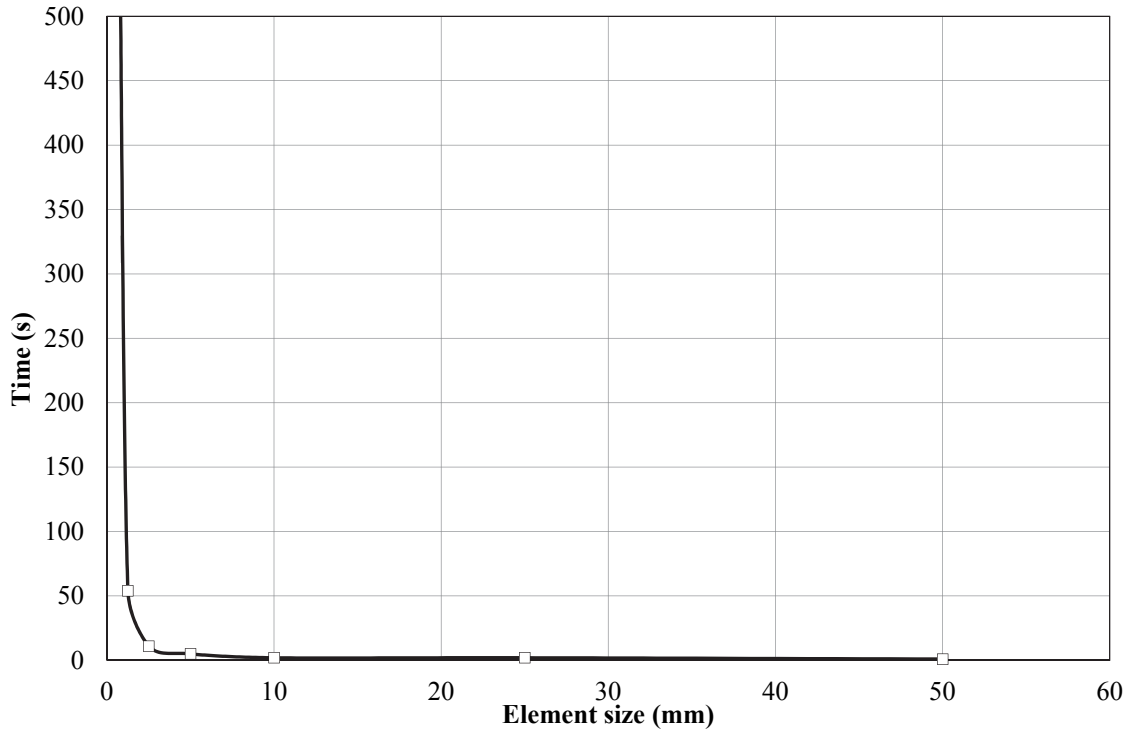
Figure 6-1 Finite element convergence study: Computational time for BT plate.
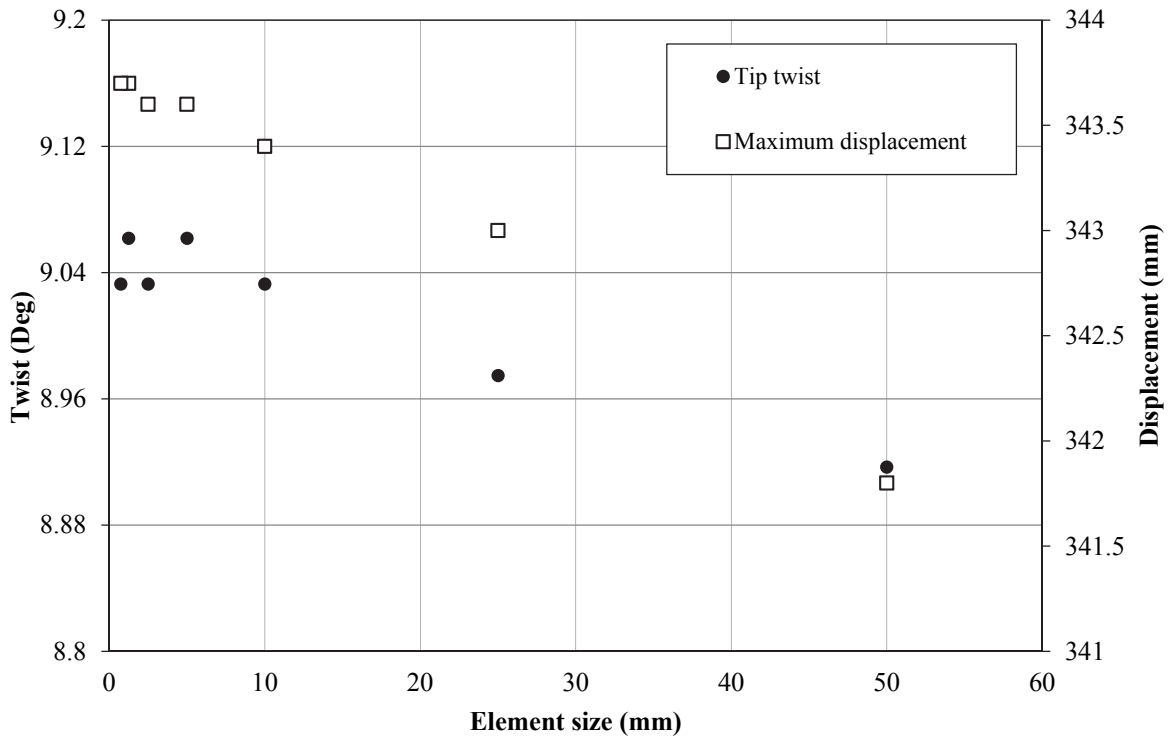
Figure 6-2 Finite element convergence study: Bending displacement and twist for BT plate.

Based on the results shown in Figure 6-1 and Figure 6-2, although small fluctuations in the twist appeared for elements smaller than 5 mm, the magnitude of these fluctuations was less than 0.3 %. Elements with 2.5 mm edge-lengths were chosen based on the convergence results (0.3 % difference between 1 mm and 2.5 mm elements) which showed this element size gave converging results within acceptable computational time.

6.1.3 Model Verification

Figure 6-3 shows the FEM displacement for the laminate plate with 3 layers, a uniform thickness of 2.72 mm, the average value as measured by a CMM (discussed in 4), and a layup of [30°, 0°, 30°] with a 25 N tip load.

From the contour plot of the displacements of the laminate, the z-displacement of the free end of the plate varied in the y-plane. This is a clear indication of twist in the plate. With a 25 N load applied, the maximum tip displacement was 111.4 mm, with a tip twist of 10.64º, for this layup and laminate thickness.

Contour Plot Displacement (z) in mm

| 111.4 |
| 99.0 |
| 74.18 |
| 61.77 |
| 49.36 |
| 24.54 |
| 12.13 |
| 0.0 |

Max= 111.4
Grids 674667
Min= 0.0
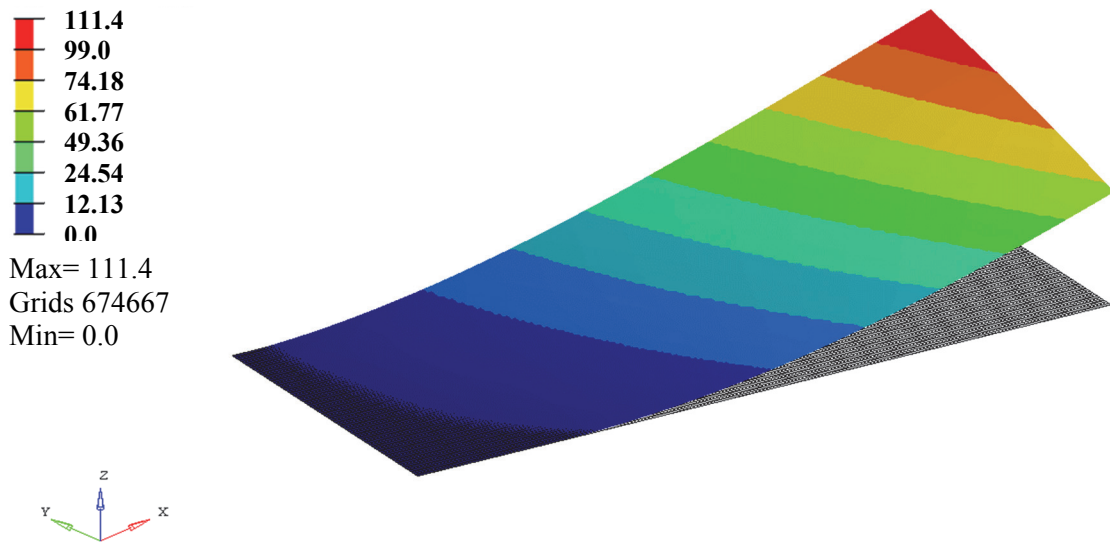
Figure 6-3 FEM of BT laminate plate bending displacement, with 25 N tip load.

Figure 6-4 and Figure 6-5 show results obtained for the [30º, 0º, 30º] laminate test samples compared to a FEM with an average thickness of 2.72 mm. The tip displacement is the maximum displacement of the free end of the plate, relative to the initially unloaded plate.
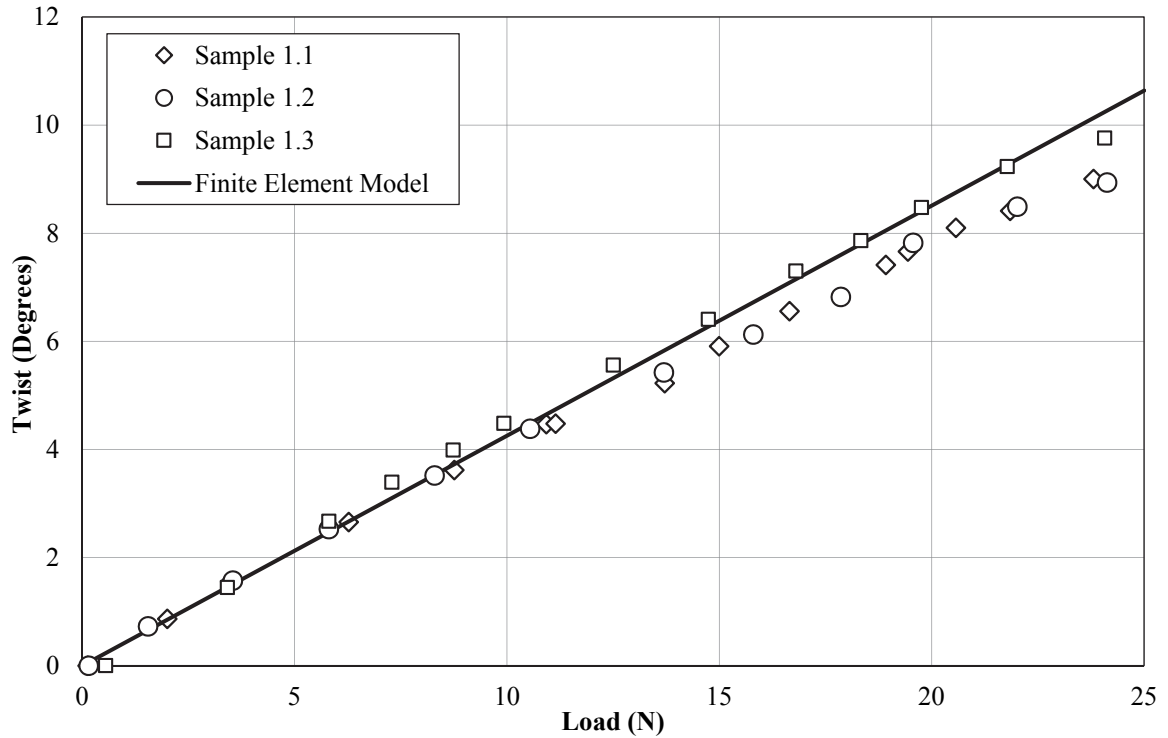
Figure 6-4 Twist vs. load for the experimental results compared to FEM of laminate plates.
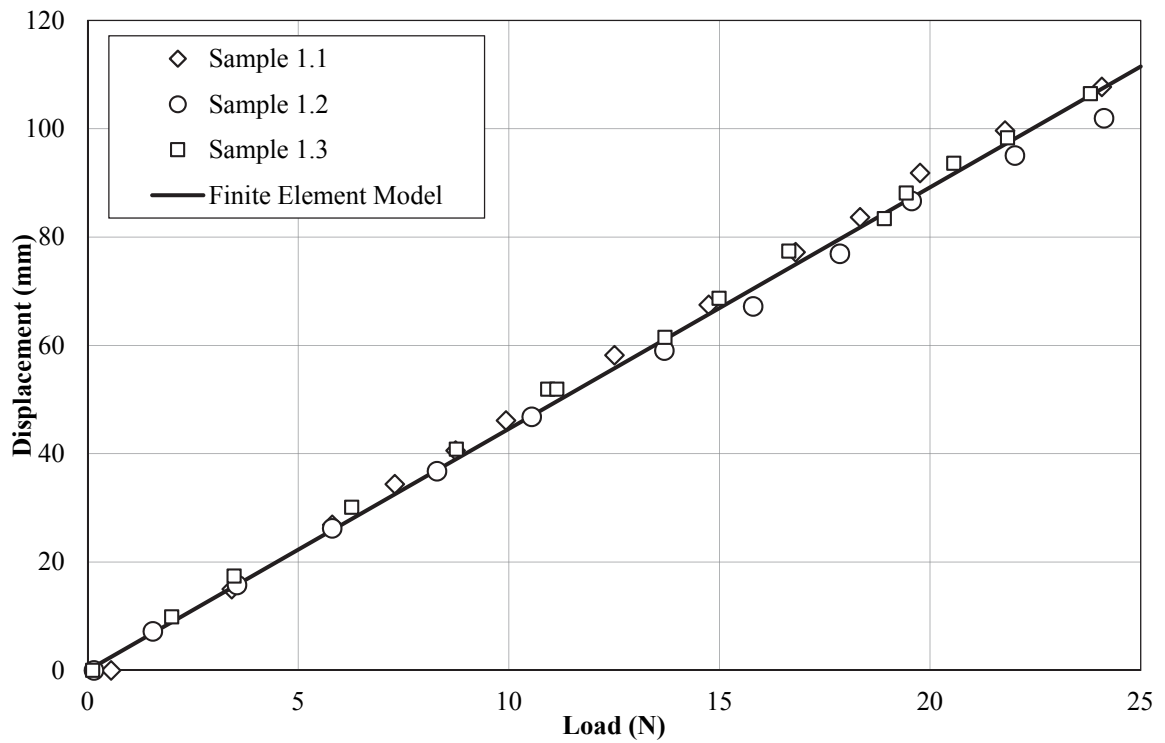
Figure 6-5 Load vs. displacement for the experimental results compared to FEM of laminate plates.

At the maximum load the FEM twist was within 12% and FEM displacement was within 2% of the experiment for Sample 1.2 and Sample 1.3. Sample 1.1 matched the FEM twist even better, to within 3.5% at the maximum load. Possible additional sources of error between the test samples and the FEM include:

- Random uncertainty in the experimental setup; for example, imperfections in the clamping mechanisms and slight offsets in the location of the point load,
- Variations in the ply angles (variances in the ply angles significantly effects the sample deformation, as discussed in Section 6.1.4),
- Variations in the mean thickness of the plate samples (each sample has a slightly different measured mean thickness, as discussed in Section 6.1.4).

6.1.4 Sensitivity to Manufacturing and Material Properties

The sensitivity of the FEM to laminate thickness and material property inputs is important, as material properties from the manufacturer are not always known to a high level of accuracy and standard mechanical tests have inherent variability in sample preparation and measurement of deformation values. As well, the performance of tailored composite structures is critically dependent on the accuracy and reliability of the manufacturing techniques used [131]. Manufacturing of composites can be costly and labor intensive, and the quality of the laminate is dependent on the skill of the operators [214]. As well, curved shapes make plies more difficult to drape into molds, particularly for shapes like turbine blades, requiring complex cutting patterns and further adding to the labor hours [46].

The importance of manufacturing and process control on long term durability of tidal turbines was illustrated by an example done by Davies *et al.* [151] which compared two specimens based on the same materials but different manufacturing batches. Quality control checks, including interlaminar shear, revealed one set of samples to be of better quality, and tests indicated that the lower quality samples resulted in poorer fatigue performance compared to specimens of better quality. For a composite marine propeller, random variations due to fiber misalignments, voids, laminate property uncertainties, and boundary conditions add to the uncertainty of the overall propeller response compared to homogeneous metallic propellers [102]. One study showed that an adaptive composite

propeller that depends on fluid–structure interaction is more sensitive to random variations in geometric, material stiffness, and material strength properties than an equivalent rigid metallic structure [253]. In this study, the hydroelastic performance was particularly influenced by fiber angles. This study made a probabilistic estimate of the reliability of the propeller by determining the probability of failure at each point within the design space.

The foregoing findings makes the consideration of the uncertainty associated with manufacturing processes an important part of the design of composite structures. Therefore a sensitivity study was performed to investigate the effects of model inputs, such as material property inputs, composite thickness and ply angles, on the overall performance of the laminate.

Using the verified laminate FEM, it was found that variations of $\pm 10\%$ in the longitudinal Young's modulus (parallel to the fibers, E_1) changed the predicted twist at maximum load, predicted by the FEM, by 1.1% and changed the displacement at maximum load by 3.8%. This indicates that the displacement is more sensitive to changes in E_1 than the twist. Variations in the transverse (perpendicular to the fibers) elastic modulus, E_2, by $\pm 10\%$ changed the twist at maximum load by 3.1% and changed the displacement at maximum load by 2%. Hence, the twist angle is more sensitive to changes in E_2 than the displacement: opposite to what was found for E_1. This is because E_2 affects bending in the transverse direction which is directly related to the twisting, and therefore a lower E_2 means the plate is more elastic and can bend more in the transverse direction, resulting in more twisting. It was also found that changes in Poisson's ratio, ν, of up to $\pm 15\%$ affected the FEM results by less than 1%.

The results of the FEM with the maximum and minimum (mean $\pm$ standard deviation) and average uniform thicknesses, from the CMM scan given in Section 4.1.3, were plotted against the experimental data, as shown in Figure 6-6 and Figure 6-7. To determine the importance of modeling realistic thickness contours, the actual thickness contours shown in Figure 4-7 were input to the FEM (taking the average thickness on a grid of 2 mm) and are also shown in Figure 6-6 and Figure 6-7.
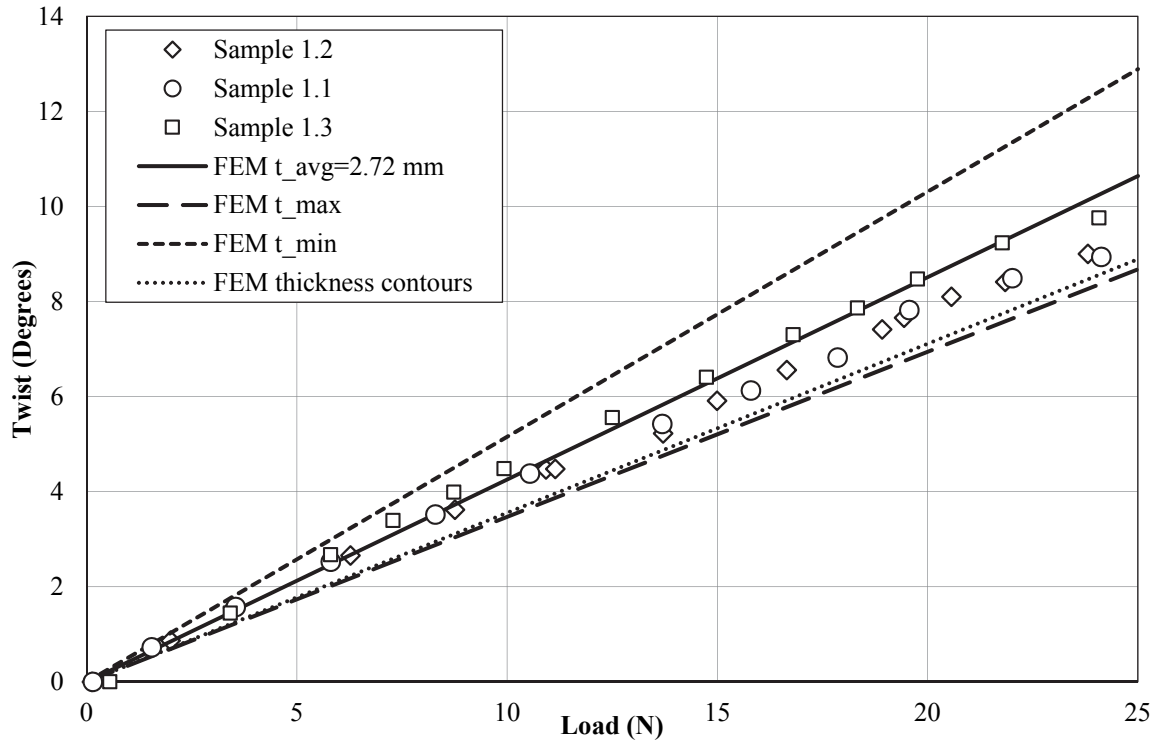
Figure 6-6 Load vs. twist, max, min and mean thicknesses for laminate plates.
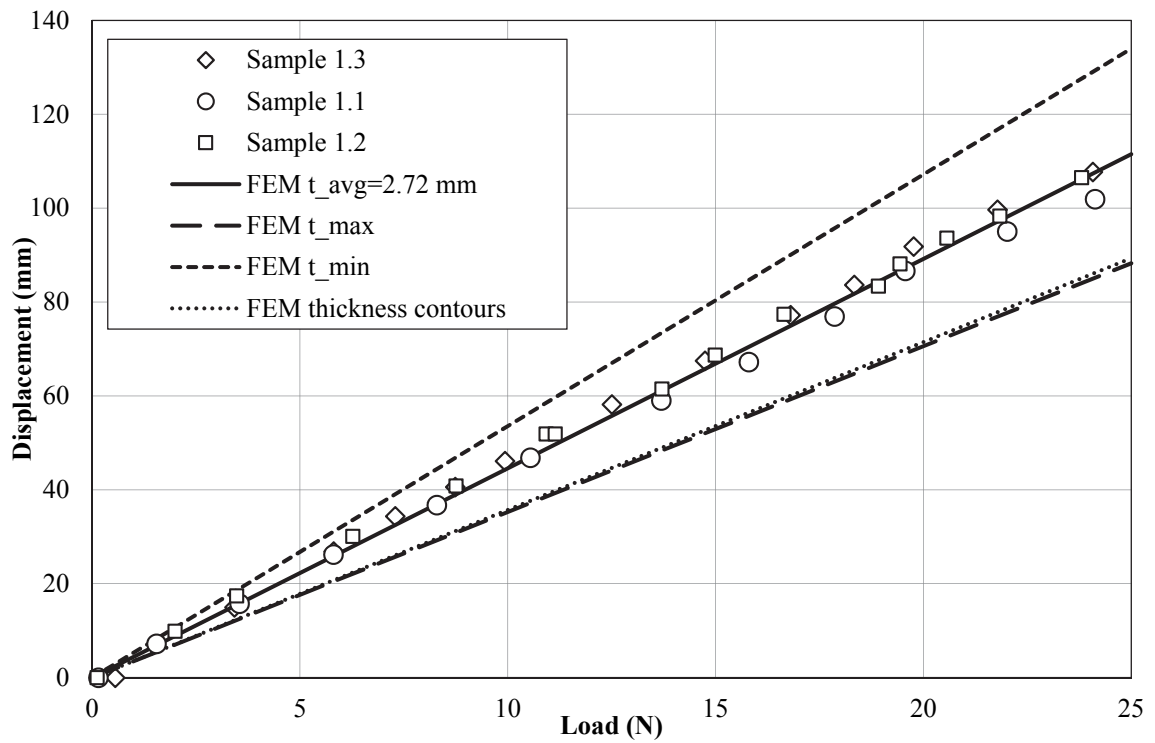

Figure 6-7 Load vs. displacement, max, min and mean thicknesses for laminate plates.

The experimental results fell between the maximum and minimum thickness FEM results, with the average thickness predicting the twist and displacement well. From the above results, the bending and twisting deformation were largely influenced by the laminate thickness. For example, a 6.6% difference in the FEM thickness resulted in roughly a 20% change in both the bending displacement and the induced twist. Such a variation in deformation would undoubtedly affect the overall performance of the structure.

The average thickness for each of the three test samples also varied slightly between samples, which is thought to account for the slight differences in twist and bending response for each of the three samples. Modeling the average thicknesses therefore gave an acceptable range for matching experimental data. It was found that including the detailed thickness contours did not add to the level of accuracy of the FEM, in fact, the FEM with the detailed contours better matched the response predicted by the FEM with the maximum uniform thickness (*i.e.* less displacement than the plate with average uniform thickness). It is thought that this was due to the location of the maximum thickness contours. The greatest thickness was oriented diagonally across the outer half of the plate, as shown in Figure 4-7, which may have resulted in the most resistance to bending at the in the outer part of the plate, where the most bending and twisting occurs.

The laminate plate displacement was also found to be sensitive to the ply angles. Figure 6-8 and Figure 6-9 show the FEM sensitivity to variations of ± 5% from the specified laminate fiber angles.

The FEM bending displacement was sensitive to increases in the ply angles, with smaller angles resulting in less bending. For example, there was an average 6% increase in bending with a 5% increase in ply angles, and an average 6% decrease in bending with a 5% decrease in ply angles, at maximum load. However, the twisting deformation was not as sensitive to changes in ply angles, with a slight increase in twist (0.6%) with increasing ply angles, and slight decrease in twist (1%) with decreasing ply angles. Since the FEM model slightly over predicted the experimental twisting deformation but accurately predicted the bending displacement, these results are not likely attributed to variations in the specified ply angles.
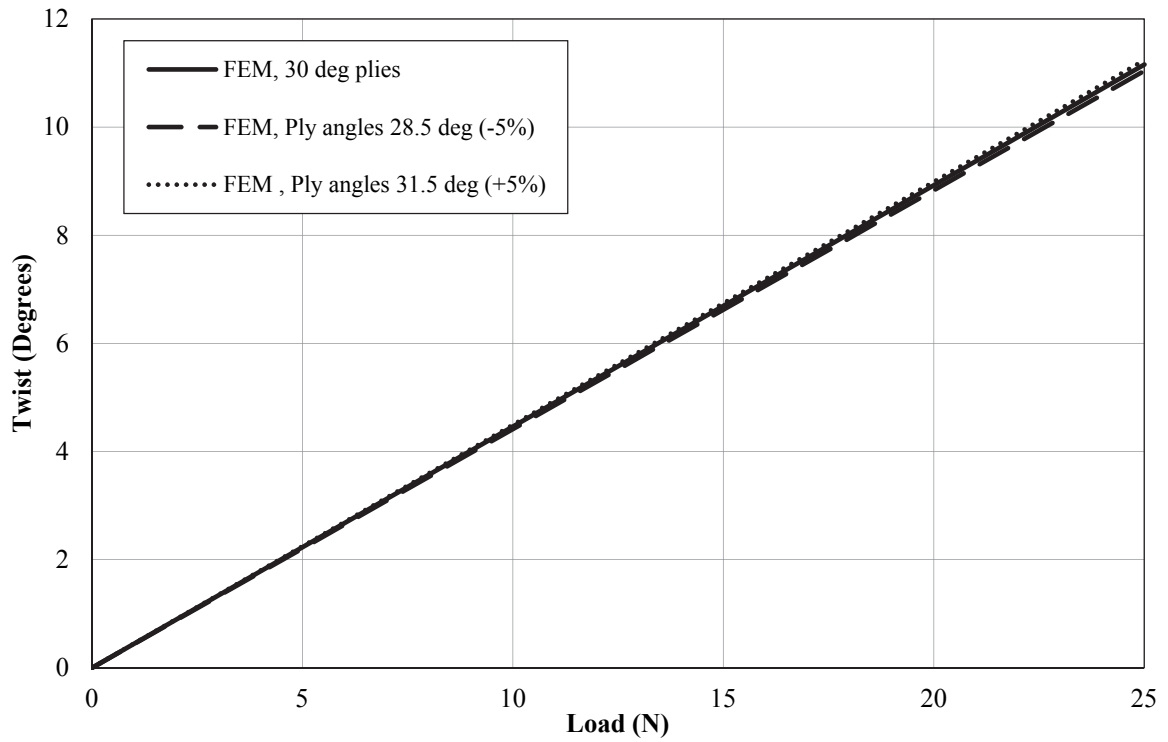
Figure 6-8 Load vs. twist, varying ply angles for laminate plates.
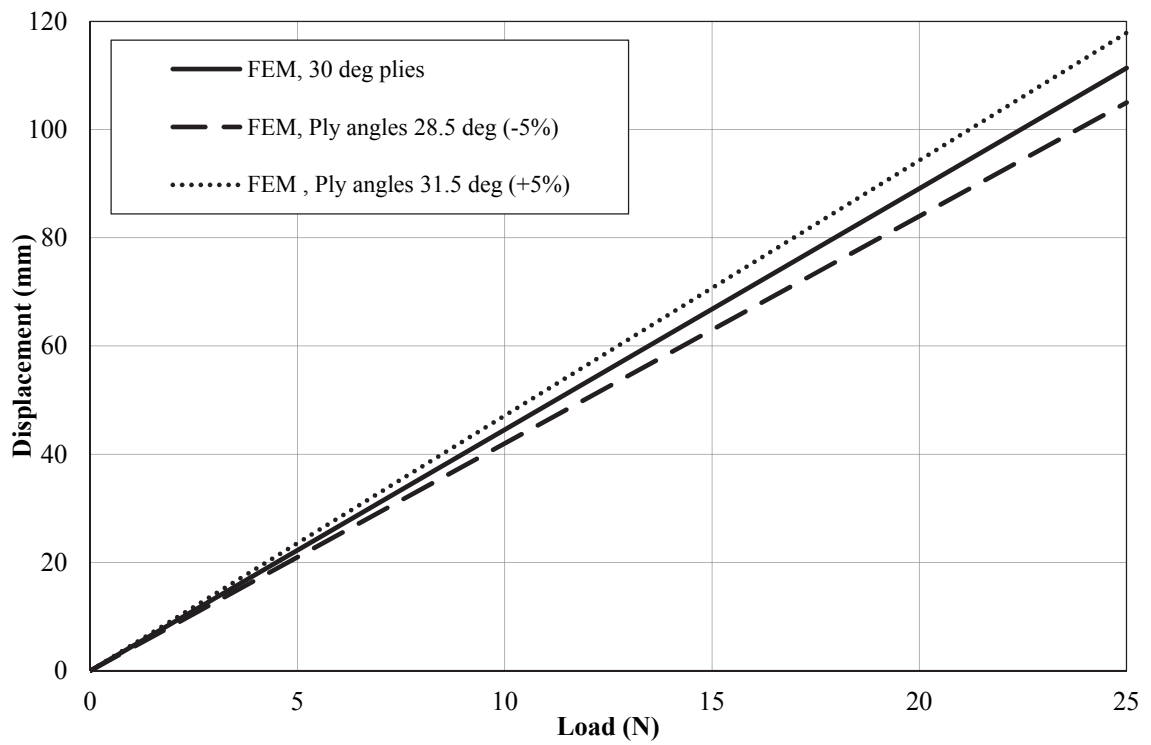
Figure 6-9 Load vs. displacement, varying ply angles for laminate plates.

143

These results indicate the importance of considering uncertainty in the materials and layups of composite structures, since a 5% variation in ply angles resulting in up to 6% variation in bending could have a significant effect on the performance of subsea components, and is therefore an important consideration for developers.

6.1.5 Design Study: Laminate Plate

The FEM was verified experimentally in Section 6.1.3 and considered suitable to be used for design studies. Using the design of experiment (DOE) functionality in Hyperstudy, a number of design curves were created to be used in the selection of ply angles to maximize twist and minimize stress in a composite BT structure. Initially, results were explored for all possible combinations of ply angles for a three layer laminate, each layer fixed at 0.906 mm thick (with the total thickness of 2.72 mm corresponding to the experimentally testes plates), however, it was decided that the middle layer should have a 0° fiber orientation. This reduced the possible design choices to a reasonable number which are displayed in the form of design curves in Figure 6-10, Figure 6-11 and Figure 6-12.
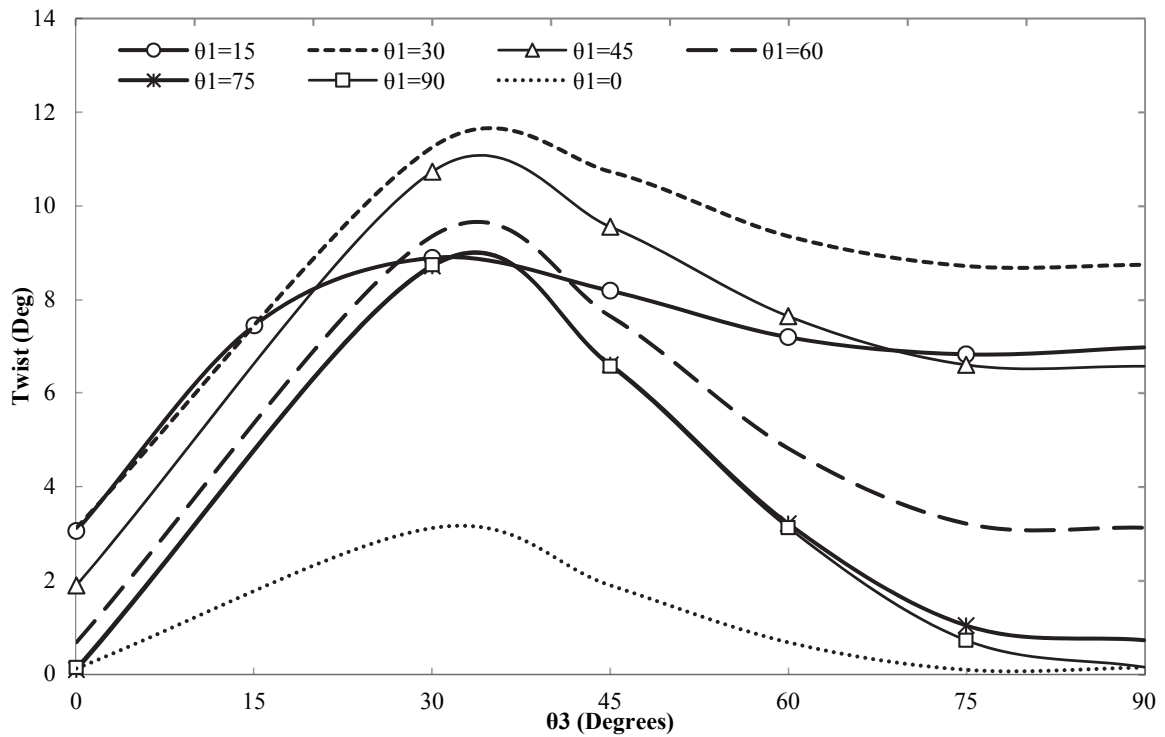
Figure 6-10   Design curves for θ_1 and θ_3 with resulting twist angle (with $\theta_2 = 0°$) for laminate plates.
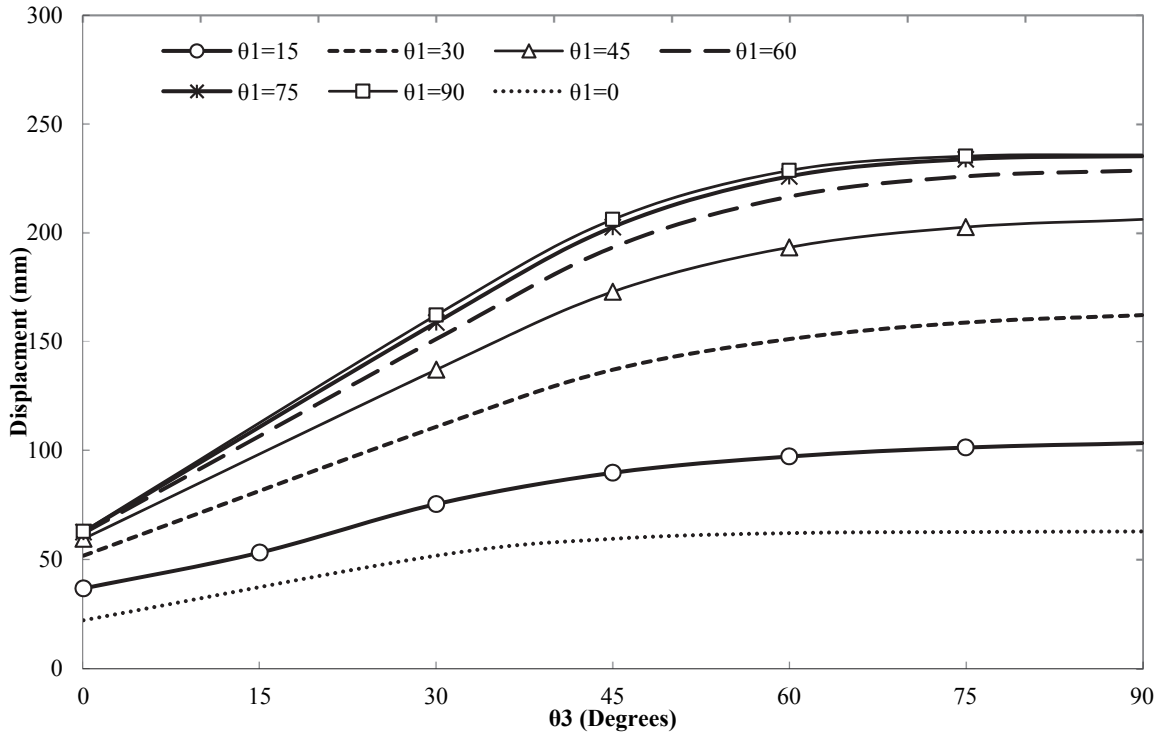
Figure 6-11 Design curves for θ₁ and θ₃ with maximum bending displacement (with θ₂ = 0°).
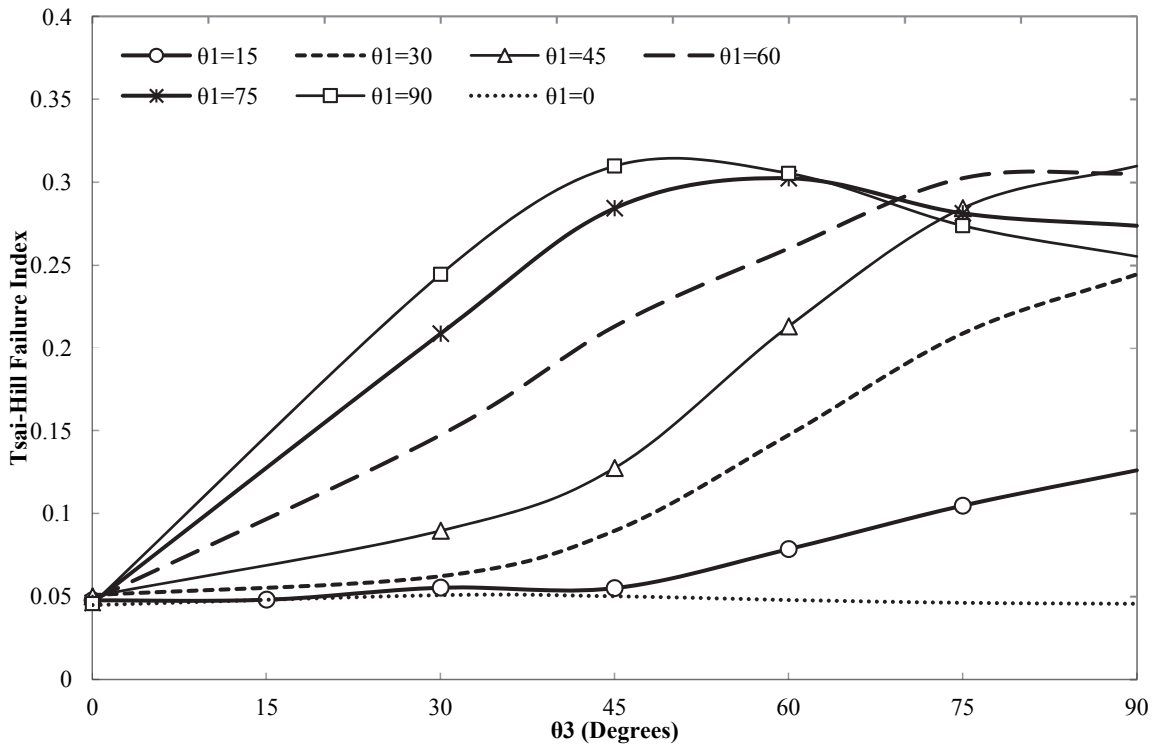
Figure 6-12 Design curves for θ₁ and θ₃ with maximum value of Tsai-Hill failure index (with θ₂ = 0°).

Figure 6-10 shows the tip twist of the plate, Figure 6-11 shows the maximum bending displacement of the plate, and Figure 6-12 shows the Tsai-Hill failure index, all as a function of the composite layup angles for an applied load of 25 N. The design curves predict the twist in the plate to be maximized for angles of θ_1 and θ_3 between 30° and 45°. These results qualitatively correspond with the trends shown in Figure 6-8. From Figure 6-11, the maximum bending displacement was predicted to occur for ply angles of 90°, decreasing with decreasing ply angles. This is a result of the higher elasticity in the transverse material direction compared to the longitudinal direction.

The maximum value of the Tsai-Hill failure index (which is the inverse of the SF and an indication of failure occurrence) was found to be largest for ply angles that resulted in the most bending displacement, as shown in Figure 6-12. For example, although 30° plies result in the most twist, they only result in moderate displacement, and have a lower failure index compared to 45° plies, which have slightly less twist but more bending displacement. This is because the transverse tensile stress in the laminate increases more with increased bending than it does with increased twisting. For example, the maximum tensile transverse stress in the plate with maximized twisting was 7.8 GPa, whereas the maximum transverse tensile stress in the plate with maximized bending was 20.2 GPa. This also indicates the dominance of the tensile transverse stress in laminate failure.

A similar study was done to investigate the influence of ply thickness. With the ply angles held constant at [45°, 0º, and 45°], the thickness was varied from 0 (no layer) to 2 mm for each layer in step sizes of 0.25 mm. The maximum twist was found to occur with the fewest number of layers (*i.e.* two of the layers having zero thickness means that the plate has only one laminate layer), as predicted by the analytical model. As well, as the total laminate thickness decreases, the amount of twist increases, however, the bending displacement and maximum stress in the plate increase as well. Therefore, there is a clear balance between layer thickness, allowable stress, and BT coupling.

6.1.6 Analytical Model: Classical Laminate Theory (CLT)

For BT composite structures such as turbine blades and propellers, the BT coupling effects are paramount, since the amount of local pitch angle change (induced twist) is directly

related to performance and load reduction. The two primary factors that influence the deformation coupling effects are the material properties and lamination schemes (thickness and angle of plies) [128]. To gain insight into the conceptual design of a BT coupled structure and for qualitative verification of the DOE results, an analytical model was used to study the influence of these parameters on the twist response.

A laminate with non-zero ply angles exhibits BT coupling with a certain twisting curvature, or mid-plane curvature, according to Classical Laminate Theory (CLT) [215]. Appendix A provides the details of the application of CLT for this problem. The mid-plane curvature is an indication of the amount of twist (or BT coupling for a structure loaded in pure bending) at the mid-plane of the laminate as a result of loading. In this case, the plate is subjected to a bending moment in the *x-x* direction, and the twisting curvature of interest is in the *x-y* plane. The twist induced by the deformation coupling of the composite laminate, k_{xy} in units (1/m), states how the *x*-direction mid-plane slope changes with *y* (or how the *y*-direction slope changes with *x*), and is therefore the parameter of interest.

Based on the assumptions of CLT, no transverse shear strain components are considered. In this case it is also assumed that the maximum stress is less than the yield stress of the material, and hence no failure is assumed. Although CLT provides a sound initial prediction for a BT coupled structure, these assumptions are limiting. For example, large shear deformations are neglected by CLT [254], and through thickness stresses are neglecting, limiting the applicability to thin composite structures.

6.1.6.A.   *Analytical Model Results*

The analytical model was run with an increasing number of alternating ply layers, each layer taking angles of θ and $-\theta$, as was done by Liu and Young in [128]. For example, a laminate with three layers will have a layup of $[\theta, -\theta, \theta]$, where θ ranges from 0 to 90° in step sizes of 5°.

In the case of alternating [+/-] ply layers, to induce BT coupling, the number of ply layers must be odd, as an even number of layers will result in a net-zero fiber angle and no anisotropy. The most twist occurs for a laminate with the fewest number of layers, because with an increasing number of layers, the degree of anisotropy decreases, which decreases

the BT coupling [128]. Although the most twist occurs in the sample with the smallest number of layers, and the inter-laminar shear strength has been shown to decrease with increasing number of layers [255], it is desirable to have layers with varying angles to support loads in different directions, which requires the laminate to have more than one layer. Furthermore, off axis plies tend to try to straighten out, causing high strain levels in the matrix material, where matrix cracking has to be sustained by supporting fibers in the loading direction. Therefore, the remaining analytical studies were performed for a three layer composite laminate with a layup of [θ, -θ, θ], for simplification purposes.

Figure 6-13 shows the effect of the number of layers on twisting curvature k_{xy}. Figure 6-14 shows the results obtained for the twisting curvature as a function of the ply angles for a three-layer laminate with a layup of [θ, -θ, θ].
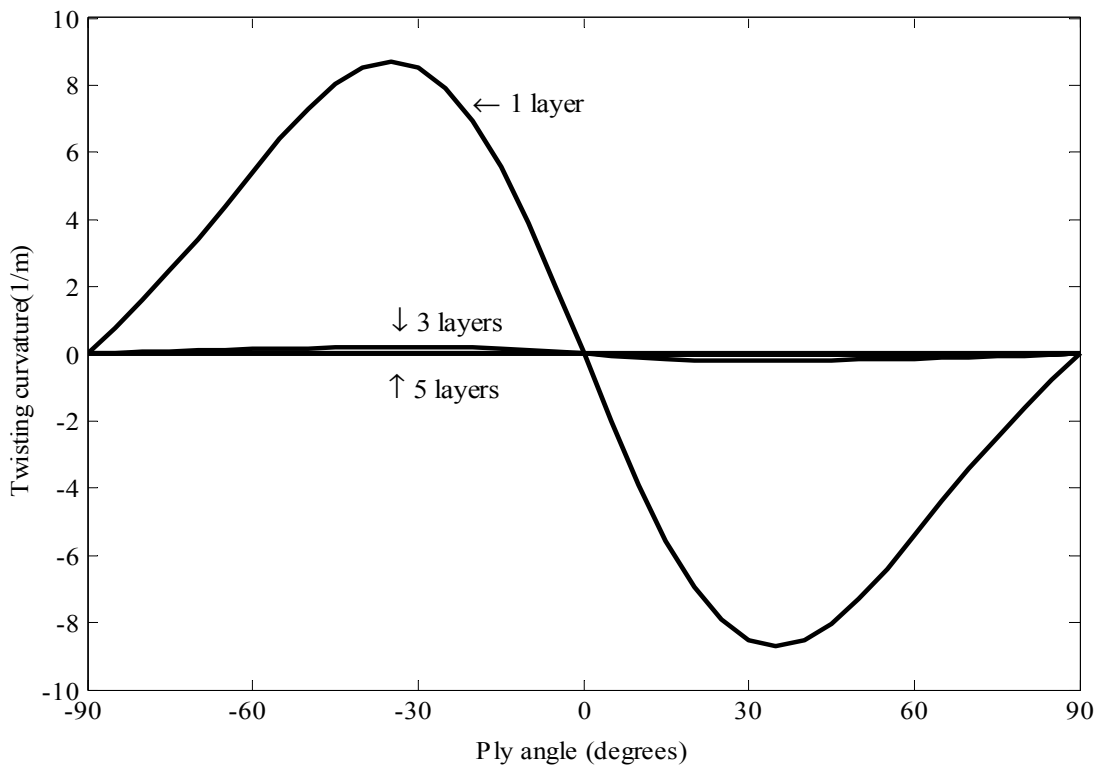
Figure 6-13 Analytical model showing effect of number of layers on twisting curvature, k_{xy}.
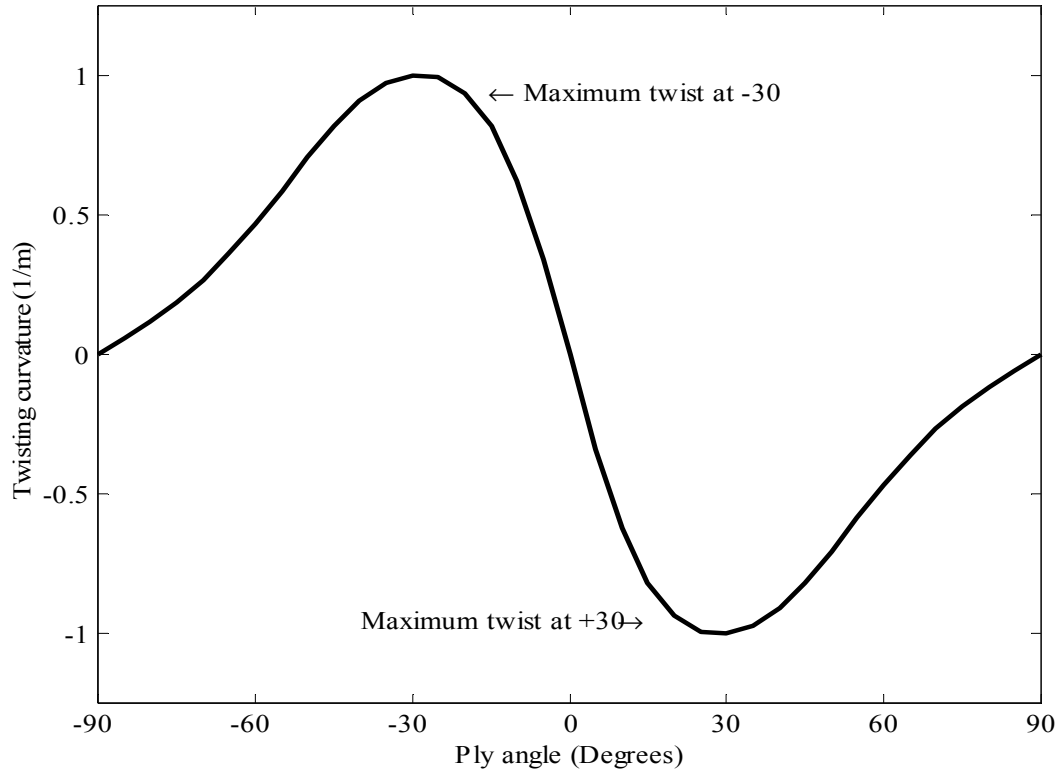
Figure 6-14 Analytical model showing effect of ply angles for a three layer laminate.

This simplified three layer laminate model shows the most twisting curvature to occur at ply angles of $\pm 30°$, which agrees qualitatively with the FEM DOE.

6.2 Composite Blade

The implicit finite element code, Altair Hyperworks RADIOSS® [223], was used to develop a FEM of the 360 mm composite blade previously tested in bending. The geometry and material properties used in this model are outlined in Section 4.2. The blade FEM was verified by the static test results given in Section 4.2 and results of these verifications are presented in this chapter. Ply angles of 26.8º were used for the outer skin, as this was the average for the three blades.

As discussed in Section 4.2, the composite blades had an additional 5 mm length of composite on the TE to allow the composite skins to bond. Including this additional TE length in the geometry for the FEM resulted in a 0.02º (approximately 1.82% at 25 N load) change in twisting deformation and 0.09 mm (approximately 1.8% at 25 N) difference in bending displacement compared to a FEM built using a CAD with the theoretical airfoil

shape. The additional 5 mm TE length was added to the chord lengths given in Table 4-3 for modeling the blade in the BEMT tool.

6.2.1 Model Setup

It was assumed that there was no inter-laminar shear between ply layers, the ply thicknesses were as given by the manufacturer, and there was 0% void content. Tetrahedral 3-D elements were used to mesh the blade core, and COMPG 2-D quadrilateral shell elements were used to model the composite skin of the blade. The ply thickness and fiber angle of the composite blade skin were defined in the HyperLaminate module. It was assumed that no slipping occurred between the blade core and the composite surface, and the interface nodes between the 2-D and 3-D meshes were tied. The circular blade root, including attachments such as bolts and inserts, were not considered in the model as they were assumed to be rigid and not contribute to the BT response of the blade.

Material properties for the blade FEM are given in Table 4-4. An anisotropic constitutive material model, MAT8, was implemented in RADIOSS® to model the composite skin. This material model considers the material properties in the longitudinal (fiber) and transverse (matrix) directions in both tension and compression. Modeling foam materials is more complex, as they exhibit non-linear stress-strain relations after an initial linear deformation period [256], and have properties which are a function of the density [257]. Using the FEM model described in this section, with an isotropic linear elastic material model and a Young's Modulus of 0.02 GPa for the foam, for a maximum tip load of 50 N (twice the maximum applied load during static bending tests), the strain was predicted by the FEM to be 0.006 m/m. Due to the lack of available stress-strain data for this material at the actual manufactured density of 250 kg/m^3, curves for both higher [258] and lower [256] density epoxy foams were referenced. A strain of 0.006 m/m was in the linear range of the stress-strain curve for both the higher and lower density foams (0.27% in the linear range for the higher density foam and 0.81% for the low density foam). Therefore, it was assumed that it would also be in the linear range for the 250 kg/m^3 epoxy foam and was modeled as an isotropic linear elastic material, MAT1.

To estimate the material properties for the 250 kg/m^3 foam, a linear interpolation was done between the higher and lower density epoxy foams. The two materials used for this

calculation had densities of 120 kg/m^3 [256] and 300 kg/m^3 [258], with Young's Modulus' of 0.0045 GPa and 0.0245 GPa, respectively, giving a Young's Modulus for the 250 kg/m^3 foam of 0.018 GPa. It was assumed that the density of the foam was constant over the entire blade.

One simplification to the FEA is the assumption of small deformations, which means that the load direction in the model does not change due to deformations, and all material data is linear for the level of loading in the model. In Hyperworks RADIOSS®, small deformation theory assumes that strains are within the linear elastic range for the material (less than 5% strain), and rotations within the small rotation range (5° rotation). For some blade models, the small deformation assumption is not valid. For example, from a literature review done by Verelst [234], it was concluded that non-linearities due to large blade deflections should be considered in the design of light and flexible wind turbines [234]. However, from the FEM, a 60 N load at the tip of the 360 mm composite blade resulted in approximately 1% strain, making small deformation theory suitable. As the blade is loaded more heavily, it is expected that it would respond non-linearly, however, in the region of loading, it responds linearly with displacement, as shown in Section 4.2.3, hence a linear model was used. As a check, a non-linear quasi-static model was executed for the composite blade with a point load applied over both 1 and 2 load steps (*i.e.* applied all at once, and applied over two time steps), and the results were identical to the linear model results, as shown in Figure 6-15.

As long as the mesh is fine enough and the element size has converged, there should be no difference between first and second order elements, other than the computational time. This was found to be the case for the composite blade, however, the second order element formation took approximately twice as long to execute, and hence first order elements were used.

The usage of thin shell elements can lead to limitations in capturing delamination effects and out-of-plane stresses for thick composite materials, which are important in fracture mechanics [224]. However, for the thin composite material used here, a shell element formulation was chosen for computational efficiency, since through-thickness effects are expected to be negligible due to the small skin thickness.
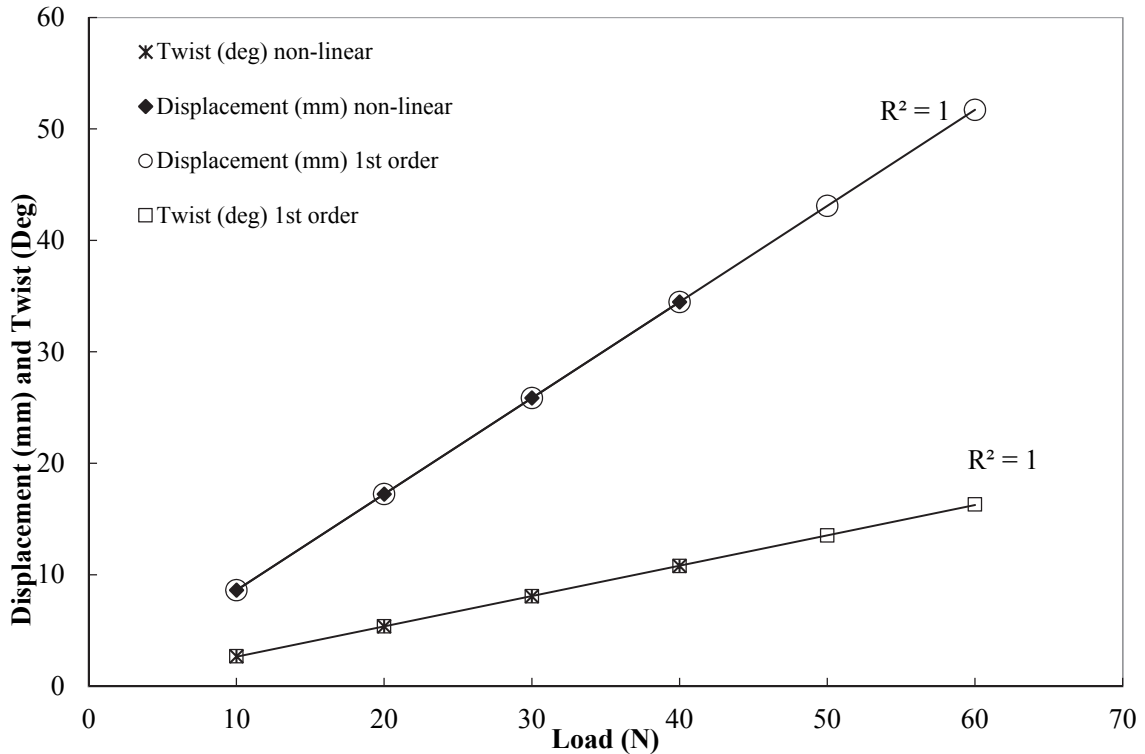
Figure 6-15 Linear and non-linear element formation for BT blade FEM.

6.2.2 Mesh Convergence Study

A mesh convergence study was performed to investigate the sensitivity of the model to element size, and to choose an element size that has good convergence but reasonable computational time. Figure 6-16 shows the computational time for the FEM as a function of the element size. As the element size increases, the computational time decreases approximately exponentially. Figure 6-17 shows the maximum bending displacement of the blade, and Figure 6-18 shows the normal tensile stress at a fixed geometrical location near the root of the blade as a function of element size.

For elements of 2 mm and smaller, the displacement and stress converge to within 1.7%. As the element size increases beyond 4 mm, the results become less stable (over 5% difference in deformation compared to 3 mm elements). However, the model results are not highly sensitive to element size, which means that the designer can have more flexibility over varying element size, to within reasonable bounds.
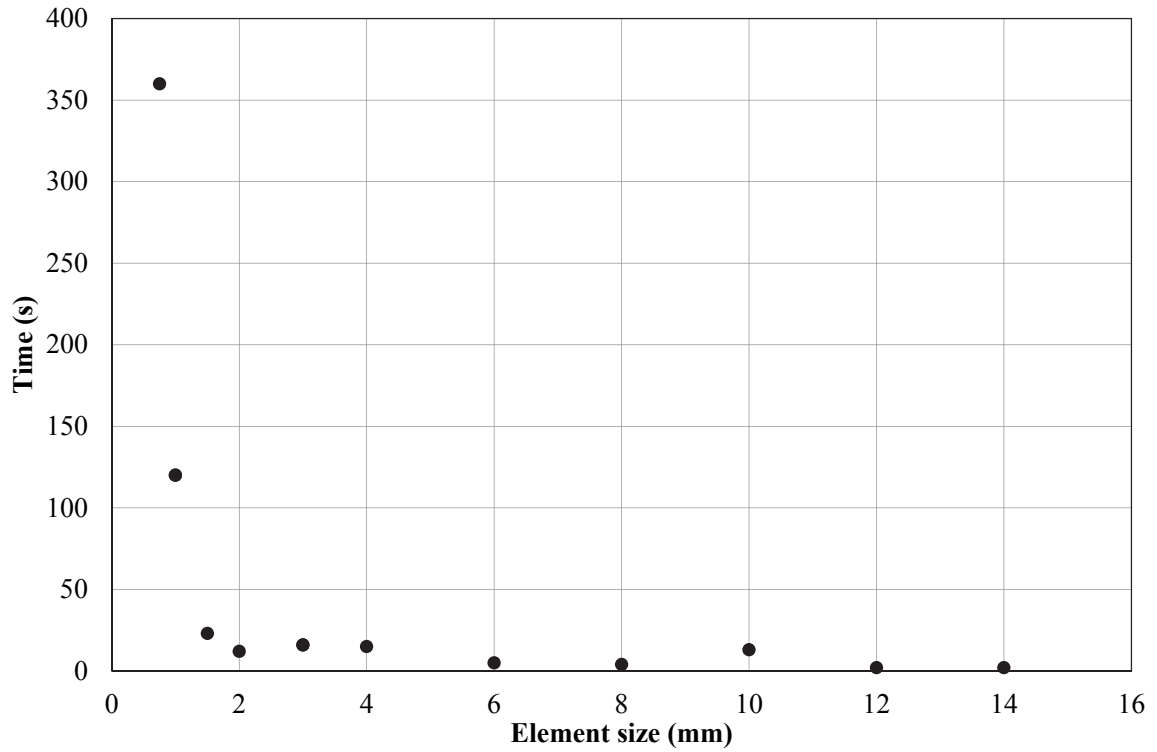
Figure 6-16 Finite element convergence study: Computational time for BT blade FEM.
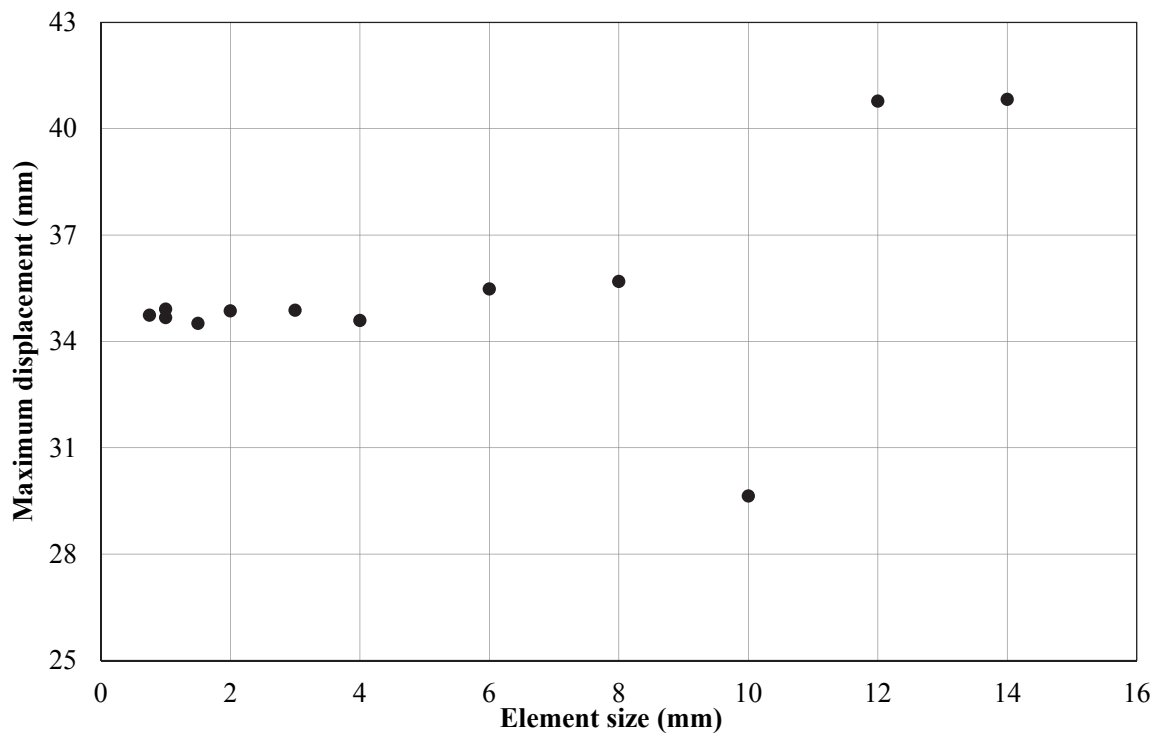
Figure 6-17 Finite element convergence study: Bending displacement for BT blade FEM.
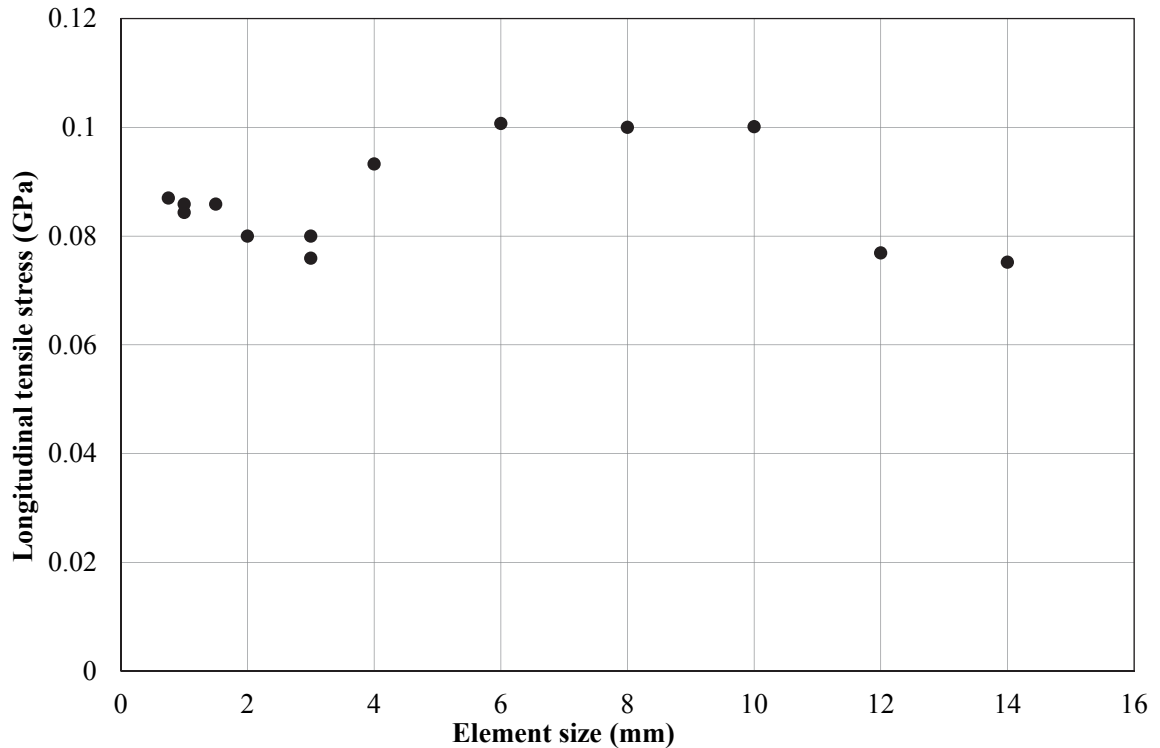
Figure 6-18 Finite element convergence study: Longitudinal tensile stress for BT blade FEM.

The outlying displacement at 10 mm is due to the incorrect node being used to calculate the displacement; the stress at this point had a similar trend to the stress measured for other element sizes. In this case, 1.5 mm elements were chosen, as they require only 23 seconds for the model to run, and show converged results compared to smaller elements. A total of 16,200 2-D shell elements were used, as shown in Figure 6-19.
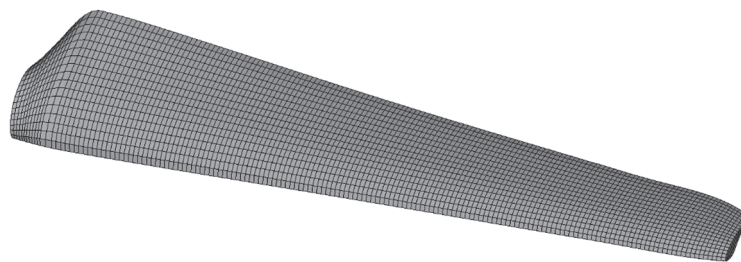
Figure 6-19 BT blade mesh, 1.5 mm 2-D quad elements.

6.2.3 Model Verification

Figure 6-20 and Figure 6-21 show the blade bending displacement and tip twist, respectively, as a function of applied load, and Figure 6-22 shows the FEM displacement of the blade tip for blade 3 with a maximum of 30 N applied point load.
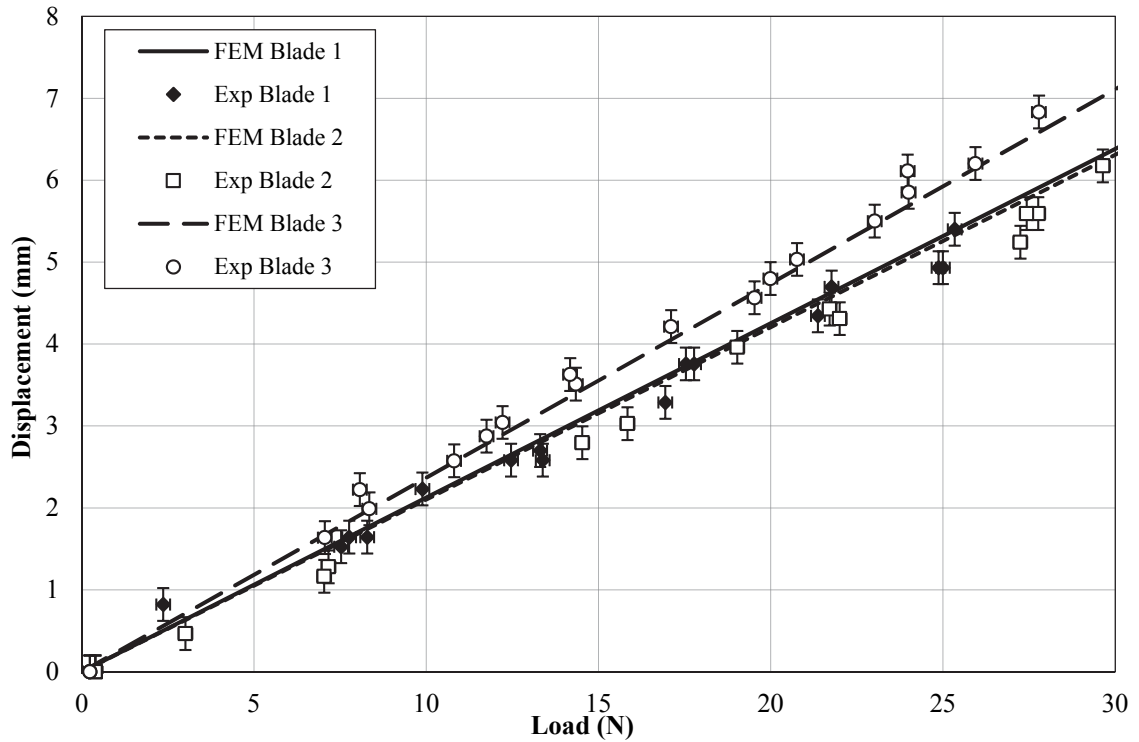
Figure 6-20 Load vs. displacement for composite blades compared to FEM.
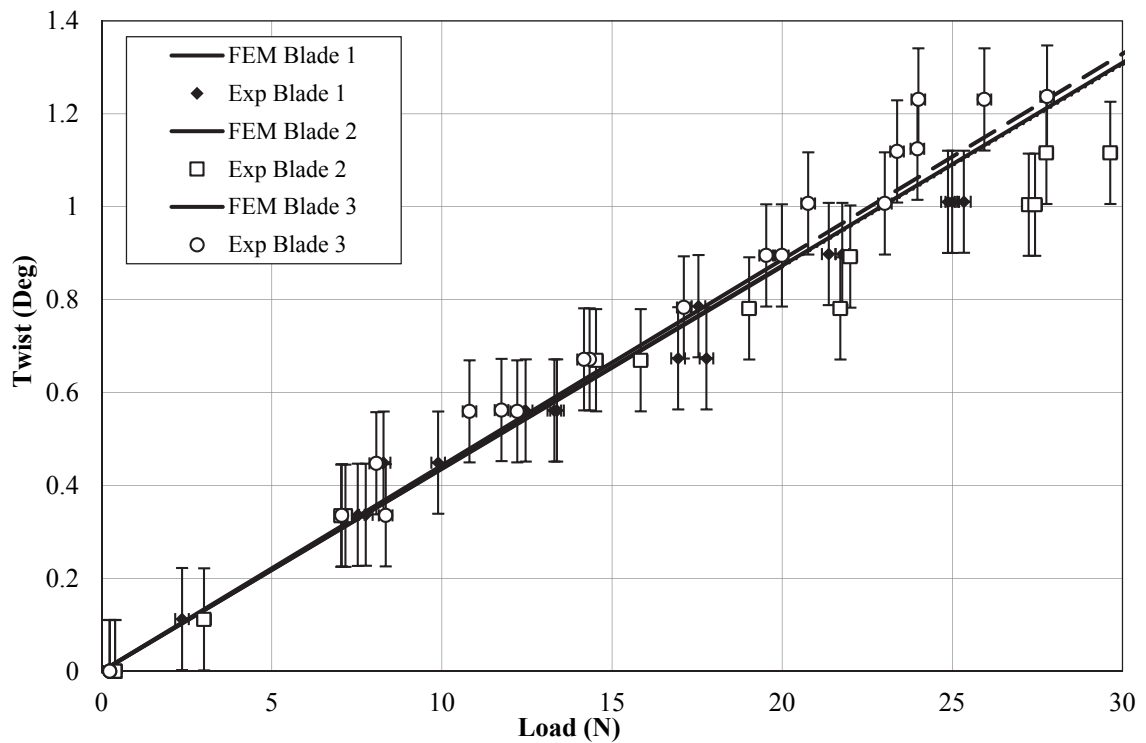
Figure 6-21 Load vs. twisting for composite blades compared to FEM.

Contour Plot
Displacement(Y)
Analysis system
7.39
6.57
5.75
4.92
4.10
3.28
2.46
1.64
0.81
-0.01
No result
Max = 7.39
Min = -0.01
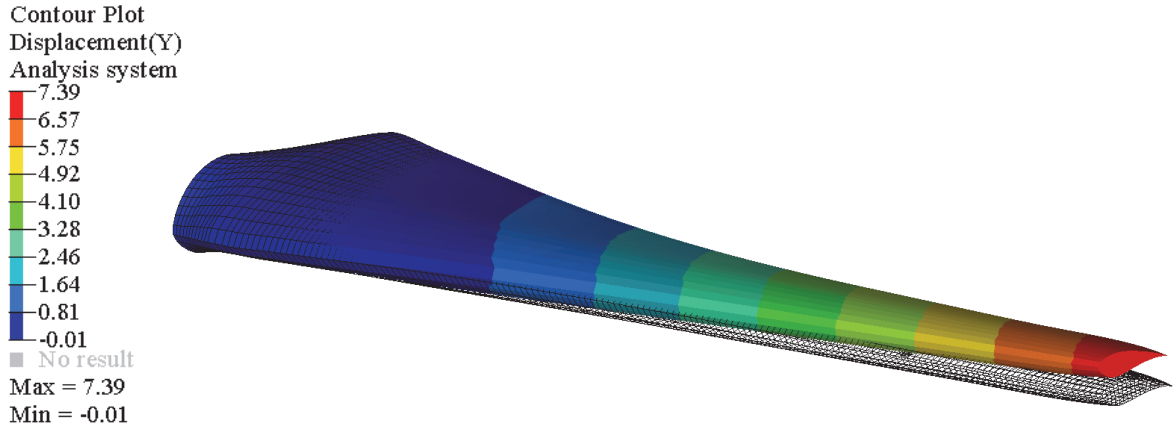
Figure 6-22 FEM tip displacement (in mm), composite blade 3, with 30 N point load.

The displacement shown in the plot is that of the leading edge at the tip of the blade. The bending displacement and tip twist of the composite blade were linear (see discussion in Section 4.2.3) and were in good agreement with the FEM; the FEM predicted the experimental blade bending response to within 5.8% and predicted the blade twisting response to within 10.7%, at maximum load (worst case scenario). The different deformation predictions for each blade were based on the slightly differing ply angles, as discussed in Section 4.2.3, which were included in each FEM.

Due to the small values of twist and the limitations in pixel accuracy (±0.20 mm giving approximately ±0.11° uncertainty), the percent difference between the experiment and FEM was high, however, the agreement between the experiment and FEM bending displacement is considered acceptable. For larger blades, it is expected that the relative uncertainty in such experiments will be decreased as the measured twist values increase.

CHAPTER 7
HYDRODYNAMIC MODEL

A BEMT code, developed for HATTs by Nevalainen [31] in a similar method as Masters and Orme [208], was used to simulate the thrust and torque on a turbine blade. The explanation of the equations behind the BEMT code are discussed in Chapter 3. This code was verified experimentally for rigid blades using several data sets, with results presented in this chapter.

Several correction factors were implemented in the BEMT model. Both Prandtl's tip and hub loss correction factors were applied to account for the vortex shedding reducing the turbine efficiency from both the blade tip and the hub. The Buhl high induction correction was utilized to account for thrust coefficients at values greater than a critical value of the axial induction factor. Finally, the Viterna-Corrigan post stall correction was applied, causing the blade to essentially behave like a 3-D flat plate when fully stalled [212]. A full description and details on these corrections are outlined in Section 3.4.4. This BEMT model was coupled with a FEM to predict the response of a BT blade in Chapter 8.

7.1 Batten and Pinon Verification

An initial verification for the BEMT model developed by Nevalainen [31] was undertaken using two sets of experimental test results: Gaurier *et al.* [192] and Bahaj *et al.* [146]. Airfoil data for these models was obtained using XFOIL [259] at the appropriate Reynolds numbers (as was done by Bahaj *et al.* in [149]). Blade and turbine geometries are given in the respective publications.

Figure 7-1 and Figure 7-2 show C_P and C_T as a function of λ for the Bahaj *et al.* experimental test results and BEMT, and Figure 7-3 shows C_P and C_T as a function of λ for the Gaurier *et al.* experiment and BEMT.
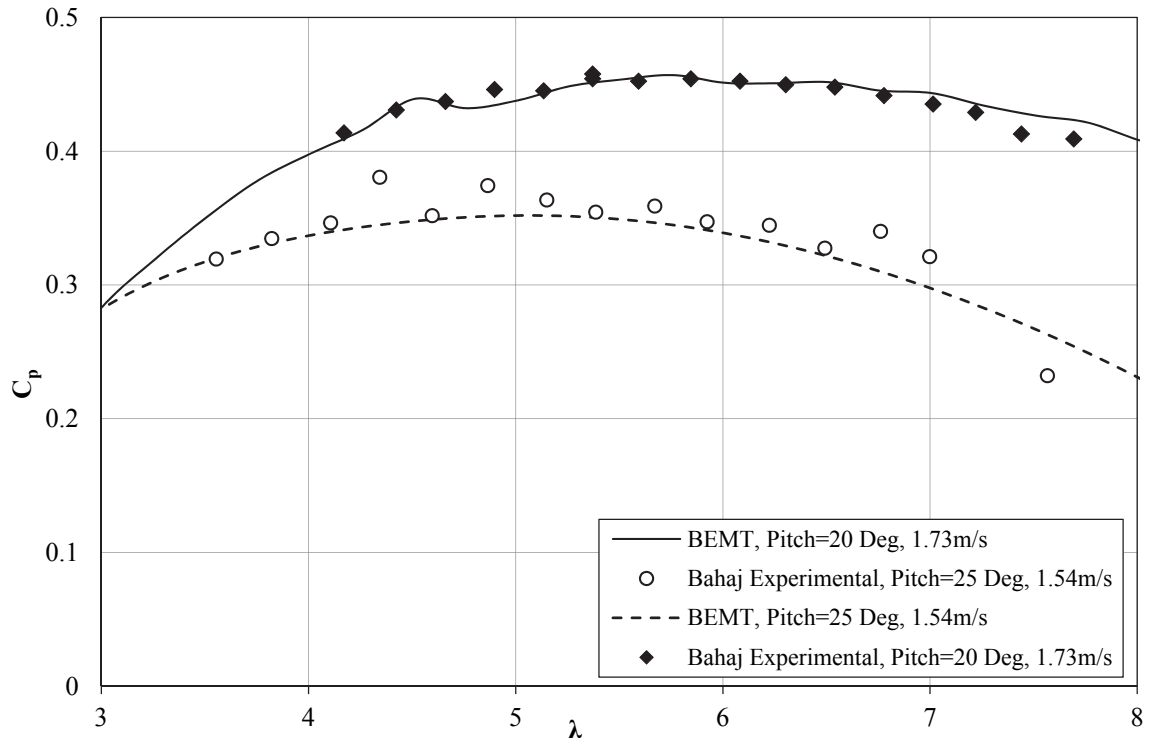
Figure 7-1 $C_p - \lambda$ curves for Bahaj et al. experiment and BEMT.
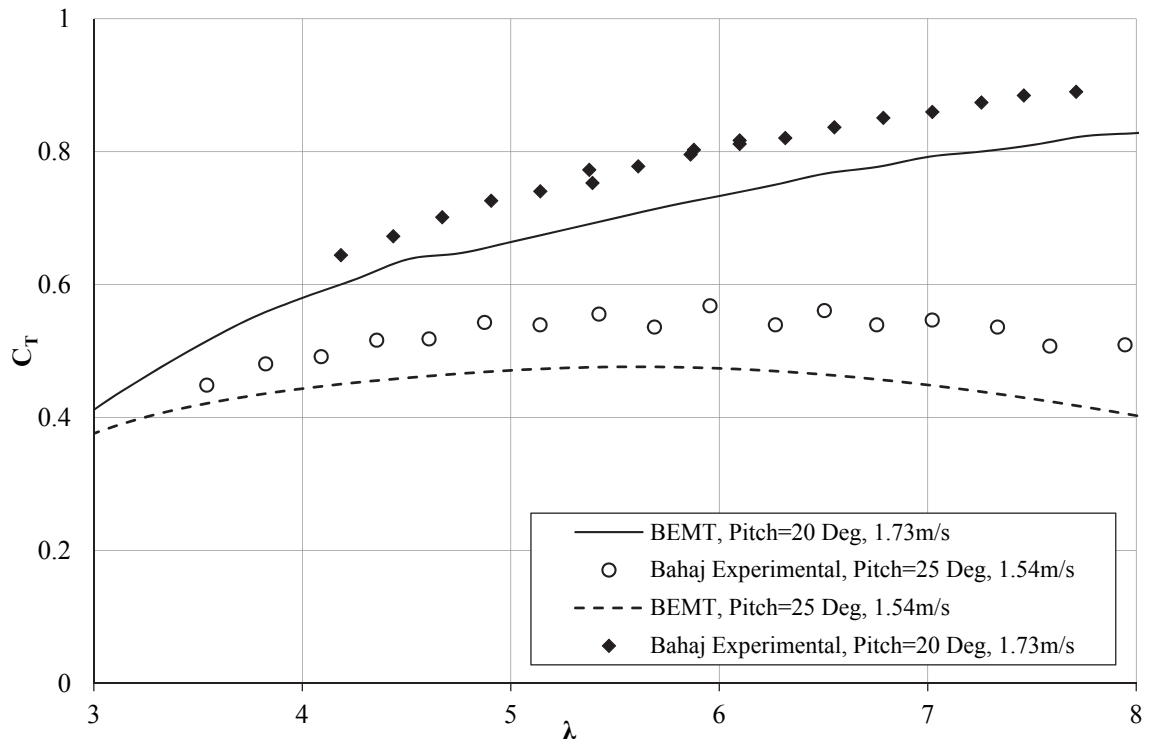
Figure 7-2 $C_T - \lambda$ curves for Bahaj et al. experiment and BEMT.
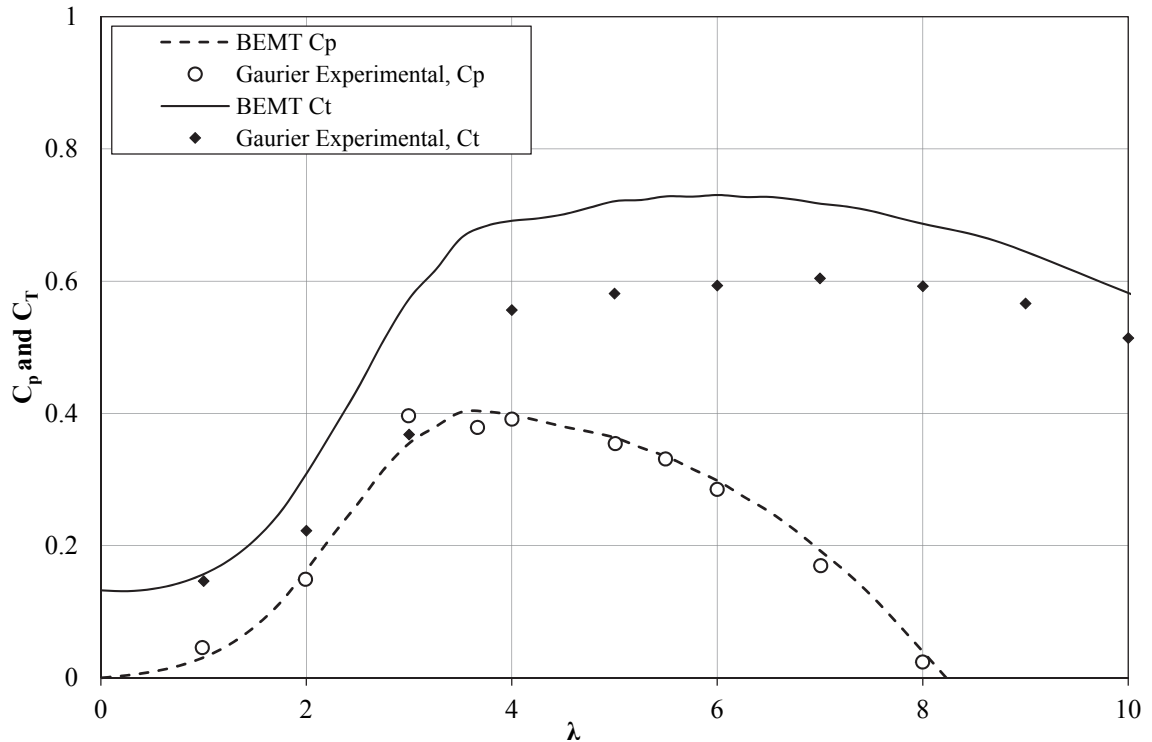
Figure 7-3 $C_p - \lambda$ and $C_T - \lambda$ curves for Gaurier et al. experiment (0.8 ms^{-1} and 5% turbulence) and BEMT results.

Since these models were only run once, computational time was not a significant consideration in the number of elements used, hence, 100 blade elements were used to model both turbine blades. Although a lesser number of elements showed convergence (convergence up to 2% for greater than 10 elements), 100 elements was conservative.

The fluctuations in the BEMT-predicted C_p curve for Bahaj *et al.* with a 20º pitch setting was due to small fluctuations in the XFOIL airfoil data. The BEMT predicted the performance of the Bahaj *et al.* [146] tidal turbine in steady flow conditions well and showed a good match to the Gaurier *et al.* [192] experimental power data. However, the BEMT results over-predicted the Gaurier *et al.* [192] experimental thrust. This discrepancy between the thrust data and the BEMT results was thought to be due to the relatively high turbulence intensity in the IFREMER flume (turbulence intensity of 5%). The steady flow airfoil data used in the BEMT to model this turbine was obtained using XFOIL with an NCRIT value of 5. This means that the airfoil data used in BEMT did not account for the turbulence in the experiment, which could have resulted in differing boundary layer (BL) behavior.

7.2 NREL S814 Verification

This section presents a comparison of the BEMT tool to the rigid blades tested and detailed in Chapter 5 (381 mm rotor radius, 89 mm hub radius, and 292 mm blade length).

7.2.1 Airfoil Data

For the 0.762 m diameter turbine tested during the first set of hydrodynamic tests at the University of Strathclyde the chord-Reynolds number ranged from 7×10^4 to 1.7×10^5 (for the 0.8 m/s to 1.0 m/s tests). Obtaining appropriate airfoil data experimentally at these low Reynolds numbers can be challenging due to the sensitivity of airfoil performance to flow conditions (such as turbulence) and the precise details of the experimental facility used [155, 165]. Typically, airfoil data obtained using computational tools such as XFOIL [259] is used in BEMT codes [21]. However, in this case, experimental airfoil data was used, due to issues numerically predicting the NREL S814 airfoil performance at these Reynolds numbers. At the range of expected Reynolds numbers, computational tools such as XFOIL were unstable and unable to converge on a solution at certain angles of attack. Milne [163] proposed that this is due to the inability of XFOIL to predict the point of laminar separation and turbulent reattachment on both the pressure and suction surfaces of the airfoil. Particularly for thick airfoils, like the 24% thick NREL S814, the inability to accurately model full boundary layer (BL) separation on the pressure surface means that the plateau region in the lift curve and high drag coefficients at low angles of attack are not properly accounted for. On the suction surface, the extent of the drag inducing separation bubble is also not accurately modelled. For this reason, experimentally obtained airfoil data is considered the most appropriate for modeling this airfoil at these low Reynolds numbers.

Milne [163] obtained 2-D NREL S814 airfoil data in a wind tunnel at Reynolds numbers ranging from 8.5×10^4 to 1.5×10^5, and Togneri *et al.* [260] at Swansea University obtained 2-D lift and drag data for the NREL S814 airfoil in a flume at a Reynolds number of 5×10^4. The experimental results presented in Chapter 5 were compared to BEMT predictions using both of these data sets.

7.2.2 Element Convergence Study

A convergence study was done to determine the minimum number of blade elements that produces a converged BEMT solution in minimal computational time. For an inflow velocity of 0.8 m/s, and λ of 4, using the airfoil data from Togneri *et al.* [260], Figure 7-4 and Figure 7-5 show the results of the convergence study.

The torque and thrust converged for more than 20 blade elements, with less < 0.35% difference in thrust between 20 and 100 blade elements. However, there was only a 0.87% difference in thrust results between 10 elements and 100 elements, and a 77% decrease in computational time using 10 blade elements compared to 100 elements. This 0.87% difference was considered to be insignificant, as it correlates to less than 1% difference in torque, which is within the normal measurement error. Therefore, 10 elements were used in the BEMT model.
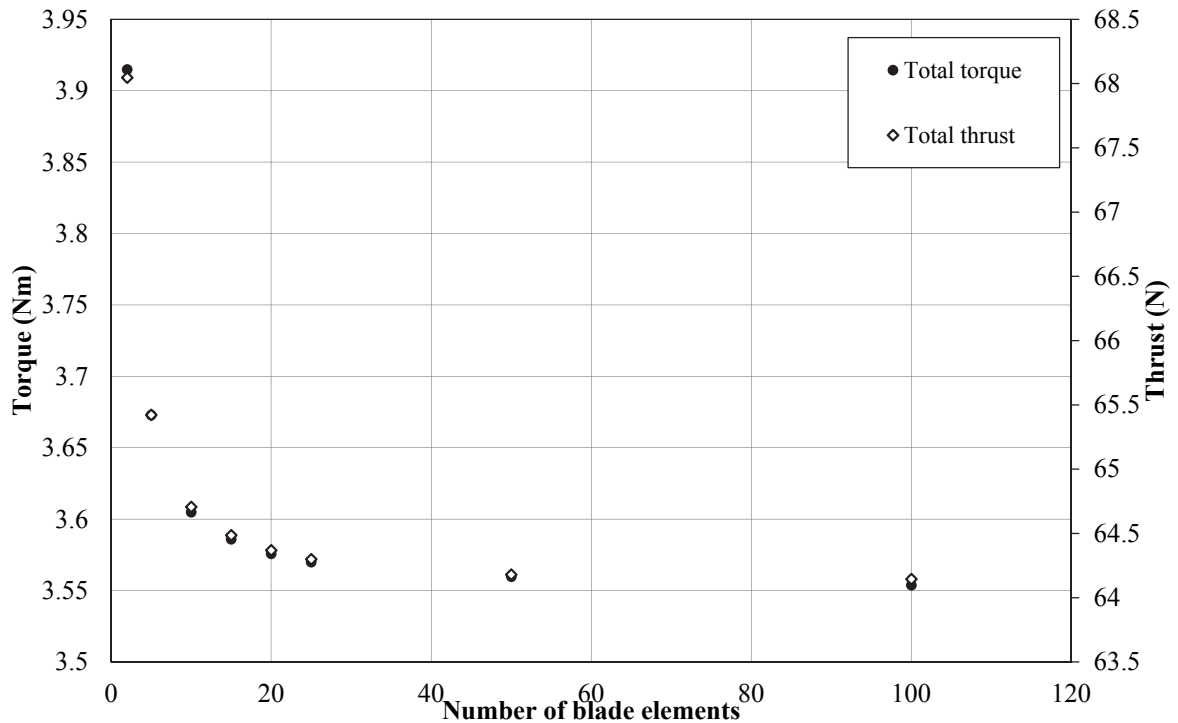
Figure 7-4 Thrust and torque on the turbine rotor as a function of number of blade elements.
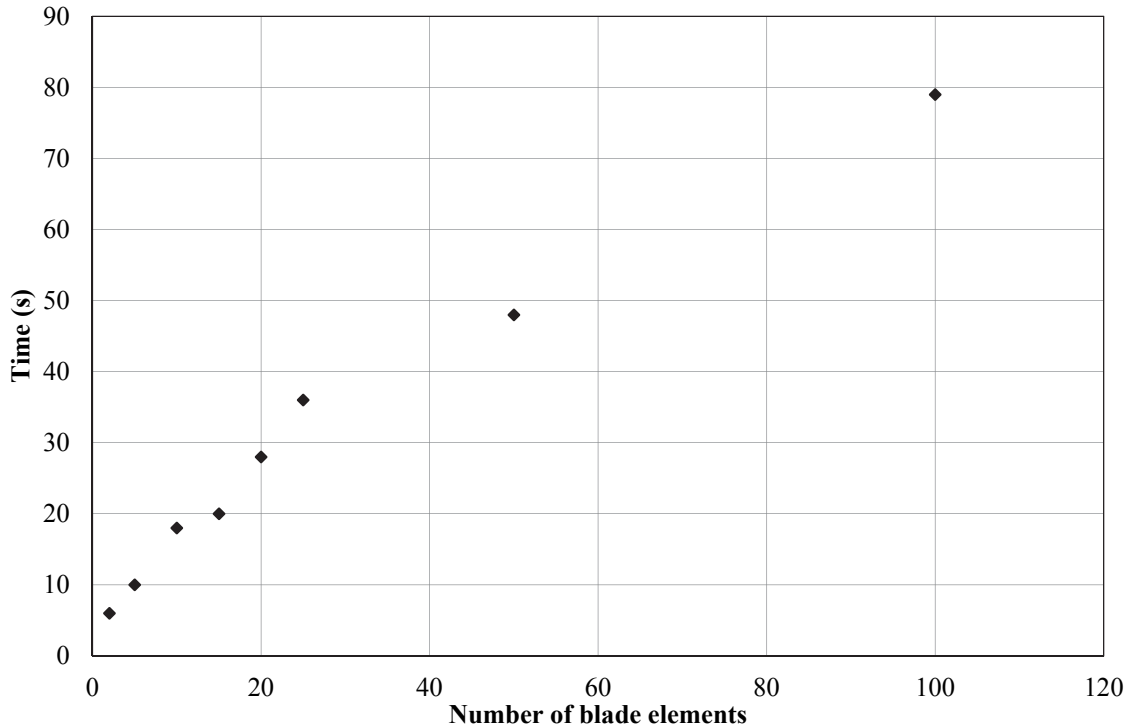
Figure 7-5 Computational time as a function of number of blade elements.

7.2.3   Verification with Milne Airfoil Data

The airfoil data produced experimentally in a wind tunnel by Milne [163] at Reynolds numbers of $8.5{\times}10^4$, $1.05{\times}10^5$, and $1.5{\times}10^5$ was selected for use in the BEMT due to the Reynolds number range that match that of the experiment. For these three discreet Reynolds numbers, the airfoil data spanned a range of α from about -1° to 12°. Wall corrections based on the methodology provided by Rae and Pope [190] for a closed test section were applied to the 2-D section data by Milne, and were included in the data used here. The total uncertainties in the lift and drag coefficients were estimated by Milne to be approximately 0.1% and 1%, respectively [163].

To be used in BEMT, the data had to be extrapolated from -180° to 180° [93]. The preprocessor AIRFOILPREP [261], developed by NREL, was used to extrapolate this data up to α of ±180° using Viterna's method [262]. Because the data were acquired at three discreet Reynolds numbers, the lift and drag coefficients were estimated in BEMT using a linear interpolation.

162

Figure 7-6 and Figure 7-7 show the results of the towing tank tests, with a pitch setting of 28.88° relative to the rotor plane, compared to the BEMT results using the previously mentioned corrections in BEMT. The 0.5 m/s tests were not compared to BEMT, as the airfoil performance was shown in Section 5.1.3 to be greatly degraded.

Although the Milne airfoil data was at the same Reynolds number as the tests, there was a poor match to the experimental data, with the BEMT significantly over-predicting the thrust loads. However, the power measurements were captured reasonable well by the BEMT for $\lambda > 3.5$. The discrete changes in the shape of the curve are due to the linear interpolation between the different airfoil data. Potential reasons for the mismatch between BEMT and experiment using the Milne airfoil data are discussed in following sections.

The wall corrections that were applied by Milne only accounted for a 1.5% decrease in drag coefficient and 2.3% decrease in the lift coefficient, and using the un-corrected data made a negligible difference in the BEMT thrust and power.
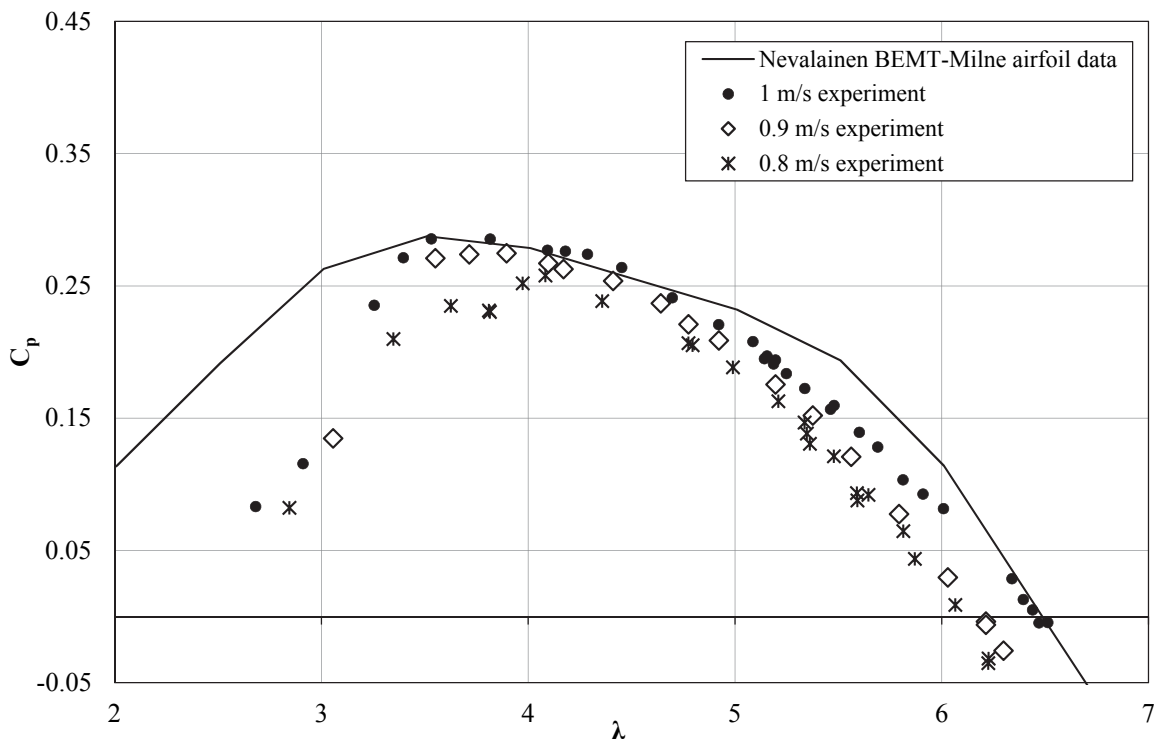
Figure 7-6 $C_p – \lambda$ curve for NREL S814 blades and Nevalainen BEMT, Milne airfoil data.
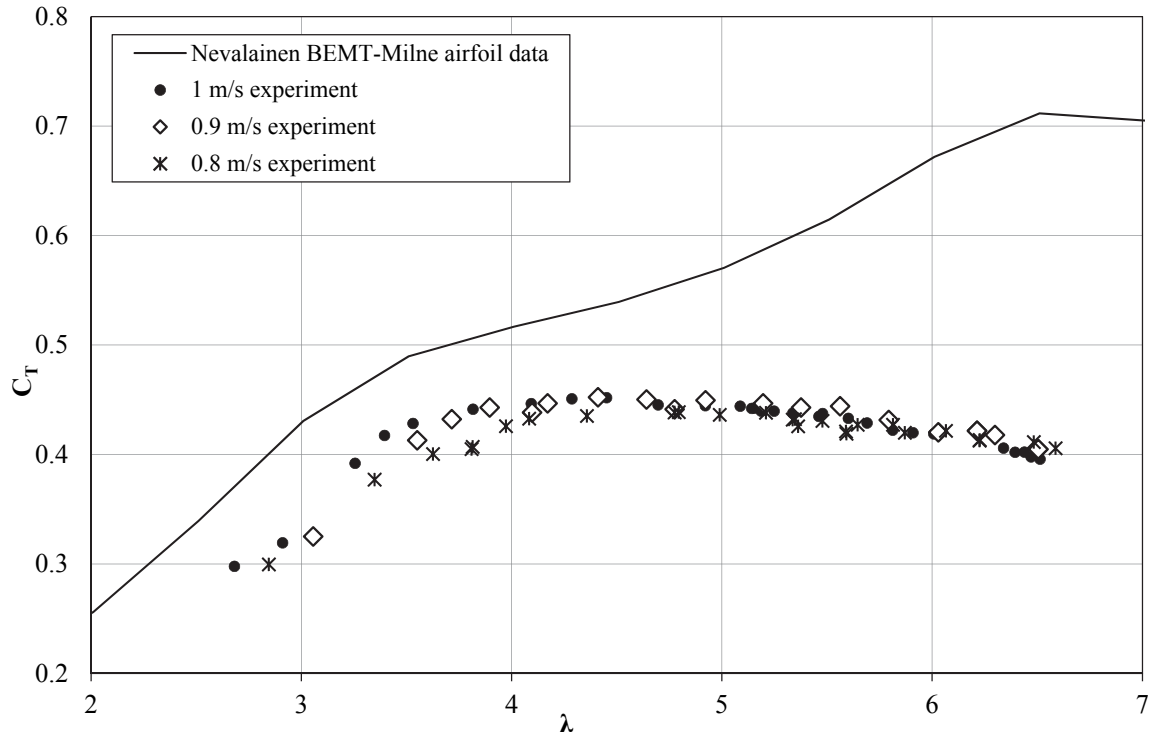
Figure 7-7 $C_t - \lambda$ curve for NREL S814 blades and Nevalainen BEMT, Milne airfoil data.

7.2.4 Alternative Airfoil Data

The following section outlines an alternative airfoil data set which has been trialed in the BEMT code and found to give a better match to the experiment. Togneri *et al.*, at Swansea University [260], performed tests on the same NREL S814 airfoil in a flume at a Reynolds number of 5×10^4. Figure 7-8 and Figure 7-9 shows the airfoil data from Milne [163] compared to Togneri *et al.* [260].

The Togneri *et al.* lift data was generally lower than the Milne lift and the Togneri *et al.* drag varied from Milne, depending on the Reynolds number. In the range of α tested by Milne, the average percent difference between the 8.5×10^4 Milne data and the 5×10^4 Togneri *et al.* data was 30% for lift and 25% for drag.
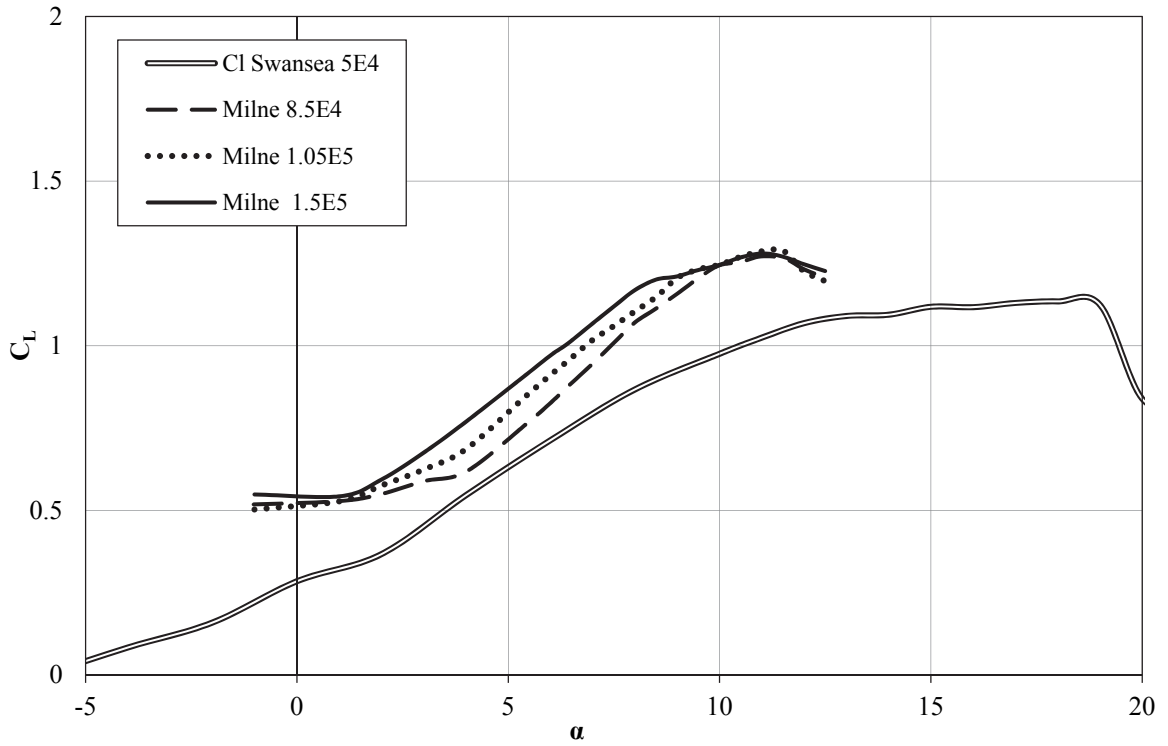
Figure 7-8 Togneri et al. *flume lift data at 5×10⁴ [260] and Milne data from wind tunnel [163].*
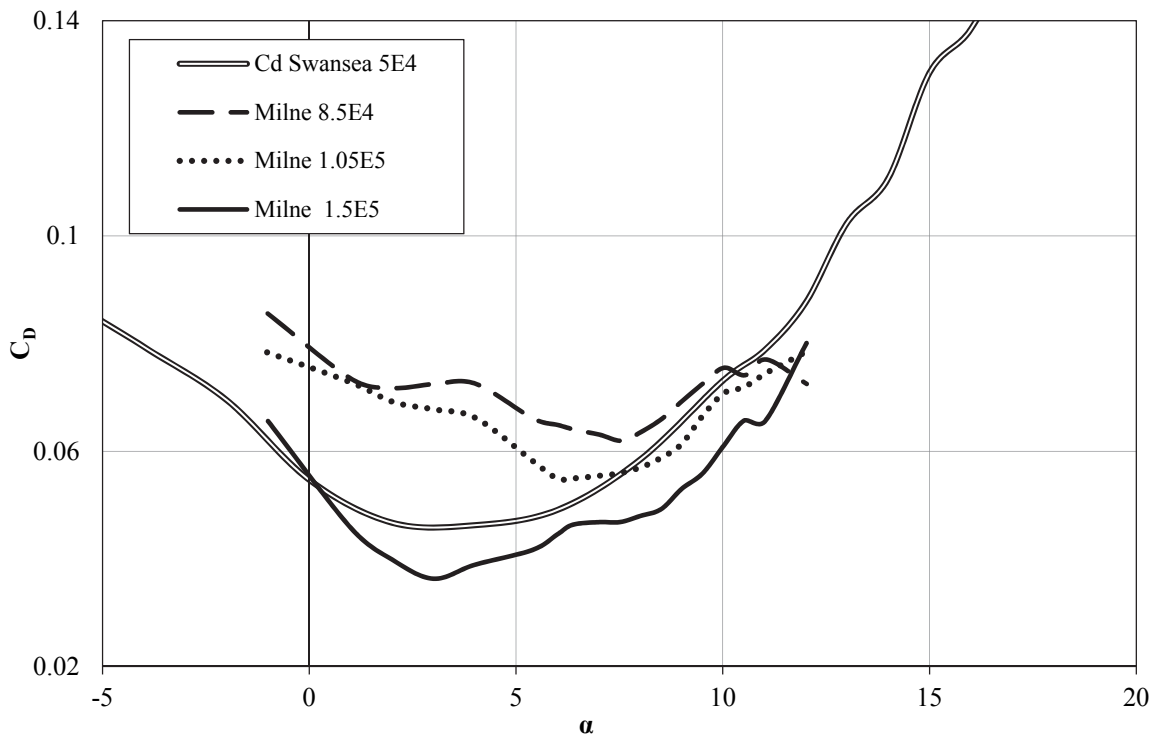
Figure 7-9 Togneri et al. *flume drag data at 5×10⁴ [260] and Milne data from wind tunnel [163].*

It is not unexpected that these two data sets are different [155]. Mueller stated that because the forces, pressure differences and velocities are small in small-scale tests, a great deal of care must be exercised to obtain accurate and meaningful data at low Reynolds numbers, and therefore it is not surprising that similar experiments on the same geometry model at low Reynolds numbers often produce results which differ from one wind tunnel to the next [165, 263]. Lissaman stated that test data in the low-Reynolds-number range have long been regarded with skepticism, because there is a substantial record of non-repeatability of data from tests in different facilities. Even in modern wind-tunnel test facilities with advanced instrumentation and airflows of turbulence levels lower than 0.1%, striking differences in airfoil performance have been reported, particularly near the critical Reynolds number of about 7×10^4, which was postulated to be due to span-wise flow variations [155]. The following section outlines potential reasons for the differences between these airfoil data sets.

The lower lift of the Togneri *et al.* data is expected since, as discussed, at lower Reynolds numbers lift can be degraded. However, the drag as measured by Togneri *et al.* in the flume is lower than that measured by Milne in the wind tunnel at higher Reynolds numbers. This is counter to what is expected; the lower Reynolds number Togneri *et al.* data would be expected to have higher drag than the Milne data if the flow regimes were the same other than the differing Reynolds numbers. Therefore, the differences between the Togneri *et al.* airfoil data and Milne data are thought to be due to more than just the differences in Reynolds number (turbulence intensity, turbulence length scale *etc.*).

The flume at Togneri *et al.* was measured to have a turbulence intensity of 5 to 9%, which was found to be non-uniform through the depth, with areas in the flume where turbulence was as low as 2.3%. This is significantly higher than the turbulence intensity of 0.17 to 0.6% from the wind tunnel Milne tested in, but was typical of a flume [264]. Along with Reynolds number effects, turbulence intensity differences could have contributed to differences between the Togneri *et al.* and Milne airfoil data. Research has demonstrated a sensitivity of turbine performance to turbulence [265]; Mueller attributed differences in airfoil tests performed at the same Reynolds number in a water tunnel (flume) and a wind tunnel to differences in the turbulence intensity [184].

For airfoils with significant surface curvature operating in a particular flow regime, BL separation can occur on the pressure surface as well as the suction surface. Pressure surface BL separation has the effect of significantly reducing the suction pressures on the pressure (lower) surface of the airfoil, similarly to the reduced suction (lift) observed with BL separation on the suction (upper) surface. Suction on the lower surface of the airfoil acts against the lift force generated on the upper airfoil surface, therefore, reduced suction on the lower surface means a higher net lift force. Milne's pressure measurements from the wind tunnel tests showed BL separation occurring on both the suction and pressure surfaces of the airfoil, which he stated was evident by the plateau in the lift curve shown in Figure 7-8 around $\alpha = 0°$ [163]. However, the Togneri *et al.* data showed a more linear decrease in lift with decreasing α, indicating that the higher turbulence intensity in the Togneri *et al.* tests may have given the BL enough energy to overcome the adverse pressure gradient and not separate on the pressure surface. This could have also led to the relatively low drag measured at Togneri *et al.*. The lower Reynolds number Togneri *et al.* data also showed different stall characteristics, stalling at α of 18° compared to 11° for Milne, which is also consistent with a higher turbulence intensity delaying BL separation. This highlights the extreme sensitivity of the BL and airfoil performance to flow conditions.

Finally, Milne's airfoil data was only collected for α ranging from -2 to 12°, and therefore AIRFOILPREP was used to extrapolate this data, adding uncertainty to the wider range of lift and drag data used in BEMT. The Togneri *et al.* data was collected for the full range of possible α, eliminating the requirement to extrapolate the data.

7.2.5 Verification with Togneri *et al.* Airfoil Data

Using the Togneri *et al.* airfoil data in the BEMT, with the inclusion of the correction factors previously mentioned, Figure 7-10 and Figure 7-11 show the results of the towing tank tests with a pitch setting of 28.88°, compared to the BEMT results.
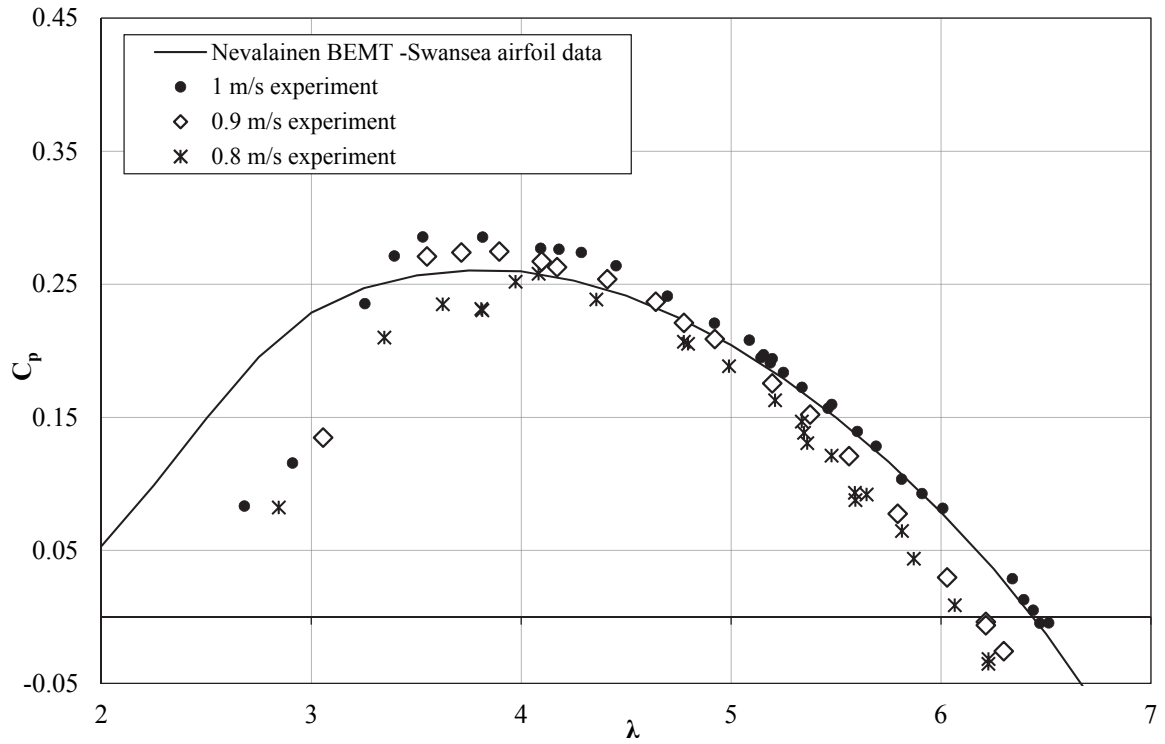
Figure 7-10 C_p–λ curve for NREL S814 blades and Nevalainen BEMT, Togneri et al. *airfoil data.*
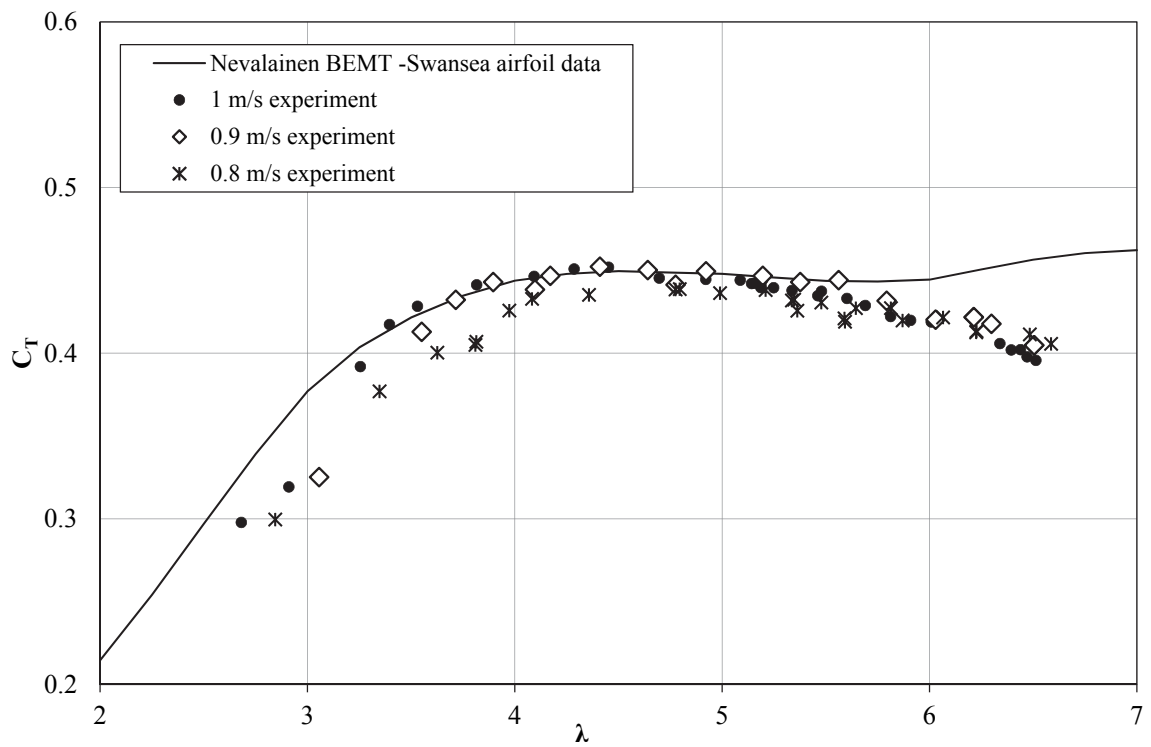
Figure 7-11 C_T–λ curve for NREL S814 blades and Nevalainen BEMT, Togneri et al. *airfoil data.*

In general, although there were discrepancies at low λ, the BEMT tool was able to capture the physical trends and performed acceptably for λ greater than 3.5; the prediction of C_p was accurate for λ between 3.5 and 5.5, with less than 2.8% difference between the BEMT and experimental C_p at the optimum λ of 4. The C_T data was slightly over predicted for the 0.8 m/s case by the BEMT code, and was at worst off by 9% for λ greater than 3.5. However, the BEMT predicted C_T accurately for the 1.0 and 0.9 m/s tests for λ between 3 and 6. For $\lambda > 6$, the BEMT tool diverged from the experimental thrust results, which decreased after approximately $\lambda = 6$, whereas the BEMT predictions had a slight increase in C_T. The match achieved between the experiment and BEMT is comparable to similar verifications done in the tidal energy industry [21, 266].

For λ less than 3.5 there was a significant decrease in the efficiency of the blades (drop in C_p). This is thought to be due to the increasingly low Reynolds number at low λ. At $\lambda = 3$, the average chord-Reynolds number was $8.5{\times}10^4$ for the 1.0 m/s tests, whereas at the peak C_p of around $\lambda = 4$, the Reynolds number was $1.1{\times}10^5$ (a 37% increase). The average Reynolds number for the 0.5 m/s tests, as shown in Figure 5-10, was $7.0{\times}10^4$. From Figure 5-5, the performance of the airfoil was highly degraded for the 0.5 m/s tests at this Reynolds number, hence it is not unexpected that the performance be degraded at the higher inflow speed tests at low λ. This section discusses some potential reasons for the match between the BEMT prediction and towing tank tests using the Togneri *et al.* airfoil data.

Although rotational effects have been demonstrated in prior research [178], they are not well characterized or understood, particularly at low Reynolds numbers [177], and previous work has shown that predictions from BEMT are likely to be weakest at low λ due to 3-D effects becoming more pronounced [163]. Due to the high rotational speeds of the small-scale turbine, 3-D rotational effects were postulated to have been present in the towing tank tests. As discussed in Section 3.1.3.B, a rotating airfoil may have different lift and drag characteristics compared to a 2-D non-rotating airfoil due to a delay in the onset of stall. Previous work (tests done by NREL/NASA) showed an increase in lift and drag at the inner span of the blade, and a reduction in lift and drag at the blade tip due to stall delay from 3-D rotation, particularly at higher α [267]. Along with vortex shedding from the blade tip, a decrease in lift at the tip due to the rotation of the turbine could have resulted in a decrease

in efficiency in the tested turbine, particularly at low λ, compared to that predicted by BEMT.

Milne's pressure measurements from wind tunnel tests on the NREL S814 airfoil showed BL separation occurring on both the suction and pressure surfaces of the airfoil [163]. Pressure surface BL separation has the effect of reducing the suction pressures on the lower surface of the airfoil, leading to a higher net lift force. However, the effect of span-wise flow due to 3-D rotation (as in the towing tank tests) is to delay BL separation. A delay in the BL separation on the pressure surface would result in a reduction in the net lift force on the airfoil, and hence could lead to reduced power. Delayed separation associated with rotational effects also corresponds to Milne's observation that flow remained attached to the pressure surface of the airfoil at lower angles of attack during towing tank tests, performed at the University of Strathclyde on the same NREL S814 bladed turbine (details in [268]), than in the wind tunnel [163].

In this case, the Viterna-Corrigan post stall correction was used in BEMT to account for the airfoil performance once it was stalled, but this correction does not take into account 3-D rotational effects that could delay the occurrence of stall [180]. This means that stall delay was not accounted for in this BEMT model. As well, during the towing tank tests, the bolts attaching the blade to the hub may have caused vortex shedding close to the hub that was more significant than that corrected for using Prandtl's loss correction factors in BEMT. This may have countered the increase in lift expected at the blade root section due to 3-D stall delay. As well, although Prandtl's tip and hub loss corrections were used, literature shows that these corrections may be less effective at small-scale and at low λ [269].

Figure 7-12 shows the thrust loads at the various carriage speeds compared to the BEMT predictions.
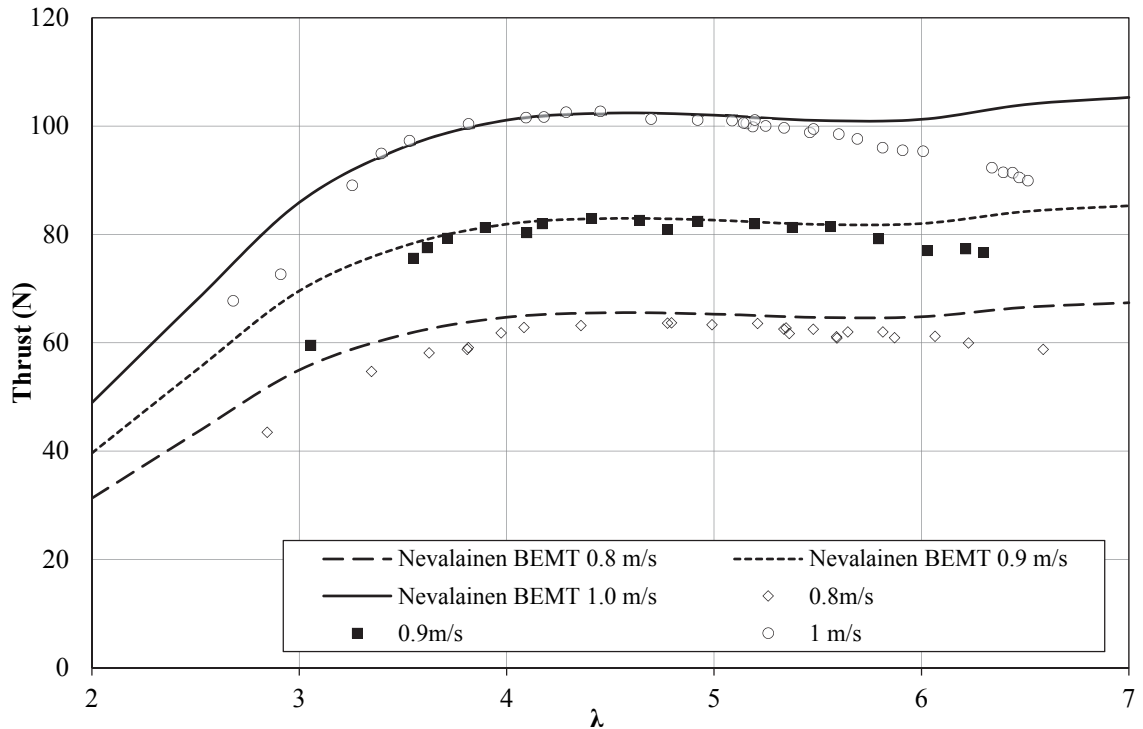
Figure 7-12 Thrust–λ curve for NREL S814 blades and Nevalainen BEMT, Togneri et al. *airfoil data.*

At this range of low Reynolds numbers, the magnitude of the thrust loads decreased significantly with decreasing carriage speed (and decreasing Reynolds number). Because the 2-D Togneri *et al.* airfoil data was at one Reynolds number, C_T and C_p predicted by the BEMT code were only a function of the non-dimensional λ (*i.e.* for each λ and *α*, there was only one possible combination of lift and drag). However, as shown in Figure 7-12, comparing the magnitude of thrust to the BEMT-predicted values, the BEMT code was able to capture the trend of increasing thrust loads with increasing carriage speed.

7.2.6 Discussion

The largest source of error and most significant limitation to the use of BEMT is the uncertainty in the airfoil data used in the model [173]. NREL researchers discussed how they "tune" a model to achieve a better match with test results by making small changes in the airfoil tables to realize improvements in all predicted quantities. However, they highlighted that there is not currently a consistent method to improve the accuracy of airfoil data for modeling real blades in normal operating conditions [173]. Currently, the tidal

energy industry has accepted the use of similar "tuning" of airfoil data, or using airfoil data at incorrect Reynolds numbers, to fit 2-D airfoil data to 3-D rotating turbine tests. For example, Nicholls-Lee represented a NACA 63-2xx airfoil in BEMT by a single series of lift and drag data, but modified the lift in BEMT to account for 3-D behavior which delayed stall and gave a higher working lift coefficient before stall was initiated [101]. However, it was not clear how this modification was made to the lift data. Previous work has also shown that rotational effect corrections typically used in the wind industry are not effective for tidal energy applications [182], leaving a gap in knowledge that needs to be addressed.

The current lack of understanding on the performance of 3-D rotating airfoils at low Reynolds numbers makes it difficult to gauge which flow characteristics are appropriate to obtain representative airfoil data for matching BEMT to experiment. However, it is evident that matching airfoil data for use in BEMT is not only dependent on the Reynolds number, but for data that has been obtained experimentally, on the conditions of the flow (turbulence intensity and length scale) and the facility used (test setup). This merits further investigation, for example, flow visualization may be useful to interpret 3-D flow effects.

Based on the comparison of BEMT predictions to the towing tank test results using the two data sets, the Togneri *et al.* airfoil data better predicted the small-scale turbine performance. For this reason, the Togneri *et al.* airfoil data was chosen for use in the FEM-BEMT coupled design tool to model the NREL S814 blades. However, further investigations into the performance of low Reynolds number airfoils are important for further development of BEMT for modeling small-scale tidal turbines.

CHAPTER 8
FLUID-STRUCTURE
DESIGN TOOL

The BEMT code discussed in Chapter 7 was shown to be able to predict the performance of rigid turbine blades reasonably well. However, the increased flexibility of BT turbine blades makes BEMT alone unable to predict turbine performance and necessitates a fluid-structural interaction design methodology. This chapter outlines the development of a steady state, coupled FEM-BEMT tool for the design of BT coupled blades, considering both the structural and hydrodynamic performance of the blades. An iterative design tool allows for the design and optimization of both the local blade structure (stresses, failure criteria, blade deformation) and the turbine global performance (power output and loads).

The FEM, discussed in Chapter 6, and the BEMT code, discussed in Chapter 7, were coupled using a MATLAB® interface. In this case, the FEM and BEMT components of the design tool were executed consecutively with inputs from the prior iteration.

8.1 Procedure

A MATLAB® interface was developed to iterate between the BEMT code and the FEM. The FEM software can be executed from within a Mathworks MATLAB® script, enabling the BEMT and FEM to run iteratively through this MATLAB® interface. Figure 8-1 shows the process flow chart for the FEM-BEMT coupled design tool for a single iteration.

Blade data (radial chord length, and pre-twist geometry, and airfoil data) and operating conditions (flow velocities and rotational velocities) were input to the design tool and the BEMT was executed to estimate the axial loads (thrust forces) and tangential loads (multiplied by radius to give torque) on each blade element along the blade span.
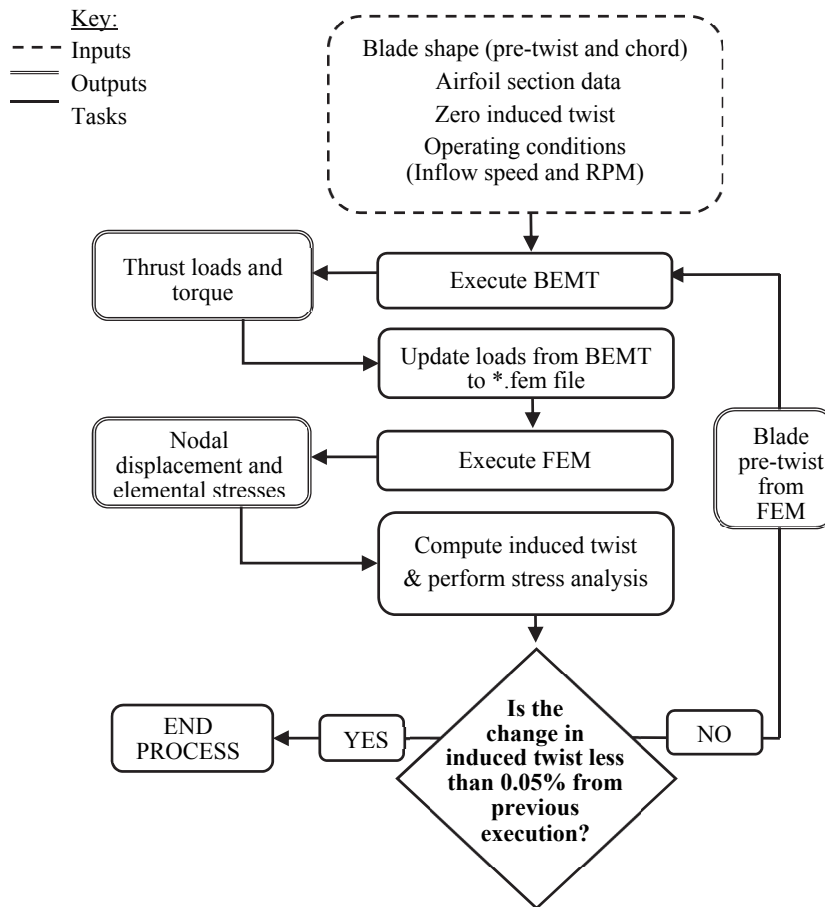
Figure 8-1 Flow chart of coupled iterative FEM-BEMT design tool.

The axial and tangential loads were applied to nodes in the FEM. For the initial BEMT simulation, the blade had zero induced twist, $\phi_i = 0$. The FEM was then run using the BEMT-predicted loads, and the induced twist and composite stresses were computed based on nodal and elemental outputs from the FEM in the form of ASCII files, which were processed in MATLAB®.

HATT power capture and blade loads depend on how the lift and drag coefficients vary with α, and α depends on the flow conditions and the pre-twist geometry of the blade, β_o. In this case, α also depends on the induced twist of the blade due to BT coupling, ϕ_i. The induced twist predicted by the FEM was added to the pre-twist of the baseline blade, giving a new pre-twist blade geometry, $\beta_n = \beta_o + \phi_i$, to be used in the BEMT code, leading to an iterative process between the FEM and BEMT.

It was found that convergence was well indicated by the induced twist as calculated based on the FEM displacement output. With the induced twist as the convergence criterion, a comparison to the last iteration's twist value was performed, and the iterations were executed until the induced twist of the current iteration was < 0.05% different from the previous iteration, as given by Eq. (8-1),

$$\frac{|(\phi_{i,k} - \phi_{i,k-1})|}{\phi_{i,k-1}} =< 0.0005 \, , \qquad 8\text{-}1$$

where k is the iteration number. A 0.05% difference in the induced twist resulted in less than 0.1% difference in the rotor thrust, which was considered within the sensitivity of the design tool.

The design tool used several input files. The *.fem file contained the blade mesh properties, material assignments, and nodal constraints and loading. The *.disp and *.cstr files were ASCII formatted outputs of the FEM analysis and contain the nodal displacements and elemental stresses, respectively. Airfoil lift and drag data and the blade geometry (radial chord and pre-twist) were input from a *.txt file.

Although there are benefits of this design tool, there are also limitations: no aerodynamic moment was considered, perfect rotational speed control system was assumed, Reynolds number effects were not considered, no dynamic simulations or fatigue analysis, and interactions with other turbine parts were not simulated. These limitations are further discussed throughout this chapter.

8.2 Load Application

The 2-D loads predicted by BEMT can be transferred to the 3-D FEM as point loads on nodes or as pressure loads over an elemental area. Surface pressures are the most realistic load application for a tidal turbine blade. Based on an investigation by Knill [237], for detailed stress/strain analysis a pressure distribution loading gives better results, but using a discrete sectional loading was found to be sufficient in measuring the general blade deflections and aeroelastic response. Pressure loading requires a knowledge of the pressure distribution over the entire airfoil cross section, which is not readily available for the NREL

S814 airfoil at the operational Reynolds numbers. Therefore, in this case, pressure loading was not a suitable option and nodal loads were used in the FEM.

The BEMT code predicts the axial (thrust) and tangential (resulting in rotor torque) loads at each blade element along the span. In this case, the axial and tangential loads were applied to the FEM at the aerodynamic center (AC) of the blade cross section (a fixed point a quarter of the chord length from the nose) as shown in Figure 8-2.
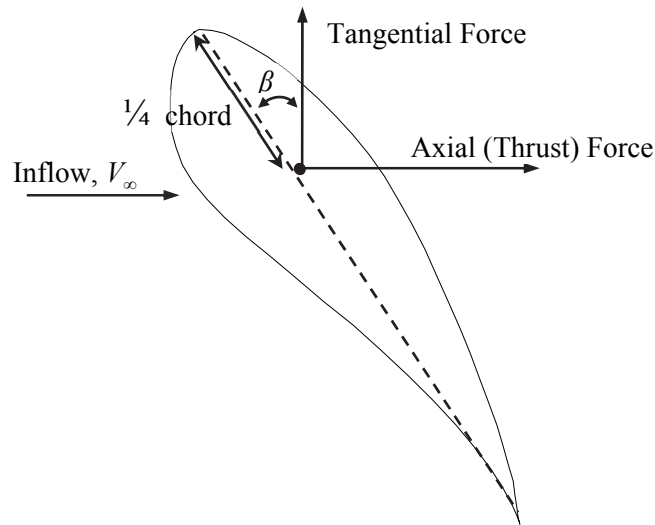
Figure 8-2 Axial and tangential loads at the aerodynamic center for one blade element cross section of the NREL S814 blade.

Two FEM nodal load application scenarios were considered: 1) loads from the BEMT elements summed and applied as a single point load to the AC at 60% radius (determined by experiment to be the approximate span-wise point of load application [270]), and 2) loads on each blade element from BEMT applied to the AC of the corresponding blade section in the FEM (loading the blade with 10 point loads along the span). In this case, 10 span-wise loads were used, corresponding to the 10 blade elements determined from the convergence study in Section 7.2.2, as shown in Figure 8-3.
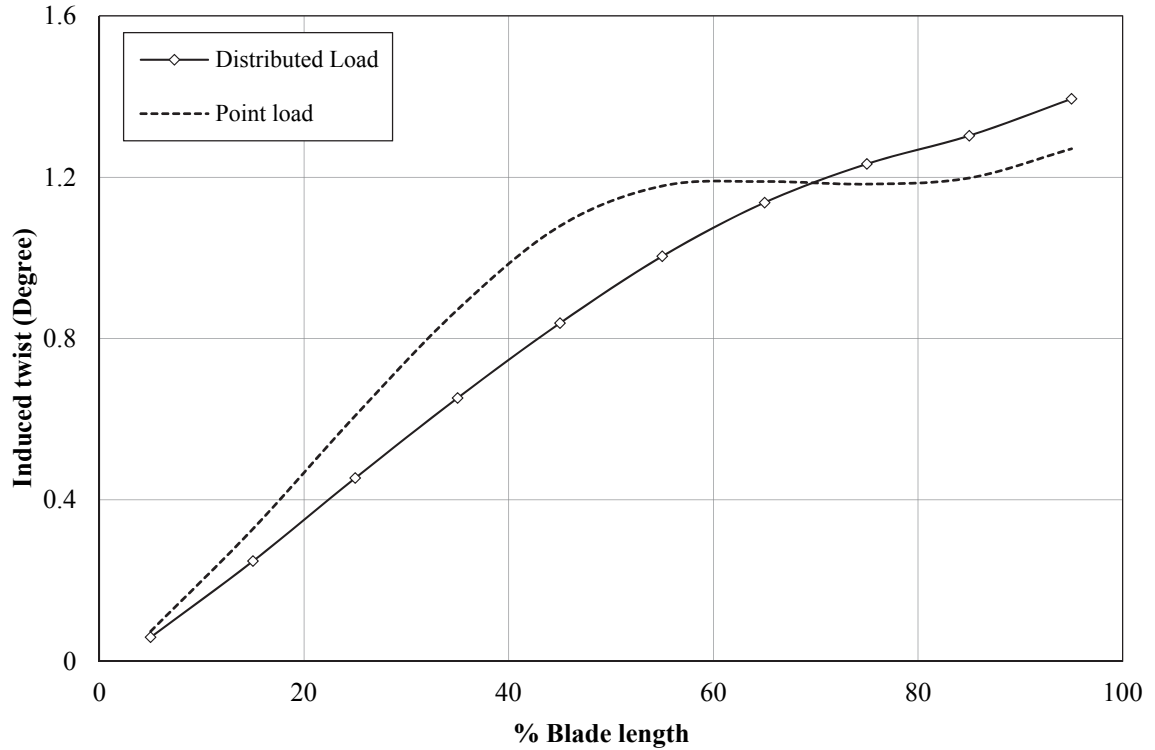
Figure 8-3 Induced twist: Point load and load distributed over 10 elements.

From Figure 8-3, the tip twist of the blade predicted using a single point load deviated from predictions made with span-wise loads. Although a single point load is less computationally intensive, applying distributed span-wise loads more realistically simulates how a blade would be loaded. Therefore, span-wise loads were applied to nodes at the AC of 10 blade sections in the FEM, as shown in Figure 8-4.
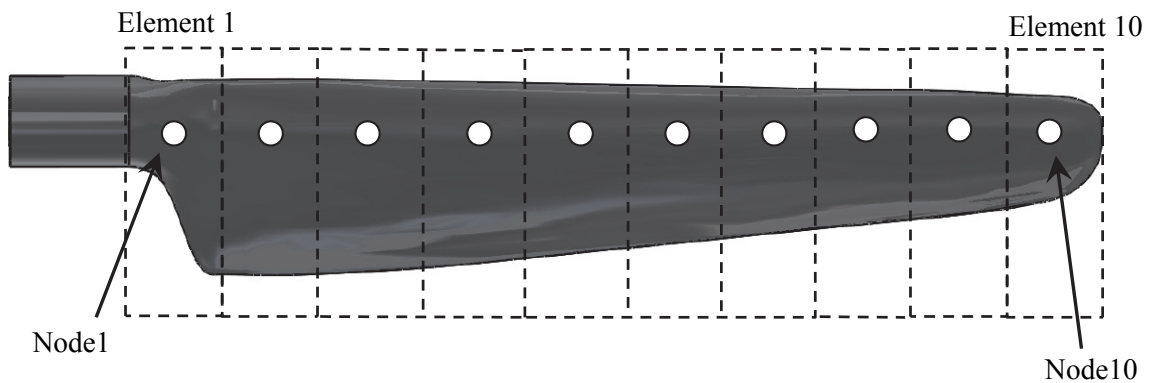
Figure 8-4 FEM loading along 10 blade elements.

In this case, the pitching moment on the airfoil was neglected; a necessary assumption due to the lack of moment coefficient data for the NREL S814 airfoil at the operational Reynolds numbers. In agreement with Maheri [236], this assumption was considered valid since the moment coefficients for the NREL S814 airfoil at low Reynolds numbers are small compared to the lift and drag coefficients, and were typically negative (thus would contribute to feathering).

Fatigue loading is also an important consideration in the design of BT blades, with an HATT expected to experience on the order of 10^7 cycles of reversed loading over a 20 year life span [44]. However, it has been shown that ultimate static loads are significantly higher than fatigue loads on a tidal turbine blade, and at early stages of blade design, fatigue loads are typically unknown. Therefore ultimate static loads are used in the design process [47]. These ultimate loads are anticipated to occur at the highest flow speed expected at the site in a specific time period (the extreme conditions).

8.3 Stress Analysis

As a check on the durability of the composite blades, a failure analysis was implemented in the design tool. This failure analysis quantified the strength of the composite blade design based on elemental stresses in the composite material, which were output from the FEM after each iteration. Safety factors (SFs), which give the capacity of a structure to support loads before yielding, based on both the Maximum Stress failure theory and Tsai-Hill failure theory, were computed for each element in the composite FEM after each iteration. These SFs were used as an indication of the robustness of the design, with higher SFs predicting a more robust design, and SFs of less than one indicating a high likelihood of failure for that element. The design tool has an integrated alert system which identifies areas of the blade with unacceptably low SFs. In this case, SFs of greater than 1.3 for all elements were considered acceptable; this imposed a stress limit that was less than the composite ultimate strength to account for fatigue effects and other uncertainties, which must be considered later in the blade design process.

Composite material failure theories are detailed in Section 3.5.1. The two models used in this analysis were the Maximum Stress failure theory and the Tsai-Hill failure theory. The

Maximum Stress failure theory predicts a laminate to fail if the compressive or tensile stresses in the longitudinal or transverse directions, or the shear stress, surpass the ultimate strength in the corresponding direction [221]. SFs in each of the material directions based on the Maximum Stress failure theory are the ratio of the ultimate strength to the stress computed by the FEM. This method of failure analysis is simple and direct but does not consider the interaction between the stresses acting on the laminate (*i.e.* stresses in each material direction are considered independent of whether other components of the stress tensor are present). Therefore, it tends to over predict the likelihood of failure [215].

Tsai-Hill failure is based on the failure theory of von-Mises' distortional energy yield criterion as applied to anisotropic materials [215], and proposes, for a plane stress assumption, that a laminate fails if the SF given in Eq. (8-2) is less than 1:

$$\frac{1}{\text{SF}} = \left(\frac{\sigma_1}{\sigma_{1ult}^T} \right)^2 - \frac{\sigma_1 \, \sigma_2}{\sigma_{1ult}^{T\,2}} + \left(\frac{\sigma_1}{\sigma_{2ult}^T} \right)^2 + \left(\frac{\tau_{12}}{\tau_{12ult}} \right)^2 \qquad \text{8-2}$$

The basic form of the Tsai-Hill failure theory does not consider compression loading, and since the transverse direction of a laminate is much stronger in compression, it tends to over predict the likelihood of failure. This was corrected for by adding a condition that if the transverse stress is negative (*i.e.* compression), Eq. (8-2) was updated by replacing the tensile transverse strength, σ_{2ult}^T, with the compressive transverse strength, σ_{2ult}^C.

8.4   Design Tool Verification

The 1/20th scale three-bladed HATT with BT coupled NREL S814 blades, detailed in Section 5.1.4, was modeled using the coupled FEM-BEMT design tool to both verify the design tool and further investigate the performance of a turbine with BT blades.

8.4.1   Model Setup

The design tool requires inputs for both the FEM (details in Chapter 6) and BEMT (details in Chapter 7) components. The blade and turbine geometry used in the BEMT is given in Table 8-1, with dimensions shown in the schematic in Figure 8-5. This blade geometry was

also modeled in the FEM. The blade materials and composite layup are detailed in Section 4.2. Loads were applied as discussed in Section 8.2.
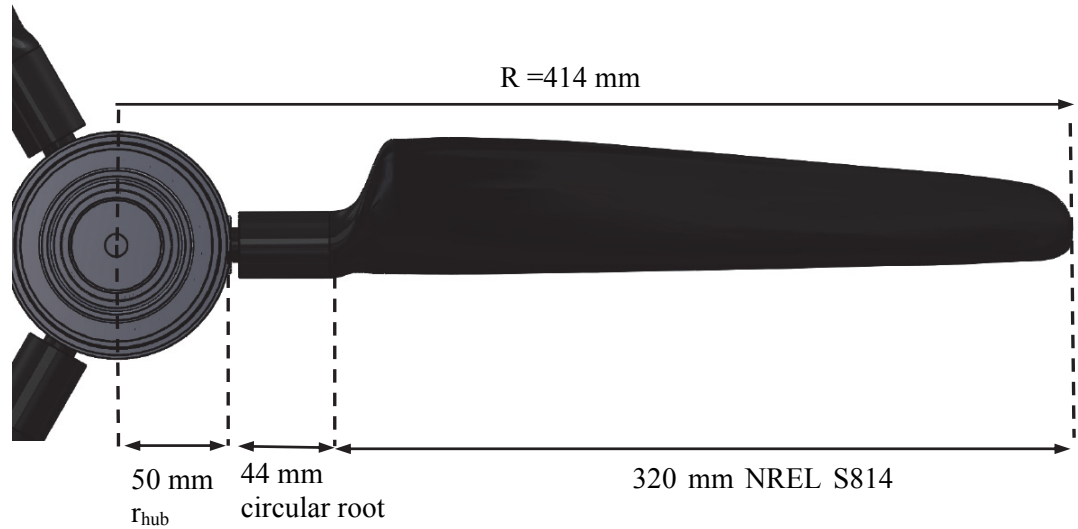
Figure 8-5 Schematic of turbine rotor with dimensions.

Table 8-1 Turbine and blade geometry for design tool verification.

Turbine radius (mm)	Blade length (mm)	Blade twist (Degrees)	Blade chord (mm)	Airfoil shape
0	0	N/A	N/A	Circular root
50	0	N/A	15	Circular root
54	4	N/A	15	Circular root
94	44	N/A	29	Circular root
110	60	N/A	N/A	Lofted (ellipse)
120	66	N/A	N/A	Lofted (ellipse)
122	72	0	64.3	NREL S814
147	97	-4.38	62.9	NREL S814
216	166	-14.8	56	NREL S814
249	199	-17.33	51.6	NREL S814
284	234	-18.91	47.3	NREL S814
319	269	-19.75	42.6	NREL S814
354	304	-20.39	38.1	NREL S814
388	338	-20.87	33.7	NREL S814
414	364	-21.11	24.9	NREL S814

8.4.2 BEMT Inputs

The 364 mm long blade (the 360 mm blade made by Airborne Marine with an additional 4 mm circular root section for attachment to the hub) was considered in the BEMT model using 11 blade elements, giving 33.1 mm long blade elements, which was found from a convergence study to give converged results in a short time period. The additional 5 mm chord length, discussed in 4.2, was added to the chord lengths given in Table 8-1, for modeling the blade in the BEMT tool. The outer 320 mm, shown in Figure 5-16, was modeled using the Togneri *et al.* [260] experimental section data for the NREL S814 airfoil, produced in a flume at Swansea University at a Reynolds number of 5×10^4. The circular blade root was considered in BEMT using drag coefficients for a cylinder at the Reynolds number of the test, assuming no lift generated by this section.

The lofted section between the circular root at 44 mm and the first NRELS814 airfoil at 72 mm was also modeled using the Togneri *et al.* airfoil data. As a check on the accuracy of modeling the blade root this way, it was modeled using an Eppler E863 strut airfoil with a maximum thickness of 35.7% at 28.5% chord. This airfoil closely approximated the lofted section based on the section geometry obtained from the CMM scan of the composite blade. However, using this airfoil data resulted in less than 1% difference in thrust and torque compared to modeling this section with the same NREL S814 airfoil, therefore the NREL S814 airfoil data was used for the entire working section of the blade.

8.4.3 Results

Figure 8-6 to Figure 8-9 show the rotor thrust and torque as a function of λ for both the composite and aluminum blades, as compared to the FEM-BEMT design tool predictions using the Togneri *et al.* [260] airfoil data. The aluminum blade performance prediction from the design tool was from the first iteration of the tool prior to the effects of BT coupling (effectively rigid blade shape), and the composite blade performance prediction was from the converged design tool.
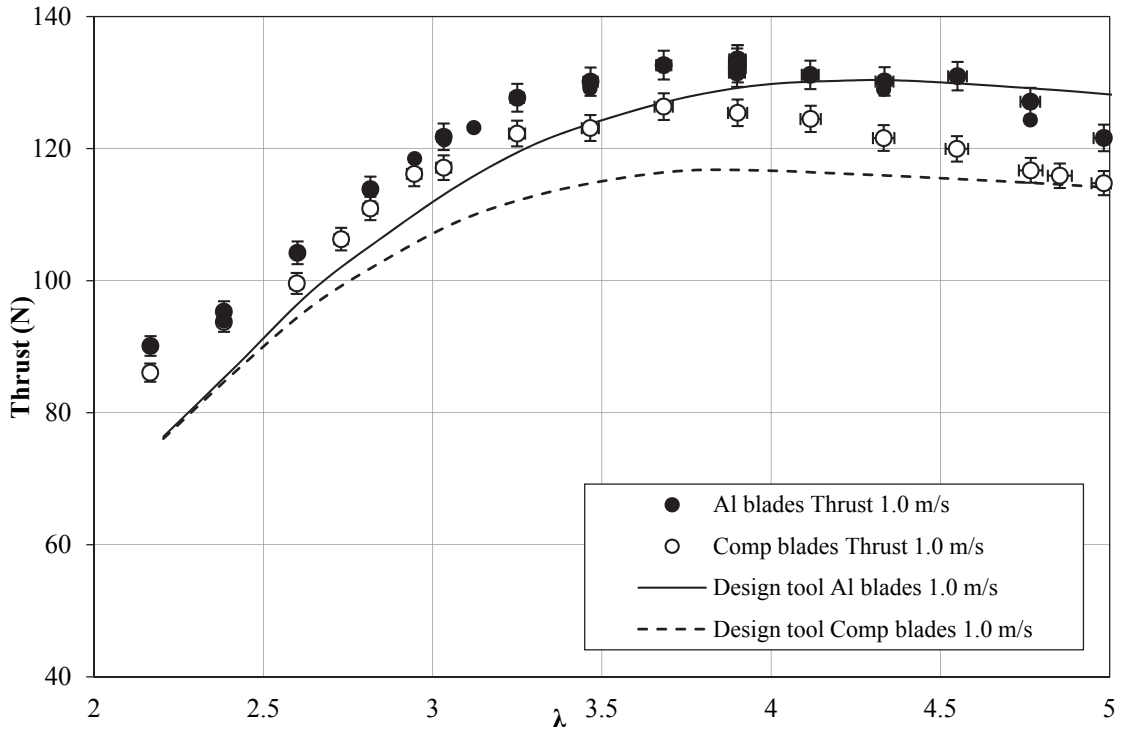
Figure 8-6 Thrust–λ for design tool and experiment, BT blades and aluminum blades, 1.0 m/s.
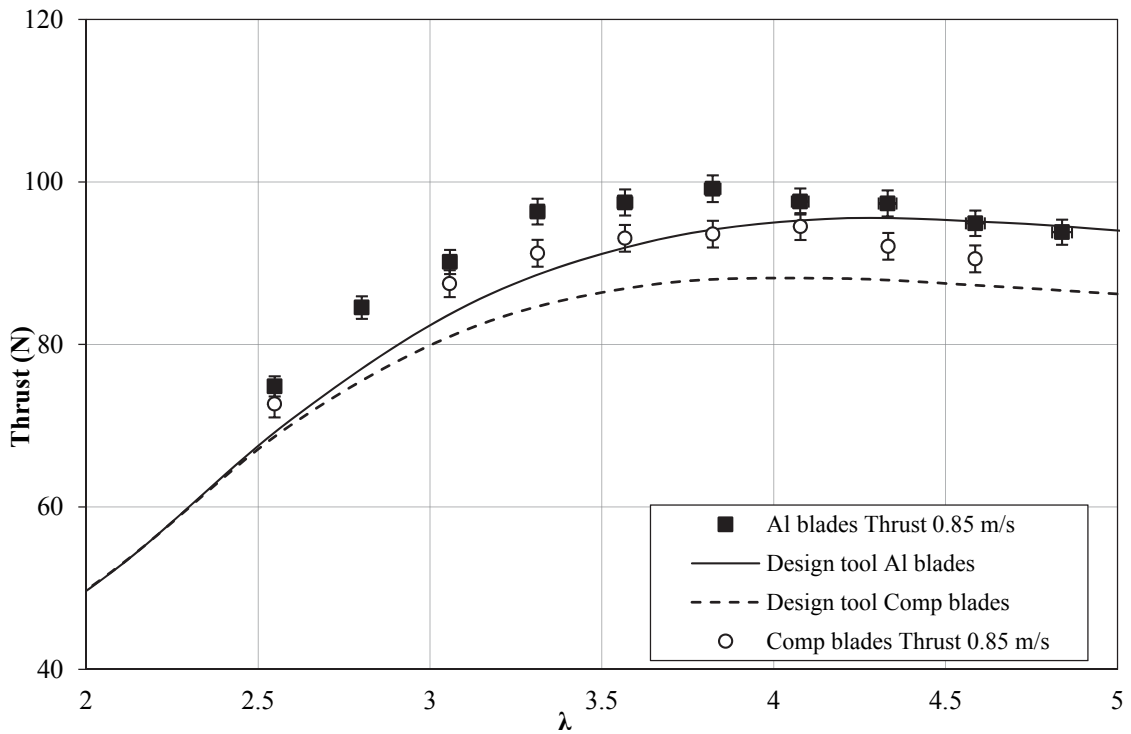
Figure 8-7 Thrust–λ for design tool and experiment, BT blades and aluminum blades, 0.85 m/s.
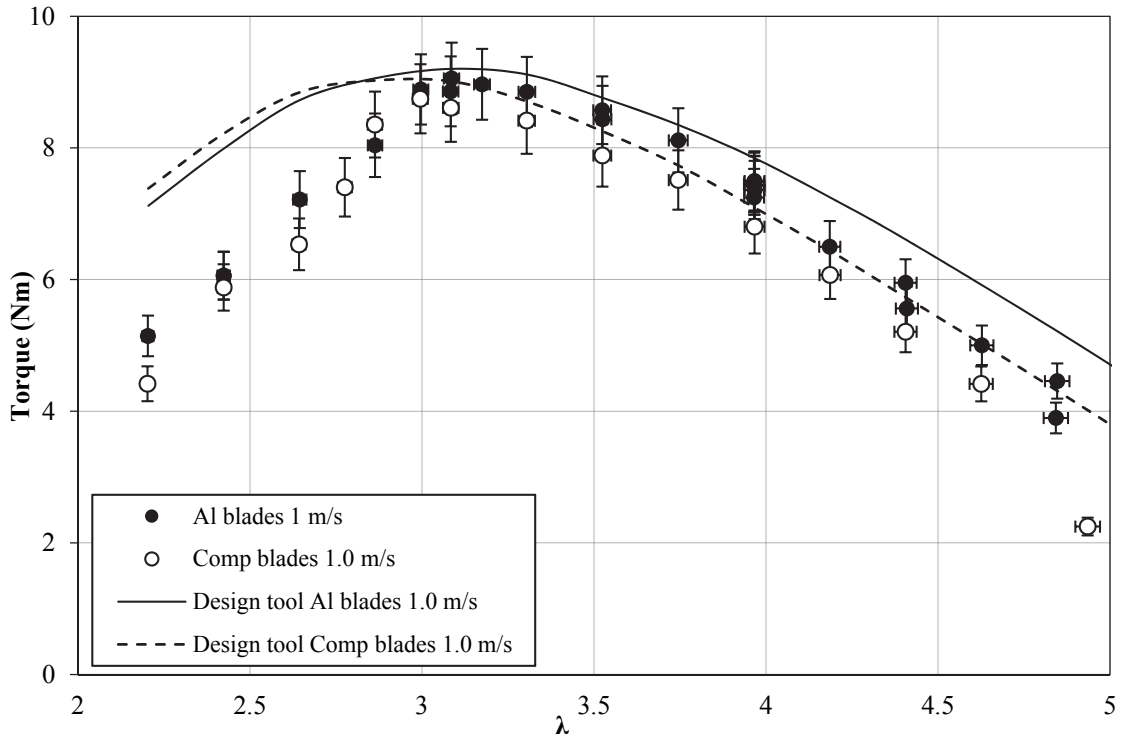
182

Figure 8-8 Torque–λ for design tool and experiment, BT blades and aluminum blades, 1.0 m/s.

Figure 8-9 Torque–λ for design tool and experiment, BT blades and aluminum blades, 0.85 m/s.

183
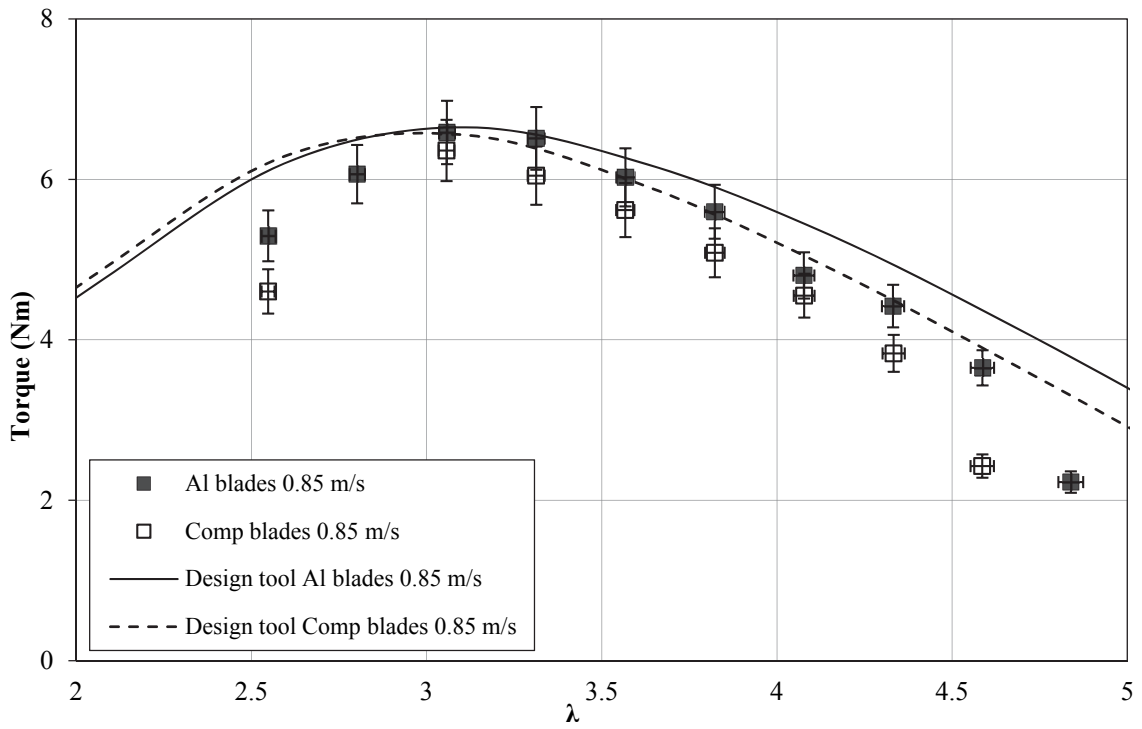
Although the trend of thrust and λ was similar between the experiment and the design tool, the tool under-predicted the rotor thrust. The rotor torque predicted by the design tool had a similar trend to the experiment for high rotational speeds (λ greater than 3.2), and predicted the same peak torque value, but at lower values of λ, where the blades had higher angles of attack and lower Reynolds numbers (moving toward stall), the design tool over-predicted the performance.

The BT blades at these conditions were predicted using the design tool to have up to 8.7 mm of bending displacement and 1.8° of tip twist. Although the BT blade deformation was not measured during towing tank testing, the relative difference in thrust between the composite blades and the rigid blades suggests that the BT blades were twisting to feather as anticipated. Figure 8-10 shows the percent difference in thrust between the composite BT and rigid blades, as a function of λ.
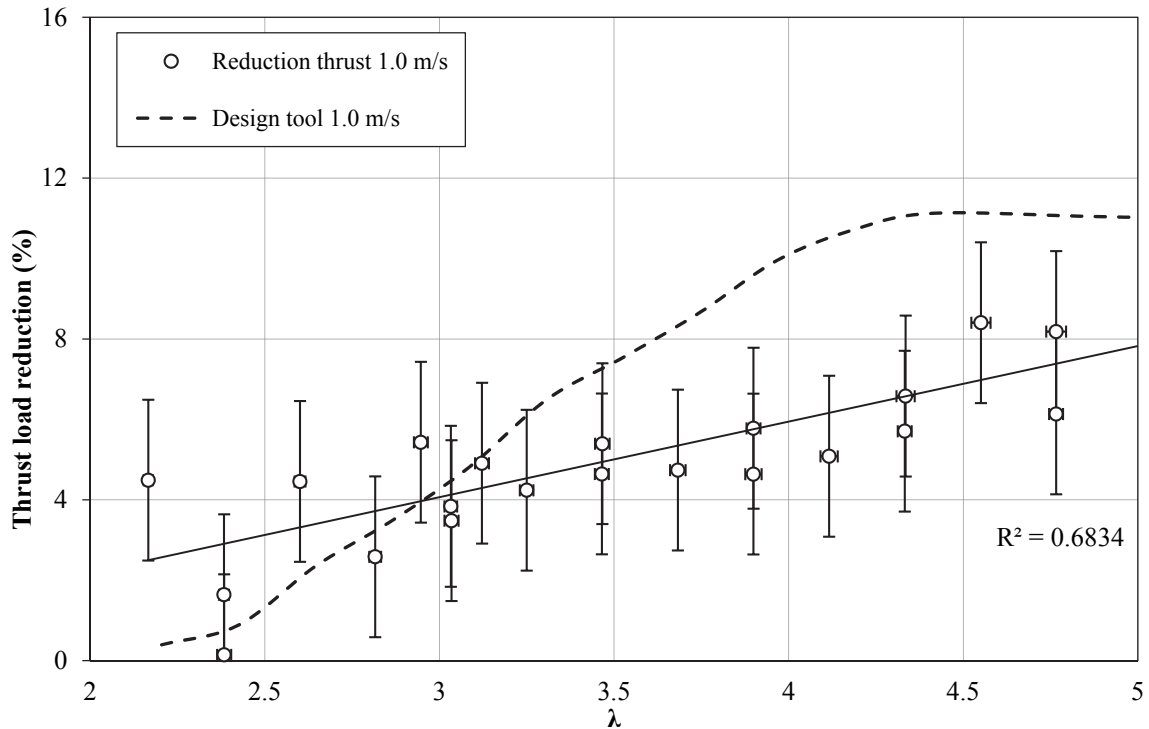
Figure 8-10 Percent difference in thrust loads between composite and aluminum blades predicted by the design tool compared to experiment.

The general range of thrust reductions of the experiments was close to that of the design tool (average of 6 %), however, the design tool predicted more load reduction than the

experiment showed. The design tool predicted the percent reduction in loads associated with the composite BT blades to increase with λ until about λ = 4.5, and then to plateau as the thrust loads stopped increasing. The uncertainty and scatter in the experimental data made this plateau in the design tool trend difficult to observe. However, with the exception of operating at 50 RPM (λ = 2.2), the thrust was predicted by the design tool to within 8% for both the composite and rigid blades. However, at low λ (low rotational speeds), the design tool over-predicted the torque at λ = 2.2 by 70% for the composite blades and 30% for the aluminum blades.

The low torque measured experimentally at low λ indicates that there was performance degradation in the towing tank tests that was not accurately captured by the BEMT component of the design tool.
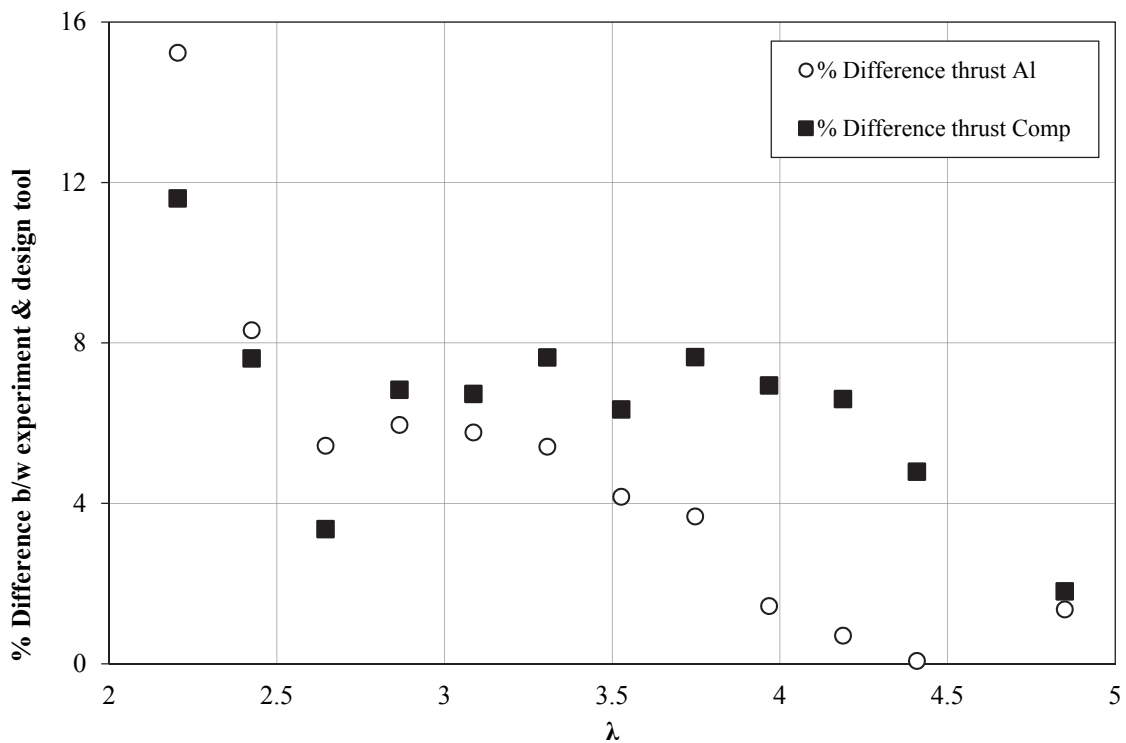
Figure 8-11 Percent difference in thrust between design tool predictions and experimental results, 1.0 m/s tests.
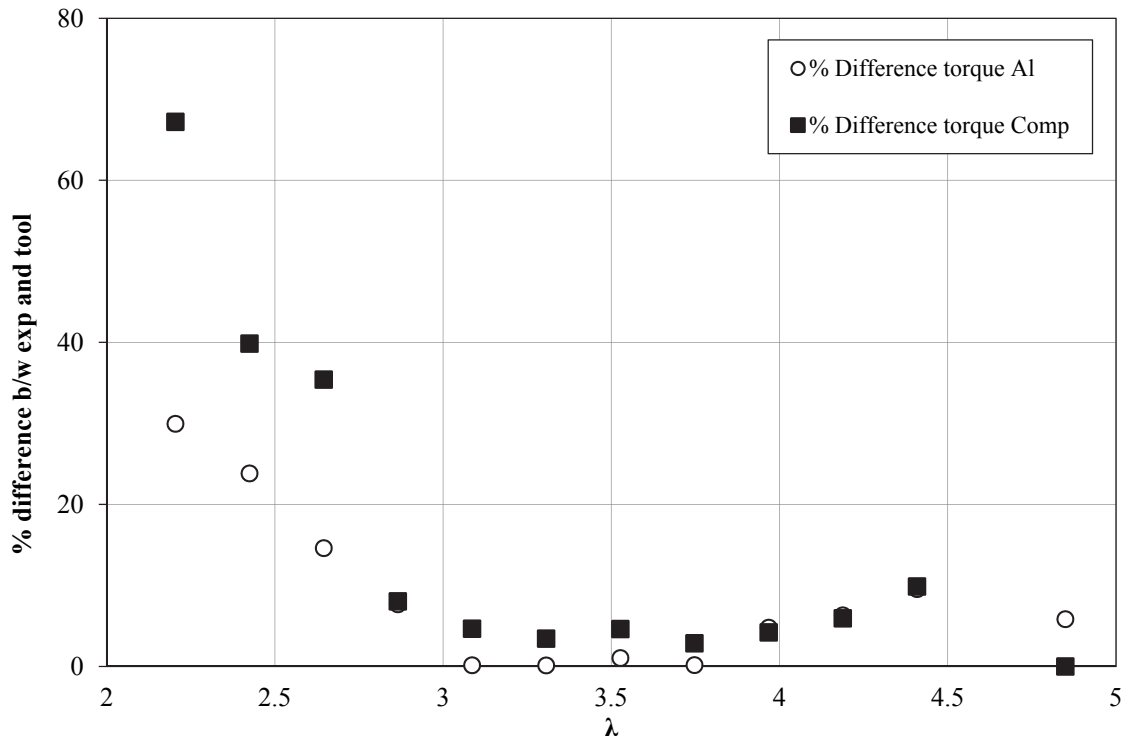
Figure 8-12 Percent difference in torque between design tool predictions and experimental results, 1.0 m/s tests.

The performance decrease observed experimentally at low λ was expected; the blades were expected to stall at low λ, with an associated decrease in lift and increase in drag. This is similar to what was found for the first set of hydrodynamic tests, shown in Section 7.2.5. This is thought to be largely due to the operation of the turbine at low Reynolds numbers, but could also be related to 3-D rotational effects that were not accounted for by the 2-D airfoil data. Further discussion on the possible causes of decreased power at low λ is given in Section 7.2.5.

Another potential reason for the mismatch between the design tool and the experimental test results was the 5 mm extension of the trailing edge of the blades (shown in Figure 4-10). This was considered in the design tool by increasing the chord length of the NREL S814 airfoil by 5 mm, however, this additional length slightly altered the tip geometry of the airfoil as compared to the theoretical NREL S814 airfoil. To mitigate the effect of this TE on the comparison of rigid blade and BT blade performance, the aluminum blades were machined with the same TE geometry. However, the BEMT-FEM design tool results are based on experimental airfoil data for the theoretical airfoil shape, and hence, the airfoil

section modeled in BEMT did not take this TE geometry into consideration. To investigate the significance of this altered geometry, XFOIL was used to estimate lift and drag coefficients for both the 2-D theoretical and altered airfoil shapes. The altered airfoil shape was input to XFOIL using the 2-D CMM scan data normalized by the chord length. Because XFOIL did not converge on a result at the low Reynolds number of the tests, higher Reynolds number simulations were performed. Figure 8-13 and Figure 8-14 show the lift and drag coefficients predicted by XFOIL over a range of α for the theoretical airfoil shape and the CMM altered TE shape. Reynolds numbers of 1×10^6, 2×10^6, and 5×10^5, and an NCRIT value of 2 were used. Using different NCRIT values (values of 1, 2, 5, and 8 were trialed) had less than a 1.5% difference in the results, and did not change the relative difference between the performances of the two airfoil shapes.
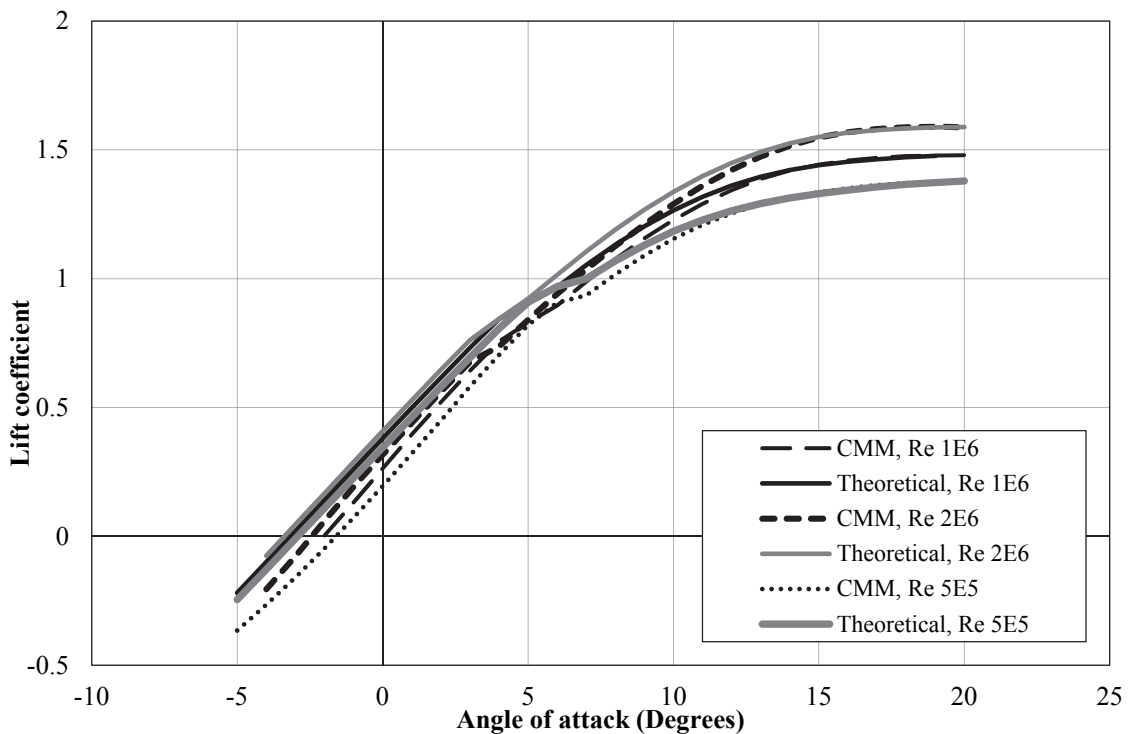
Figure 8-13 XFOIL predictions of lift coefficients for theoretical and altered (CMM) airfoil shape.
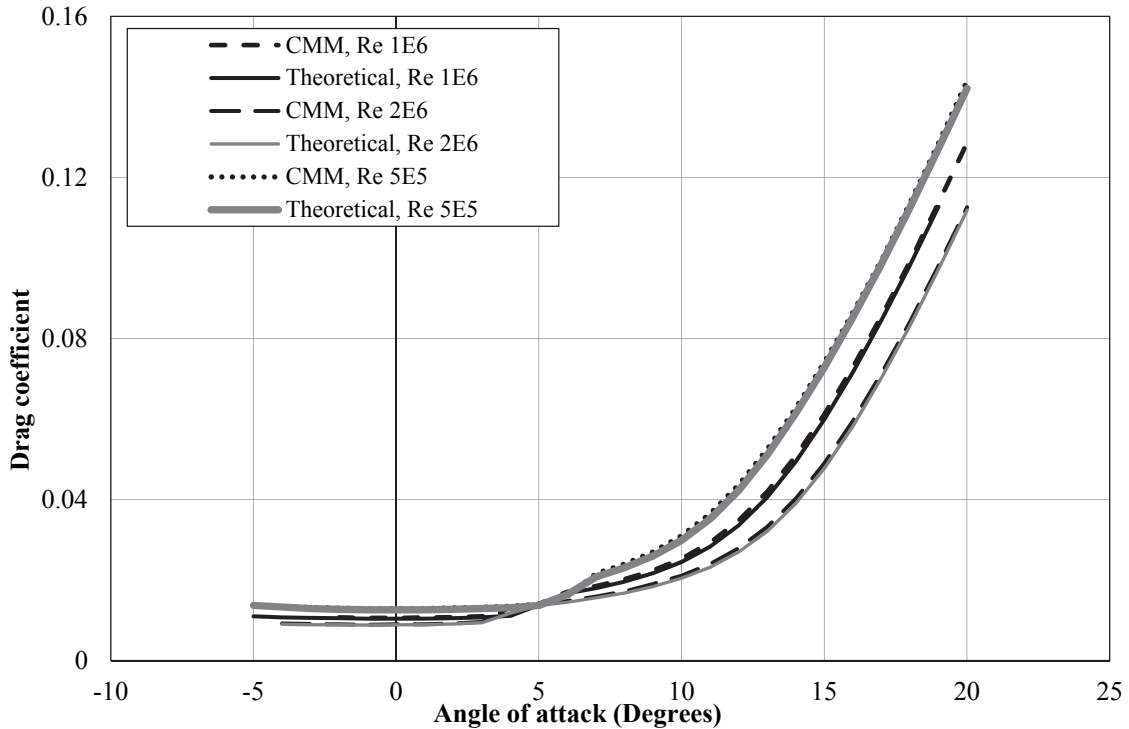
Figure 8-14 XFOIL predictions of drag coefficients for theoretical and altered (CMM) airfoil shape.

On average there was less than 2.6% difference in lift and less than 2.1% difference in drag between these two airfoil shapes for α greater than 5. At lower α, the percent difference was greater due to the smaller values of lift and drag, however, from the plots in Figure 8-13 and Figure 8-14, there was still a close match between the two shapes. The difference in airfoil performance is within the uncertainty range for the experiment, and hence is not expected to have a significant contribution to the mismatch of the design tool. Although this XFOIL prediction has not been verified, it gives a relative estimate of the sensitivity of the airfoil to the TE alteration. A more in-depth investigation is recommended to compare these airfoil shapes at the low Reynolds numbers that were tested.

Figure 8-15 shows the tip twist for the BT blades as predicted by the design tool for these conditions.
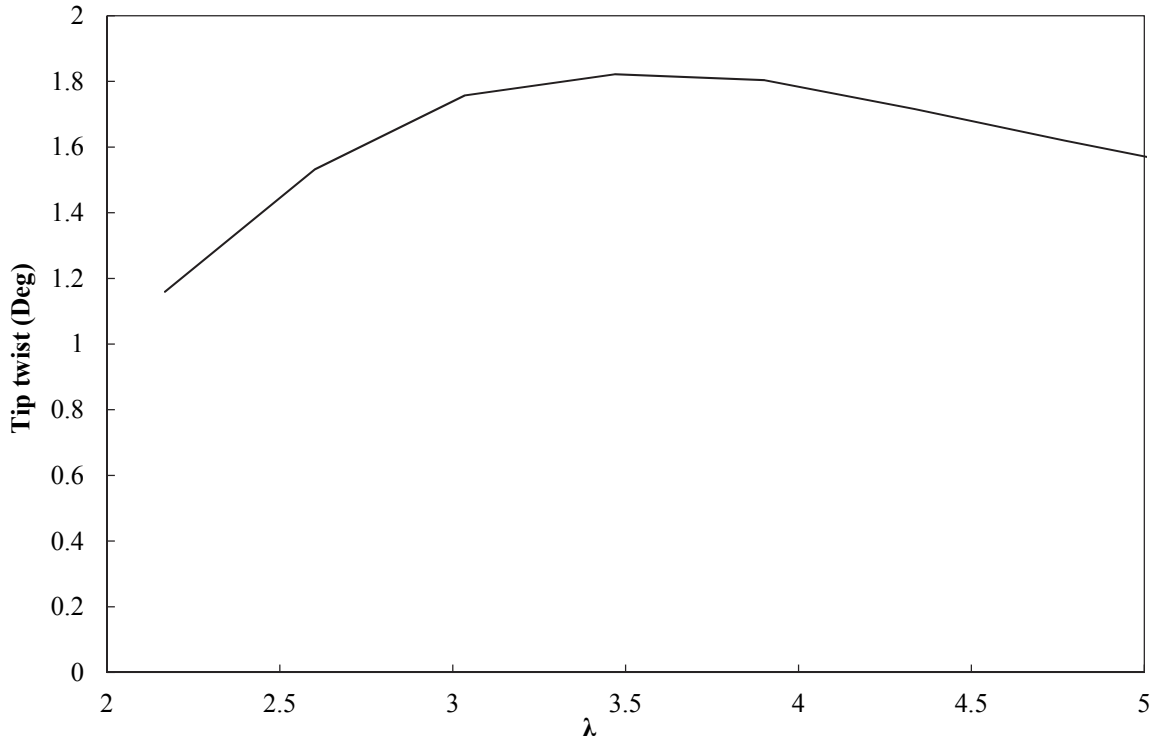
Figure 8-15 Tip twist predicted by design tool for compoiste BT blades, for 1.0 m/s.

The design tool predicted a maximum tip twist for the BT blade of approximately 1.8° at a λ of 3.5. Based on the experimental data, this coincides approximately with the peak thrust loads, where the thrust on the rotor plateaus after λ = 3.5. This means the maximum twisting curvature is predicted to occur when the highest loads are applied to the blades, which is in agreement with the structural bending tests shown in Section 4.2.

8.5   Sensitivity to Model Inputs

Turbine performance predictions were found to be highly sensitive to the airfoil data used in the BEMT component of the design tool. The tool also had varying degrees of sensitivity to other input variables. This section outlines the model inputs, the potential variance in these inputs based on the experimental setup given in Section 5.1.4, and how this affected the overall design tool predictions.

8.5.1   Airfoil Data

The BEMT component of the design tool calculates the thrust and torque produced by the rotor as a function of the blade geometry, relying on the section lift and drag coefficients

input to the model. The Togneri *et al.* [260] airfoil data at a Reynolds number of 5×10^4 gave an acceptable match to the experiment, even though the turbine in the towing tank operated at a higher Reynolds number (average Reynolds number at 1.0 m/s of 1.45×10^5). This is similar to the findings discussed in Section 7.2.6 for the first set of hydrodynamic tests. In order to investigate the sensitivity of the BEMT component of the design tool to the input airfoil data, several other data sets were trialed in the design tool.

The first airfoil data set trialed was collected in a wind tunnel by Milne [163] at three discrete Reynolds numbers- 8.5×10^4, 1.05×10^5, and 1.5×10^5. This data is discussed in detail in Section 7.2.1. Figure 8-16 shows the rigid aluminum blade experimental results at 1.0 m/s compared to the BEMT predictions (first iteration of the design tool) for both the Togneri *et al.* and Milne airfoil data. In this section, the rigid blade experimental data at 1.0 m/s was compared to the first iteration of the design tool in this section to allow easy observation of trends. Since the composite blade performance depends on the geometry change predicted by the FEM, it was not included in the investigation of the effect of airfoil data on BEMT predictions.
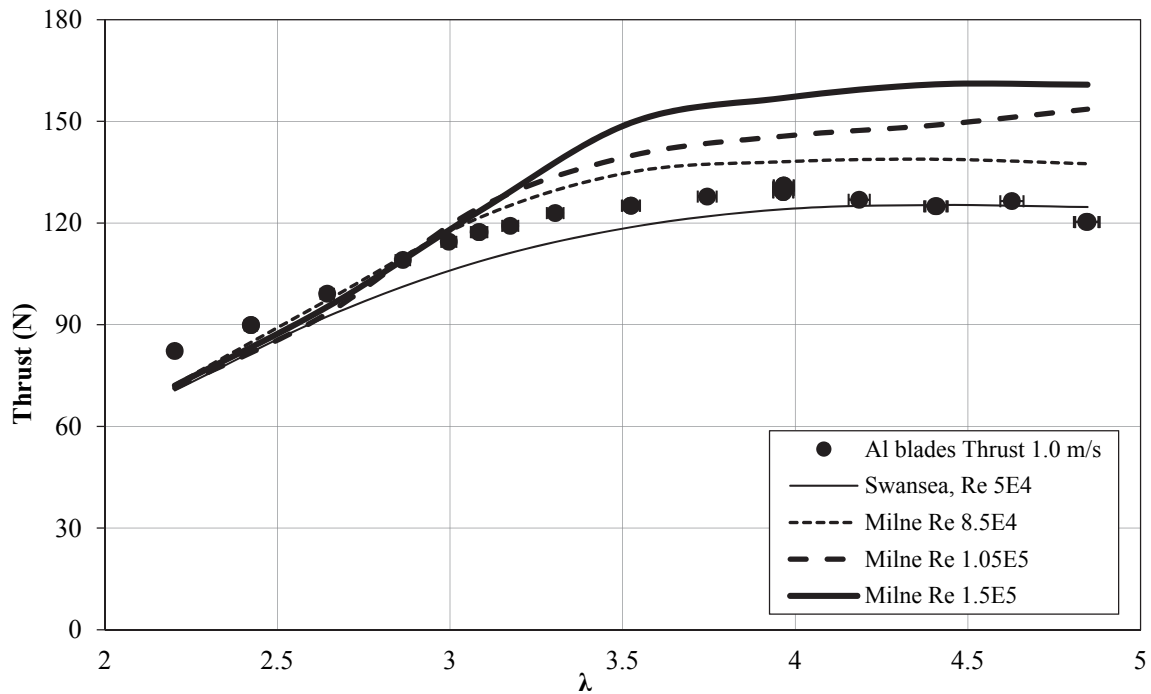
Figure 8-16 Thrust –λ using the Togneri et al. *airfoil data, and Milne airfoil data at three Reynolds numbers.*
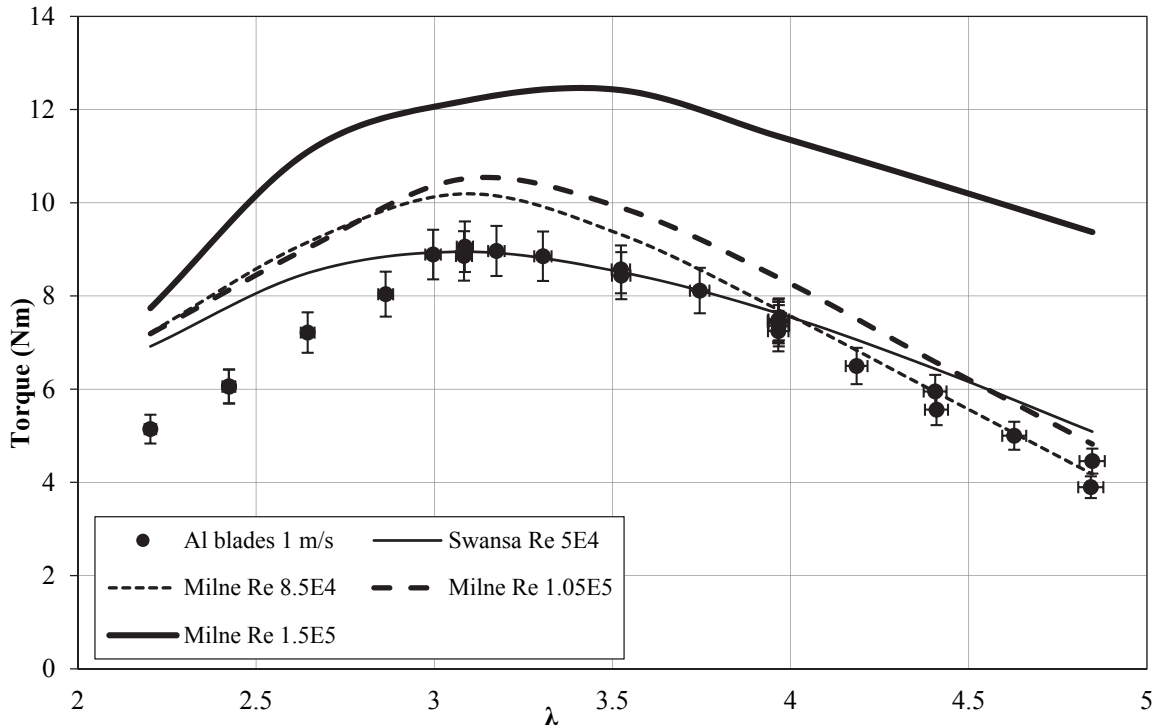
Figure 8-17 Torque –λ using the Togneri et al. *airfoil data, and Milne airfoil data at three Reynolds numbers.*

Interestingly, although the turbine operated at Reynolds numbers that better matched the Milne airfoil data, the Togneri *et al.* airfoil data at the lower Reynolds number of $5×10^4$ still matched the experimental data better, particularly for the torque. This reinforces the discussion presented in Section 7.2.6 and highlights the uncertainty in which flow characteristics are the most important in matching airfoil data to scale-model testing.

To further explore the sensitivity of the BEMT component of the design tool to the input airfoil data, the Togneri *et al.* airfoil data was used as a base-case and the lift and drag coefficients were altered. Initially the lift and drag were altered independently to investigate the sensitivity of the overall BEMT predictions to both. Following this, lift and drag were altered simultaneously to mimic both improved and degraded airfoil performance. The lift and drag alterations were based on those done by Masters *et al.* [271] in a similar study.

Table 8-2 outlines the modifications made to the Togneri *et al.* airfoil data to investigate the sensitivity of the design tool to lift coefficients.

Table 8-2 Modifications in lift, original drag data, sensitivity investigation.

Case	Lift	Drag	Reason
1	10% increase	Original	Mimic airfoil performance enhancement
2	5% increase	Original	
3	5% decrease	Original	Mimic airfoil performance degradation
4	10% decrease	Original	

Figure 8-18 and Figure 8-19 show the original design tool thrust and torque predictions made using the Togneri *et al.* airfoil data (solid black line), compared to the four cases given in Table 8-2 (where only the lift was altered). From Figure 8-18 and Figure 8-19, the turbine performance was sensitive to variations in the lift. A 10% increase in the lift coefficient resulted in over a 10% increase in torque and 12.5% increase in the thrust predicted by BEMT.
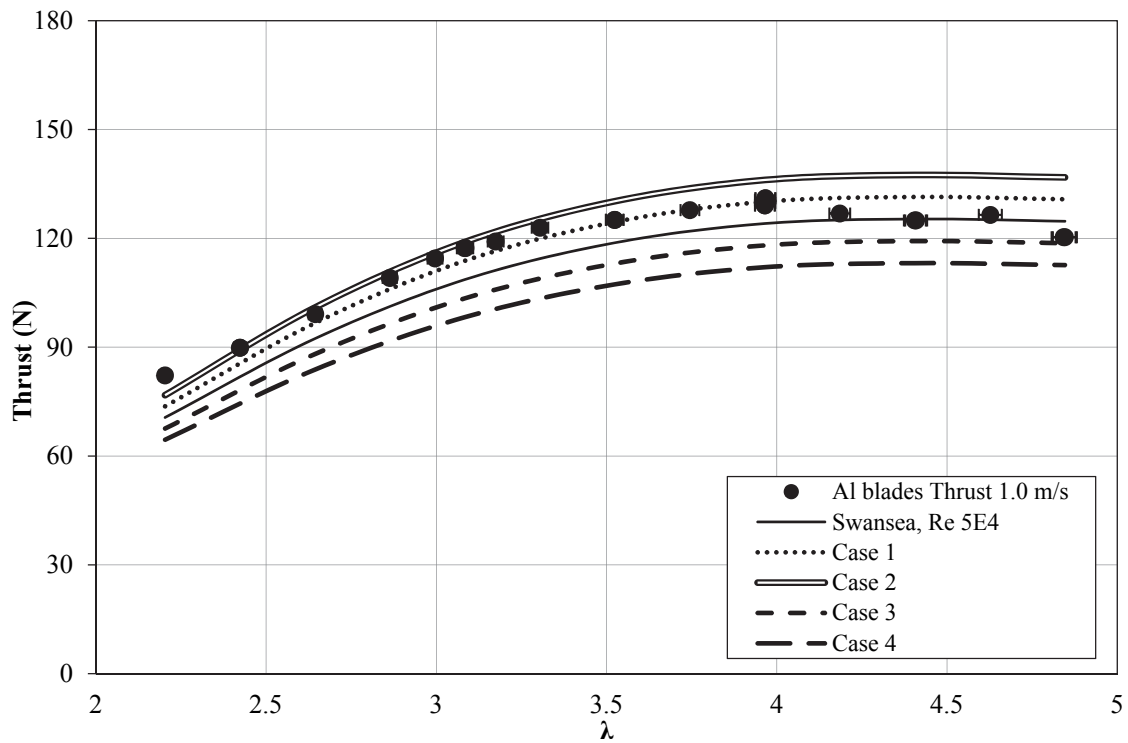
Figure 8-18 Thrust–λ as a function of varying lift, from the Togneri et al. *base-case.*
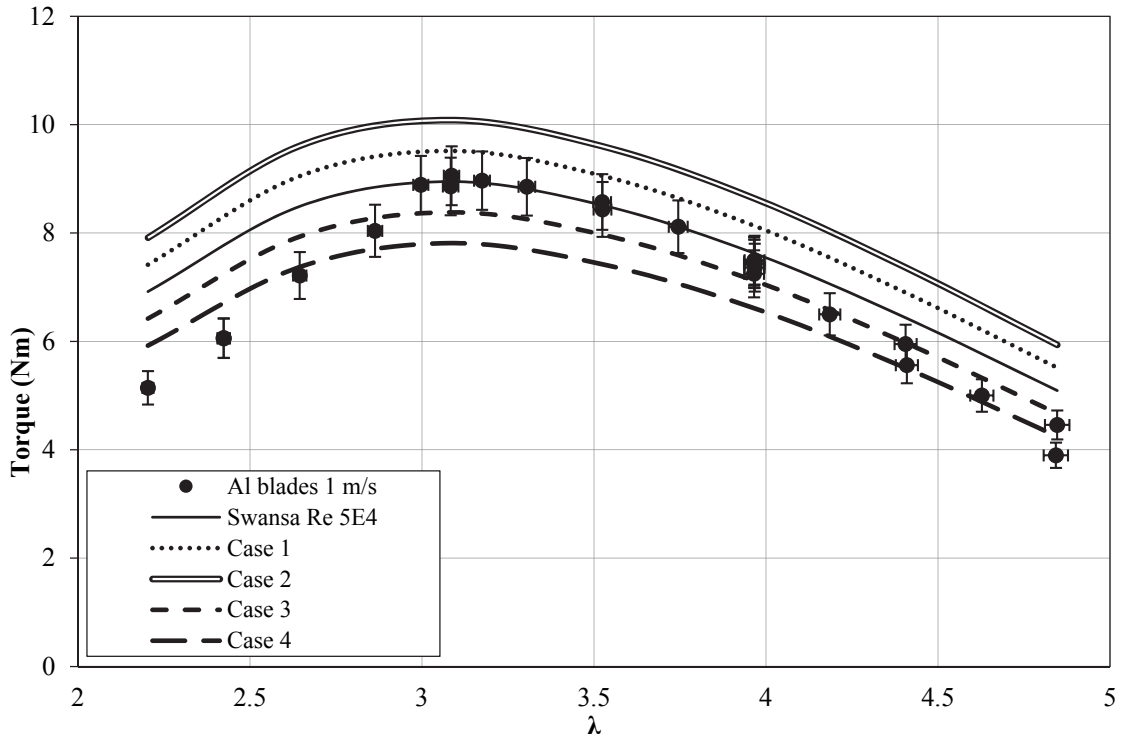
Figure 8-19 Torque–λ as a function of varying lift, from the Togneri et al. *base-case.*

Table 8-3 gives the modifications made to the Togneri *et al.* airfoil data to investigate the sensitivity of the design tool to drag coefficients.

Table 8-3 Modifications in drag, original lift data, sensitivity investigation.

Case	Lift	Drag	Reason
5	Original	50% increase	Mimic airfoil performance degradation
6	Original	25% increase	
7	Original	25% decrease	Mimic airfoil performance enhancement
8	Original	50% decrease	

Figure 8-20 and Figure 8-21 show the original design tool predictions made using the Togneri *et al.* airfoil data (solid black line), compared to the four cases given in Table 8-2 (where only the drag coefficients were altered), for both thrust and torque.

Figure 8-20 Thrust–λ as a function of varying drag, from the Togneri et al. *base-case.*
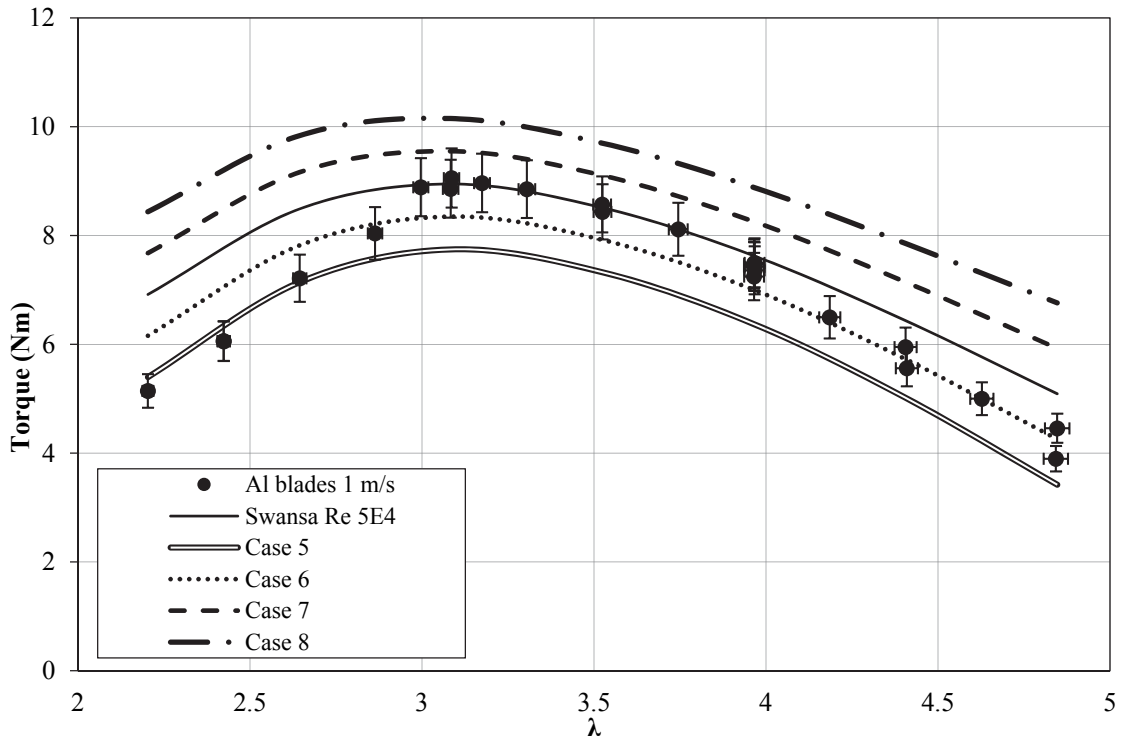
Figure 8-21 Torque–λ as a function of varying drag, from the Togneri et al. *base-case.*

194

Interestingly, the thrust was not highly sensitive to the drag coefficient used in BEMT, however, the turbine torque was sensitive to drag. In this case, an increase in drag (Case 5 and 6) gave close to the same performance as a decrease in lift (Case 3 and 4). It is not surprising that the lower lift and higher drag cases better matched the torque predicted at λ less than 3, where the turbine performance degraded as the airfoil α moved toward stall.

To investigate the coupled effect of altering lift and drag coefficients to mimic airfoil degradation and enhancement, four cases were trialed, given in Table 8-4. A similar investigation was done by Masters *et al.* [271], in which they sequentially altered the lift and drag coefficients from a base case. Masters *et al.* studied the effects of significant performance degradation due to factors such as biofouling or surface pitting due to cavitation by using cases with decreased lift (C_L decreased by 10% at all inflow angles) and increased drag (C_D increased by 50% at all inflow angles). They stated that these alterations in airfoil data were in line with those found in other investigations, and therefore similar alterations have been made here.

Table 8-4 Modifications in lift and drag data for sensitivity investigation.

Case	Lift	Drag	Reason	Outcome
9	10% decrease	50% increase	Mimic airfoil performance degradation	Under predicts thrust and torque at $\lambda>3$, but better match to torque at $\lambda<3$
10	5% decrease	25% increase		Under predicts thrust and torque at $\lambda>3$
11	5% increase	25% decrease	Mimic airfoil performance enhancement	Better match to experimental thrust, but over-predicts torque
12	10% increase	50% decrease		Better match to experimental thrust, but over-predicts torque

Figure 8-22 and Figure 8-23 show the variations in thrust and torque based on the four cases. Torque was the most sensitive to simultaneous variations in lift and drag. It has been shown to be highly sensitive to independent variations in both lift and drag, and hence varying both at the same time resulted in drastic changes in the BEMT predictions.

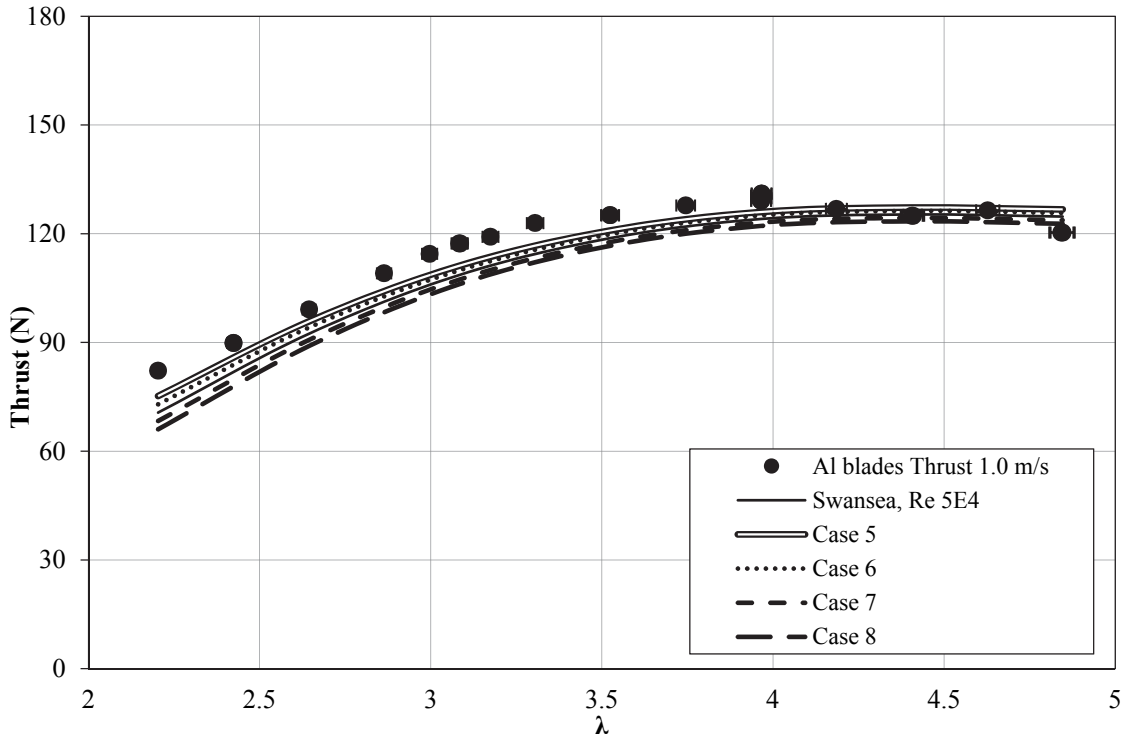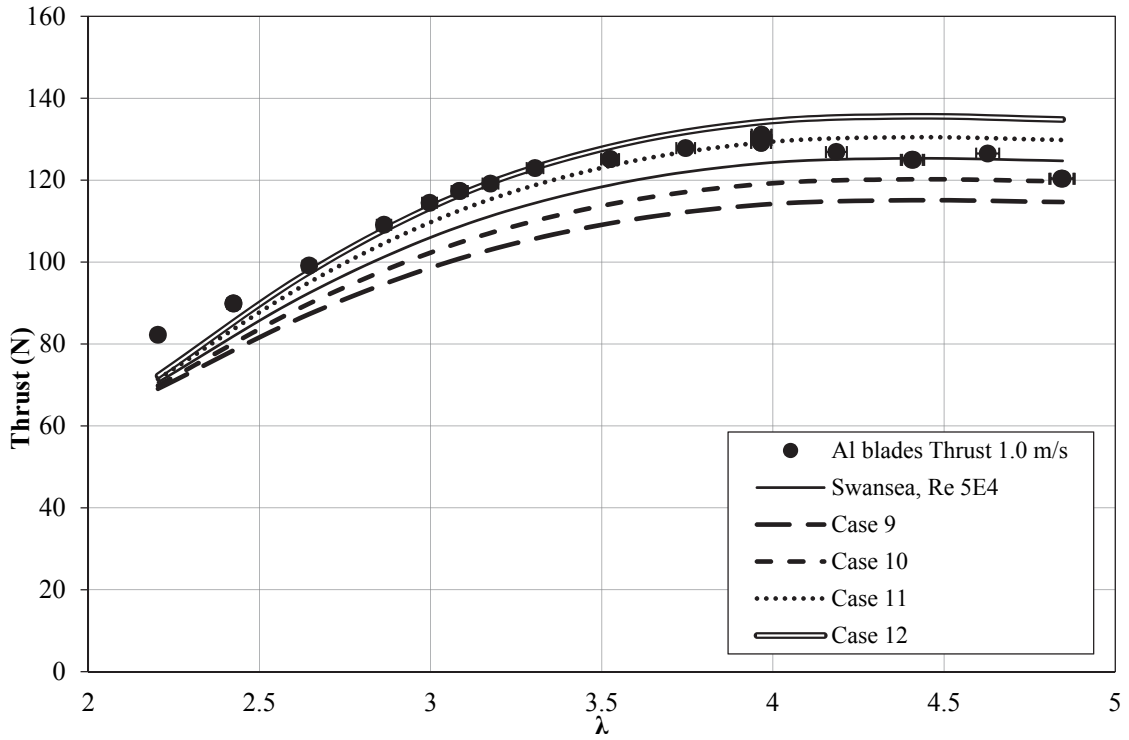*Figure 8-22 Thrust–λ as a function of varying lift and drag, from the Togneri* et al. *base-case.*
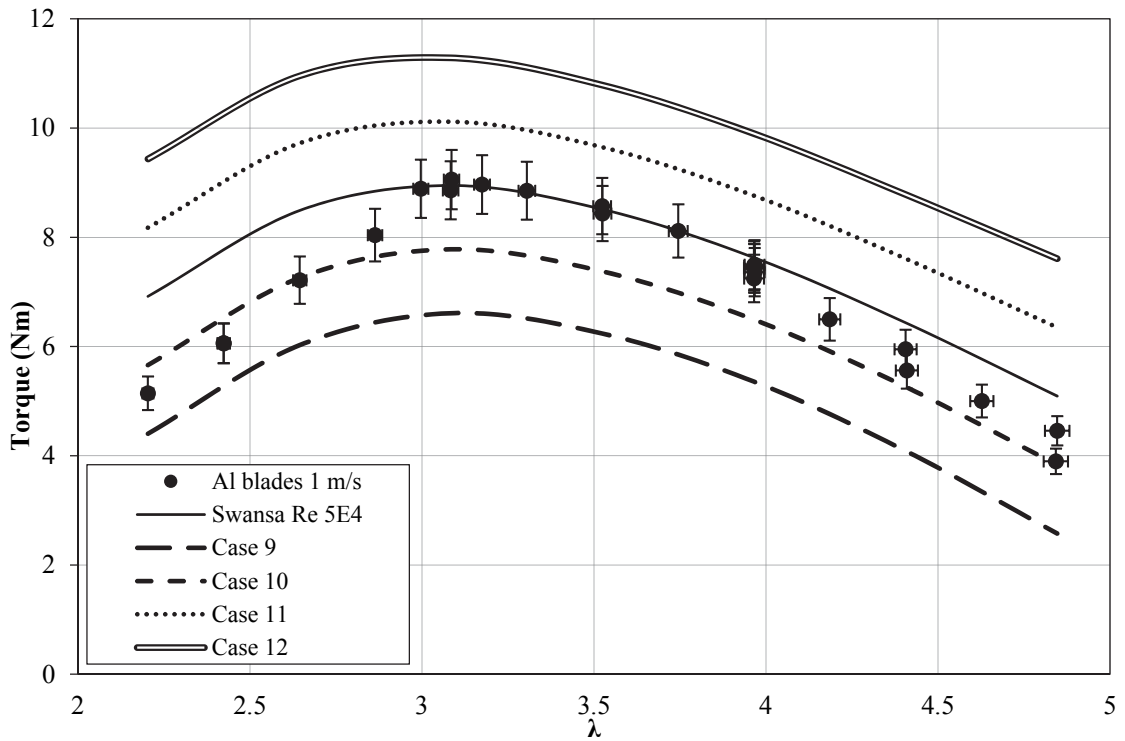
Figure 8-23 Torque–λ as a function of varying lift and drag, from the Togneri et al. *base-case.*

Case 12 (enhanced airfoil performance) had 27.8% higher torque predicted by BEMT than the baseline airfoil data, whereas thrust was only different by 8.5% at the most. This is likely do to the thrust being more sensitive to lift, which was only altered by 10% compared to the 50% alteration in drag. With the degraded airfoil performance (Case 9), the predicted torque was reduced by 25.4%, which would have major implications on the overall power capacity of the turbine.

Interestingly, an improvement in the airfoil performance (higher lift and lower drag, Case 11 and 12), resulted in a better match to the thrust experimental data, but greatly over-predicted the torque at low λ. In order to better match the torque data at low λ, a degraded airfoil performance (increased drag and lower lift, Case 9) was required. This is in agreement with the airfoil performance degradation expected at low λ. However, the degraded airfoil performance (Case 9) did not fit the experimental thrust data at low λ. These observations highlight the sensitivity of the BEMT predictions to airfoil performance, but require further investigation into the potential reasons for this sensitivity.

8.5.2 Blade Geometry

Due to the high quality of manufacturing, the dimensions of the blades and hub, as well as the pitch setting, were well quantified for the second set of hydrodynamic tests. However, variations in these parameters were all considered using the design tool at the peak $\lambda =$ 3.08. Compared to the influence of the airfoil data (from Figure 8-18 and Figure 8-19), for all values of λ, the relative sensitivity of the design tool to the input geometrical parameters was small. A $\pm0.5°$ change in pitch angle (less than the $\pm 0.381°$ of uncertainty in the pitch setting) resulted approximately in a 3% change in the thrust and torque predictions. This is small compared to the roughly 10% reduction in thrust loads associated with the 1.8° of tip twist predicted by the design tool based on BT coupling, but would still affect the overall performance results. This highlights the importance of accurately knowing the blade root pitch setting such that this uncertainty can be minimized to increase confidence in the BT performance of the composite blades.

8.5.3 Composite Materials

Section 6.1.4 showed the sensitivity of a laminate BT plate FEM to variations in the ply angles and thicknesses, but relative insensitive to material input parameters. The sensitivity of the FEM-BEMT design tool predictions of global thrust and torque to these inputs was investigated. Five percent variations in the ply angles and skin thicknesses were found to have less than a 1% effect on the composite blade global performance. This indicates a relative insensitivity of the design tool to the composite FEM inputs compared to the sensitivity to the BEMT inputs, highlighting the stability of the FEM component of the design tool.

8.6   Small-Scale Turbine Case Study

The prototype turbine modeled in Section 8.4 was simulated using the design tool to investigate operational conditions that were not tests experimentally, for both the composite BT blades and the rigid aluminum blades. Variable speed (VS) control was simulated to maintain an optimum λ of 3.8. A cut-in flow velocity of 0.5 m/s, design (rated) velocity of 1.0 m/s, and an extreme velocity of 1.3 m/s were simulated, and the rotational velocity was varied to maintain this optimum λ. A range of inflow velocities were simulated as this was considered more representative of the varying flow speeds observed at a typical tidal site.

At flow speeds above design conditions, typically VS control systems reduce the power coefficient of the turbine by increasing the rotational speed and λ (called over-speed power regulation [204]). However, in this case, a constant λ was maintained for all flow speeds. Due to the passive feathering of BT blades, the required increase in λ for power regulation was found to be less than that of rigid blades. A constant λ was therefore maintained to allow a comparison, in the same operating conditions, between the rigid blade and BT blade performance, isolating the effects of BT coupling from those of over-speeding.

Figure 8-24 and Figure 8-25 show the thrust loads and twist along the span of the blade (from blade element 1 at the root and blade element 10 at the tip) after each iteration until convergence for design conditions of 1.0 m/s and 86 RPM. The un-deformed blade shown in the plots is the blade before the consideration of BT coupling, effectively making it rigid.
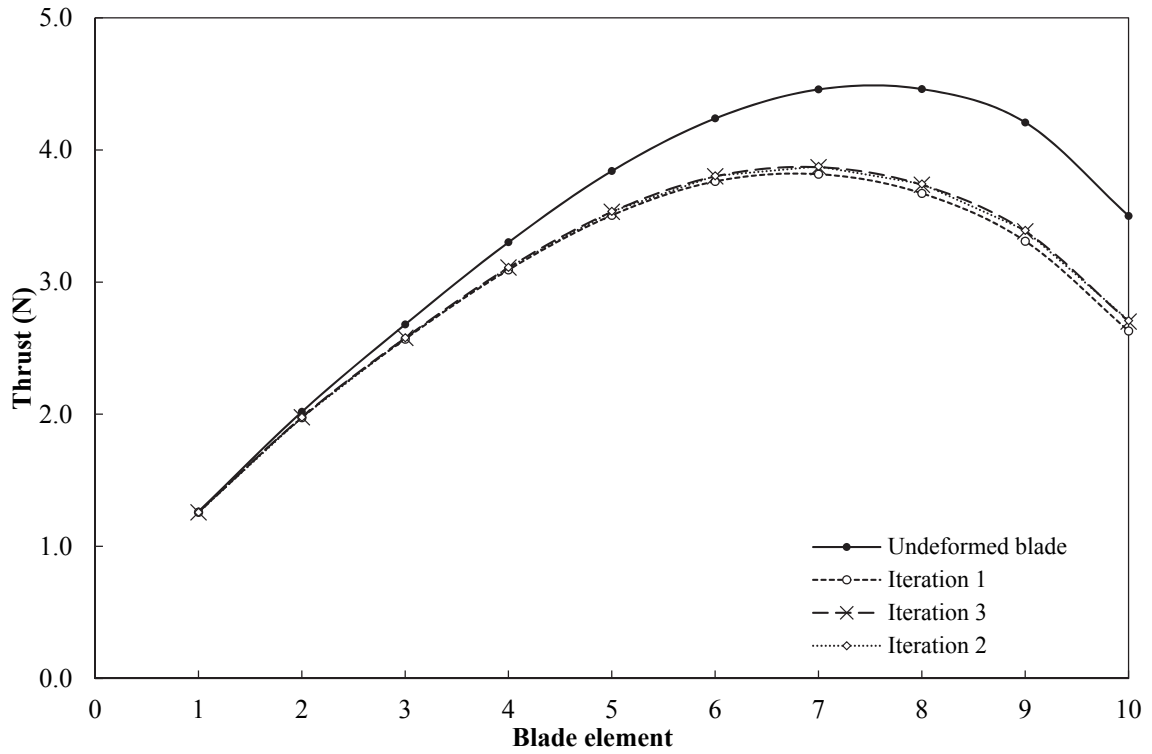
Figure 8-24   Thrust loads at each blade element along the blade span (1.0 m/s, 86 RPM).
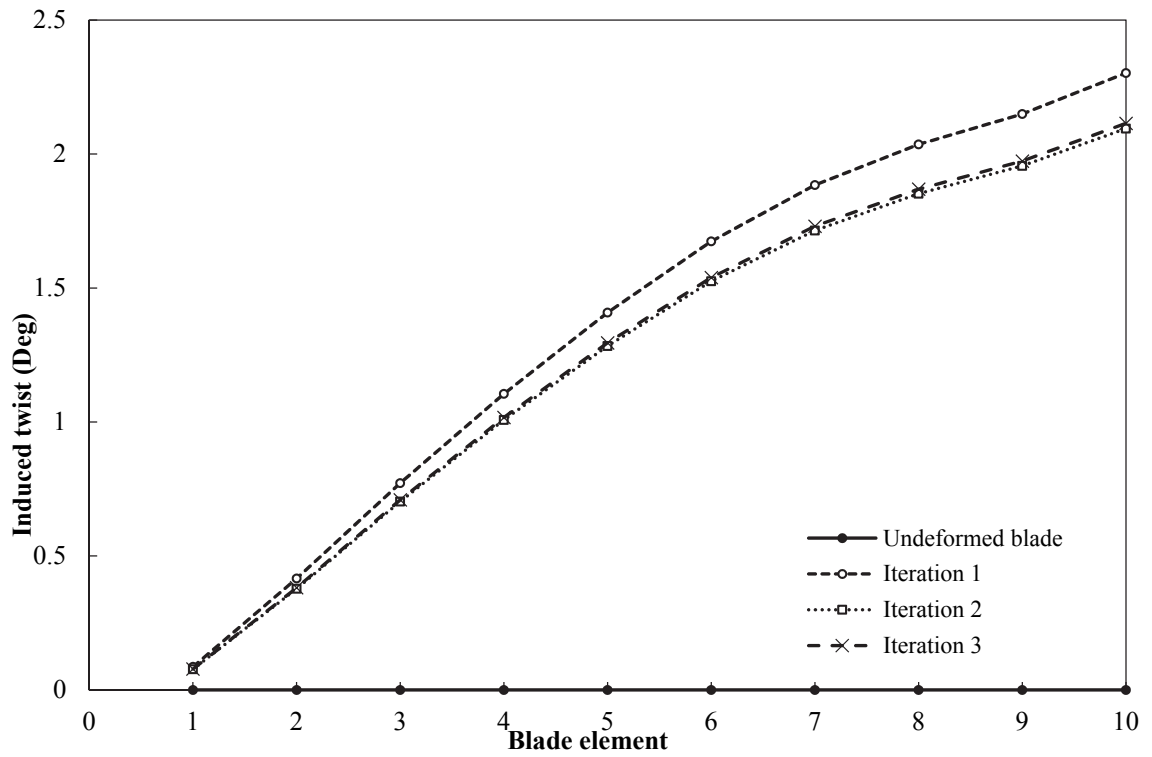
Figure 8-25 Induced twist at each blade element along the blade span (1.0 m/s, 86 RPM).

199

The induced twist over the blade span (from the root at blade element 1 to the tip at blade element 10) was 8.15% greater for the un-deformed blade compared to the final iteration (iteration 3), indicating that the initial BEMT-predicted loads caused greater deformation than the converged loads. As well, the thrust initially predicted by the design tool for an effective rigid blade was 16% greater than the final thrust prediction for the BT blade. As suggested by Maheri [235], this indicates the importance of iterating between the rotor performance and the blade structural response, as there are significant differences between single stage results (first iteration) and iterative results for a flexible blade.

Figure 8-26 shows the percent change in thrust and torque between the BT and rigid blades, as well as the maximum tip twist toward feather for the BT blades.
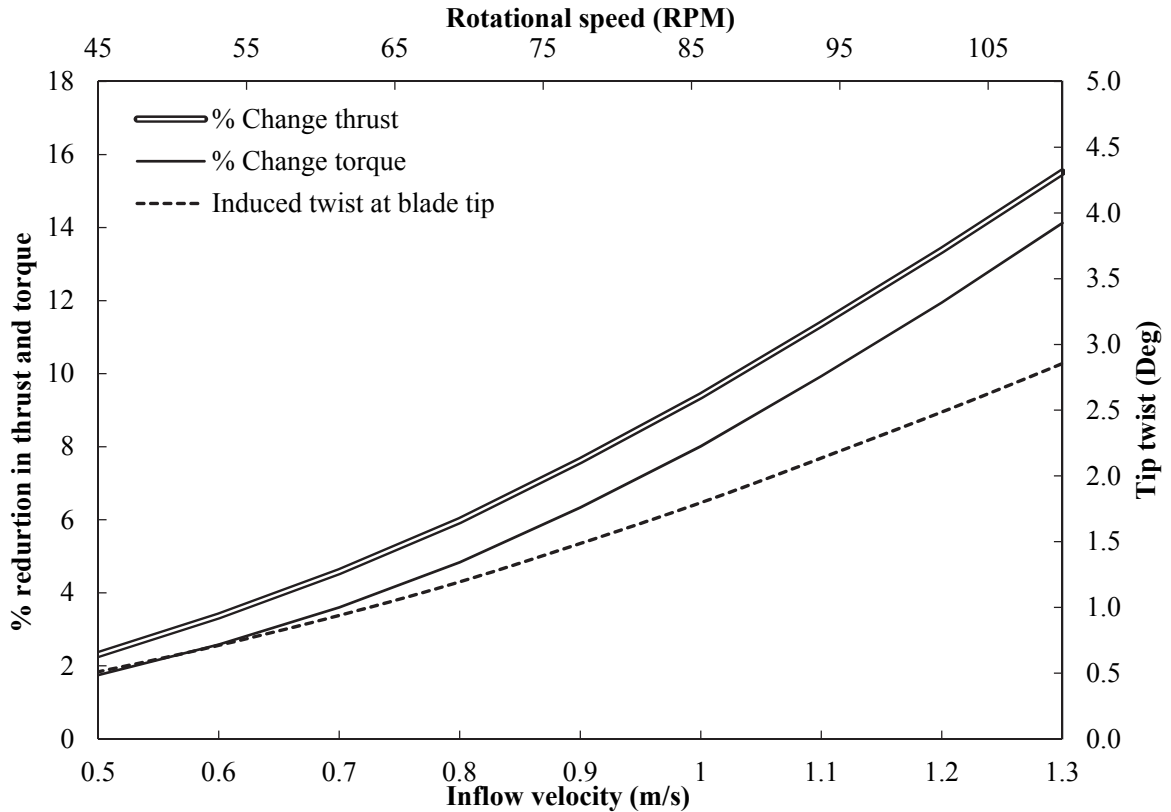
Figure 8-26 Percent decrease in thrust and torque, and induced twist at the tip of the blade at λ = 3.8.

The induced twist of the blade, as predicted by the FEM, changed proportionally to the square of the inflow velocity, with an R^2 value of 0.999. From Figure 8-26, at the maximum inflow velocity of 1.3 m/s (assumed to be the extreme load case), there were 2.95° of

induced tip twist, an 15.5% decrease in thrust loads, and 14.12% decrease in torque from the rigid blade. However, at design flow conditions (1.0 m/s and 86 RPM), the BT blades were predicted to have 1.82º of induced twist at the blade tip, giving an 9.40% reduction in thrust loads and a 8.01% reduction in torque. The large percent reduction in thrust at design and extreme flow speeds is desirable; however, the reduction in rotor torque between cut-in speed and design conditions is undesirable due to the decreased power this will produce in this operating range. This is addressed further through the consideration of a pre-deformed blade geometry for the full-scale turbine investigated in Section 9.3.

The trend of both reduced thrust loads and reduced torque is aligned with Wada's [139] experimental findings in which reduced thrust loads had associated reduced power for a small-scale turbine with flexible composite blades. Interestingly, this is counter to Nichols-Lee's [101] FSI results which showed a decrease in thrust coefficient and increase in power coefficient with the use of BT blades for a larger scale turbine with a minimum diameter of 10 m. This is thought to be due to differences in blade geometry and airfoil shape, including the pitch setting and pre-twist distribution of the blades, as well at the turbine operating conditions. Depending on the operational range of angles of attack, feathering could potentially increase drag while reducing lift, which could lead to increased power with decreased thrust, depending on the influence of both lift and drag on the axial and tangential loads (thrust and power). Although these results indicate the possibility of reducing thrust while increasing power capture, it is thought that the range of angles of attack would not be optimal.

As BT blades bend axially, the swept area of the rotor is decreased, decreasing the available area for power capture. However, when the reduced rotor area from axial bending was considered in the BEMT model, there was less than 0.5% difference in the power and thrust loads, and hence this effect was considered negligible for this scale turbine. As well, the assumption of the point of load application and the neglect of the aerodynamic moment is recommended for further consideration in future work. Although in this case the aerodynamic moments are small compared to lift and drag for the NREL S814 airfoil, if this design tool were used for blades with other airfoils, this may not be the case. In this case it was assumed that thin-airfoil theory was applicable to the NREL S814 airfoil, and

hence ¼ chord was used as the point of load application. Future work should investigate how applicable this theory is to the relatively thick (24%) NREL S814.

8.6.1 Stress Analysis

Using the design tool, the stress in the composite blade described in this section was analyzed. The stresses in the composite material are directly related to the level of deformation of the blade. Figure 8-27 shows the Tsai-Hill failure index (inverse of the Tsai-Hill SF), the *y*-displacement of the blade and the tensile normal stresses in the longitudinal fiber direction, at 1.0 m/s and 86 RPM.
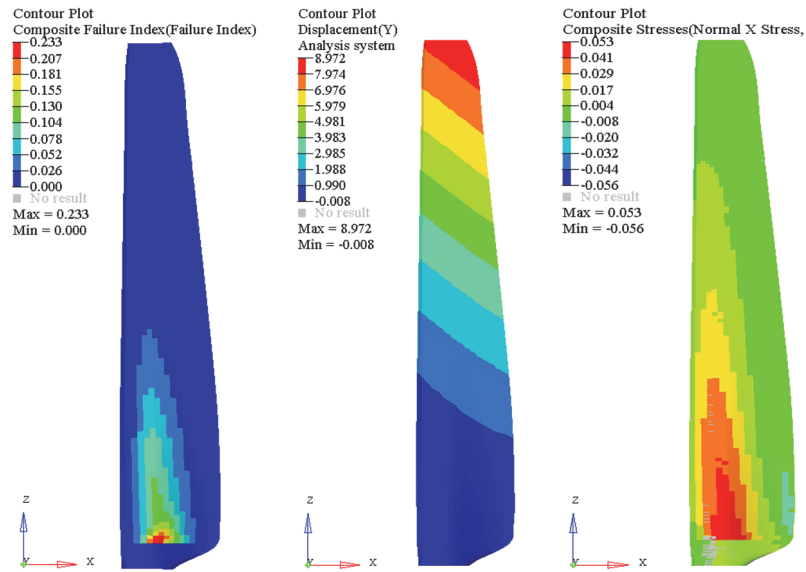
Figure 8-27 FEM composite blade contour plots after convergence for a 1.0 m/s and 86 RPM design case, left) Tsai-Hill failure index, middle) y-displacement (mm), right) normal stress in 1-direction (GPa).

From the displacement contour plot, the trailing edge of the blade has greater *y*-direction bending than the leading edge, indicating twisting to feather, particularly at the outer span of the blade. The highest stresses in the composite material occurred at the base of the working section of the blade, where a ply drop (sudden change in composite thickness) caused a stress concentration. As shown in Figure 8-27, at design conditions, the Tsai-Hill failure index was 0.233, giving a SF of 4.29, which is considered acceptable.

Figure 8-28 shows the composite SFs, based on the Maximum Stress failure theory (transverse tension and compression, longitudinal tension and compression, and shear) and

Tsai-Hill failure theory, as a function of inflow velocity. From Figure 8-28, the transverse tension and shear directions had the lowest SFs, indicating high stresses compared to material strengths. Therefore, the transverse tensile and shear stresses are limiting factors in the composite blade design.
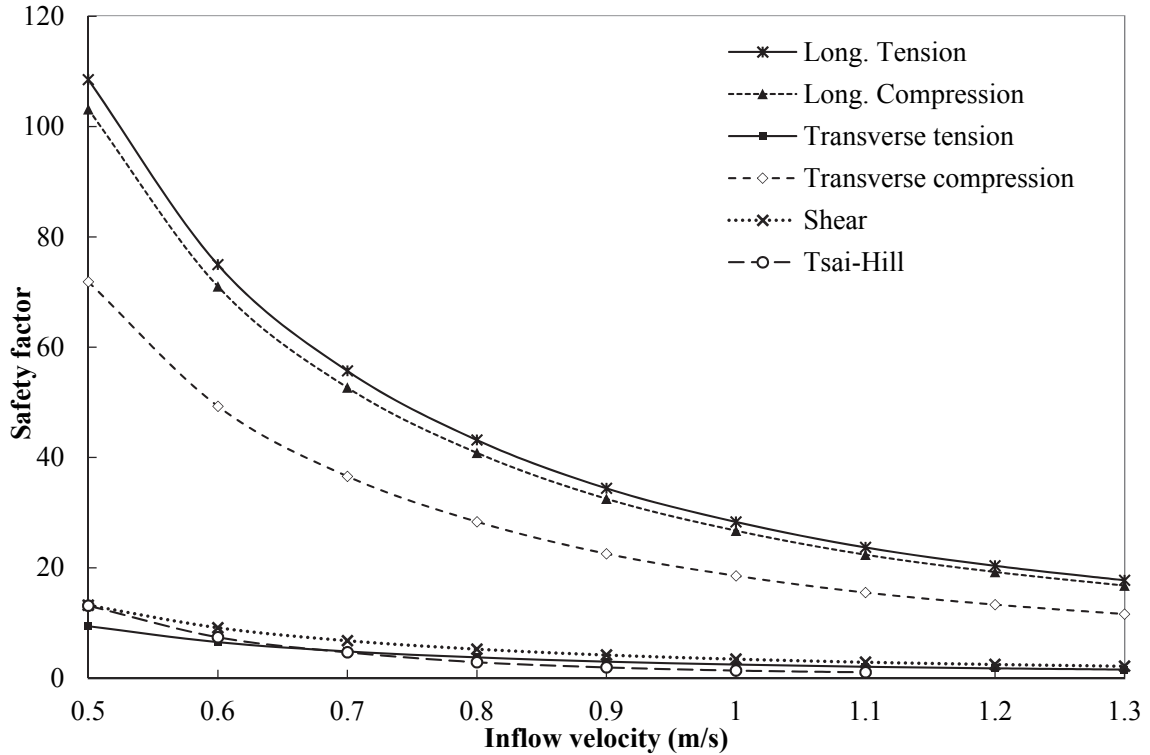
Figure 8-28 Safety factors for composite blade based on FEM predicted stresses.

For a BT blade, the pressure (lower) surface of the blade experiences transverse tension and shear due to the off-axis fibers and the torsion that is induced by *x*-direction (axial) bending. In this simulation, as the flow speeds increased, the material SFs decreased, with the transverse tensile SF reaching a value of 1.55 and the shear SF reaching a value of 2.16 at the maximum (extreme) flow speed of 1.3 m/s.

From Figure 8-28, Tsai-Hill failure theory predicted SFs that were the same or higher than the transverse tensile SF based on Maximum Stress failure theory. Tsai-Hill failure theory considers the interaction between stresses in the different material directions, and, although more accurate compared to experiment [215], tends to be less conservative than the Maximum Stress failure theory. The Tsai-Hill failure theory also does not explicitly specify the directionality of failure. For example, the high likelihood of failure in the transverse

tensile direction for this blade design would not have been identified if only the Tsai-Hill failure theory was used, even though the design would have been identified as having a low material SF. For this reason, a combination of Tsai-Hill and Maximum Stress failure theories is preferable for early stage design.

This simulation took less than 10 minutes to converge over the range of velocities from 0.5 to 1.3 m/s, in increments of 0.1 m/s, on a standard engineering workstation. This indicates that the objective of a fast and efficient design tool was met for the simulation of the small-scale turbine.

8.7 Design Study: Composite BT Blades

Initial results of an analytical study indicated ply angles of 30º optimized the BT response of a laminate plate. However, to inform more detailed composite material design, the design tool was used to investigate the effect of composite ply angles on BT blade performance. The objective of the study was to maximize twist and minimize stress in a small-scale composite BT blade. The same material properties and set-up in Section 8.4 were used here. For design conditions of 1.0 m/s and $\lambda = 3.8$, the small-scale turbine was simulated with a range of ply angles from 0º to 90º, in increments of 5º. Figure 8-29 shows the percent reduction in thrust and torque, Figure 8-30 gives the tip twist and bending displacement of the blade, and Figure 8-31 shows the transverse tensile and shear SFs (based on Maximum Stress failure theory), and the SFs based on Tsai-Hill failure theory.

The design curves in Figure 8-29 demonstrate that for angles of 30º, the BT composite blade has the greatest amount of tip twist, and corresponding highest thrust reductions. The slight increase in blade twist for ply angles of 90º indicates that based on the geometry of the blade, a 90º ply angle as defined in this investigation is slightly off-axis toward the tip of the blade due to the high surface curvature of the NREL S814 airfoil. The Tsai-Hill and transverse tensile SFs generally decrease with increasing ply angle, as bending displacement increases, whereas the shear stress SF reaches a minimum corresponding roughly with the maximum twist, and then increases as the blade twist decreases. These results are in line with the findings of the design studies for BT laminate plates given in Section 6.1.5.
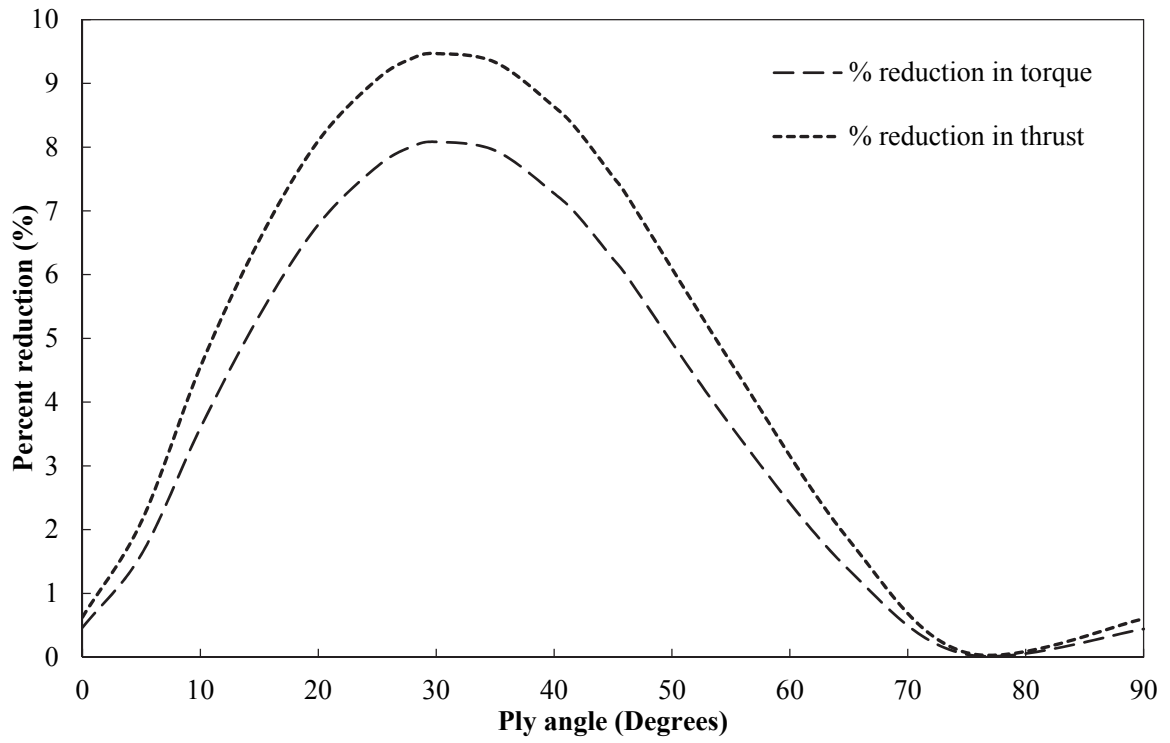
Figure 8-29 Percent reduction in thrust and torque as a function of ply angle.
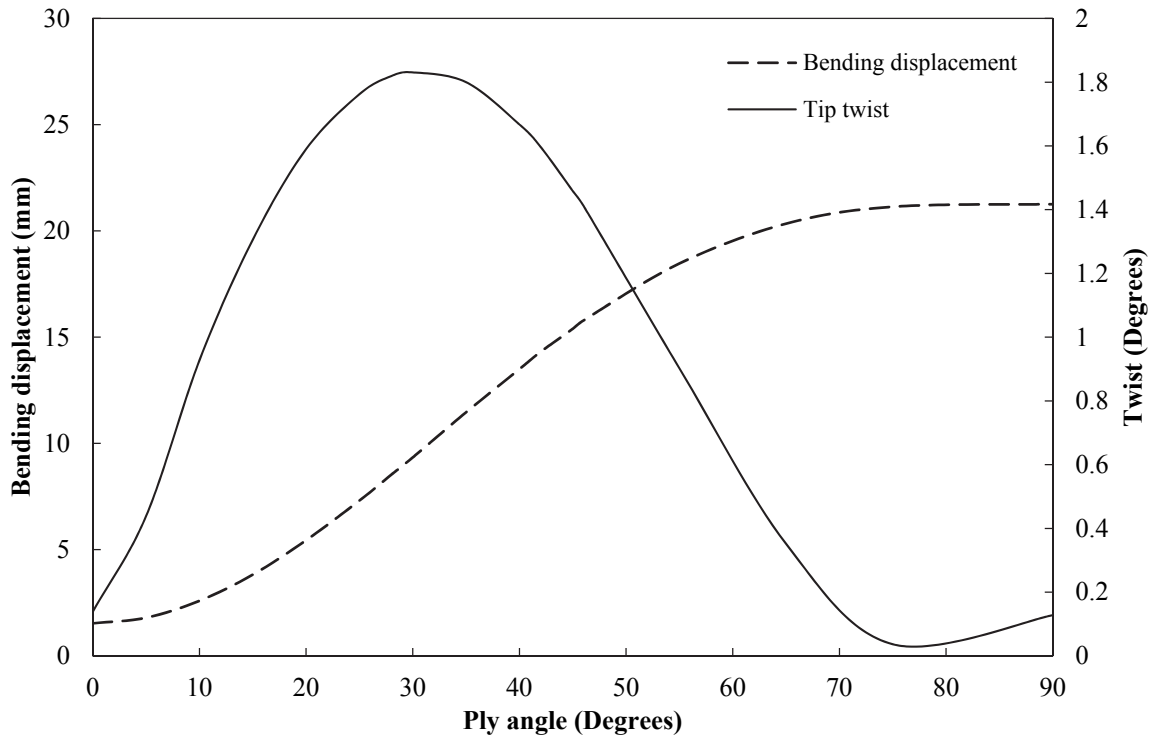
Figure 8-30 Tip twist and bending displacement as a function of ply angle.
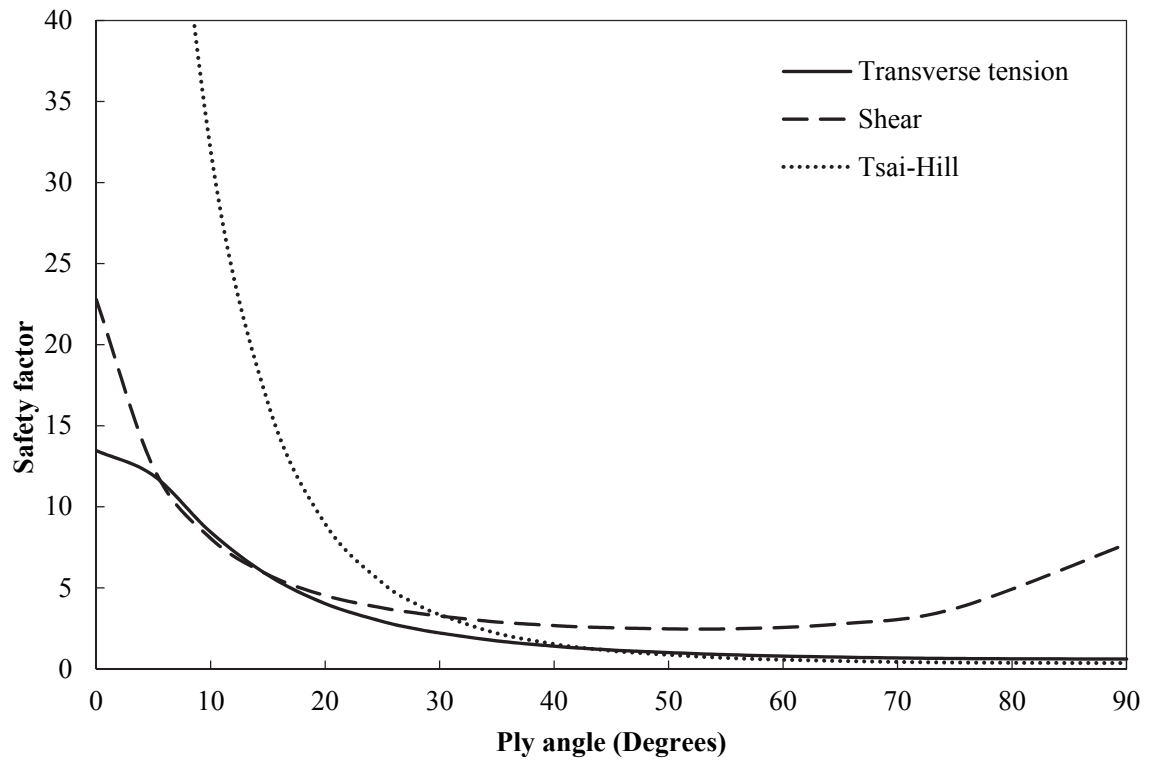
Figure 8-31 SFs as a function of ply angle.

CHAPTER 9
CASE STUDY:
FULL-SCALE TURBINE

For full-scale turbine blade designs, the FEM-BEMT design tool can be used to narrow down the design space, reducing the computational time for broader design investigations. The FEM-BEMT design tool was used to perform a case study for a full-scale 10.4 m diameter hypothetical three-bladed turbine with 4.0 m NREL S814 BT blades (hub radius of 1.2 m). The blade length and chord lengths were scaled linearly by a factor of 13.6986 from the blade geometry presented in Section 4.2. The pre-twist of the blade is discussed in Section 9.3.

For larger scale blades operating at higher Reynolds numbers, XFOIL can be used effectively to predict airfoil data. As well, at higher Reynolds numbers airfoil performance is less variable and more predictable [184], hence airfoil data at a single Reynolds numbers may be sufficient to capture the performance of the full-scale turbine. At this scale, the simulated turbine operated at Reynolds numbers ranging from 2×10^6 to 8×10^6, and XFOIL was used to obtain airfoil section data over this range, in increments of 1×10^6, for use in the BEMT code. A linear interpolation was performed to estimate the lift and drag coefficients at Reynolds numbers between these discreet curves. In XFOIL, the user-specified parameter NCRIT mimics the effects of free-stream disturbances, such as turbulence, on BL transition [259]. An NCRIT value of 9 is typically used for average wind tunnel conditions, and values of 4 to 8 for more turbulent wind tunnels. For the full-scale device assumed to be operating in a turbulent environment, an NCRIT value of 2 was used, as was done by other researchers working in tidal energy [272].

9.1 Simulation Conditions

Based on resource characteristics of the Northern Admiralty Inlet of Puget Sound [65], a cut-in flow velocity of 0.75 m/s, design (rated) flow velocity of 2.5 m/s, and extreme flow velocity of 3.5 m/s (1.4 times the design speed) were used, for an assumed hub height of approximately 30 m from the seabed. An acoustic Doppler current profiler survey [65] at this site showed the mean water velocity to be approximately 1 m/s, although velocities as high as 3 m/s occur during the tidal cycle and hence have to be considered. At this scale, preliminary BEMT results for rigid blades showed this turbine to have an optimum λ of 4. For the design speed of 2.5 m/s, a rotational speed of 18.3 RPM was used to achieve an optimal λ of 4. The rotational speed was varied over the range of flow speeds to maintain this λ using simulated VS control.

9.2 Blade Element Convergence Study

Figure 9-1 shows the results of a blade element convergence study for the 4.0 m NREL S814 blades.
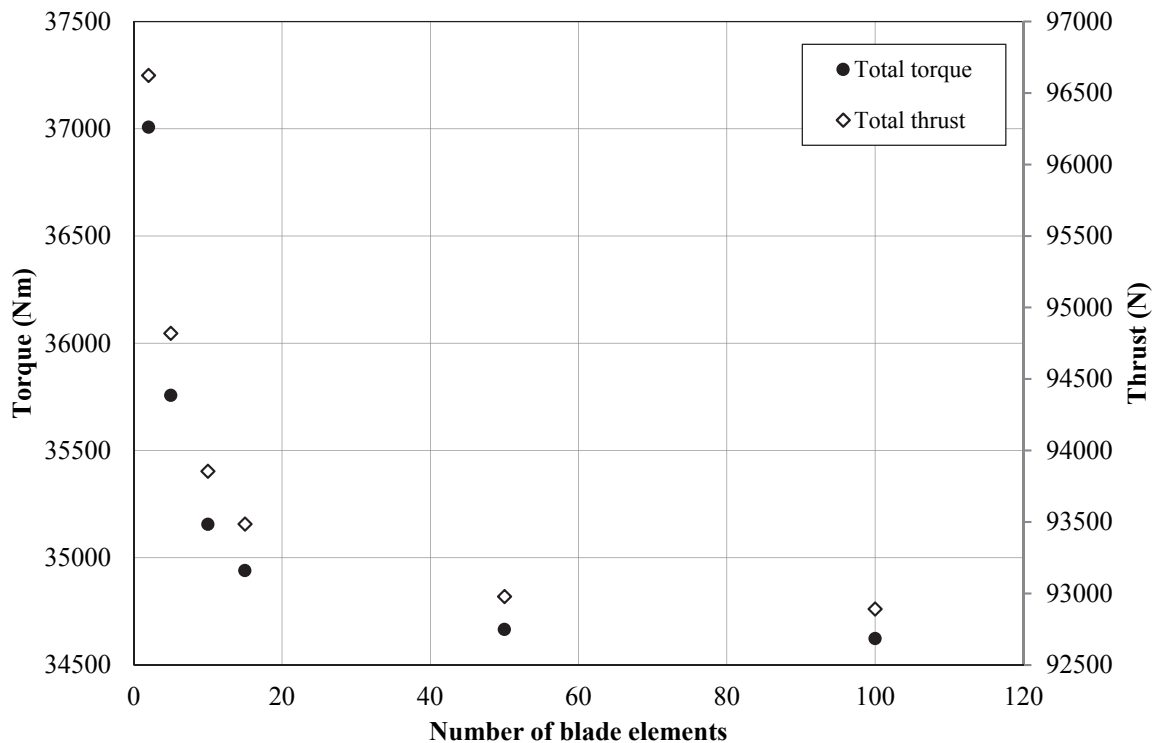
Figure 9-1 Blade element convergence for 4.0 m blade.

For the 4 m blade, there was less than 4% difference between using 2 elements and using 100, and less than 1% difference between using 10 elements and 100 elements, which is within the normal measurement error. However, the trend clearly shows better convergence with increasing element numbers. In this case the objective was to minimize computational time, therefore, 10 blade elements were used in the BEMT.

9.3   FEM Development

In the FEM, the blade skin was constructed of unidirectional graphite epoxy composite with 30º off-axis plies to induce BT coupling. This ply angle was chosen based on a design of experiment investigation showing maximized BT coupling, discussed in Section 8.7. The skin thickness was tapered linearly in 11 sections using ply drops (discrete decreases in composite thickness), from 24 mm at the blade root to 2 mm at the blade tip, as shown in Figure 9-2. This thickness was determined iteratively using the design tool to obtain a required minimum SF of 1.3 for shear stress (using the Maximum Stress failure theory) at extreme flow conditions. In this case shear stress was the limiting factor to composite thickness, and, for this skin thickness, all other SFs were greater than 1.3 at extreme conditions. The stresses in the blade were highest at the root, hence more material was required in this area. However, the majority of the twist behavior occurred at the blade tip, therefore the blade still had sufficient BT coupling to result in load reductions as desired. An investigation and discussion of the associated stresses in this composite design are given here.

Section 1
24 mm thick

Decreasing skin thickness →

Section 11
2 mm thick
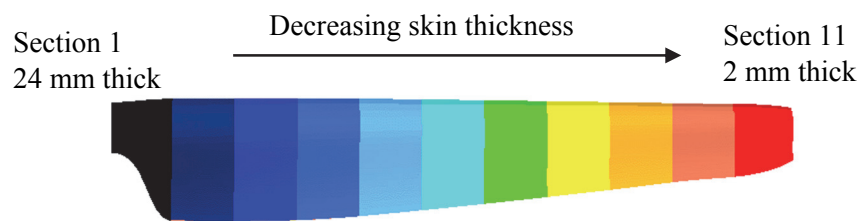
Figure 9-2 Blade skin thickness showing location of ply drops.

Closed-cell foam was used for the body of the blade for buoyancy, to prevent flooding, and for ease of manufacturing. Material properties are given in Section 4.2. Based on the results of a mesh convergence study, 30 mm tetrahedral 3-D elements were used to mesh the blade

core, and 30 mm 2-D shell elements were used to model the composite skin of the blade. For a conservative design, it was assumed that the blade skin carried the full load and that additional layers such as a gelcoat would not be load-bearing and were not considered in the model. This no-spar design is aligned with the one-shot resin transfer molded manufacturing process which is currently being used by some developers in the industry [273]. The blade root, including attachments such as bolts and inserts, was not considered.

9.4 Pre-Deformed Blade Geometry

From the small-scale turbine simulations in Section 8.6, there was a reduction in torque (and hence power capture) at design conditions. To increase power capture at design conditions, a pre-deformed blade shape was obtained by slightly altering the pre-twist distribution of the baseline blade (given in Section 4.2). The pre-twist of a HATT blade is the twist distribution along the span of the blade as manufactured (discussed in Section 2.2.1). The goal was for the pre-deformed blade to be designed such that it twisted to the optimum α at design conditions, and continued to twist to feather to reduce loads and power at extreme flow speeds. This is shown schematically in Figure 9-3, which gives the airfoil cross section at the tip of the blade for a rigid blade, BT blade with the original twist distribution, and pre-deformed BT blade for a range of loading scenarios.

As shown in Figure 9-3, a rigid blade maintains the same shape at unloaded, design, and extreme conditions. Assuming that this rigid blade shape (pre-twist) gives the optimum α at design conditions, the BT blade has a comparatively reduced α at design conditions. Although this results in reduced loads, it also leads to less power capture at design conditions. This is the scenario with the rigid and BT blades tested in Section 5.2. However, a pre-deformed BT blade (blue section in Figure 9-3) has an unloaded shape that is twisted toward stall compared to the rigid blade. As this blade is loaded, it will twist into the optimum α (same shape as the rigid blade) at design conditions, but continue to twist at extreme conditions to reduce loads and power, as desired. This is also demonstrated in the power and thrust coefficient curves in Figure 9-5 and Figure 9-6. A pre-deformed blade shape was therefore selected for the 4.0 m case-study blade.
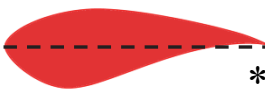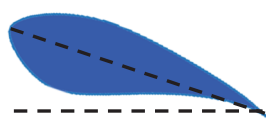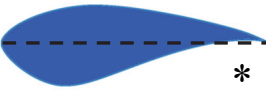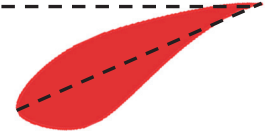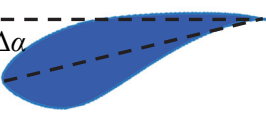
Figure 9-3 Schematic of rigid blade (black), BT blade (red), and pre-deformed BT blade (blue), the [*] denotes the optimum α for design conditions.

The original pre-twist shape of the blade (black and red sections in Figure 9-3) is given by β_o and the induced twist from BT coupling at design conditions is given by ϕ_i. To select an appropriate pre-twist for the blade, an iterative process was used to obtain a pre-deformed shape that resulted in the same α as the rigid blade at design conditions; a small amount of twist was subtracted from β_o, giving the new pre-twist blade shape, β_n.

As a first approximation, the blade was pre-twisted toward stall by ϕ_i (pre-deforming the blade toward stall by the amount that it was predicted to twist toward feather from BT coupling). However, due to the increased loads on a blade that has a more stalled α, this resulted in the blade twisting past the optimum α. Therefore, the amount of pre-twist was slightly less than ϕ_i. The final pre-deformed shape of the 4.0 m blade compared to the original shape is given in Figure 9-4.
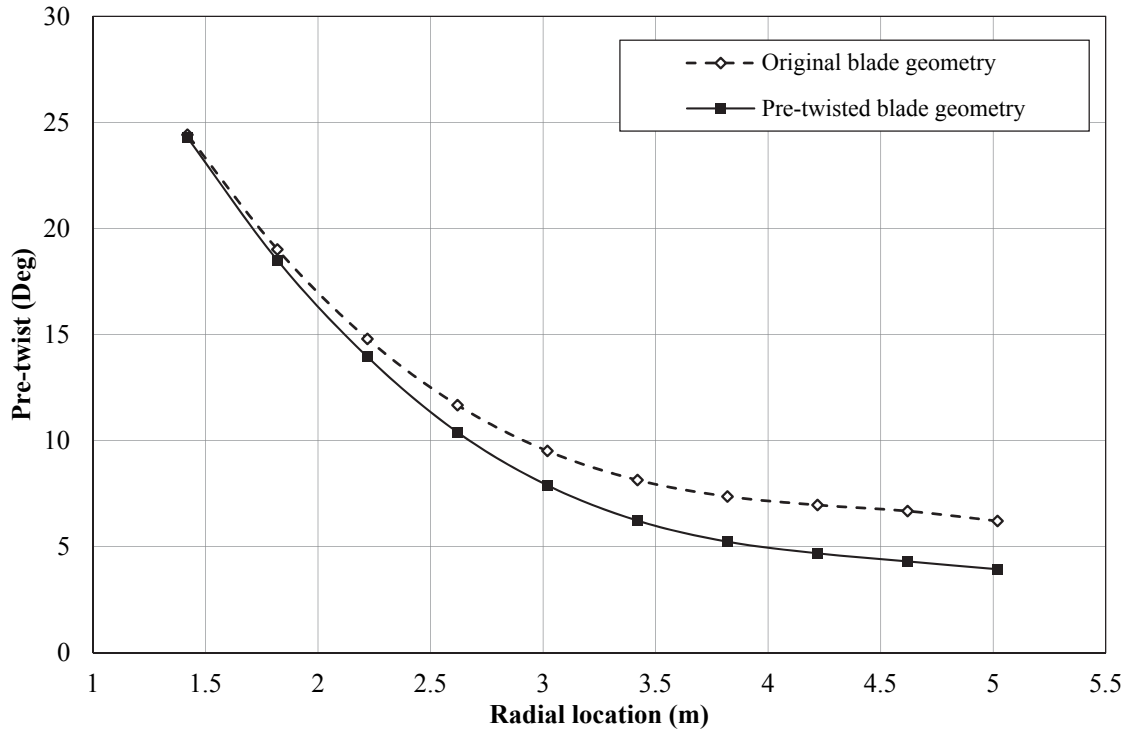
Figure 9-4 Original and pre-deformed blade pre-twist geometry along the span.

Table 9-1 gives the blade geometry with respect to the case-study turbine.

Table 9-1 Geometry of 4.0 m long full-scale NREL S814 blades relative to theoretical turbine.

Blade element	Turbine radius (m)	Blade length (m)	Pre-twist (Original blade geometry) (Degrees)	Pre-twisted blade geometry (Degrees)	Chord length (m)
1	1.42	0.22	24.42	24.28	0.87
2	1.82	0.62	19.01	18.49	0.84
3	2.22	1.02	14.79	13.94	0.80
4	2.62	1.42	11.67	10.39	0.75
5	3.02	1.82	9.51	7.88	0.70
6	3.42	2.22	8.14	6.22	0.645
7	3.82	2.62	7.365	5.23	0.60
8	4.22	3.02	6.963	4.68	0.55
9	4.62	3.42	6.674	4.30	0.49
10	5.02	3.82	6.209	3.93	0.42

9.5 Results

Figure 9-5 and Figure 9-6 show the power and thrust coefficients (C_p and C_T, respectively), for both the pre-deformed and original blade shapes with BT coupling. The rigid blade performance predictions are also shown here for both blade shapes to enable a comparison.

Using VS control, at design conditions of 2.5 m/s, the pre-deformed BT blades (small dashed line) had approximately the same power and thrust coefficients as the original rigid blade (thick solid line). However, at the maximum flow speed of 3.5 m/s, the pre-deformed BT blades had a 5.4% reduction in power and 8.7% reduction in thrust loads compared to the original rigid blade, with 4.62º of induced twist at the tip of the blade. To put this in perspective, the power capture and thrust loads are both proportional to the swept area of the blades. Therefore, to increase the power capture at cut-in speed by the same 5.4% not using BT blades, the blades would have to be lengthened by the same percent. As well, to get the 8.7% thrust reductions at the extreme flow speed would require a decrease in the blade length of 8.7%, resulting in an equivalent reduction in power capture.
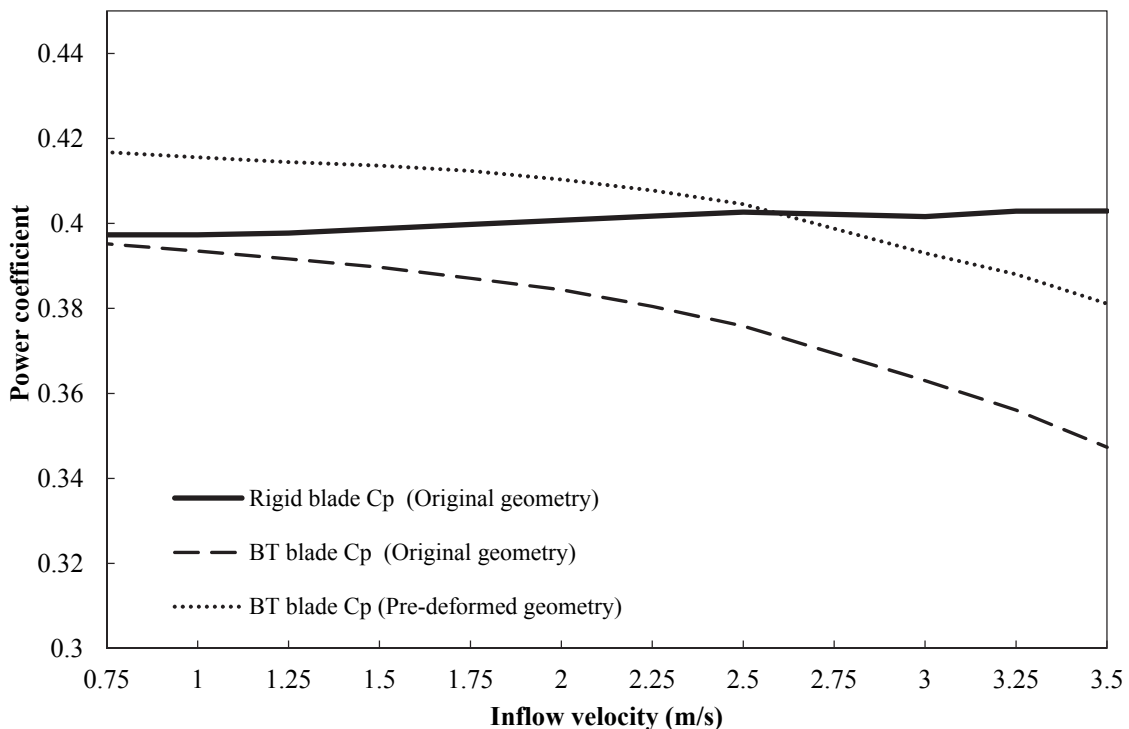
Figure 9-5 Power coefficient for pre- deformed and original blade shape.
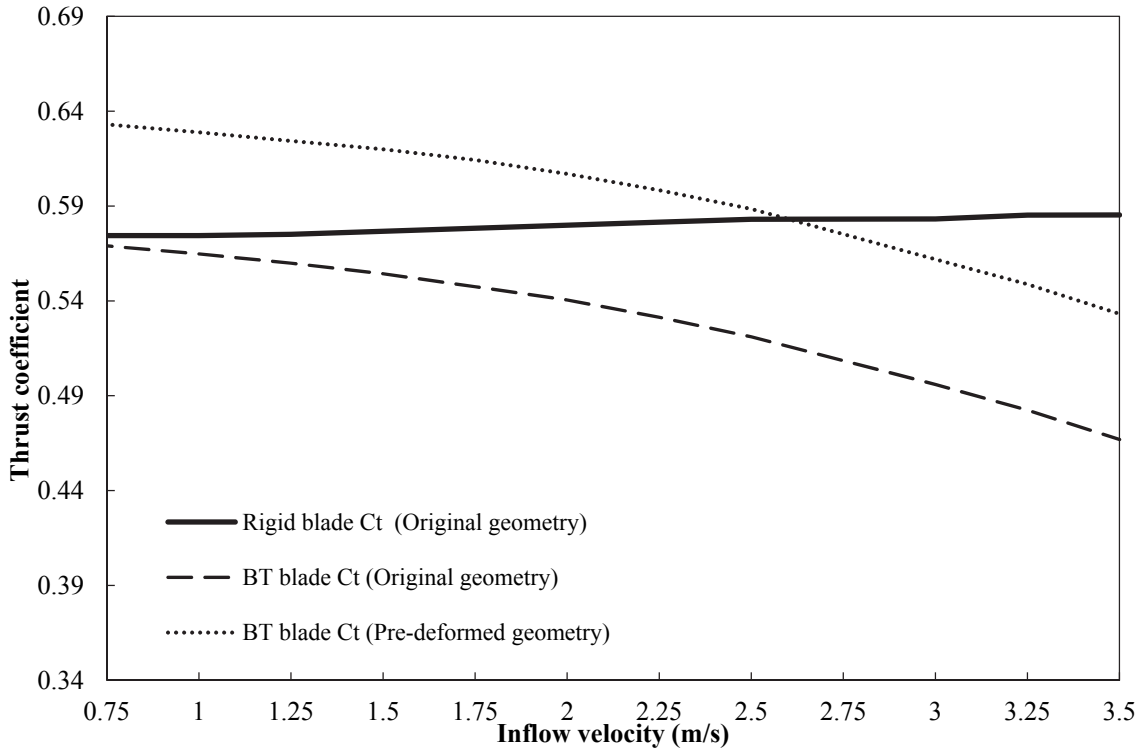
Figure 9-6 Thrust coefficient for pre- deformed and original blade shape.

Although this is less than the thrust reductions realizable using the original BT blade geometry (19.9% reduction in thrust loads at extreme flow speeds compared to the rigid blades, as shown by the thick dashed line in Figure 9-6), the increased power capture between cut-in and rated speeds means that for the design loads, more power is captured. At the cut-in-speed of 0.75 m/s there was a 4.9% increase in power capture using the pre-deformed BT blades compared to the original rigid blade geometry, with an associated 10.3% increase in thrust loads. The thrust loads at this low flow speed were significantly lower than at design conditions, so this percentage increase in thrust is not expected to affect sizing and design of structural components.

The power coefficients for the full-scale model, although a similar blade geometry and airfoil shape to the small-scale turbine simulated in Section 8.6, was higher than for the small-scale turbine because of the increased lift and decreased drag of the airfoil operating at higher Reynolds numbers. The use of airfoil data from XFOIL over the range of operational Reynolds numbers also caused the initial C_p and C_T to increase slightly with inflow speed, as the lift coefficient predicted by XFOIL increased with Reynolds number.

If airfoil data at a single Reynolds number were used in this simulation, the rigid blade power and thrust coefficient predictions would be constant with λ.

9.5.1 Stress Analysis

At each iterative step, the FEM component of the design tool outputs the stresses for each element of the blade. Figure 9-7 shows the composite stresses in the longitudinal (z-direction) and transverse (x-direction) directions, as well as shear, for the blade at extreme conditions.
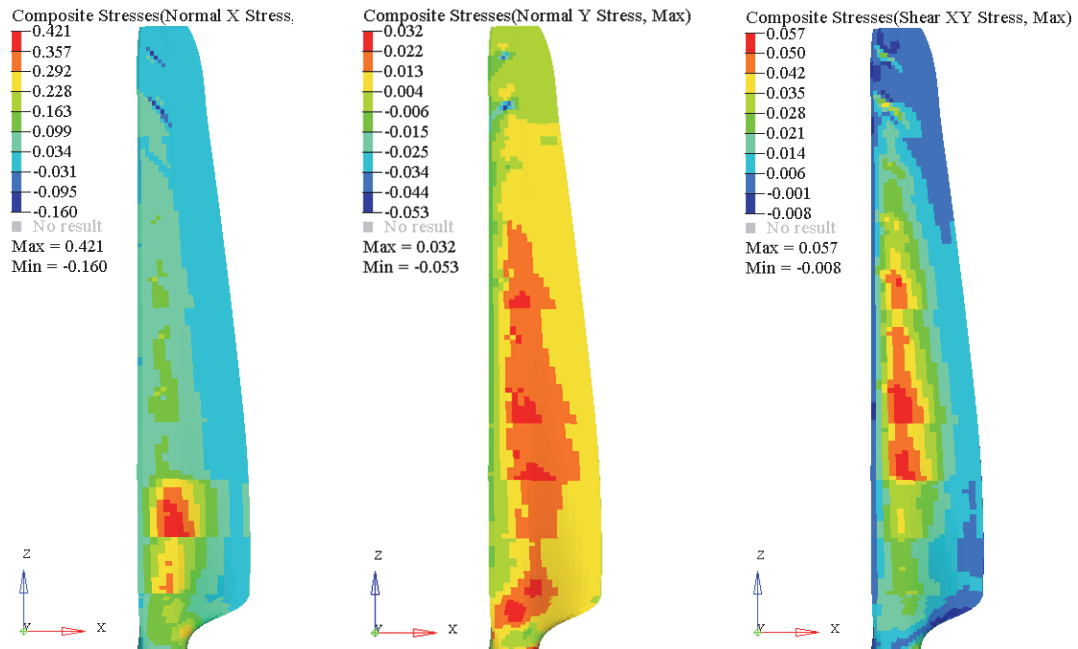
Figure 9-7 Stress in composite blade design for full-scale blade.

From Figure 9-7, the highest stresses occurred in the blade at the root section, at the interface between ply drops where stress concentrations were formed. For an optimized and cost effective design, material costs can be reduced by tapering the composite thickness toward the blade tip using ply drops. However, ply drops can result in stress concentrations which have been shown to increase the failure likelihood of a composite structure. A study by Vidyashankar [274] showed that a large number of plies dropped at the same location result in a higher failure likelihood compared to several locations with less plies at each drop. This paper also showed that plies oriented at an angle of 30° had a higher likelihood of failure at the location of the ply drop than those at angles of greater than 60°. This

indicates the importance of considering both the location and orientation of the dropped plies. Future work should investigate decreasing the stress in the blade by spreading out the ply drops or by dropping the plies parallel to the fibers instead of perpendicular to the z-axis of the blade as is done in this model.

At each iterative step, the design tool calculated a SF for the composite material based on both the Maximum Stress and Tsai-Hill failure theories. Figure 9-8 shows the SFs in transverse tension and compression, longitudinal tension and compression, and shear, for the pre-deformed BT blade shape. The SF based on Tsai-Hill failure theory is shown as well. Figure 9-9 shows the same SFs, but narrowed in on the higher flow speeds. These SFs were calculated for the element with the highest stress over the entire blade, hence giving the lowest SF for the entire blade for each material direction (and the most conservative estimate of failure).
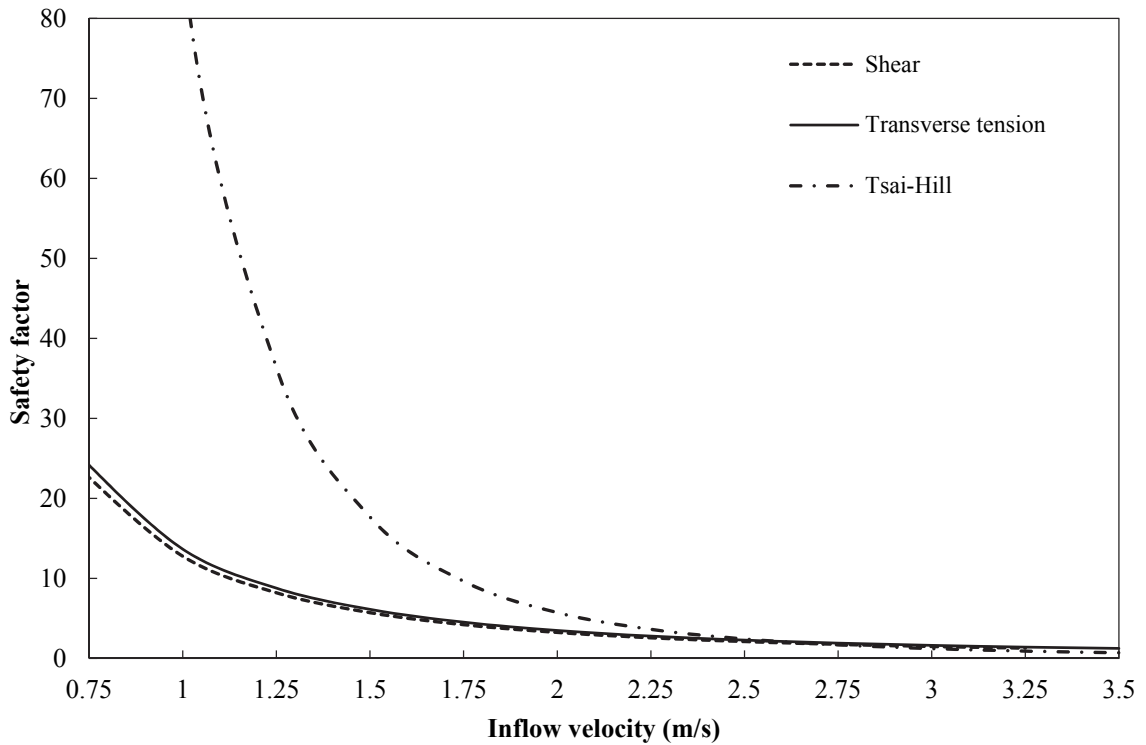
Figure 9-8 SFs for original and pre-twisted blades with BT coupling.
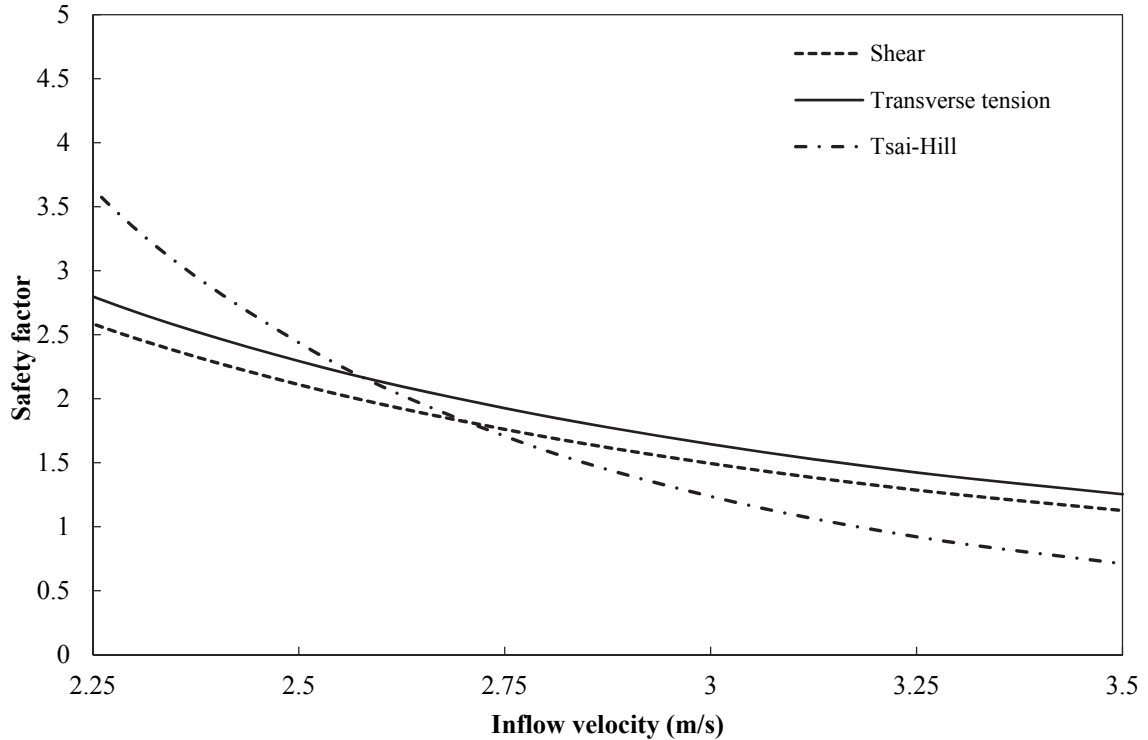
Figure 9-9 SFs for original and pre-twisted blades with BT coupling, zoomed in on higher flow speeds.

From Figure 9-8, for the pre-deformed blade shape at design conditions of 2.5 m/s, the design tool predicted a SF of 2.29 in the transverse tensile direction and 2.21 in the shear direction, indicating an acceptable level of confidence in the composite design. However, at extreme conditions, there was a SF of 1.25 in the transverse tensile direction and 1.13 in the shear direction.

The Tsai-Hill SF at an inflow of 3.5 m/s was approximately 1. This indicates that for this design, loading the blade beyond extreme conditions would result in an increased likelihood of failure. Although there are limitations of the design tool, as discussed, this gives an idea of a reasonable blade design to start with when using more computationally expensive tools.

9.6 Cost Discussion

This section gives a general overview of the potential cost reductions associated with using BT blades. Due to the current lack of financial data available for TECs, this section is meant only to give an estimate of the savings associated with structural load reductions.

Currently, the capital cost required to install offshore hydrokinetic turbines is 1.5 to 2 times greater than on land applications, with operation and maintenance costs that are 3 times that of land based devices [275]. The capital cost of TEC devices include the capital cost of the device and components, the costs associated with installation and deployment, the costs of foundations or moorings, and the costs of connecting it to the grid [28]. Additional costs are required in order to marinize a device, protecting against salt water and corrosion [275]. Of these costs, the structure is estimated to make up 39% of the total capital cost of the device [28]. Although there is currently little data available on the cost breakdown of TEC's, the offshore wind industry has estimated that the support structures cost represents anywhere from 15% [276] to 20–30% of the capital cost [29, 277]. The cost of the support structure is also strongly related to the size (and mass) of the turbine blades [278].

Based on a simplified force analysis of a HATT system, the worst case scenario thrust forces were estimated to account for 35% of the design axial load for a mono-pile support structure, and 83% of the design bending moment. The force used in this analysis included a fluctuating load which was assumed to increase the thrust load on a blade by ±25% of the total thrust force, and was added to account for variable wave loads as well as turbulence. A worst case bending moment was therefore assumed by having two blades with a +25% fluctuating load component, and the other with a -25% fluctuating load component. This number was based on experimental data in which the loads experienced in unsteady flow were found to be approximately 25% greater than that for steady flow [51]. Although the axial component of these loads may even out over the rotor area, the effect of the bending moment on the shaft and support structure is not expected to be negligible. This also assumes that the blades are FP and hence do not pitch to reduce loads.

Assuming that the cost of the support structure is 30% of the total capital cost, and is related only to the forces and bending moments it is required to withstand, then a 10% reduction in thrust loads would equate to a 10% reduction in design loads for the structure. This would ultimately mean the support structure could be 10% smaller, saving 3% of the capital cost of the device. This is in agreement with the statement made by MCT that an increase of over 10% in maximum thrust loads could to have a profound impact on MCT's design philosophy and installation costs [21].

Reduced loads due to BT coupling also reduce the capacity and size requirements of other turbine components, such as the shaft and bearings, and the reduced torque at the extreme site conditions would lead to a reduction in the capacity required for the generator. All of this would lead to overall cost reductions for the TEC. However, cost data is not currently available to allow an estimate of the savings associated with these reductions.

The increase in the cost of blades due to BT coupling depends on the amount of additional material (composite thickness) needed to achieve the required stiffness of the blade using off-axis plies compared to a blade with more 0° plies, which is stiffer. The manufacturing technique used will also affect the cost comparison (the time required to lay up a composite blade by hand will be proportional to the composite thickness). It is recommended that this cost analysis be investigated further in future work.

CHAPTER 10
CONCLUSIONS AND RECOMMENDATIONS

This work has demonstrated experimentally and numerically that passively adaptive BT blades have the potential to reduce structural loads and regulate power for in-stream HATTs. As well, through appropriate design of the blade geometry, increased annual energy production is possible using BT blades. The main objectives of this work were to design and test BT blades, and to develop and verify a design tool for passively adaptive blades. These objectives have been met and the following contributions made:

- A FEM was shown to accurately predict the bending and twisting deformation of BT laminate plates and BT composite blades. An analysis of the sensitivity of the composite FEM indicated that BT coupling effects are highly influenced by the input modeling parameters (such as ply angles and thicknesses), particularly for thin composite materials. This highlighted the importance of accurate composite manufacturing, leading to well-quantified input parameters for FEMs.

- A design of experiment study using a verified FEM indicated ply angles of between $\pm30°$ and $\pm40°$ give the most BT coupling for a composite laminate plate, but also have high associated transverse tensile stresses. Ply angles of 90º were shown to maximize bending, and smaller angles, such as 0º (plies along the long axis of the plate), increase the blade's resistance to bending. By coupling a composite stress analysis to the design of experiment study, ply angles could be chosen to optimize the BT response while minimizing the composite stresses. These results were consistent with results of an analytical model based on CLT, which predicted angles of $\pm 30º$ to give the most BT coupling in a three layer laminate plate.

- Hydrodynamic testing of a turbine with rigid aluminum blades in the towing tank at the University of Strathclyde provided baseline turbine data which was used to verify a BEMT model with a high level of confidence in the experimental results. The BEMT model was found to accurately predict the global turbine performance (thrust and torque) of the rigid blades for a specific range of λs.

- Hydrodynamic testing of a turbine with composite and aluminum blades of identical geometry in the towing tank at the University of Strathclyde demonstrated that composite BT blades have reduced loads compared to effectively rigid blades. This proved the methodology for the design of BT coupled blades for load reduction in a controlled laboratory scale test, relating the composite layup (blade skin with roughly $\pm 30^\circ$ plies with a mirror layup) to a thrust load reduction of about 8% at $\lambda = 4.5$ and carriage speed of 1.0 m/s. This provides hydrodynamic test data for scale composite blades as a function of the blade composite layup and materials, and can be used by researchers and industry to verify composite blade models.

- An iterative FEM-BEMT design tool was shown to reasonably predict the deformation and performance of a BT blade in a short computational time; the current design tool took less than 10 minutes to converge over the range of velocities in increments of 0.1 m/s, on a standard engineering desktop computer (6.0 GB of RAM and an Intel Xeon® processor), independent of the size of the blade. This enabled fast and efficient design of experiment investigations for BT blades, making it useful for the early stages of blade engineering. The computational time would be increased by using more blade elements in the BEMT code, however, the relative difference predicted using a greater number of blade elements did not justify the increased computational time.

- A composite stress analysis based on the Maximum Stress failure theory and Tsai-Hill failure theory indicated that the transverse tensile and shear stresses limit the amount of BT coupling realizable for a particular composite blade design. As well, stress concentrations at the location of ply drops were found in a blade FEM to be significant and required many small ply drops to smooth out these concentrations. This failure analysis method allows BT blade designs to be optimized for maximum load reductions, while still meeting required structural safety factors. This highlights the

importance of considering not only global stresses in the structure (for example, von Mises stresses), but also the directionality of the stresses and areas of stress concentrations.

- Based on case study results using the design tool, a full-scale turbine with 4.0 m BT composite blades and a pre-deformed blade geometry was predicted to increase the energy capture between cut-in and design speed, while reducing structural loads and power capture at flow speeds at extreme conditions by 8.7%. It is anticipated that these findings will influence the design of composite blades.

10.1 Recommendations

This section outlines the recommendations for future work in the area of composite FSI modeling of adaptive blades using BEMT and FEM.

One of the limitations of the FEM-BEMT design tool developed through this work was the sensitivity of the BEMT model to the input airfoil data. For small-scale turbine modeling, it was found that two sets of airfoil data for the same airfoil in a close range of Reynolds numbers resulted in significantly different performance predictions by BEMT. The airfoil data used to model the turbine with NREL S814 blades in BEMT was obtained at a lower Reynolds number than the towing tank tests, but the BEMT results using this data matched the experimental results reasonably well. It is thought that other effects present during towing tank testing decreased the blade hydrodynamic performance such that this airfoil data represented the BL behavior in the tests. However, the uncertainty associated with these assumptions necessitates further investigation into low Reynolds number airfoil performance, with emphasis on a comparison to small-scale turbine tests.

The lift and drag data used in the design tool was obtained for a non-rotating airfoil, and rotational effects were not accounted for in the BEMT model. The effect of rotating blades on the airfoil BL can have a significant impact on the experimental results. However, at this time, there is no method for correlating non-rotating and rotating airfoil data. In fact, previous work has shown that rotational effect corrections typically used in the wind industry are not effective for tidal, leaving a gap in the current knowledge [182]. This gives the BEMT model presented herein an inherent uncertainty when trying to match it to

towing tank test results for small-scale turbines, particularly due to the high rotational speeds of small-scale tests compared to full-scale turbines. Future work should focus on correlating non-rotating 2-D airfoil data to rotating blade airfoils at low Reynolds numbers, such that small-scale turbine tests can be modeled with a higher degree of certainty.

With increasing blade size toward full-scale blades, composite thickness will be significantly greater than conventional wind turbine blades due to the high fluid loads subsea. Thick composite structures pose challenges, as it has been postulated that the relative strength of a laminate may decrease with thickness [230], but the amount of this reduction is not easily predictable. As well, manufacturing thick composites poses challenges in ensuring even resin distribution and curing. This is a research topic that is recommended for investigation in future work as the research moves toward full-scale blades.

Although the design tool is fast and efficient, it is limited to steady state models, and hence cannot consider fatigue effects, unsteady loads, or effects of time-dependent flow variations. Although additions to the BEMT described in this thesis could enable the consideration of unsteady flow such as waves, the static FEM would not be suitable for investigating fatigue effects. As the engineering blade design process proceeds from early stages to pre-commercial stages, more in-depth analysis is recommended, and will likely necessitate dynamic FEM models to capture such effects, as well as higher resolution CFD modeling.

REFERENCES

1.   Province of Nova Scotia, 2011. *Renewable Electricity Regulations-Renewable Electricity Standard 2020*. Available from: http://www.novascotia.ca/just/regulations/regs/elecrenew.htm#TOC2_7.

2.   Offshore Energy Research Association of Nova Scotia, 2015. *Building a Tidal Energy Industry in Canada Offers Substantial Opportunity According to Study*. Available from: http://www.oera.ca/OEER/StrategicEnvironmentalAssessment/BackgroundreportfortheFundyTidalEnergySEA/tabid/280/Default.aspx

3.   Reuk.Co.Uk, 2014. *La Rance Tidal Power Plant.* [Online 2016] Available from: http://www.reuk.co.uk/La-Rance-Tidal-Power-Plant.htm.

4.   Junqiang Xia, Roger A. Falconer, Binliang Lin, and Guangming Tan, *Estimation of Annual Energy Output from a Tidal Barrage Using Two Different Methods.* Applied Energy, 2012. **93**: p. 327-336.

5.   Fundy Ocean Reseach Center for Energy, 2016. *Barrage vs In-stream.* [Online 2016] Available from: http://fundyforce.ca/technology/in-stream-vs-barrage/.

6.   Julie Houde, *Cost-Benefit Analysis of Tidal Energy Generation in Nova Scotia: A Scenario for a Tidal Farm with 300MW of Installed Capacity in the Minas Passage in 2020*, Master of Development Economics: Development Economics, Dalhousie University, 2012.

7.   Miles Willis, Nick Croft, Binliang Lin, Alison Williams, Allan Mason-Jones, Rob Fidler, Jo Loman, Chris Wooldridge, Sara Thomas, Andy Cook, Rebecca Gallie, Tim O'Doherty, Daphne O'Doherty, Guanghai Gao, Reza Ahmadian, Medzid Muhasilovic, Ian Masters, Ian Horsfall, Mark Cross, Roger Falconer, Ian Fryett, and Paul Evans, *Tidal Turbine Deployment in the Bristol Channel: A Case Study.* Proceedings of the ICE - Energy, 2010. **163** (3): p. 93-105.

8.   T. M. Delorm, D. Zappala, and P. J. Tavner, *Tidal Stream Device Reliability Comparison Models.* Proceedings of the Institution of Mechanical Engineers, Part O: Journal of Risk and Reliability, 2011. **226** (1): p. 6-17.

9.   Jeremy Thake, *Development, Installation and Testing of a Large Scale Tidal Current Turbine*, Contractor: It Power, 2005 Contract: T/06/0021/00/REP.

10.   Province of Nova Scotia, 2015. *Developmental Tidal Feed-in Tariff Program*. [Online Oct 29, 2015] Available from: http://energy.novascotia.ca/renewables/programs-and-projects/tidal-fit.

11.   J. King and T. Tryfonas. *Tidal Stream Power Technology – State of the Art*, in *Proc. Oceans,* 2009, Bremen.

12.   D. S. Jenne, Y.-H. Yu, and V. Neary. *Levelized Cost of Energy Analysis of Marine and Hydrokinetic Reference Models*, in *3rd Marine Energy Technology*

Symposium, 2015, Washington, D.C.: National Renewable Energy Laboratory and Sandia National Laboratories.

13.   Pengfei Liu and Brian Veitch, *Design and Optimization for Strength and Integrity of Tidal Turbine Rotor Blades.* Energy, 2012. **46**: p. 393-404.

14.   George Marsh, *Wave and Tidal Power – an Emerging New Market for Composites.* Reinforced Plastics, 2009. **53** (5): p. 20-24.

15.   CBC News, 2014. *Failed Tidal Turbine Explained at Symposium. CBC News* Available from: http://www.cbc.ca/news/canada/nova-scotia/failed-tidal-turbine-explained-at-symposium-1.1075510.

16.   Kittridge D Fowler M, Pemberton M, Litchfield, *Tidal Turbine Hub-Blade Connection Design*, 2011, University of Maine

17.   Daniel Kittridge, Mark Pemberton, Andrew Litchfield, and Matthew Fowler, *Computer Modeling and Analysis of Tidal Turbine Hub-Blade Designs*, *Project report,*2009, Crosby Laboratory, University of Maine

18.   Dan White, *Tidal Systems Challenge - Blade Design!*, in *Ocean News & Technology* 2011. p. 38-39.

19.   Marine Current Turbines, July 22, 2008. *Delay in Commissioning One of Seagen's Rotors.*   Available from: http://www.marineturbines.com/3/news/article/11/delay_in_commissioning_one_of_seagen_s_rotors.

20.   Alberto Aliseda Danny Sale, Michael Motley,Ye Li. *Structural Optimization of Composite Blades for Wind and Hydrokinetic Turbines*, in *Global Marine Renewable Energy Conference,* 2013.

21.   W. M. J. Batten, A. S. Bahaj, A. F. Molland, and J. R. Chaplin, *Experimentally Validated Numerical Method for the Hydrodynamic Design of Horizontal Axis Tidal Turbines.* Ocean Engineering, 2007. **34** (7): p. 1013-1020.

22.   B. Boukhezzar, L. Lupu, H. Siguerdidjane, and M. Hand, *Multivariable Control Strategy for Variable Speed, Variable Pitch Wind Turbines.* Renewable Energy, 2007. **32** (8): p. 1273-1287.

23.   Peter J. Schubel and Richard J. Crossley, *Wind Turbine Blade Design.* Energies, 2012. **5** (12): p. 3425-3449.

24.   Triton, 2012. *Triton Platform Halves the Cost of Energy Relative to Single Installed Turbines- Black & Veatch Validation* [Online 2016] Available from: http://www.tidalstream.co.uk/html/costs.html.

25.   Rachel F. Nicholls-Lee, *Adaptive Composite Blades for Horizontal Axis Tidal Turbines*, Doctor of Philosophy: School of Engineering Sciences*,* Southampton, 2011.

26.   Y. L. Young, *Time-Dependent Hydroelastic Analysis of Cavitating Propulsors.* Journal of Fluids and Structures, 2007. **23** (2): p. 269-295.

27.   H.J.T. Kooijman, *Bending-Torsion Coupling of a Wind Turbine Rotor Blade*, Technical University of Delft Aerospace Engineering, 1996

28.   John Callaghan and Richard Boud, *Future Marine Energy -Results of the Marine Energy Challenge: Cost Competitiveness and Growth of Wave and Tidal Stream Energy*, Carbon Trust and Entec Uk Ltd., 2007

29.   Wei Shi, Jonghoon Han, Changwan Kim, Daeyong Lee, Hyunkyoung Shin, and Hyunchul Park, *Feasibility Study of Offshore Wind Turbine Substructures for Southwest Offshore Wind Farm Project in Korea.* Renewable Energy, 2015. **74**: p. 406-413.

30.   Mark Capellaro, *Design Challenges for Bend-Twist Coupled Blades for Wind Turbines: And Application to Standard Blades*, Http://Energy.Sandia.Gov/Wp/Wp-Content/Gallery/Uploads/2b-B-1-Capellaro.Pdf, 2012: University Stuttgart

31.   Thomas Nevalainen, Cameron Johnstone, and Andrew Grant. *Characterising Unsteady Eccentric Loads on Tidal Stream Turbines Using a Dynamic Blade Element Momentum Theory*, in *EWTEC,* 2015, Nantes, France.

32.   Alireza Maheri, Siamak Noroozi, Chris A. Toomer, and John Vinney, *Wtab, a Computer Program for Predicting the Performance of Horizontal Axis Wind Turbines with Adaptive Blades.* Renewable Energy, 2006. **31** (11): p. 1673-1685.

33.   M. J. Khan, G. Bhuyan, M. T. Iqbal, and J. E. Quaicoe, *Hydrokinetic Energy Conversion Systems and Assessment of Horizontal and Vertical Axis Turbines for River and Tidal Applications: A Technology Status Review.* Applied Energy, 2009. **86** (10): p. 1823-1835.

34.   Edinburgh Designs Ltd., *Variable Pitch Foil Vertical Axis Tidal Turbine- Final Report* 2006, Edinburgh Designs Ltd Contract work.

35.   Chul Hee Jo, Jin Young Yim, Kang Hee Lee, and Yu Ho Rho, *Performance of Horizontal Axis Tidal Current Turbine by Blade Configuration.* Renewable Energy, 2012. **42**: p. 195-206.

36.   Peter Fraenkel, *Breifing on Tidal Turbines- Part 2*, Personnel communication, 2013.

37.   Fergal O. Rourke, Fergal Boyle, and Anthony Reynolds, *Marine Current Energy Devices: Current Status and Possible Future Applications in Ireland.* Renewable and Sustainable Energy Reviews, 2010. **14** (3): p. 1026-1036.

38.   J.D.L.Winchester and S.D.Quayle. *Torque Ripple and Power in a Variable Pitch Vertical Axis Tidal Turbine*, in *EWTEC,* 2011.

39.   Alexander M. Gorlov, *Helical Turbine Assembly Operable under Multidirectional Fluid Flow for Power and Propulsion Systems*, 1995, US5642984.

40.   Alessandro Schönborn and Matthew Chantzidakis, *Development of a Hydraulic Control Mechanism for Cyclic Pitch Marine Current Turbines.* Renewable Energy, 2007. **32** (4): p. 662-679.

41.	Shujie Wang and Peng Yuan. *Flexible Vane Turbine Tidal Current Energy Conversion Device - from Concept to Application*, in *EWTEC,* 2011.

42.	Martin O. L. Hansen, *Aerodynamics of Wind Turbines*. Second ed. 2008, UK and USA: Earthscan.

43.	Princeton University. *Drag of Blunt Bodies and Streamlined Bodies*. Available from: http://www.princeton.edu/~asmits/Bicycle_web/blunt.html.

44.	D. M. Grogan, S. B. Leen, C. R. Kennedy, and C. M. Ó Brádaigh, *Design of Composite Tidal Turbine Blades.* Renewable Energy, 2013. **57**: p. 151-162.

45.	Pascal W. Galloway, Luke E. Myers, and Abubakr S. Bahaj, *Quantifying Wave and Yaw Effects on a Scale Tidal Stream Turbine.* Renewable Energy, 2014. **63**: p. 297-307.

46.	L. N. Mcewen, R. Evans, and M. Meunier. *Cost-Effective Tidal Turbine Blades*, in *4th International Conference on Ocean Energy, ICOE,* 2012, Dublin.

47.	G.S. Bir, M.J. Lawson, and Y. Li. *Structural Design of a Horizontal-Axis Tidal Current Turbine Composite Blade*, in *ASME 30th International Conference on Ocean, Offshore, and Arctic Engineering,* 2011.

48.	Luke E. Myers Pascal W. Galloway, Abubakr S. Bahaj. *Experimental and Numerical Results of Rotor Power and Thrust of a Tidal Turbine Operating at Yaw and in Waves*, in *WREC,* 2011, Sweden

49.	R. J. Wood, A. S. Bahaj, S. R. Turnock, L. Wang, and M. Evans, *Tribological Design Constraints of Marine Renewable Energy Systems.* Philos Trans A Math Phys Eng Sci, 2010. **368** (1929): p. 4807-27.

50.	M. R. Motley, Z. Liu, and Y. L. Young, *Utilizing Fluid–Structure Interactions to Improve Energy Efficiency of Composite Marine Propellers in Spatially Varying Wake.* Composite Structures, 2009. **90** (3): p. 304-313.

51.	I. A. Milne, A. H. Day, R. N. Sharma, and R. G. J. Flay, *Blade Loads on Tidal Turbines in Planar Oscillatory Flow.* Ocean Engineering, 2013. **60**: p. 163-174.

52.	D.C. Maniaci and Y. Li. *Investigating the Influence of the Added Mass Effect to Marine Hydrokinetic Horizontal-Axis Turbines Using a General Dynamic Wake Wind Turbine Code*, in *Oceans 11 Conference,* 2011, Kona, Hawaii.

53.	Carbon Trust, *Tidal Streams and Tidal Stream Energy Device Design*?

54.	Pradeep Suman Sujeet Swami, Dharmendra Kumar Jain, *Performance of Pitch and Stall Regulated Tidal Stream Turbines.* Int. Journal of Engineering Research and Applications, 2014. **4** (4): p. 50-53.

55.	Haydar Faez Hassan, Ahmed El-Shafie, and Othman A. Karim, *Tidal Current Turbines Glance at the Past and Look into Future Prospects in Malaysia.* Renewable and Sustainable Energy Reviews, 2012. **16** (8): p. 5707-5717.

56.   W. M. J. Batten, A. S. Bahaj, A. F. Molland, and J. R. Chaplin, *The Prediction of the Hydrodynamic Performance of Marine Current Turbines.* Renewable Energy, 2008. **33** (5): p. 1085-1096.

57.   L. Myers and A. S. Bahaj, *Power Output Performance Characteristics of a Horizontal Axis Marine Current Turbine.* Renewable Energy, 2006. **31** (2): p. 197-208.

58.   Tony Burton, David Sharpe, Nick Jenkins, and Ervin Bossanyi, *Wind Energy Handbook.* 2001, West Sussex, England: John Wiley & Sons, Ltd.

59.   Ju Hyun Lee, Sunho Park, Dong Hwan Kim, Shin Hyung Rhee, and Moon-Chan Kim, *Computational Methods for Performance Analysis of Horizontal Axis Tidal Stream Turbines.* Applied Energy, 2012. **98**: p. 512-523.

60.   F. Maganga, G. Germain, J. King, G. Pinon, and E. Rivoalen, *Experimental Characterisation of Flow Effects on Marine Current Turbine Behaviour and on Its Wake Properties.* IET Renewable Power Generation, 2010. **4** (6): p. 498.

61.   C. M. Johnstone, D. Pratt, J. A. Clarke, and A. D. Grant, *A Techno-Economic Analysis of Tidal Energy Technology.* Renewable Energy, 2013. **49**: p. 101-106.

62.   Matthew Allmark, Carwyn Frost, and Tim O'Doherty, *Tidal Turbine Autocad Drawings*, Personnel communication, 2016 Cardiff University

63.   C. Frost, C. E. Morris, A. Mason-Jones, D. M. O'Doherty, and T. O'Doherty, *The Effect of Tidal Flow Directionality on Tidal Turbine Performance Characteristics.* Renewable Energy, 2015. **78**: p. 609-620.

64.   W.M.J. Batten, A.S. Bahaj, A.F. Molland, and L.S Blunden. *Yawed Performance of Horizontal Axis Marine Current Turbines*, in *Conference on Renewable Energy in Island Maritime Climate,* 2006, Dublin.

65.   B. Polagye and J. Thomson, *Tidal Energy Resource Characterization: Methodology and Field Study in Admiralty Inlet, Puget Sound, Wa (USA).* Proceedings of the Institution of Mechanical Engineers, Part A: Journal of Power and Energy, 2013. **227** (3): p. 352-367.

66.   Pengfei Liu and Neil Bose, *Prototyping a Series of Bi-Directional Horizontal Axis Tidal Turbines for Optimum Energy Conversion.* Applied Energy, 2012. **99**: p. 50-66.

67.   Log+1, Alstom, and Wumttia, *Economic Viability of a Simple Tidal Stream Energy Capture Device*, Department of Trade and Industry's Technology Programme: New and Renewable Energy, 2007, DTI Project No: TP/3/ERG/6/1/15527/REP URN 07/575

68.   Chris Lang, 2003. *Harnessing Tidal Energy Takes New Turn: Could the Application of the Windmill Principle Produce a Sea Change?* Available from: http://spectrum.ieee.org/green-tech/geothermal-and-tidal/harnessing-tidal-energy-takes-new-turn.

69. Fergal O'Rourke, Fergal Boyle, and Anthony Reynolds, *Marine Current Energy Devices: Current Status and Possible Future Applications in Ireland.* Renewable and Sustainable Energy Reviews, 2010. **14** (3).

70. D M O'Doherty, A Mason-Jones, T O'Doherty, and C B Byrne. *Considerations of Improved Tidal Stream Turbine Performance Using Double Rows of Contra-Rotating Blades*, in *8th European Wave and Tidal Energy Conference,* 2009, Uppsala, Sweden.

71. Department of Trade and Industry Uk, *Economic Viability of a Simple Tidal Stream Energy Capture Device* Log+1 Limited, Alstom Power Limited, and Wumtia, 2007 Contract number: TP/3/ERG/6/1/15527/REP URN 07/575.

72. Dimitri V. Val and Leon Chernin. *Reliability-Based Design of Rotor Blades in Tidal Stream Turbines*, in *EWTEC 2011,* 2011.

73. B. K. Kirke and L. Lazauskas, *Limitations of Fixed Pitch Darrieus Hydrokinetic Turbines and the Challenge of Variable Pitch.* Renewable Energy, 2011. **36** (3): p. 893-897.

74. In Seong Hwang, Yun Han Lee, and Seung Jo Kim, *Optimization of Cycloidal Water Turbine and the Performance Improvement by Individual Blade Control.* Applied Energy, 2009. **86** (9): p. 1532-1540.

75. J. R. M. Taylor and S. H. Salter. *Vertical-Axis Tidal-Current Generators and the Pentland Firth*, in *Proceedings of the Institution of Mechanical Engineers, Part A: Journal of Power and Energy,* 2007.

76. B. Paillard, F. Hauville, and J. A. Astolfi, *Simulating Variable Pitch Crossflow Water Turbines: A Coupled Unsteady Onera-Edlin Model and Streamtube Model.* Renewable Energy, 2013. **52**: p. 209-217.

77. S.R. Turnock, R. Nicholls-Lee, R.J.K. Wood, and J.A. Wharton, Presentation: *Tidal Turbines That Survive?*

78. K.Steiner-Dicks, 2011. *Is the Pitch System Still the Answer for Tidal Turbines?* Available from: http://social.tidaltoday.com/installation/pitch-system-still-answer-tidal-turbines.

79. Ridho Hantoro, I.K.A.P Utama, Erwandi, and Aries Sulisetyono, *An Experimental Investigation of Passive Variable-Pitch Vertical-Axis Ocean Current Turbine.* ITB J. Eng. Sci.,, 2011. **43** (1).

80. Xue-Wei Zhang, Shu-Qi Wang, Feng Wang, Liang Zhang, and Qi-Hu Sheng, *The Hydrodynamic Characteristics of Free Variable-Pitch Vertical Axis Tidal Turbine.* Journal of Hydrodynamics, Ser. B, 2012. **24** (6): p. 834-839.

81. L. Lazauskas and B. K. Kirke, *Modeling Passive Variable Pitch Cross Flow Hydrokinetic Turbines to Maximize Performance and Smooth Operation.* Renewable Energy, 2012. **45**: p. 41-50.

82. N.C.K. Pawsey, *Development and Evaluation of Passive Variable-Pitch Vertical Axis Wind Turbines*, Doctor of Philosophy: School of Mechanical and Manufacturing Engineering, The University of New South Wales, 2002.

83. C. Sicard, *Fluid Current Turbine*, United States Patent, 1977.

84. B. Brenneman, *Transverse Axis Fluid Turbine*, 1983, United States Patent.

85. Intertek Testing and Certification Ltd, *Bwea Small Wind Turbine Performance Adn Safety Standard*, 2008

86. Daisuke Yanagihara, Hidetsugu Iwashita, and Yukio Watanabe, *A Passive Pitch-Angle Control of Blades for the Hawt Using Fiber-Reinforced Rubber.* Journal of Environment and Engineering, 2011. **6** (4): p. 869-881.

87. Arkadiusz Mroz and Janusz Grzedzinski, *1st Order Evaluation of Smart Blade-Hub Connection*, Project UpWind Contract No.:019945 (SES6).

88. Bunlung Neammanee, Somporn Sirisumrannukul, and Somchai Chatratana, *Control Strategies for Variable-Speed Fixed-Pitch Wind Turbines.* Wind Power. 2010, King Mongkut's University of Technology, North Bangkok, National Science and Technology Development Agency, Thailand.

89. P.W. Carlin, A.S. Laxson, and E.B. Muljadi, *The History and State of the Art of Variable-Speed Wind Turbine Technology*, 2001, National Renewable Energy Laboratory

90. Ben Whitby and Carlos E. Ugalde-Loo, *Performance of Pitch and Stall Regulated Tidal Stream Turbines.* IEEE Transactions On Sustainable Energy, 2014. **5** (1).

91. M. A. Abdullah, A. H. M. Yatim, C. W. Tan, and R. Saidur, *A Review of Maximum Power Point Tracking Algorithms for Wind Energy Systems.* Renewable and Sustainable Energy Reviews, 2012. **16** (5): p. 3220-3227.

92. E. Muljadi and C.P. Butterfield. *Pitch-Controlled Variable-Speed Wind Turbine Generation*, in *IEEE Industry Applications Society Annual Meeting,* 1999, Phoenix, Arizona.

93. C. Deilmann, *Evaluation of Design Concepts for Adaptive Wind Turbine Blades*, MASc: MIT, 2008.

94. Y. L. Young, *Dynamic Hydroelastic Scaling of Self-Adaptive Composite Marine Rotors.* Composite Structures, 2010. **92** (1): p. 97-106.

95. D.W. Lobitz, P.S. Veers, and P.G. Migliore. *Enhanced Performance of Hawts Using Adaptive Blades*, in *Wind Energy '96, ASME Wind Energy Symposium,* 1996, Houston, U.S.A.

96. Matthias Piening Andreas Buter, *Patent: Rotor Blade*, 1996, US5730581.

97. Guy Wayne Deleonardo, Scott Roger Finn, Peter Michael Finnigan, and Donald Joseph Kasperski, *System and Method for Passive Load Attenuation in a Wind Turbine*, 2006, US, US7153090, General Electric Company.

98. Emilian Mieczyslaw Moroz, *Multi-Piece Passive Load Reducing Blades and Wind Turbines Using Same*, 2010,US7690895, General Electric Company.

99. Laurel A. Kroo and Iian Kroo, *Efficient Low-Cost Wind Energy Using Passive Circulation Control*, 2011, US20110206531.

100. Bryan Michael Pelley Christopher Douglas Hemmelgarn, Kristin Marie Cable, Brandon Charles Kirby, *Passive Adaptive Structures*, 2011, Passive adaptive structures US 2011/0084174 A1, Cornerstone Research Group, Inc. .

101. R. F. Nicholls-Lee, S. R. Turnock, and S. W. Boyd, *Application of Bend-Twist Coupled Blades for Horizontal Axis Tidal Turbines.* Renewable Energy, 2013. **50**: p. 541-550.

102. Yin Lu Young and Michael R. Motley. *Influence of Material and Loading Uncertainties on the Hydroelastic Performance of Advanced Material Propellers*, in *Second International Symposium on Marine Propulsors,* 2011.

103. Inderjit Chopra, *Review of State of Art of Smart Structures and Integrated Systems.* AIAA Journal, 2002. **40** (11).

104. Friedrich K Straub, *A Feasibility Study of Using Smart Materials for Rotor Control.* Smart Mater. Struct, 1996. **5**.

105. Capt François Dufault, *Smart Materials in Aircraft, Canadian Air Force.* 2008.

106. Thanasis Barlas, *Smart Rotor Blades and Rotor Control for Wind Turbines – State of the Art, Upwind Project Deliverable*, 2006

107. T. K. Barlas and G. A. M. Van Kuik, *Review of State of the Art in Smart Rotor Control Research for Wind Turbines.* Progress in Aerospace Sciences, 2010. **46** (1): p. 1-27.

108. Anton W. Hulskamp, Adriaan Beukers, Harald E.N. Bersee, Jan Willem Van Wingerden, and Thanasis Barlas. *Design of a Wind Tunnel Scale Model of an Adaptive Wind Turbine Blade for Active Aerodynamic Load Control Experiments*, in *16th International Conference on Composite Materials*.

109. P.A. Joosse, *The Tentortube: An Innovative Improvement of a Passive Tip Mechanism*, 2000, Stork Product Engineering B.V. Contract JOR3-CT95-0005

110. Unanimous, *Twisting Naturally*, in *Windpower Monthly Magazine* 1998.

111. David Macphee and Asfaw Beyene. *A Flexible Turbine Blade for Passive Blade Pitch Control in Wind Turbines*, in *IEEE,* 2011.

112. Wei-Haur Lam and Aalisha Bhatia, *Folding Tidal Turbine as an Innovative Concept toward the New Era of Turbines.* Renewable and Sustainable Energy Reviews, 2013. **28**: p. 463-473.

113. Mike Zuteck, *Adaptive Blade Concept Assessment: Curved Planform Induced Twist Investigation, Contract Report*, 2002, Sandia National Laboratories

114. Bryan M. Pelley Christopher D. Hemmelgarn, *Passive Adaptive Structures*, 2012, EP20100174298, EP 2423104 A1.

115. Rémy Cuenca Laurent Bianchi, Mathieu Galan, Damien Reveillon, *Blade with Adaptive Twisting, and a Rotor Provided with Such a Blade* 2011, US 2011/0211959 A1.

116. N. Karaolis, P. Mussgrove, and G. Jeronimidis. *Active and Passive Aeroelastic Power Control Using Asymmetric Fibre Reinforced Laminates for Wind Turbine Blades*, in *10th British Wind Energy Conference,* 1988, London, U.K.

117. Po-Wen Cheng Wim Bierbooms, *Stochastic Gust Model for Design Calculations of Wind Turbines.* Journal of Wind Engineering and Industrial Aerodynamics 2002. **90**: p. 1237-1251.

118. Paul S. Veers and Donald W. Lobitz, *Load Attenuating Passively Adaptive Wind Turbine Blade*, United States Statutory Invention Registration, 2003, USH2057.

119. Paul Veers, Gunjit Bir, and Donald Lobitz. *Aeroelastic Tailoring in Wind-Turbine Blade Applications*, in *Windpower '98, American Wind Energy Association Meeting and Exhibition,* 1998, California.

120. Wangyu Liu and Jiaxing Gong, *Adaptive Bend-Torsional Coupling Wind Turbine Blade Design Imitating the Topology Structure of Natural Plant Leaves*, www.intechopen.com

121. Mark Capellaro and Po Wen Cheng, *An Iterative Method to Optimize the Twist Angle of a Wind Turbine Rotor Blade.* Wind Engineering, 2014. **38** (5): p. 489–498.

122. W.C. De Goeij, M.J.L. Van Tooren, and A. Beukers, *Implementation of Bending-Torsion Coupling in the Design of a Wind-Turbine Rotor-Blade.* Applied Energy, 1999. **63**: p. 191-207.

123. Cheng-Huat Ong and Stephen W. Tsai, *Design, Manufacture and Testing of a Bend-Twist D-Spar*, Sandia National Laboratories, 1999, Stanford University

124. George Marsh, *A New Start for Marine Propellers?* Reinforced Plastics, 2004. **48** (11): p. 34-38.

125. Y.L. Young, T.J. Michael, M. Seaver, and M.T. Trickey. *Numerical and Experimental Investigations of Composite Marine Propellers* in *26th Symposium on Naval Hydrodynamics,* 2006, Rome, Itlay.

126. Yin L. Young. *Hydroelastic Behavior of Flexible Composite Propellers in Wake Inflow*, in *16th International Conference on Composite Materials,* 2007.

127. S. Gowing, Coffin, P., and Dai, C. *Hydrofoil Cavitation Improvements with Elastically Coupled Composite Materials*, in *25th American Towing Tank Conference,* 1998, Iowa City, USA.

128. Zhanke Liu and Yin L. Young. *Utilization of Deformation Coupling in Self-Twisting Composite Propellers*, in *16th International Conference on Composite Materials,* 2007.

129. Y. L. Young, *Fluid–Structure Interaction Analysis of Flexible Composite Marine Propellers.* Journal of Fluids and Structures, 2008. **24** (6): p. 799-818.

130. Zhanke Liu and Yin L. Young, *Utilization of Bend–Twist Coupling for Performance Enhancement of Composite Marine Propellers.* Journal of Fluids and Structures, 2009. **25** (6): p. 1102-1116.

131. Y. L. Young, J. W. Baker, and M. R. Motley, *Reliability-Based Design and Optimization of Adaptive Marine Structures.* Composite Structures, 2010. **92** (2): p. 244-253.

132. Ya-Jung Lee and Ching-Chieh Lin, *Optimized Design of Composite Propeller.* Mechanics of Advanced Materials and Structures, 2004. **11** (1): p. 17-30.

133. Ching-Chieh Lin, Ya-Jung Lee, and Chu-Sung Hung, *Optimization and Experiment of Composite Marine Propellers.* Composite Structures, 2009. **89** (2): p. 206-215.

134. I.A. Saleh S.M. Habali, *Local Design, Testing and Manufacturing of Small Mixed Airfoil Wind Turbine Blades of Glass Fiber Reinforced Plastics Part I: Design of the Blade and Root.* Energy Conversion & Management, 2000. **41**: p. 249-280.

135. Sara Black, 2011. *Composite Propeller for Royal Navy Minehunter -Composite-for-Metal Replacement Brings Multiple Benefits.*   Available from: http://www.mmsonline.com/articles/composite-propeller-for-royal-navy-minehunter(2).

136. Paul W. Harper and Stephen R. Hallett, *Advanced Numerical Modelling Techniques for the Structural Design of Composite Tidal Turbine Blades.* Ocean Engineering, 2015. **96**: p. 272-283.

137. G. Richard Eisler and Paul S. Veers, *Parameter Optimization Applied to Use of Adaptive Blades on a Variable Speed Wind Turbine*, 1998, Sandia National Laboratories

138. Kevin Cox and Andreas Echtermeyer, *Geometric Scaling Effects of Bend-Twist Coupling in Rotor Blades.* Energy Procedia, 2013. **35**: p. 2-11.

139. Hiroki Wada, Hideaki Murayama, and Yoshimasa Minami. *Deformation Evaluation of Elastic Composite Blade Models for Tidal Power Generation by Fluid-Structure Interaction Analysis*, in *18th International Conference on Composite Materials,* 2011.

140. Y. Minami, T. Nimura, N. Sasaki, H. Murayama, K. Uzawa, and H. Wada. *Development of Tidal and Ocean Current Power Plant Using Elastic Turbine*, in *Underwater Technology (UT), 2011 IEEE Symposium on and 2011 Workshop on Scientific Use of Submarine Cables and Related Technologies (SSC),* 2011.

141. Schottel, Pamphlet: *Schottel Tidal Generator- Scalable Power from Currents Stg,* 2013

142. Penny Jeffcoate, Ralf Starzmann, Bjoern Elsaesser, Stefan Scholl, and Sarah Bischoff, *Field Measurements of a Full Scale Tidal Turbine.* International Journal of Marine Energy, 2015.

143.   Michael R. Motley and Ramona B. Barber, *Passive Control of Marine Hydrokinetic Turbine Blades.* Composite Structures, 2014. **110**: p. 133-139.

144.   Ramona B. Barber and Michael R. Motley. *A Numerical Study of the Effect of Passive Control on Cavitation for Marine Hydrokinetic Turbines*, in *EWTEC,* 2015, Nantes, France.

145.   David Snowberg and Jochem Weber, *Marine and Hydrokinetic Technology Development Risk Management Framework*, 2015, National Renewable Energy Laboratory

146.   A. S. Bahaj, A. F. Molland, J. R. Chaplin, and W. M. J. Batten, *Power and Thrust Measurements of Marine Current Turbines under Various Hydrodynamic Flow Conditions in a Cavitation Tunnel and a Towing Tank.* Renewable Energy, 2007. **32** (3): p. 407-426.

147.   J.A. Clarke, G. Connor, A.D. Grant, C. Johnstone, and D. Mackenzie. *Development of a Contra-Rotating Tidal Current Turbine and Analysis of Performance*, in *EWTEC,* 2007, Southampton , UK.

148.   B. Gaurier, G. Germain, J. V. Facq, C. M. Johnstone, A. D. Grant, A. H. Day, E. Nixon, F. Di Felice, and M. Costanzo, *Tidal Energy "Round Robin" Tests Comparisons between Towing Tank and Circulating Tank Results.* International Journal of Marine Energy, 2015.

149.   A. S. Bahaj, W. M. J. Batten, and G. Mccann, *Experimental Verifications of Numerical Predictions for the Hydrodynamic Performance of Horizontal Axis Marine Current Turbines.* Renewable Energy, 2007. **32** (15): p. 2479-2490.

150.   C. M. Johnstone, A. D. Grant, G. Connor, and J. A. Clarke, *Design and Testing of a Contra-Rotating Tidal Current Turbine.* Proceedings of the Institution of Mechanical Engineers, Part A: Journal of Power and Energy, 2007. **221** (2): p. 171-179.

151.   P. Davies, G. Germain, B. Gaurier, A. Boisseau, and D. Perreux, *Evaluation of the Durability of Composite Tidal Turbine Blades.* Philos Trans A Math Phys Eng Sci, 2013. **371** (1985): p. 20120187.

152.   J.A. Clarke, J. Cockroft, A.D. Grant, C.M. Johnstone, T. McCombes, S. Barrett, B. Holmes, A.S. Bahaj, and L. Myres, *Equimar Deliverable 3.2 Concept Appraisal and Tank Testing Practices for 1st Stage Prototype Devices, Equitable Testing and Evaluation of Marine Energy Extraction Devices in terms of Performance, Cost and Environmental Impact,* 2009.

153.   R.A. Shenoi L.S. Sutherland, S.M. Lewis, *Size and Scale Effects in Composites: I. Literature Review.* Composites Science and Technology, 1999. **59**.

154.   T. McCombes, C. Johnstone, B. Holmes, L. E. Myers, A.S. Bahaj, V. Heller, J.P. Kofoed, J. Finn, and C. Bittencourt, *Equimar Deliverable 3.3 Assessment of Current Practice for Tank Testing of Small Marine Energy Devices, Equitable Testing and Evaluation of Marine Energy Extraction Devices in terms of Performance, Cost and Environmental Impact,* 2010.

155. P. B. S. Lissaman, *Low-Reynolds-Number Airfoils.* Ann. Rev. Fluid Mech, 1983. **15**: p. 223-239.

156. Thomas De Leeuw, *Investigation on the Influence of Scaling Effects in Propeller Testing through the Use of Theoretical Prediction Codes*, Master of Science: Dept. of Aerospace Engineering, Delft University of Technology, 2013.

157. Suzanne Fielding, *Boudary Layer Theory,* 2013

158. David C. Hazen. *Boundary Layer Control*, 1968, Princeton University

159. H. Sturm, G. Dumstorff, P. Busche, D. Westermann, and W. Lang, *Boundary Layer Separation and Reattachment Detection on Airfoils by Thermal Flow Sensors.* Sensors (Basel), 2012. **12** (11): p. 14292-306.

160. L. F. Crabtree, *The Formation of Regions of Separated Flow on Wing Surfaces Part I Low-Speed Tests on a Two-Dimensional Unswept Wing with a 10 Per Cent Thick Rae 101 Section Part Ii Laminar-Separation Bubbles and the Mechanism of the Leading-Edge Stall*, Aeronautical Research Council Reports And Memoranda, 1959 R~ & M. No. 3122 (17,524.19.881) A.R.C. Technical Report.

161. R. Liebeck, R. Blackwelder, and S. Lekoudis, *Low Reynolds Number - Separation Bubble*, 1984-1987 Final Technical Report N00014-84-K-0500.

162. Mechanical & Mechatronic Engg. Aerospace, 2005. *Separation of Flow*. Available from: http://www-mdp.eng.cam.ac.uk/web/library/enginfo/aerothermal_dvd_only/aero/fprops/introvisc/node9.html.

163. Ian Angus Milne, *An Experimental Investigation of Turbulence and Unsteady Loading on Tidal Turbines*, Doctor of Philosophy in Mechanical Engineering: The University of Auckland, 2014. p. 256.

164. M. M. O'Meara and T. J. Mueller, *Laminar Separation Bubble Characteristics on an Airfoil at Low Reynolds Numbers.* AIAA Journal, 1987. **25** (8): p. 1033-1041.

165. T. J. Mueller, L. J. Pohlen, P. E. Conigliaro, and Jr. B. J. Jansen, *The Influence of Free-Stream Disturbances on Low Reynolds Number Airfoil Experiments.* Experiments in Fluids, 1983 (1): p. 3-14.

166. Yongsheng Lian and Wei Shyy, *Laminar-Turbulent Transition of a Low Reynolds Number Rigid or Flexible Airfoil.* AIAA Journal, 2007. **45** (7).

167. Michael S. Selig, James J. Guglielmo, Andy P. Broeren, and Philippe Giguere, *Summary of Low-Speed Airfoil Data* 1995, SoarTech Publications, Virginia: Department of Aeronautical and Astronautical Engineering, University of Illinois

168. D.M. Somers, *The S814 and S815 Airfoils*, National Renewable Energy Laboratory, 1991-1992: State College, Pennsylvania

169. Paul Mycek, Benoît Gaurier, Grégory Germain, Gregory Pinon, and Elie Rivoalen, *Experimental Study of the Turbulence Intensity Effects on Marine Current Turbines Behaviour. Part I: One Single Turbine.* Renewable Energy, 2014.

170. Ning Cao, *Effects of Turbulence Intensity and Integral Length Scale on an Asymmetric Airfoil at Low Reynolds Numbers*, Master of Applied Science: Mechanical, Automotive, and Materials Engineering, University of Windsor, 2010.

171. S. Watkins, S. Ravi, and B. Loxton, *The Effect of Turbulence on the Aerodynamics of Low Reynolds Number Wings.* Engineering Letters, 2010.

172. R. H. Howard and D. W. Kindelspire, *Free-Stream Turbulence Effects on Airfoil Boundary-Layer Behavior at Low Reynolds Number.* Journal of Aircraft, 1990. **27** (5): p. 469-470.

173. P.J. Moriarty and A.C. Hansen, *Aerodyn Theory Manual*, 2005, National Renewable Energy Laboratory, Golden, Colorado

174. E. Branlard, K. Dixon, and M. Gaunaa. *An Improved Tip-Loss Correction Based on Vortex Code Results*, in *European Wind Energy Conference & Exhibition,* 2012, Denmark. DTU Wind Energy and Siemens Energy Inc.

175. H. Himmelskamp, *Profiluntersuchungen an Einem Umlaufenden Propeller*, Max-Planck-Institut fur Stromungsforschung Gottingen, 1945.

176. W. Banks and G. Gadd, *Delaying Effect of Rotation on Laminar Separation.* AIAA Journal, 1963: p. 941-942.

177. L. Fingersh S. Schreck, K. Siegel, M. Singh, and P. Medina. *Rotational Augmentation on a 2.3 Mw Rotor Blade with Thick Flatback Airfoil Cross-Sections*, in *AIAA Aerospace Sciences Meeting,* 2013, Grapevine, Texas.

178. Christian Bak, Jeppe Johansen, and Peter B. Andersen. *Three-Dimensional Corrections of Airfoil Characteristics Based on Pressure Distributions*, in *European Wind Energy Conference & Exhibition,* 2006, Athens, Greece.

179. Iván Herráez, Bernhard Stoevesandt, and Joachim Peinke, *Insight into Rotational Effects on Awind Turbine Blade Usingnavier–Stokes Computations.* Energies, 2014. **7** (10): p. 6798-6822.

180. Zhaohui Du and M.S Selig, *The Effect of Rotation on the Boundary Layer of a Wind Turbine Blade.* Renewable Energy, 2000. **20** (2): p. 167–181.

181. H Snel, R Houwink, and J Bosschers, *Sectional Prediction of Lift Coefficients on Rotating Wind Turbine Blades in Stall*, 1994, Netherlands Energy Research Foundation ECN-C-93-052.

182. James Harrison, Robert Howell, Graeme Manson, Carl Sequeira, and Paul Vigars. *An Evaluation of Steady Radial Flow Modelling for Horizontal Axis Tidal Turbines*, in *EWTEC,* 2015, Nantes, France.

183. Zifeng Yang, Hirofumi Igarashi, Mathew Martin, and Hui Hu. *An Experimental Investigation on Aerodynamic Hysteresis of a Low-Reynolds Number Airfoil*, in *46th AIAA Aerospace Sciences Meeting and Exhibit,* 2008, Reno, Nevada.

184. Thomas J. Mueller. *Aerodynamic Measurements at Low Reynolds Numbers for Fixed Wing Micro-Air Vehicles*, in *Development and Operation of UAVs for Military and Civil Applications,* 1999, VKI, Belgium.

185. Ece Sagol, Marcelo Reggio, and Adrian Ilinca, *Issues Concerning Roughness on Wind Turbine Blades.* Renewable and Sustainable Energy Reviews, 2013. **23**: p. 514-525.

186. H. Bagheri Esfe, M. J. Kermani, and M. Saffar Avval, *Effects of Surface Roughness on Deviation Angle and Performance Losses in Wet Steam Turbines.* Applied Thermal Engineering, 2015. **90**: p. 158-173.

187. Jessica M. Walker, Karen A. Flack, Ethan E. Lust, Michael P. Schultz, and Luksa Luznik, *Experimental and Numerical Studies of Blade Roughness and Fouling on Marine Current Turbine Performance.* Renewable Energy, 2014. **66**: p. 257-267.

188. Tao Bai, Jingyuan Liu, Weihao Zhang, and Zhengping Zou, *Effect of Surface Roughness on the Aerodynamic Performance of Turbine Blade Cascade.* Propulsion and Power Research, 2014. **3** (2): p. 82-89.

189. Takafumi Igarashi and Hui Hu Yan Zhang. *Experimental Investigations on the Performance Degradation of a Low-Reynolds-Number Airfoil with Distributed Leading Edge Roughness*, in *49th AIAA Aerospace Sciences Meeting,* 2011, Orlando, Florida.

190. William H. Rae Alan Pope, *Low-Speed Wind Tunnel Testing.* 2nd ed. 1984: John Wiley and Sons.

191. Pascal Galloway Luke Myers, Abubakr Bahaj. *Operational Issues Surrounding the Use of Towing Tanks for Performance Quantification of Marine Current Energy Converters*, in *EWTEC,* 2011, Southhampton, U.K. .

192. Benoît Gaurier, Peter Davies, Albert Deuff, and Grégory Germain, *Flume Tank Characterization of Marine Current Turbine Blade Behaviour under Current and Wave Loading.* Renewable Energy, 2013. **59**: p. 1-12.

193. R. J. Poole and I. Owen S. C. Tedds. *Wake Characteristics of Horizontal Axis Tidal Stream Turbines in Uniform and Non-Uniform Steady Flows*, in *4th International Conference on Ocean Energy,* 2012, Dublin, Ireland.

194. Francesco Salvatore, A.S. Iyer, Sandy Day, and Fabio Di Felice, *Wp2: Marine Energy System Testing - Standardisation and Best Practice Deliverable 2.23 Review of Tow Tank Limitations*, 2014, MARINET (Marine Renewables Infrastructure Network)

195. G. A. Lowe and N. Satterly, *Chapter 9: Comparison of Coupon and Spar Tests.* 1996. p. 153.

196. N. Tual, N. Carrere, P. Davies, T. Bonnemains, and E. Lolive, *Characterization of Sea Water Ageing Effects on Mechanical Properties of Carbon/Epoxy Composites for Tidal Turbine Blades.* Composites Part A: Applied Science and Manufacturing, 2015. **78**: p. 380-389.

197.   Iso 527, *Plastics -- Determination of Tensile Properties -- Part 1: General Principles,* 2012

198.   Rafee A.R. Ahamed, Cameron M. Johnstone, and Margaret M. Stack. *Mapping Blade Angle Effects for the Erosion of Polymer Based Composites: An Approach to Developing Smart Materials for Tidal Turbines*, in *EWTEC,* 2015, Nantes, France.

199.   T. McCombes, C. Johnstone, B. Holmes, L. E. Myers, A.S. Bahaj, and J.P. Kofoed, *Equimar Deliverable 3.4 Best Practice for Tank Testing of Small Marine Energy Devices, Equitable Testing and Evaluation of Marine Energy Extraction Devices in terms of Performance, Cost and Environmental Impact* 2010 213380.

200.   International Towing Tank Conference, *Recommended Procedures and Guidelines: Guide to the Expression of Uncertainty in Experimental Hydrodynamics,* 2008

201.   International Towing Tank Conference -Specialist Committee on Uncertainty Analysis, *Recommended Procedures and Guidelines Uncertainty Analysis and Instrument Calibration,* 2008

202.   National Institute of Standards And Technology, *Engineering Statistics Handbook- Propagation of Error for Many Variables,* 2014

203.   H. Glauert, *Airplane Propellers*. Aerodynamic Theory. 1935: Springer Berlin Heidelberg.

204.   K. Gracie, T.M. Nevalainen, C.M. Johnstone, R.E. Murray, D.A. Doman, and M.J. Pegg. *Development of a Blade Design Methodology for Overspeed Power-Regulated Tidal Turbines*, in *EWTEC,* 2015, Nantes, France.

205.   Stephen R. Turnock, Alexander B. Phillips, Joe Banks, and Rachel Nicholls-Lee, *Modelling Tidal Current Turbine Wakes Using a Coupled Rans-Bemt Approach as a Tool for Analysing Power Capture of Arrays of Turbines*. Ocean Engineering, 2011. **38** (11-12): p. 1300-1307.

206.   H. C. Buckland, I. Masters, J.C. Chapman, and J.A.C. Orme. *Blade Element Momentum Theory in Modelling Tidal Stream Turbines*, in *18th UK Conference on Computational Mechanics,* 2010.

207.   Wen Zhong Shen, Robert Mikkelsen, Jens Nørkær Sørensen, and Christian Bak, *Tip Loss Corrections for Wind Turbine Computations.* Wind Energy, 2005. **8** (4): p. 457–475.

208.   I. Masters and J. A. C. Orme, *A Robust Blade Element Momentum Theory Model for Tidal Stream Turbines Including Tip and Hub Loss Corrections.* Marine Engineering and Technology, 2011. **10** (1): p. 25–36.

209.   I. Masters, J.C. Chapman, J.A.C. Orme, and M.R. Willis. *Modelling High Axial Induction Flows in Tidal Stream Turbines with a Corrected Blade Element Model*, in *International Conference on Ocean Energy,* 2010, Bilbao.

210. J.C Chapman, I. Masters, M. Togneri, and J.A.C Orme, *The Buhl Correction Factor Applied to High Induction Conditions for Tidal Stream Turbines.* Renewable Energy 2013. **60**: p. 472-480.

211. J. Tangler and J. David Kocurek. *Wind Turbine Post-Stall Airfoil Performance Characteristics Guidelines for Blade-Element Momentum Methods*, in *43rd AIAA Aerospace Sciences Meeting and Exhibit,* 2005, Reno, Nevada.

212. D.A. Spera, *Wind Turbine Technology: Fundamental Concepts of Wind Turbine Engineering.* 1994: American Society of Mechanical Engineers.

213. J. R. Xiao, B. A. Gama, and J. W. Gillespie, *Progressive Damage and Delamination in Plain Weave S-2 Glass/Sc-15 Composites under Quasi-Static Punch-Shear Loading.* Composite Structures, 2007. **78** (2): p. 182-196.

214. M Mohan. *The Advantages of Composite Material in Marine Renewable Energy Structures*, in *RINA Marine Renewable Energy Conference,* 2008.

215. Autar K. Kaw, *Mechanics of Composite Materials.* Second ed, Taylor & Francis Group. 2006: CRC Press Taylor & Francis Group.

216. Martin Knops, *Analysis of Failure in Fiber Polymer Laminates: The Theory of Alfred Puck.* 2008, Springer.

217. Endel V. Iarve, Kevin H. Hoos, Michael Braginsky, Eric Zhou, and David Mollenhauer, *Tensile and Compression Strength Prediction in Laminated Composites by Using Discrete Damage Modeling*, 2015, American Institute of Aeronautics and Astronautics

218. Mohammad Amin and Abdolhossein Fereidoo, *Materials Science - Advanced Topics, Chapter 11: Progressive Failure Analysis of Glass/Epoxy Composites at Low Temperatures.* 2013: InTech.

219. Michael R. Motley Yin Lu Young. *Influence of Material and Loading Uncertainties on the Hydroelastic Performance of Advanced Material Propellers*, in *Second International Symposium on Marine Propulsors,* 2011, Hamburg, Germany.

220. Pedro Ponces Camanho, *Failure Criteria for Fibre-Reinforced Polymer Composites*, Departamento de Engenharia Mecânica e Gestão Industrial, 2002 Faculdade de Engenharia da Universidade do Porto.

221. Isaac M. Daniel and Ori Ishai, *Engineering Mechanics of Composite Materials* 1994: Oxford University Press.

222. P. D. Soden, M. J. Hintonb, and A. S. Kaddoura, *A Comparison of the Predictive Capabilities of Current Failure Theories for Composite Laminates.* Composites Science and Technology, 1998. **58**: p. 1225-1254.

223. Altair Engineering, *Altair Radioss 12.0 User Guide,* 2013.

224. Marcus Andersson and Petter Liedberg, *Crash Behavior of Composite Structures: A Cae Benchmarking Study*, Master's thesis: Applied Mechanics, Division of

Material and Computational Mechanics, Chalmers University of Technology, 2014.

225. Livermore Software Technology Corporation, *Ls-Dyna® Keyword User's Manual Volume Ii-Material Models* 2012, Livermore Software Technology Corporation (LSTC)

226. Z. Hashin, *Cumulative Damage Theory for Composite Materials: Residual Life and Residual Strength Methods.* Composites Science and Technology, 1985. **23** (1): p. 1-19.

227. B. Kurnatowski and A. Matzenmiller, *Coupled Twoscale Analysis of Fiber Reinforced Composite Structures with Microscopic Damage Evolution.* International Journal of Solids and Structures, 2012. **49** (18): p. 2404-2417.

228. C-K. Park, C-D. Kan, W. Hollowell, and S.I. Hill, *Investigation of Opportunities for Lightweight Vehicles Using Advanced Plastics and Composites*, National Highway Traffic Safety Administration, 2012, US Department of Transportation Washington, DC: DOT HS 811 692.

229. R.A. Shenoi L.S. Sutherland, S.M. Lewis *Size and Scale Effects in Composites: Ii. Unidirectional Laminates.* Composites Science and Technology, 1999. **59**.

230. J. Lee and C. Soutis, *A Study on the Compressive Strength of Thick Carbon Fibre–Epoxy Laminates.* Composites Science and Technology, 2007. **67** (10): p. 2015-2026.

231. Douglas S. Cairns, Trey Riddle, and Jared Nelson, *Wind Turbine Composite Blade Manufacturing: The Need for Understanding Defect Origins, Prevalence, Implications and Reliability*, 2011, Sandia National Laboratories SAND2011-1094.

232. M.R. Wisnom, *Size Effects in the Testing of Fibre-Composite Materials.* Composites Science and Technology, 1999. **59** (13).

233. J. Lee and C. Soutis, *Measuring the Notched Compressive Strength of Composite Laminates: Specimen Size Effects.* Composites Science and Technology, 2008. **68** (12): p. 2359-2366.

234. David Verelst, *Flexible Wind Turbine Blades: A FEM-BEM Coupled Model Approach*, Delft University of Technology, 2009.

235. Alireza Maheri, Siamak Noroozi, and John Vinney, *Combined Analytical/Fea-Based Coupled Aero Structure Simulation of a Wind Turbine with Bend–Twist Adaptive Blades.* Renewable Energy, 2007. **32** (6): p. 916-930.

236. Alireza Maheri, Siamak Noroozi, and John Vinney, *Application of Combined Analytical/Fea Coupled Aero-Structure Simulation in Design of Wind Turbine Adaptive Blades.* Renewable Energy, 2007. **32** (12): p. 2011-2018.

237. Timothy J. Knill, *The Application of Aeroelastic Analysis Output Load Distributions to Finite Element Models of Wind.* Wind Engineering, 2005. **29**.

238. M. E. Bechly and P. D. Clausent, *Structural Design of a Composite Wind Turbine Blade Using Finite Element Analysis.* Computers and Structures, 1997. **63** (3): p. 639-646.

239. M. Jureczko, M. Pawlak, and A. Mężyk, *Optimisation of Wind Turbine Blades.* Journal of Materials Processing Technology, 2005. **167** (2-3): p. 463-471.

240. Feng Zhao Wei Duan. *Loading Analysis and Strength Cacluation of Wind Turbine Blade Based on Blade Element Momentum Theory and Finite Element Method*, in *Power and Energy Engineering Conference (APPEEC), 2010 Asia-Pacific,* 2010, Chengdu.

241. Z.I. Mahri and M.S. Rouabah, *Calculation of Dynamic Stresses Using Finite Element Method and Prediction of Fatigue Failure for Wind Turbine Rotor.* WSEAS Transactions On Applied And Theoretical Mechanics, 2008. **3**.

242. Andreas Heege, Jaume Betran, and Yvan Radovcic, *Fatigue Load Computation of Wind Turbine Gearboxes by Coupled Finite Element, Multi-Body System and Aerodynamic Analysis.* Wind Energy, 2007. **10** (5): p. 395-413.

243. R. E. Murray, D. A. Doman, and M. J. Pegg, *Finite Element Modeling and Effects of Material Uncertainties in a Composite Laminate with Bend-Twist Coupling.* Composite Structures, 2015. **121**: p. 362-376.

244. Zoltek, *Panex® 35 Uni-Directional Fabrics*

245. Gurit, *Prime™ 27 Epoxy Infusion System*

246. National Instruments Corporation, 2016. *Ni Vision 2015 Concepts: Mapping Pixel Coordinates to Real-World Coordinates*.   Available from: http://zone.ni.com/reference/en-XX/help/372916T-01/nivisionconcepts/spatial_calibration_concepts/.

247. Andrew Makeev and Erian Armanios, *On a Higher Order Analysis of Laminated Composite Strips with Extension-Twist Coupling.* International Journal of Solids and Structures, 1999. **36**: p. 970-987.

248. Mitutoyo Canada Inc., *Certificate of Calibration Iso/Ibc 17025* 2008: Mississauga, Ontario, Canada

249. Sicomin, *Sicomin Foaming Epoxy: Pb 170, Pb 250, Pb 400, Pb 600 Cellular Epoxy Foam Production System* 2009

250. Asm International, *Metals Handbook - Properties and Selection: Nonferrous Alloys and Special-Purpose Materials* 1990

251. Rexroth Bosch Group, *Rexroth Indradyn T Synchronous-Torquemotors*

252. A. Mason-Jones, D. M. O'Doherty, C. E. Morris, T. O'Doherty, C. B. Byrne, P. W. Prickett, R. I. Grosvenor, I. Owen, S. Tedds, and R. J. Poole, *Non-Dimensional Scaling of Tidal Stream Turbines.* Energy, 2012. **44** (1): p. 820-829.

253. Yin L. Young Michael R. Motley, *Influence of Uncertainties on the Response and Reliability of Self-Adaptive Composite Rotors.* Composite Structures, 2011. **94**: p. 114–120.

254. Wolfram Raither, Andrea Bergamini, Farhan Gandhi, and Paolo Ermanni, *Adaptive Bending-Twist Coupling in Laminated Composite Plates by Controllable Shear Stress Transfer.* Composites Part A: Applied Science and Manufacturing, 2012. **43** (10): p. 1709-1716.

255. F. K. Chang and M. H. Chen, *The in Situ Ply Shear Strength Distributions in Graphite/Epoxy Laminated Composites.* Journal of Composite Materials, 1987. **21** (8): p. 708-733.

256. B. Song, W. Chen, and W. Y. Lu, *Compressive Mechanical Response of a Low-Density Epoxy Foam at Various Strain Rates.* Journal of Materials Science, 2007. **42** (17): p. 7502-7507.

257. Dan Zenkert and Magnus Burman, *Tension, Compression and Shear Fatigue of a Closed Cell Polymer Foam.* Composites Science and Technology, 2009. **69** (6): p. 785-792.

258. M. V. Alonso, M. L. Auad, and S. Nutt, *Short-Fiber-Reinforced Epoxy Foams.* Composites Part A: Applied Science and Manufacturing, 2006. **37** (11): p. 1952-1960.

259. Mark Drela, *XFOIL 6.94 User Guide* 2001

260. M. Togneri, I. Masters, R. Malki, and A. Rio, *Flume Measurements of Lift and Drag for Selected Tidal Turbine Blade Sections.* Under review., 2015.

261. S.A. Ning, *Airfoilprep Documentation Release 0.1.0*, National Renewable Energy Laboratory, 2013: Denver, USA

262. Larry A. Viterna and David C. Janetzke, *Theoretical and Experimental Power from Large Horizontai-Axis Wind Turbines*, 1982, National Aeronautics and Space Administration, Lewis Research Center

263. James L. Tangler. *The Nebulous Art of Using Wind-Tunnel Airfoil Data for Predicting Rotor Performance: Preprint*, in *21st ASME Wind Energy Conference,* 2002, Reno, Nevada.

264. T. McCombes and A.S. Iyer, *WP2: Marine Energy System Testing - Standardisation and Best Practice D2.2: Collation of Tidal Test Options*, 2012, Marine Renewables Infrastructure Network

265. James Mcnaughton, Stefano Rolfo, David Apsley, Tim Stallard, and Peter Stansby. *Cfd Predicted Effect of EMEC Velocity Profiles on a Tidal Stream Turbine*, in *2nd Oxford Tidal Energy Workshop,* 2013, Oxford, UK.

266. G. Germain, A.S. Bahaj, C.Huxley-Reynard, and P.Roberts. *Facilities for Marine Current Energy Converter Characterization*, in *7th EWTEC,* 2007, Portugal.

267. Tonio Sant, *Improving Bem-Based Aerodynamic Models in Wind Turbine Design Codes*, PhD: Department of Mechanical Engineering, University of Malta and Delft University of Technology, 2007.

268. I. A. Milne, A. H. Day, R. N. Sharma, and R. G. J. Flay, *Blade Loading on Tidal Turbines for Uniform Unsteady Flow*. Renewable Energy, 2015. **77**: p. 338-350.

269. Sydney Goldstein, *On the Vortex Theory of Screw Propellers*. Proceedings of the Royal Society A., 1929. **123**.

270. D. A. Doman, R. E. Murray, M.J. Pegg, K. Gracie, C.M. Johnstone, and T. Nevalainen. *Towing Tank Testing of a 1/20th Scale Tidal Turbine*. International Journal of Marine Energy, 2015. **11**: p. 105-109.

271. Ian Masters, Alison Williams, T. Croft, Michael Togneri, Matt Edmunds, Enayatollah Zangiabadi, Iain Fairley, and Harshinie Karunarathna, *A Comparison of Numerical Modelling Techniques for Tidal Stream Turbine Analysis*. Energies, 2015. **8** (8): p. 7833-7853.

272. Katie Gracie-Orr, Thomas M. Nevalainen, Cameron M. Johnstone, Robynne E. Murray, Darrel A. Doman, and Michael J. Pegg, *Development and Initial Application of a Blade Design Methodology for Overspeed Power-Regulated Tidal Turbines*. International Journal of Marine Energy, 2016. **In press.**

273. Airborne Marine, *Nautricity Goes EMEC with Airborne Marine Tidal Blades*, Personnel communication, 2013.

274. B.R. Vidyashankar and A.V. Krishna Murty, *Analysis of Laminates with Ply Drops*. Composites Science and Technology, 2001. **61**: p. 749–758.

275. M. Ishak Yuce and Abdullah Muratoglu, *Hydrokinetic Energy Conversion Systems: A Technology Status Review*. Renewable and Sustainable Energy Reviews, 2015. **43**: p. 72-82.

276. E. Lozano-Minguez, A. J. Kolios, and F. P. Brennan, *Multi-Criteria Assessment of Offshore Wind Turbine Support Structures*. Renewable Energy, 2011. **36** (11): p. 2831-2837.

277. Nicolas Maslov, Jean-Frédéric Charpentier, and Christophe Claramunt, *A Modelling Approach for a Cost-Based Evaluation of the Energy Produced by a Marine Energy Farm*. International Journal of Marine Energy, 2015. **9**: p. 1-19.

278. I. G. Bryden, S. Naik, P. Fraenkel, and C. R. Bullen, *Matching Tidal Current Plants to Local Flow Conditions*. Energy, 1998. **23** (9): p. 699–709.

279. R. E. Murray, Thomas M. Nevalainen, Katie Gracie-Orr, D. A. Doman, and M. J. Pegg, Cameron M. Johnstone, *Passively adaptive tidal turbine blades: Design tool development and initial verification*. International Journal of Marine Energy, 2016. **14**: p. 101-124.

APPENDIX A: CLASSICAL LAMINATION THEORY

Classical Laminate Theory (CLT), as described in [215] can be used to evaluate the stress-strain relationship of composite laminates. The Kirchoff hypotheses expresses the in-plane displacement of a generic point during bending as a function of the slope of the mid-plane (derivative of the vertical displacement, w_o) and the point distance from the mid-plane (z), such that the x and y-displacements are respectively:

$$u = u_o - z\frac{\partial w_o}{\partial x} \qquad\qquad \text{A-1}$$

$$v = v_o - z\frac{\partial w_o}{\partial y} \qquad\qquad \text{A-2}$$

According to assumptions made in Classical Plate Theory (CPT), the displacement, w_o , of any point in the sample can be considered identical to the vertical displacement of the mid-plane, w. This means displacements of a generic point in the plate can be expressed as:

$$u(x_o, y_o, z) = u_o(x_o, y_o) - z\frac{\partial w_o}{\partial x} \qquad\qquad \text{A-3}$$

$$v(x_o, y_o, z) = v_o(x_o, y_o) - z\frac{\partial w_o}{\partial y} \qquad\qquad \text{A-4}$$

$$w(x_o, y_o, z) \cong w_o(x_o, y_o) \qquad\qquad \text{A-5}$$

The strain in the laminate is the gradient (derivative) of the mid-plane displacements, and the expression of the displacements can be substituted into this definition of strain to give:

$$\varepsilon_{xx} = \frac{\partial u_o}{\partial x} - z\frac{\partial^2 w_o}{\partial x^2}, \quad \varepsilon_{yy} = \frac{\partial v_o}{\partial y} - z\frac{\partial^2 w_o}{\partial y^2}, \quad \varepsilon_{zz} = 0 \qquad \text{A-6}$$

$$\gamma_{yz} = \gamma_{xz} = 0, \quad \gamma_{xy} = \frac{\partial u_o}{\partial x} + \frac{\partial v_o}{\partial y} - 2z\frac{\partial^2 w_o}{\partial x \partial y} \qquad \text{A-7}$$

The strain at any point of the plate is the sum of a contribution due to membrane deformation ($\varepsilon_{o,xx} = \frac{\partial u_o}{\partial x}$) and a contribution due to flexural deformation ($k_x = \frac{\partial^2 w_o}{\partial x^2}$). The strain relationship can be expressed as:

$$[\varepsilon] = [\varepsilon_o] + z[k] \qquad \text{A-8}$$

The $[\varepsilon_o]$ matrix is the mid-pane strains, and z is the location through the thickness of the plate. The $[k]$ matrix is composed of k_x, k_y and k_{xy}. In this case, the sample is subject to a bending moment in the x-x direction, and the twisting rate of interest is that in the x-y plane, k_{xy}, which is the twist induced by the deformation coupling of the laminate.

The stress in the laminate can be determined from the strains using the transformed reduced stiffness matrix $\overline{Q_{IJ}}$, which relates strains to stresses similarly to Hookes Law.

$$[\sigma] = \overline{Q}[\varepsilon_o] + z\overline{Q}[k] \qquad \text{A-9}$$

Because there is more than one layer in a laminate, the stresses may differ for each layer because the material properties or laminate angles may vary between layers (and hence $\overline{Q}_{ij}$ may vary from layer to layer). The stress components acting in the plate can be integrated along the plate thickness to find the resultant (or applied) forces and the moments per unit width. This is done for each individual lamina and summed throughout the plate. This gives three forces per unit width (N_x, N_y and N_{xy}), and three moments per unit width (M_x, M_y and M_{xy}), as follows:

$$N_x = \int_{-\frac{h}{2}}^{\frac{h}{2}} \sigma_x dz, \quad N_y = \int_{-\frac{h}{2}}^{\frac{h}{2}} \sigma_y dz, \quad N_{xy} = \int_{-\frac{h}{2}}^{\frac{h}{2}} \tau_{xy} dz \qquad \text{A-10}$$

$$M_x = \int_{-\frac{h}{2}}^{\frac{h}{2}} \sigma_x z\,dz, \quad M_y = \int_{-\frac{h}{2}}^{\frac{h}{2}} \sigma_y z\,dz, \quad M_{xy} = \int_{-\frac{h}{2}}^{\frac{h}{2}} \tau_{xy} z\,dz \qquad \text{A-11}$$

These six components are the parameters that describe the internal forces in the plate. To transform the internal forces in the sample to stresses in the plate, or vice versa, stiffness matrices are used, which couple the membrane, ε_0, and flexural, k, deformations, as follows:

$$\begin{bmatrix} [N] \\ [M] \end{bmatrix} = \begin{bmatrix} [A] & [B] \\ [B] & [D] \end{bmatrix} \cdot \begin{bmatrix} \varepsilon_0 \\ k \end{bmatrix} \qquad \text{A-12}$$

The [A], [B], and [D] matrices are called the extensional, coupling, and bending stiffness matrices, respectively. The extensional stiffness matrix [A] relates the resultant in-plane forces to the in-plane strains, and the bending stiffness matrix [D] relates the resultant bending moments to the plate curvatures. The coupling stiffness matrix [B] couples the force and moment terms to the mid-plane strains and mid-plane curvatures [215]. These matrixes are calculated as follows:

$$A_{ij} = \sum_{k=1}^{N} \left(\overline{Q_{ij}} \right)_k \left(z_{k+1} - z_k \right) \qquad \text{A-13}$$

$$B_{ij} = \frac{1}{2} \sum_{k=1}^{N} \left(\overline{Q_{ij}} \right)_k \left(z^2_{k+1} - z^2_k \right) \qquad \text{A-14}$$

$$D_{ij} = \frac{1}{3} \sum_{k=1}^{N} \left(\overline{Q_{ij}} \right)_k \left(z^3_{k+1} - z^3_k \right) \qquad \text{A-15}$$

where k is the layer in question, and z is the z-location of the top and bottom of ply layer k, where z is positive downward, as shown in [215]. $\overline{Q_{ij}}$ is the transformed reduced stiffness matrix which relates the material properties in the principal directions (x and y) to the material properties in the ply orientations (L and T, where L and T are the local fiber and transverse directions, respectively) and is calculated by:

$$\overline{Q_{11}} = Q_{11} \cos^4 \theta + 2\left(Q_{12} + 2Q_{66}\right)\sin^2 \theta \cos^2 \theta + Q_{22} \sin^4 \theta$$

$$\overline{Q_{22}} = Q_{11} \sin^4 \theta + 2\left(Q_{12} + 2Q_{66}\right)\sin^2 \theta \cos^2 \theta + Q_{22} \cos^4 \theta$$

$$\overline{Q_{66}} = \left(Q_{11} + Q_{22} - 2Q_{12} - 2Q_{66}\right)\sin^2 \theta \cos^2 \theta + Q_{66}\left(\sin^4 \theta + \cos^4 \theta\right)$$

$$\overline{Q_{12}} = \left(Q_{11} + Q_{22} - 4Q_{66}\right)\sin^2 \theta \cos^2 \theta + Q_{12}\left(\sin^4 \theta + \cos^4 \theta\right) \qquad \text{A-16}$$

$$\overline{Q_{16}} = \left(Q_{11} - Q_{12} - 2Q_{66}\right)\cos^3 \theta \sin \theta + \left(Q_{12} - Q_{22} + 2Q_{66}\right)\sin^3 \theta \cos \theta$$

$$\overline{Q_{26}} = \left(Q_{11} - Q_{12} - 2Q_{66}\right)\sin^3 \theta \cos \theta + \left(Q_{12} - Q_{22} + 2Q_{66}\right)\cos^3 \theta \sin \theta$$

Where θ is the ply orientation for layer k, and $\overline{Q_{ij}}$ are the reduced in-plane stiffness coefficients of individual lamina, calculated by:

$$Q_{11} = \frac{E_L^2}{E_L - v^2 E_T}, \quad Q_{12} = \frac{v E_T}{1 - v^2}, \quad Q_{22} = \frac{E_T E_L}{E_L - v^2 E_T}, \quad Q_{66} = G \qquad \text{A-17}$$

E_L is Young's modulus of elasticity in the local fiber direction, and E_T is Young's modulus of elasticity in the transverse direction. v is Poisson's ratio relating strains in the L and T directions, and G is the in-plane shear modulus. The global (in x and y coordinates) strain in each lamina can be determined at any location z by:

$$\begin{bmatrix} \varepsilon_x \\ \varepsilon_y \\ \gamma_{xy} \end{bmatrix}_{\text{At } z \text{ location}} = \begin{bmatrix} \varepsilon_{x,o} \\ \varepsilon_{y,o} \\ \gamma_{xy,o} \end{bmatrix} + z \begin{bmatrix} k_x \\ k_y \\ k_{xy} \end{bmatrix} \qquad \text{A-18}$$

The stresses at any z location can then be found by:

$$\begin{bmatrix} \sigma_x \\ \sigma_y \\ \tau_{xy} \end{bmatrix}_{\text{At } z \text{ location}} = \overline{Q_{ij}} \begin{bmatrix} \varepsilon_x \\ \varepsilon_y \\ \gamma_{xy} \end{bmatrix} \qquad \text{A-19}$$

where $\overline{Q_{ij}}$ is for the layer in question. The local stresses and strains (in L and T directions) can then be found by:

$$\begin{bmatrix} \sigma_x \\ \sigma_y \\ \tau_{xy} \end{bmatrix} = [T]^{-1} \begin{bmatrix} \sigma_L \\ \sigma_T \\ \tau_{LT} \end{bmatrix} \qquad \text{A-20}$$

$$\begin{bmatrix} \varepsilon_L \\ \varepsilon_T \\ \gamma_{LT} \end{bmatrix} = [R][T][R]^{-1} \begin{bmatrix} \varepsilon_x \\ \varepsilon_y \\ \gamma_{xy} \end{bmatrix} \qquad \text{A-21}$$

where $[R]$ is the Reuter matrix:

$$\begin{bmatrix} 1 & 0 & 0 \\ 0 & 1 & 0 \\ 0 & 0 & 2 \end{bmatrix} \qquad \text{A-22}$$

and $[T]$ is the transformation matrix:

$$\begin{pmatrix} \cos^2\theta & \sin^2\theta & -2\sin\theta\cos\theta \\ \sin^2\theta & \cos^2\theta & 2\sin\theta\cos\theta \\ \sin\theta\cos\theta & -\sin\theta\cos\theta & \cos^2\theta - \sin^2\theta \end{pmatrix} \qquad \text{A-23}$$

The above equations were implemented in MATLAB® to formulate an analytical model for the laminate.

APPENDIX B: CALIBRATION- HYDRODYNAMIC TEST SET 1

The thrust, torque, and bending moment sensors were calibrated by applying a known load to the point of application on a lever arm and measuring the output voltage. The voltage was passed through amplifiers, therefore the first step in the calibration process was to zero the amplifiers and set their gains to give a voltage output range which captured the full range of the weights applied, based on a maximum voltage of 10 V. Several sets of calibrations were undertaken, with the initial calibrations being done to ensure components were working properly, and the final calibrations being done once the system was fully ready to be tested. Figure B-1 shows the specially constructed moment lever arm, designed for the calibration of the thrust and blade bending moment transducers. With accurately known lever arm dimensions, the thrust and bending moment transducers were calibrated.
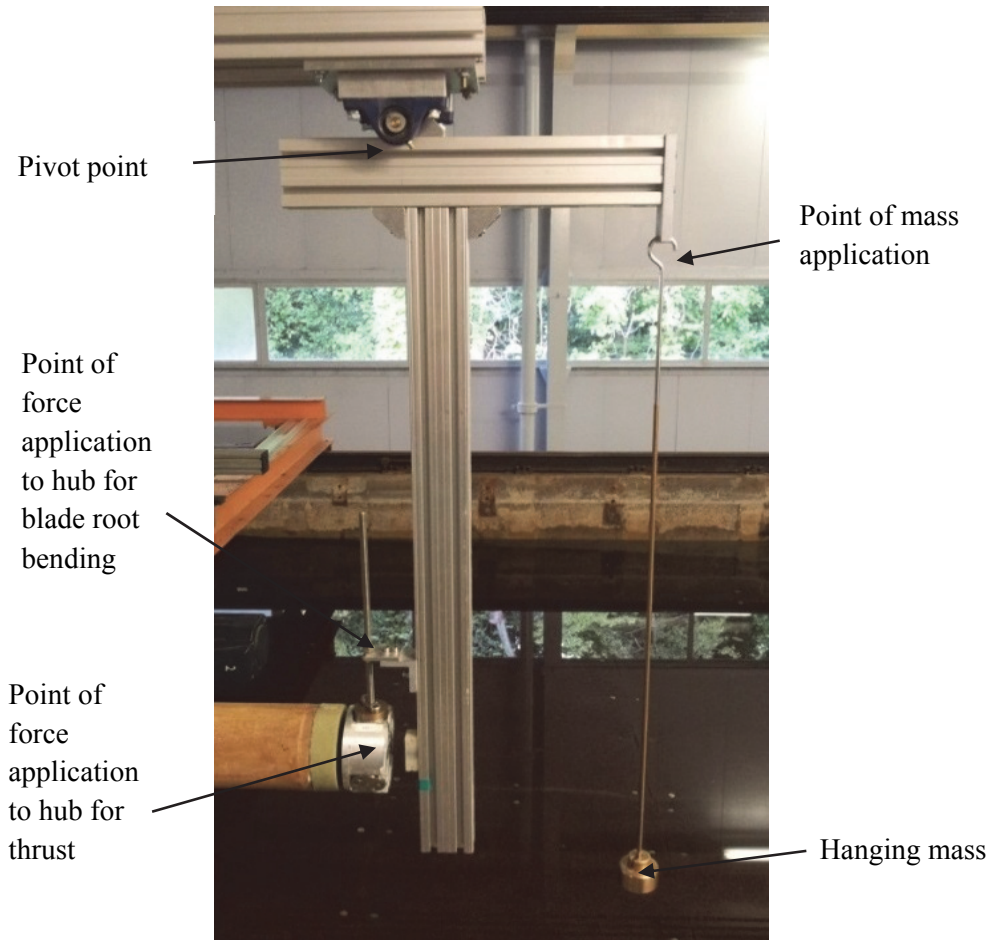
Figure B-1 Lever Arm Dimensions, top left: Thrust calibration, top right: Bending moment calibration, and bottom, photograph of calibration setup

B.1 Thrust Calibration

The thrust load cell was calibrated both statically and dynamically. Statically, there was significant static friction in the system which resulted in inaccurate and non-logical results. Therefore, dynamic calibrations were undertaken by rotating the rotor at a range of different rotational speeds while applying various weights to the moment arm. A small point load applicator was used to apply the load from the moment arm to the center of the rotor hub.

The maximum thrust expected on the hub was 175 N, which is based on the equation:

$$F_{\mathrm{T}} = \frac{1}{2}\rho A U_{\infty}{}^{2}C_{\mathrm{T}} \qquad\qquad B\text{-}1$$

where the value for C_T was from Ian Milne's upper value of 0.7 (Milne, Day, Sharma, & Flay, 2013), the inflow velocity U_∞ was 1 m/s (which is the maximum comfortable carriage speed) and the area, A of the turbine was 0.477 m^2.

Applying the theory of equilibrium to the moment lever arm, the required mass, m_1, to produce the desired calibration thrust force was given by the equation:

$$m_1 = \frac{F_T x_2}{g x_1}$$
B-2

Where g is gravitational acceleration, x_1 is the shorter, horizontal arm of the moment lever arm, and x_2 is the longer, vertical arm of the moment lever arm as in the left-hand diagram in Figure B-1. Therefore, the maximum load applied to the moment arm for the calibration exercise was 686 N (70 kg), more than double the expected thrust value, which equates to a thrust force of 246 N with a lever arm conversion of 0.358 m.

The maximum load applied was set equal to an output of 8 V output on the amplifiers, so that the voltage would be below the 10 V cut off with noise in the signal. A series of masses were loaded and unloaded, and the results were captured by Spike. Along with bigger weights of up to 10 kg, smaller weights (starting at 0.1 kg and increasing by 0.1 kg), were used as well in order to assess the sensitivity of the measurements.

It was found that for the range of expected rotational speeds (10 to 100 RPM), the thrust load as a function of voltage was almost identical, with an R^2 value of 0.99993, as seen in Figure B-2.
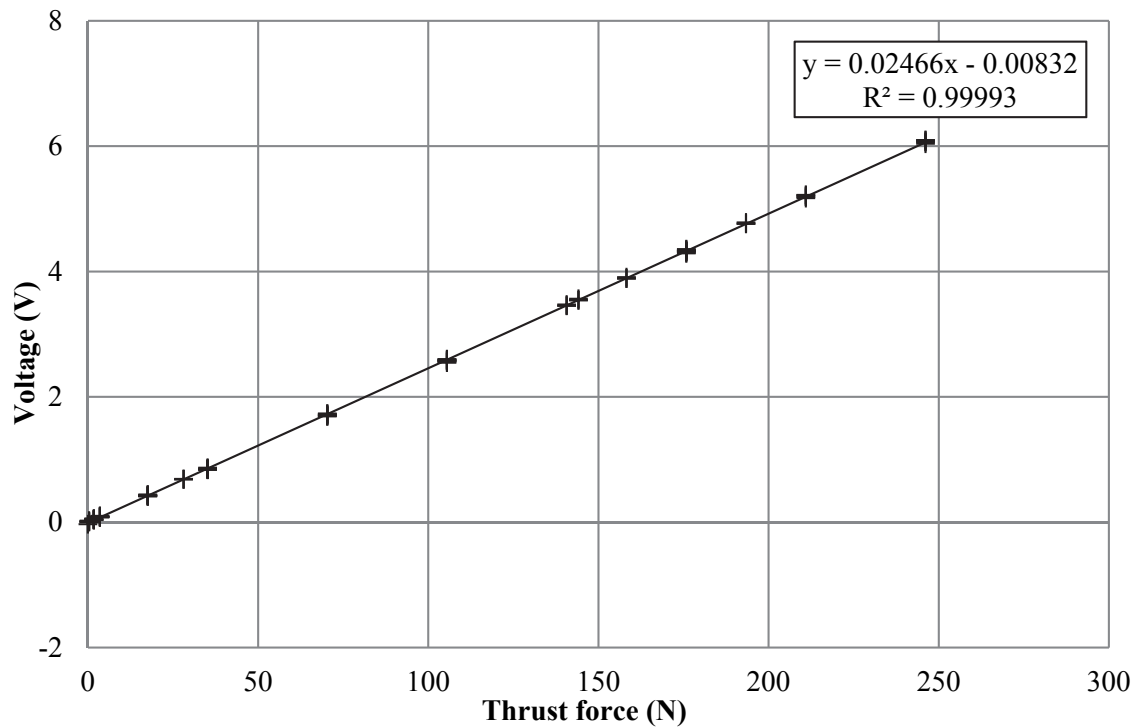
Figure B-2 Thrust load cell calibration.

B.2 Torque Calibration

The torque load cell was calibrated both statically and dynamically. Static calibration is acceptable for the steady flow speeds used for these tests, however, dynamic calibration was required for the oscillatory testing being done using the rig the following week. To calibrate the load cell statically, a metal attachment with two lever arms was bolted to the front of the hub, as shown in Figure B-3. A pulley with hanging weights was attached to one side to achieve an upward force, while hanging weights were applied to the other side to apply a downward force. Hanging weights were loaded and unloaded on both lever arms to apply a known torque. The results of the torque calibration are shown in Figure B-4.
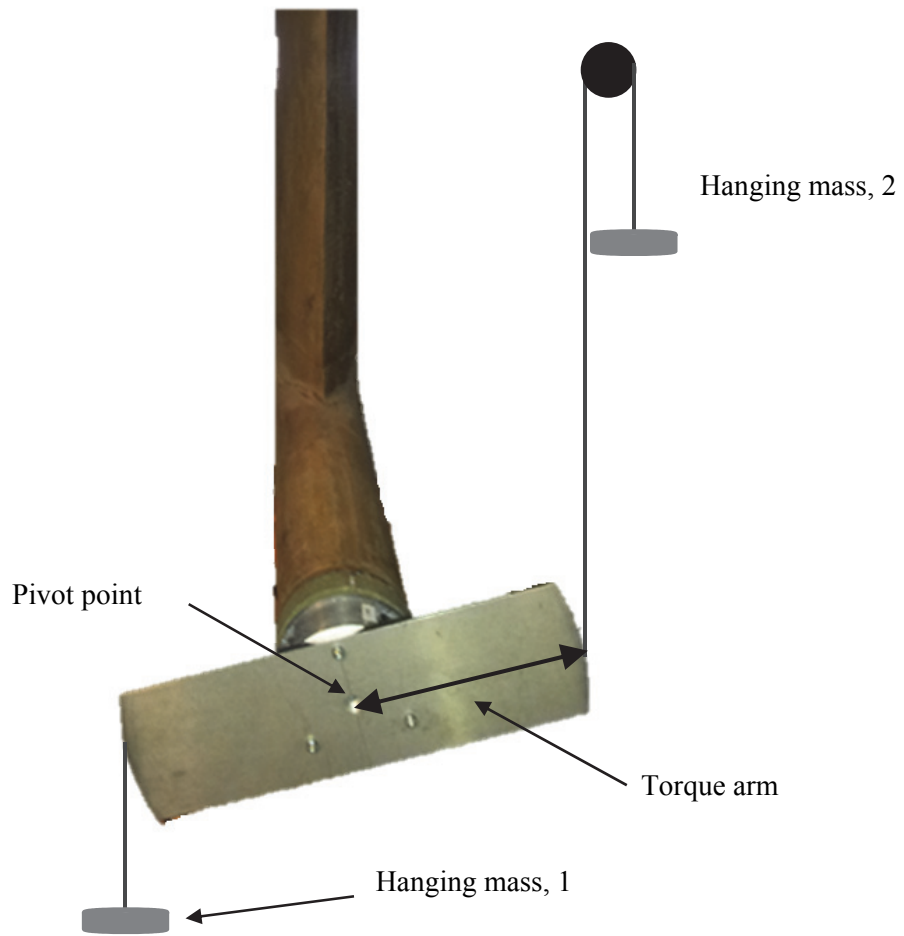
Figure B-3 Torque calibration setup.

Dynamic calibrations were undertaken by sinusoidally oscillating a disk of known mass and radius between two set rotational velocities. The angular acceleration was obtained by taking the derivative of the sine curve input to the motor to varying the rotational velocities, and the moment of inertia of the disk was calculated based on the disk size and weight. The predicted torque was then calculated and compared to the measured torque by the load cell.
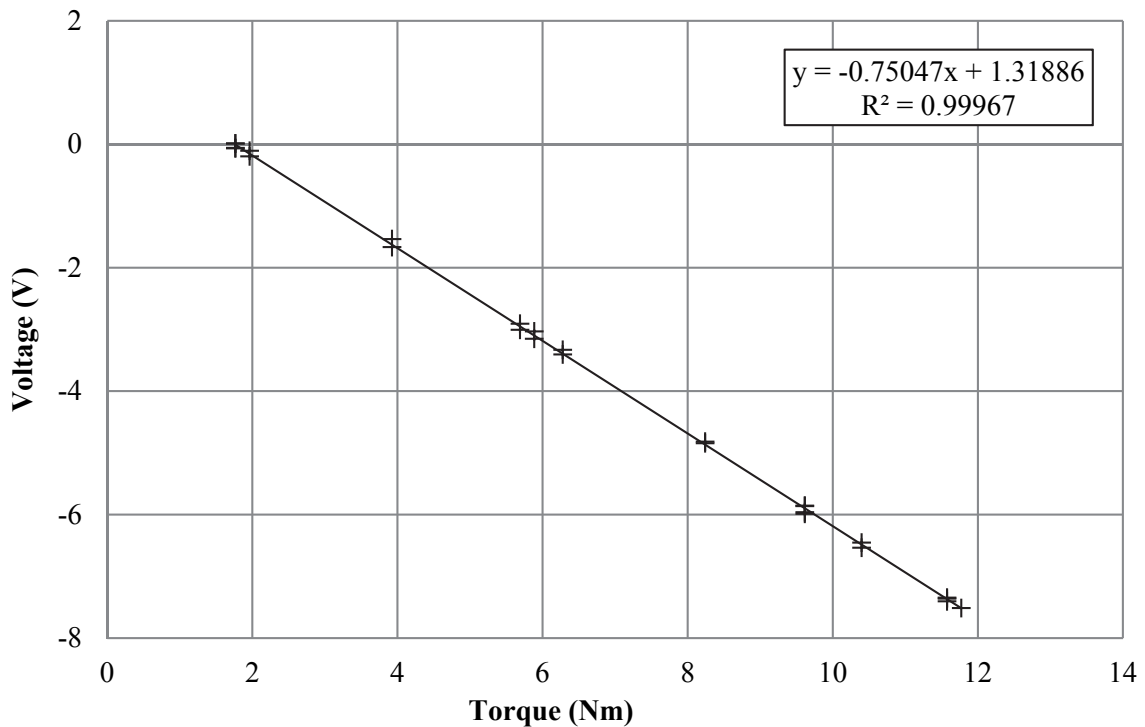
Figure B-4 Torque calibration results.

B.3 Blade Root Bending Moment Strain Gauges

Each blade root transducer required separate calibration. The transducers were calibrated by applying a known bending moment to a point approximately 1/3 of the blade length (79.79 mm, roughly the center of pressure of the blade) away from the rotor-hub connection.

For the axial bending moment sensors, the thrust applied to the hub part of the rotor was neglected, and it was assumed that each blade would take one third of the total thrust force. Taking into consideration the calculated maximum thrust value, a maximum hanging mass of 30 kg was applied to transducers 1 and 2, corresponding to a maximum bending moment at the root of the blade of 16.22 Nm. A range of masses, from 0 kg to 30 kg were applied to the lever arm in 18 steps, then removed (see Figure B-1 for the point of load application). Smaller steps in the load were applied at the lower and upper ends of the range to assess the sensitivity of the readings. The equation used to obtain the moment at the blade root is given by:

$$M_b = \frac{m_1 g x_1 x_4}{x_3}$$

<div align="right">B-3</div>

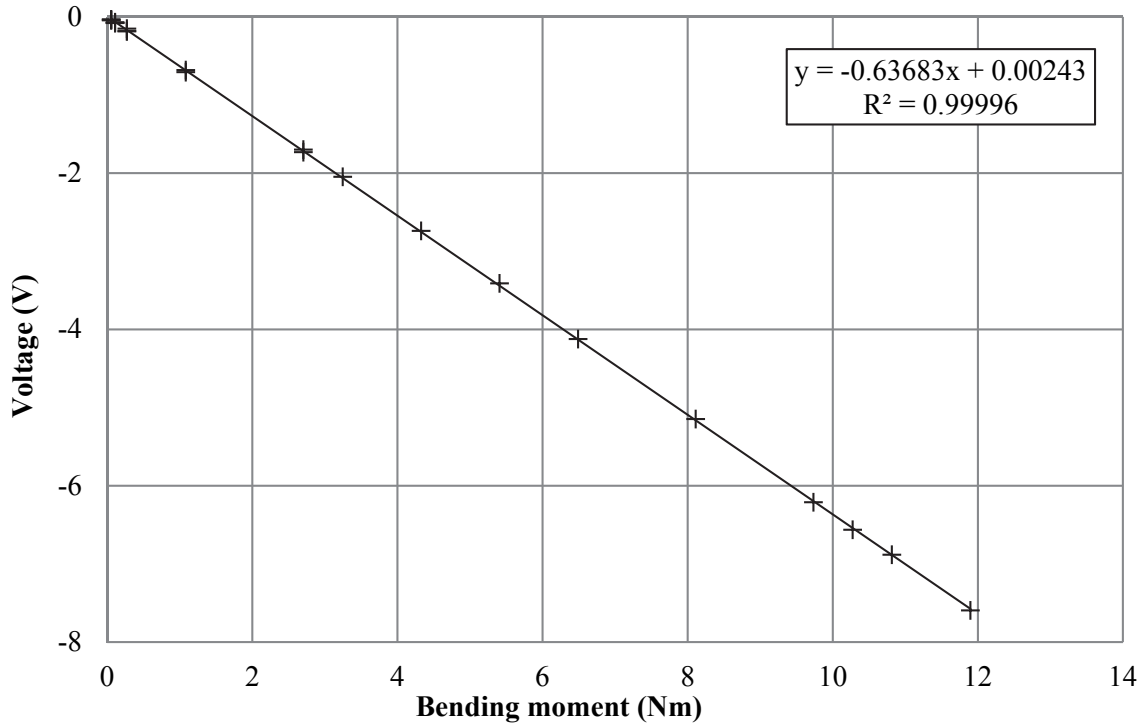As an example, the calibration curve for blade 1 is shown in Figure B-5.

Figure B-5 Bar 1 calibration data

Linear trend lines were applied– the equations of these are shown. It was expected that the calibration data would show a linear trend: the high coefficients of determination given in Figure B-5 indicate that this was the case. Initial tests saw non-linear trends, however, the system had only been plugged in for an hour, and was thought to be responding to thermal changes due to the voltage applied.

Blade 2 and blade 3 responded similarly to blade 1, with highly linear trends.

APPENDIX C: CALIBRATION- HYDRODYNAMIC TEST SET 2

The thrust strain gauge was calibrated by applying a known load to a cable attached to the center of the hub to apply a purely axial force to the center of the hub, and measuring the output voltage. Figure C-1 shows the voltage-load trend.
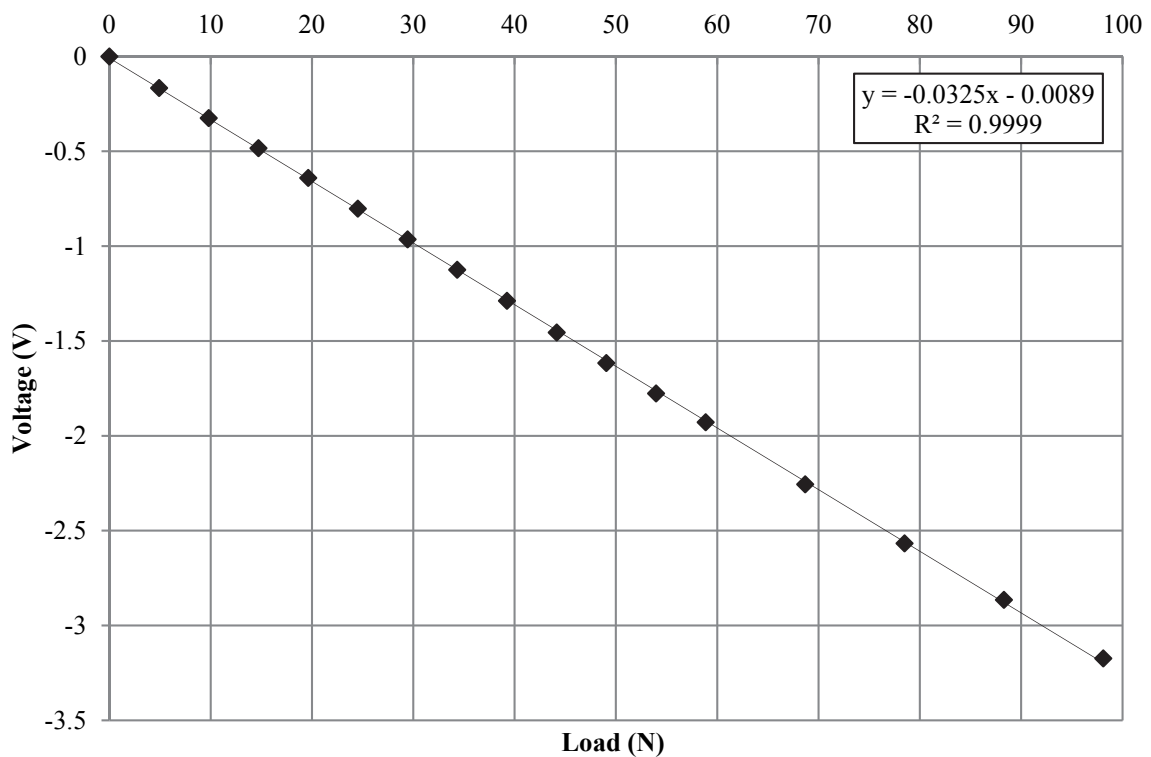
Figure C-1 Torque calibration results

The calibration results were highly linear with coefficients of determination of $R^2 = 0.9999$.